



**HAL**  
open science

# Selective gas sensors based on tin dioxide and hybrid oxohydroxoorganotin materials

Szu-Hsuan Lee

► **To cite this version:**

Szu-Hsuan Lee. Selective gas sensors based on tin dioxide and hybrid oxohydroxoorganotin materials. Other. Université de Bordeaux; Technische Universität (Darmstadt, Allemagne), 2019. English. NNT : 2019BORD0034 . tel-02927779

**HAL Id: tel-02927779**

**<https://theses.hal.science/tel-02927779v1>**

Submitted on 2 Sep 2020

**HAL** is a multi-disciplinary open access archive for the deposit and dissemination of scientific research documents, whether they are published or not. The documents may come from teaching and research institutions in France or abroad, or from public or private research centers.

L'archive ouverte pluridisciplinaire **HAL**, est destinée au dépôt et à la diffusion de documents scientifiques de niveau recherche, publiés ou non, émanant des établissements d'enseignement et de recherche français ou étrangers, des laboratoires publics ou privés.

THÈSE EN COTUTELLE PRÉSENTÉE  
POUR OBTENIR LE GRADE DE  
**DOCTEUR DE**  
**L'UNIVERSITÉ DE BORDEAUX**  
**ET TECHNISCHE UNIVERSITÄT DARMSTADT**

ÉCOLE DOCTORALE UBX

ÉCOLE DOCTORALE DU PARTENAIRE

SPÉCIALITÉ : Physico-Chimie de la Matière Condensée

Par Szu-Hsuan LEE

**Selective gas sensors based on tin dioxide and hybrid  
oxohydroxoorganotin materials**

Sous la direction de M. TOUPANCE, Thierry et de M. RIEDEL, Ralf

Soutenue le 20/03/2019

Membres du jury :

M. SERVANT, Laurent	Université de Bordeaux	Président
M. TOUPANCE, Thierry	Université de Bordeaux	Directeur
M. RIEDEL, Ralf	Technische Universität Darmstadt	Co-directeur
Mme KAHN, Myrtil	CNRS, Université de Toulouse	Rapporteur
M. SANCHEZ, Jean-Baptiste	Université de Besançon	Rapporteur
M. PONZONI, Andrea	National Research Council - Italie	Examineur
M. JAEGERMANN, Wolfram	Technische Universität Darmstadt	Invité
M. NICOLAS, Yohann	Université de Bordeaux	Invité
M. CLEMENS, Oliver	Technische Universität Darmstadt	Invité

# THESIS

presented at

**UNIVERSITY OF BORDEAUX**

and

**TECHNISCHE UNIVERSITÄT DARMSTADT**

DOCTORAL SCHOOL OF CHEMICAL SCIENCES

INTERNATIONAL DOCTORAL SCHOOL IN FUNCTIONAL MATERIALS

by

**Szu-Hsuan LEE**

to obtain the degree of

**DOCTOR**

SPECIALITY : Physical Chemistry of Condensed Material

---

## **Selective gas sensors based on tin dioxide and hybrid oxohydroxoorganotin materials**

---

defended on: 20<sup>th</sup> of March, 2019

Members of the jury:

Prof. Dr. Laurent SERVANT, University of Bordeaux	<b>President</b>
Prof. Dr. Thierry TOUPANCE, University of Bordeaux	<b>supervisor</b>
Prof. Dr. Ralf RIEDEL, Technische Universität Darmstadt	<b>co-supervisor</b>
Dr. Myrtil KAHN, University of Toulouse	<b>reviewer</b>
Dr. Jean-Baptiste SANCHEZ, University of Besançon	<b>reviewer</b>
Dr. Andrea PONZONI, National Research Council- Italie	<b>examinier</b>
Prof. Dr. Wolfram JAEGERMANN, Technische Universität Darmstadt	<b>invited</b>
Prof. Dr. Oliver CLEMENS, Technische Universität Darmstadt	<b>invited</b>
Dr. Yohann NICOLAS, University of Bordeaux	<b>invited</b>

## Acknowledgements

I would like to express my sincere gratitude to those who supported my endeavors during my PhD work:

Firstly, I express my deepest gratitude towards **Prof. Dr. Thierry Toupance**, my PhD advisor and the director of this project, for choosing me to be the PhD student in this research, offering me a fair work bench, his valuable time and closely following my work during the course of my doctoral thesis. I appreciate his constant motivation and continuous support throughout this period.

I thank **Prof. Dr. Ralf Riedel**, my PhD advisor in TUD, for selecting me as the PhD candidate in this research work, providing the working surrounding in TUD which has shaped my skills in diverse aspects to be able to face different challenges.

I am indebted to **Dr. Yohann Nicolas** for his supervision, advice, and invaluable time he gave in discussing various issues throughout my organic synthesis work. His scientific intuition has exceptionally inspired me and enriched my growth as a student, a researcher and a scientist.

I am truly grateful to **Dr. Cristina Schitco**, for bridging our cooperation with the sensor laboratory team from university of Brescia. Due to this connection she made, this work could be satisfactorily accomplished.

I especially show my deepest appreciation to **Dr. Andrea Ponzoni** and **Dr. Vardan Galstyan**, for their efforts in our gas sensing measurements and generous sharing with their experiences and professional knowledge. In any amount, I appreciate their help and it is not enough.

I also like to mention **Dr. Christian Dietz** and **Dr. Na Liu**, for their kindly help in AFM measurements; **Dr. Qingbo Wen** for his friendly assistance in SEM measurements; **Claudia Fasel**, for her TGA analyses; **Marion Gayot**, for her TEM analyses; **Christine Labrugere**, for her XPS analyses; **Dr. Cybille Rossy-Huguet**, for her NMR measurements; **Claire Mouche**, for her mass analyses; **Dr. Marie-Anne Dourges**, for her TGA analyses and N<sub>2</sub> sorption measurements; **Eric Naillou**, for his exceptional skill for making any shape of glassware that I desired.

All the people that I have met during my study in Bordeaux and Darmstadt including **Imane, Dieuwertje, Qian, Siliu, Camille, Baptiste, Shun, Juan, Yannick H, Yannick M, Susanne, Guillaume, Amandine, Luc, Marc, Celine, Ann, Laurent, Svitlana, Raphael, Thibaut, Edis, Amelie, Philippe, Nan, Hairui, Xingmin, Wenjie, Pan, Sasa, Fangtong, Cong,**



**Benjamin, Dario, Dado, Lukas, Felix, Christina, Ruihao, Cong Xin, Sergey.** Thank them for being accompanies in the process of my PhD study and for all the time we shared and experiences we had. I still appreciate those who have helped me during this period even though I might miss their names in the list.

I particularly thank to **Prof. Yen-Hsiang Liu**, my Master advisor in Taiwan, for encouraging me to study abroad and supporting my decision since the beginning of my academic study.

My Taiwanese friends including **Blanche, Pheobe, Mei, Annie, Yung-Chuan, Yi-Ching, Zoe, 12 animals**, are the ones who participate in my life as a special form in my mind.

To my beloved family:

To my dear parents and my lovely sister in Taiwan, I sincerely thank them for always supporting me behind my back unconditionally. Nothing can be compared to the love they have given to me.

To my love and my husband - **Benjamin**, I earnestly thank him for being such an important role in my life, taking care of me in every possible way, sharing all my joys and sorrows, and in particular, encouraging me to pass through the whole difficulties through this PhD journey.

To my lovable daughter - **Charlotte**, the most wonderful present arrives to me. She brings me the best happiness and loves in every single day.

To my adorable family-in-law: **Brigitte, Jean Noël, Brenda, Florent, Viktor, Brian, Elina, Lucas** and grandparents-in-law. I genuinely thank them for their generous loves and supports to make me feel as comfortable as at home.

In the end, I would also like to acknowledge the financial support from the **Erasmus Mundus** for my PhD work. This work has been performed within the framework of the project “**2014-03-EM Selective gas sensors based on organotin oxide hybrid materials**” of Erasmus Mundus Joint doctorates program “**International doctoral school in functional materials**”.

## Résumé en français

Les problèmes environnementaux liés à l'utilisation généralisée des combustibles fossiles et des composés organiques volatils (COV) ainsi que les applications industrielles de gaz dangereux tels que l'hydrogène ( $H_2$ ) et l'acide fluorhydrique (HF) nécessitent la mise au point de dispositifs efficaces pour la détection sélective de ces gaz à des teneurs très faibles. Dans ce contexte, les capteurs de gaz à l'état solide basés sur des couches actives à base d'oxydes métalliques semiconducteurs jouent un rôle majeur, en particulier ceux exploitant les changements de résistance électrique des matériaux en fonction de l'atmosphère à laquelle ils sont exposés. Ainsi, le dioxyde d'étain ( $SnO_2$ ), de structure cristalline tétragonale (type rutile) connue sous le nom de cassitérite, est le matériau prototype le plus couramment utilisé et le mieux compris à ce jour dans les capteurs de gaz commerciaux. Néanmoins, malgré les progrès récents réalisés dans le domaine de la détection de gaz, la conception de nouveaux systèmes efficaces et sélectifs reste nécessaire. L'objectif de ce travail était donc de tracer de nouvelles perspectives dans le domaine des capteurs de gaz à base d'oxyde d'étain en ajustant avec précision la nature chimique, la texture et la morphologie de la couche active. Deux approches principales ont donc été mises en œuvre pour préparer de nouveaux matériaux. La première a consisté à ajuster précisément les conditions hydrothermales pour la croissance de particules de dioxyde d'étain bien définies à partir d'un colloïde commercial largement disponible. La deuxième approche, beaucoup plus originale, a consisté à synthétiser des précurseurs organiques organométalliques uniques conduisant à des matériaux hybrides organoétain après hydrolyse et condensation selon le procédé sol-gel.

Tout d'abord, les nanoparticules de dioxyde d'étain ( $SnO_2$ ) ont été synthétisées directement à l'aide d'une voie liquide à l'échelle du multi-gramme mettant en jeu un traitement hydrothermal dans des conditions acides ou basiques, d'une suspension commerciale de particules de  $SnO_2$  contenant des ions potassium ( $K^+$ ). Après post-traitement thermique, les nanomatériaux obtenus ont été soigneusement caractérisés par spectroscopie FTIR et Raman,

par diffraction des rayons X sur poudre (DRX), par microscopie électronique à transmission (MET), par spectroscopie de photoélectrons X (XPS) et par porosimétrie d'adsorption d'azote. Quelles que soient les conditions utilisées, la diffraction des rayons X sur poudre et la spectroscopie Raman ont confirmé la formation de nanoparticules de SnO<sub>2</sub> de structure cristalline tétragonale de type cassitérite. Cependant, la variation des conditions de pH et de la température du post-traitement thermique a conduit à des nanoparticules de cassitérite SnO<sub>2</sub> avec des tailles de cristallites comprises entre 7,3 et 9,7 nm et des surfaces spécifiques Brunauer-Emmett-Teller comprises entre 61 et 106 m<sup>2</sup>.g<sup>-1</sup> (Table 1). Un bon accord entre les tailles de cristallites déduites des mesures DRX et des tailles de particules déterminées par MET a été observé indiquant un caractère quasi monocristallin des nanoparticules de SnO<sub>2</sub> obtenues. D'une manière générale, l'étape de calcination influe peu sur les propriétés des particules préparées en milieu basique tandis que cette étape induit un léger accroissement des tailles moyennes de particules pour les échantillons synthétisés en milieu acide.

Sample	Taille moyenne des cristallites (DRX) (nm) <sup>a</sup>	Taille moyenne des particules (TEM) (nm) <sup>b</sup>	S <sub>BET</sub> (m <sup>2</sup> .g <sup>-1</sup> ) <sup>c</sup>	Volume poreux total (cm <sup>3</sup> .g <sup>-1</sup> ) <sup>d</sup>	Taille moyenne des pores (nm) <sup>e</sup>
<b>TOa<sup>90</sup></b>	8.6 ± 0.5	10.7 ± 1.0	79.0 ± 2.5	0.31 ± 0.04	15.6 ± 2.0
<b>TOa<sup>600</sup></b>	9.7 ± 0.5	11.6 ± 1.0	61.0 ± 2.0	0.29 ± 0.04	19.7 ± 2.6
<b>TOb<sup>90</sup></b>	7.6 ± 0.4	8.5 ± 0.5	106.0 ± 3.0	0.53 ± 0.07	20.7 ± 2.7
<b>TOb<sup>600</sup></b>	7.3 ± 0.4	8.4 ± 0.5	98.0 ± 3.0	0.50 ± 0.07	20.6 ± 2.7

**Table 1: Tailles moyennes des cristallites et des particules, et données issues des mesures de sorption d'azote pour les nanoparticules de SnO<sub>2</sub> : TOa<sup>90</sup> et TOa<sup>600</sup> préparées à pH = 4 puis traitées à 90 ou 600°C sous air ; TOb<sup>90</sup> ou TOb<sup>600</sup> préparées à pH = 11 puis traitées à 90 et 600°C sous air. <sup>a</sup> Estimée à partir des largeurs à mi-hauteur des pics de diffraction en utilisant la relation de Scherrer. <sup>b</sup> Déduite des images MET. <sup>c</sup> Aire spécifique déterminée par la méthode BET. <sup>d</sup> Volume total poreux estimé à partir d'une analyse mono-point.. <sup>e</sup> Taille moyenne des pores calculée par la méthode BJH (appliquée à la branche de désorption).**

Par ailleurs, les images MET haute résolution et des clichés de diffraction électronique sur des zones particulières de chaque échantillon révèlent la formation de particules de SnO<sub>2</sub> bien cristallisées exposant des faces cristallines bien définies typiques du SnO<sub>2</sub> cassitérite. Par exemple, l'échantillon **TOa<sup>90</sup>** présente des plans cristallins avec des distances inter-réticulaires de 0.33, 0.21 et 0.17 nm correspondant aux plans (110), (200) et (211) du SnO<sub>2</sub> cassitérite, (Figure 1). Les mêmes faces cristallines sont aussi observées dans les images MET haute résolution des autres échantillons. Par conséquent, les nanopoudres obtenues après traitement hydrothermal exposent déjà des faces cristallines de faible énergie telles que les faces [110] (1.554 J.m<sup>-2</sup>) expliquant l'absence de changement dans la nature des faces cristallines exposées après calcination.

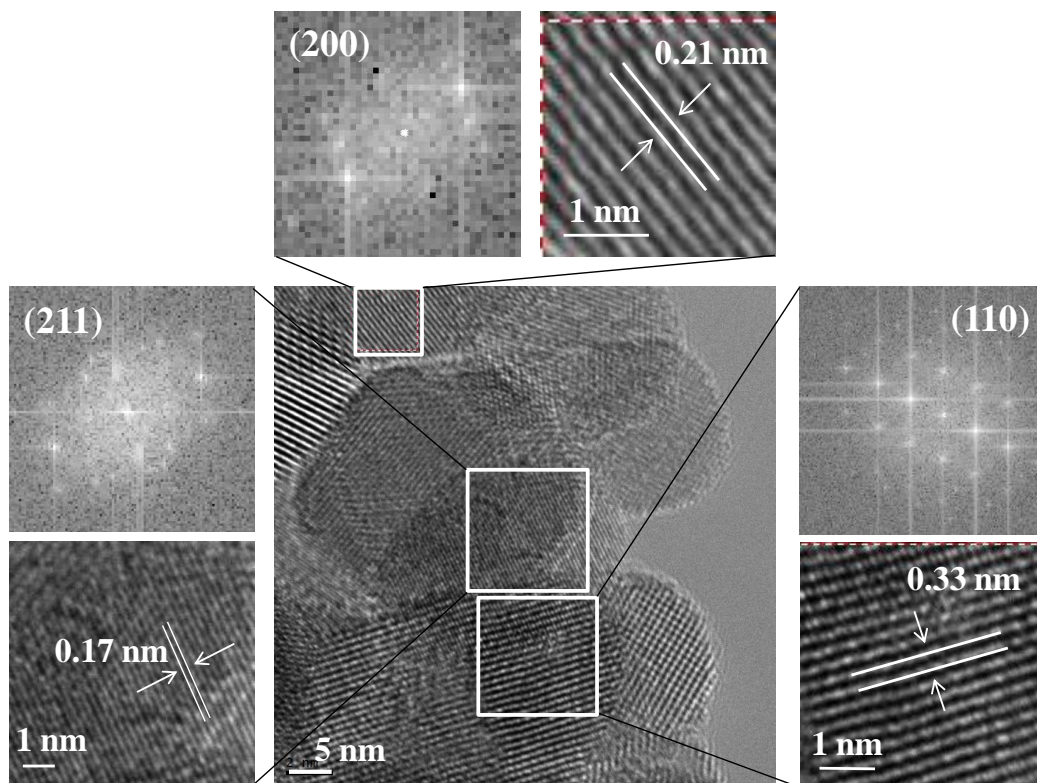


**Figure 1: Images TEM haute resolution et clichés de diffraction électronique sur des zones particulières de TOa<sup>90</sup>.**

Par ailleurs, d'après les mesures XPS, la surface des nanopoudres de SnO<sub>2</sub> synthétisées contient les raies d'émission caractéristique des éléments étain, oxygène et potassium. Quelles

que soient les conditions de préparation, la région Sn3d présente deux pics à  $487.0 \pm 0.1$  eV et  $495.4 \pm 0.1$  eV du fait du couplage spin-orbite des états 3d. La différence d'énergie entre ces deux pics a été calculée à  $8.4 \pm 0.1$  eV, ce qui est en accord avec les valeurs rapportées pour SnO<sub>2</sub> et la présence de centres Sn(IV). En revanche, le taux d'élément potassium dépend fortement des conditions de préparation. Ainsi, le rapport atomique de surface K/Sn a été évalué à 0.01-0.02 et 0.08-0.09 pour les échantillons **TOa** et **TOb**, respectivement, ce qui est significativement plus faible que la teneur observée dans le colloïde commercial séché (K/Sn = 0.19 at%). Les conditions acides favorisent donc l'élimination des cations de potassium.

Exposées à des gaz réducteurs tels que l'hydrogène (H<sub>2</sub>), le monoxyde de carbone (CO), l'éthanol (C<sub>2</sub>H<sub>5</sub>OH), l'acétone (C<sub>3</sub>H<sub>6</sub>O)] ou à des gaz oxydants tel que le dioxyde d'azote (NO<sub>2</sub>), des couches de ces nanoparticules de SnO<sub>2</sub> ont donné lieu à des réponses en capteurs de gaz réversibles et reproductibles avec une excellente sensibilité (Figure 2).

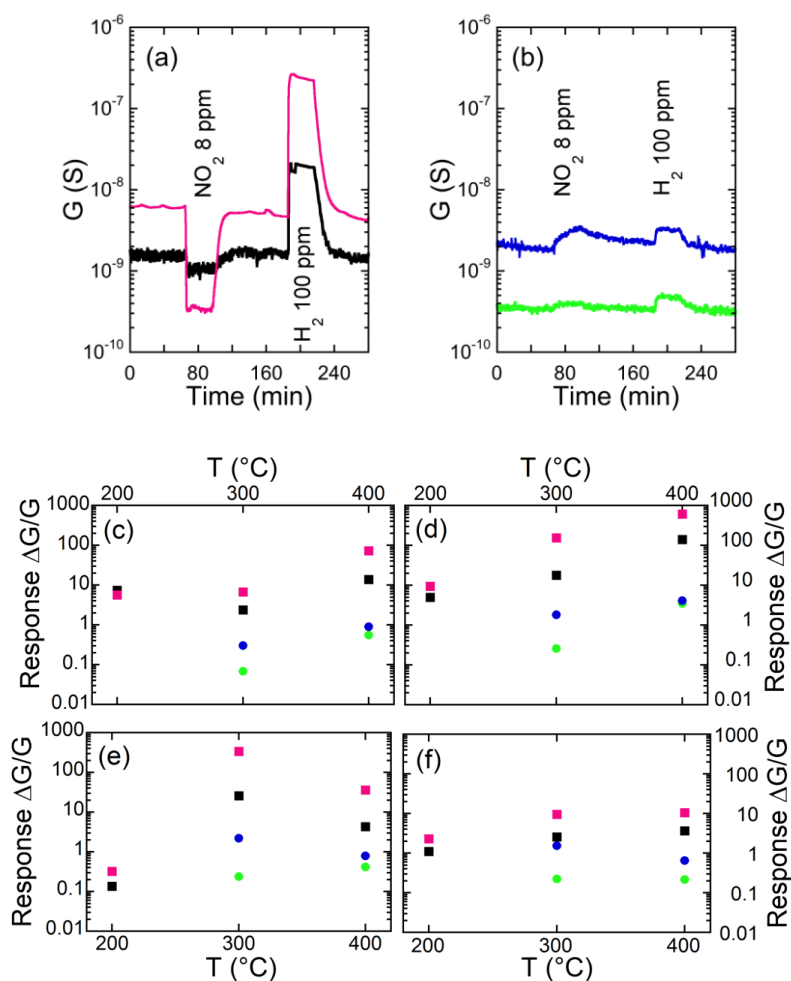
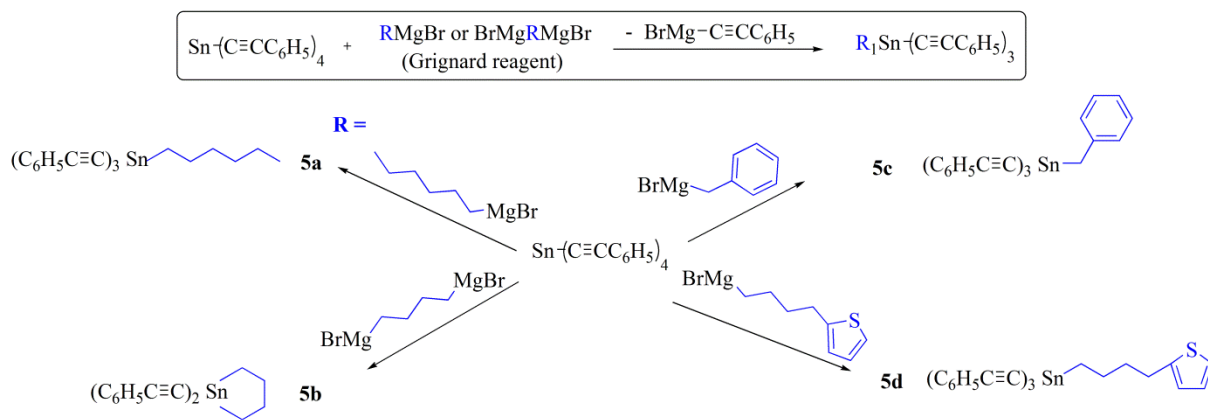


**Figure 2: Caractérisations en capteurs de gaz des échantillons TOa<sup>90</sup> (black), TOa<sup>600</sup> (pink), TOb<sup>90</sup> (green) et TOb<sup>600</sup> (bleu). Réponse dynamique à 8 ppm de NO<sub>2</sub> et à 100 ppm de H<sub>2</sub> des échantillons préparés en milieu acide (a) et en milieu basique (b) à la température de 300°C. Influence de la température sur la réponse à des gaz réducteurs: 1000 ppm de CO (c), 800 ppm de H<sub>2</sub> (d), 25 ppm d'acétone (e), 10 ppm d'éthanol (f).**

Les résultats de détection de gaz réducteur ou oxydant ont été discutés en fonction de la taille des cristallites, de l'aire spécifique BET, de l'énergie de la bande de valence, de la longueur de Debye et de la composition chimique des nanopoudres de SnO<sub>2</sub>. Les résultats mettent en évidence l'impact des résidus en contre-ions, qui affectent la performance de détection de gaz dans une mesure beaucoup plus grande que les effets de taille et de surface. Il convient donc de souligner que la composition de la suspension colloïdale commerciale de SnO<sub>2</sub> peut influencer sur le comportement du capteur de gaz en fonction de la quantité restante en contre-ions, bien que l'effet de taille des particules est très souvent invoqué dans la littérature à la fois d'un point de vue théorique<sup>1</sup> et expérimental<sup>2</sup> pour expliquer les données de détection de gaz. En général, plus la taille des cristallites est petite, plus la réponse du capteur est élevée. Or ce n'est pas le cas pour ces matériaux. Ainsi, les nanoparticules de dioxyde d'étain préparées dans des conditions acides et calcinées à l'air à 600 °C ont conduit aux meilleures performances de détection du fait d'une quantité en cations de potassium inférieure et d'une cristallinité supérieure. En ce qui concerne la sélectivité, la réponse de ces particules à l'éthanol est beaucoup plus élevée que la réponse à des gaz tels que le dihydrogène H<sub>2</sub> ou le monoxyde de carbone CO (environ 30 et 1500 fois respectivement), conduisant à une sélectivité au moins comparable aux données de la littérature.<sup>3,4</sup> En ce qui concerne l'acétone, les réponses sont similaires à celles obtenues avec l'éthanol, ce qui est conforme à ce qui a été rapporté avec des nanostructures plus complexes.<sup>5</sup> Ces travaux, récemment publiés,<sup>6</sup> constitue une étude de référence dans le domaine de la synthèse de nanostructures de SnO<sub>2</sub> afin d'interpréter les performances de détection de gaz à partir de la contamination résiduelle issue du colloïde commercial précurseur, notamment le polypyrroles et les contre-ions potassium.

Dans une seconde approche, des trialcynylorganoétains fonctionnels portant les composés hexyle (**5a**), butylène (**5b**), benzyle (**5c**) et thiophénylbutyle (**5d**) ont tout d'abord été préparées avec succès par alkylation sélective du tétraphényléthynylétain par une quantité équimolaire du réactif de Grignard approprié dans un mélange de solvants anhydres constitués de toluène et d'éther diéthylique (2:1 v:v) à 40 °C pendant 18 heures (Scheme 1). Ces conditions expérimentales optimisées de synthèse de ces organoétains diminuent non seulement le nombre d'étapes par rapport aux voies de synthèse conventionnelles, mais mettent également en évidence la diversité des fonctionnalités organiques pouvant être introduites dans la structure alcynylorganoétain, ce qui ouvre de nouvelles perspectives en chimie des organoétains pour la synthèse de dialcynyldiorganoétain ou de dérivés d'alcynyltriorganoétain par le contrôle soigné de la proportion entre le tétraphénylalcynylétain et le réactif de Grignard.



**Scheme 1: Schéma de synthèse de quatre alcynylorganoétains.**

Des matériaux hybrides organiques-inorganiques à base d'étain ont ensuite été synthétisés avec succès à partir de ces alcynylorganoétains en utilisant le procédé sol-gel. L'hydrolyse-condensation des quatre alcynylorganoétains fonctionnels a donné des poudres et des couches hybrides d'oxohydroxoorganotétain (**OXT5a**, **OXT5b**, **OXT5c** et **OXT5d**) thermiquement stables jusqu'à 200 °C sous air. L'étude de la composition chimique en volume

et en surface réalisée par les études FTIR, EDX et XPS a révélé que la fonction organique était préservée pendant les processus d'hydrolyse-condensation et qu'un réseau d'oxyde d'étain était formé avec des fonctions hydroxyle restantes pendantes. En particulier, une formule chimique a pu être proposée pour **OXT5a**, i.e.  $[(C_6H_{13})SnO(OH)]_n \cdot 0.22 H_2O$ . D'autre part, la morphologie de surface et la texture des films hybrides dépendent fortement de la nature de la fonctionnalité organique. Les matériaux hybrides comprenant des unités alkyles flexibles telles que **OXT5a** et **OXT5d** ont conduit à des couches plus denses et plus homogènes, alors que des textures plus poreuses ont été obtenues pour **OXT5b** et **OXT5c**, qui comprennent des groupes organiques plus rigides. Les propriétés électroniques de ces matériaux hybrides ont également été déterminées. L'énergie de la bande interdite optique varie de 3,64 à 4,61 eV en fonction de la fonction organique, alors que la position énergétique de la bande de valence par rapport au niveau de Fermi reste relativement constante, c'est-à-dire entre 1,7 et 1,8 eV. Enfin, l'hybride **OXT5a** donnant les films les mieux définis, les hybrides organoétain de classe II comprenant des groupes hexyle dans lesquels des réseaux organiques et inorganiques sont étroitement associés par le biais de liaisons covalentes fortes ont pu être facilement fabriqués sur des substrats utilisés pour la détection des gaz. Exposés à des gaz réducteurs [hydrogène ( $H_2$ ), monoxyde de carbone (CO), éthanol ( $C_2H_5OH$ ), acétone ( $C_3H_6O$ )] ou à des gaz oxydants [dioxyde d'azote ( $NO_2$ )], les couches hybrides **OXT5a** ont donné des réponses significatives à l'hydrogène ( $H_2$ ) et au dioxyde d'azote ( $NO_2$ ) à deux températures relativement basses (100 °C et 200 °C) (Figure 3).



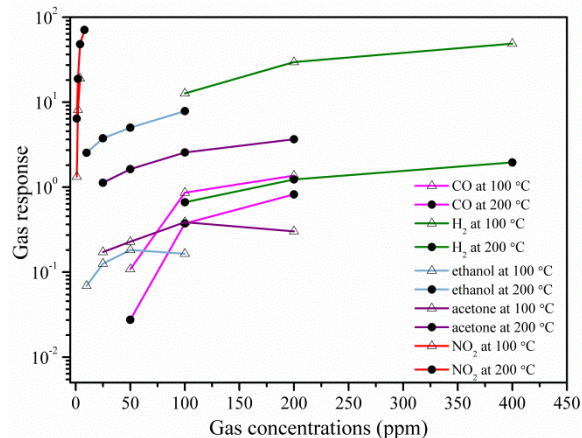
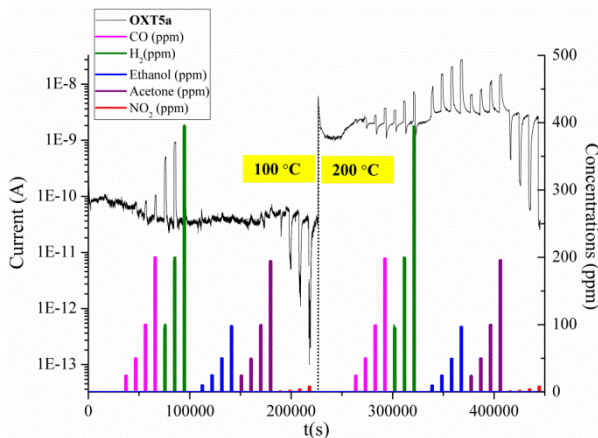


**Figure 3: Réponse dynamique en capteur de gaz (gauche) et réponse en capteur de gaz (droite) de OXT5a vis-à-vis de CO (rose), H<sub>2</sub> (vert), éthanol (Bleu) et NO<sub>2</sub> (rouge) à 100 et 200 °C.**

Les réponses enregistrées sont typiques d'un matériau de type n, comme déjà démontré par notre groupe pour des hybrides organostanniques auto-assemblés plus complexes.<sup>7</sup> Par rapport à ces études, l'originalité de l'hybride **OXT5a** repose sur sa capacité à détecter sélectivement le NO<sub>2</sub> à 200 °C (Figure 4). Cependant, le mécanisme de détection de gaz reste encore inconnu à ce stade. L'explication suivante pourrait être proposée pour expliquer cette sélectivité inattendue: à 100 °C, la couche d'oxohydroxoorganostannane (**OXT5a**) sélectionnerait les molécules de gaz principalement sur la base d'un processus d'exclusion de taille tandis qu'à 200 °C, la réaction chimique la plus complexe générée à la surface de la couche **OXT5a** dominerait les propriétés de détection sélective du gaz des matériaux hybrides oxohydroxoorganostannane.

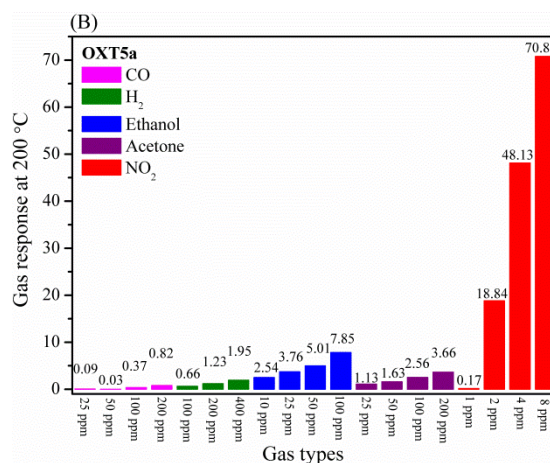
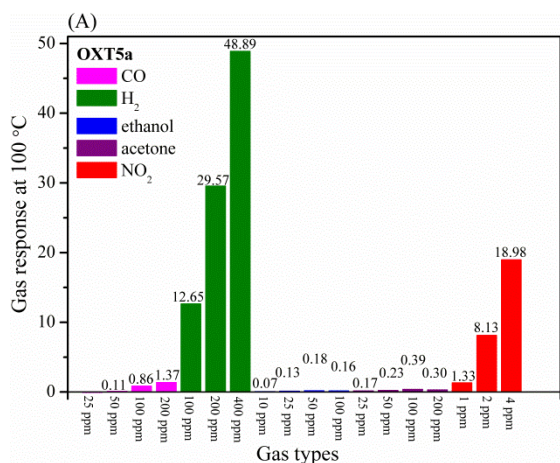


**Figure 4: Réponse en capteur de gaz de OXT5a vis-à-vis de CO (rose), H<sub>2</sub> (vert), éthanol (Bleu) et NO<sub>2</sub> (rouge) à 100 (A) et 200°C (B).**

Habituellement, les composés inorganiques présentent une stabilité chimique et thermique élevée, et ils peuvent être synthétisés par des procédés simples et peu coûteux, puis être déposés selon diverses techniques standards. En revanche, les composés organiques présentent une originalité et une polyvalence du point de vue de la synthèse. Les outils de la chimie moléculaire permettent en effet la modification à façon de la structure moléculaire pour améliorer l'interaction du matériau actif pour la détection avec des analytes spécifiques. En outre, la méthode de dépôt par gouttes a été choisie dans ce travail pour élaborer des films, car elle constitue un moyen rapide et accessible de générer un film mince sur des substrats relativement petits pour une application de détection de gaz.

Outre la percée dans le domaine de la détection sélective de gaz issue de la combinaison d'unités oxohydroxoétain et d'une chaîne carbonée, plusieurs défis restent à relever pour réaliser un capteur de gaz potentiellement sélectif à base de films hybrides d'oxohydroxoorganoétain:

- 1) le problème de la reproductibilité de la synthèse du dialcynylorganoétain (**5b**);
- 2) la faible stabilité thermique des hybrides oxohydroxoorganoétain, qui pourrait augmenter les risques de dommages structurels au cours du processus de vieillissement ou de la mesure de détection de gaz;
- 3) la difficulté à reproduire les données de détection de gaz pour l'hybride oxohydroxoorganoétain (**OXT5a**) ce qui est probablement dû au manque de maîtrise du procédé sol-gel employé pour obtenir les films ; cependant, il existe également de nombreux autres facteurs qui influent sur le résultat de la détection de gaz;
- 4) l'absence de conditions sol-gel optimales pour fabriquer des couches minces adéquates pour les matériaux oxohydroxoorganoétain (**OXT5b**, **OXT5c** et **OXT5d**), afin d'obtenir des données de détection de gaz fiables pour ces hybrides;
- 5) le mécanisme de détection de gaz à ce jour inconnu de ce type de matériaux hybrides

oxohydroxoorganoétain, ce qui nécessite des instruments de détection de gaz plus complexes pour déterminer ce mécanisme.

Pour prolonger ce travail à l'avenir, il conviendrait d'explorer d'autres types de fonctionnalités organiques pour synthétiser de nouveaux matériaux hybrides oxohydroxoorganoétains et les conditions du procédé sol-gel utilisé pour élaborer ces matériaux devraient être bien contrôlées de manière à déterminer précisément le rôle de la fonction organique dans les études de détection de gaz. Parallèlement, des méthodes de caractérisations avancées pourraient être envisagées telles la caractérisation spectroscopique in situ et operando des propriétés de détection de gaz, électrique et catalytique, car il s'agit des propriétés clés régissant la détection de gaz. Le système qui associe des techniques électriques (spectroscopie de conductance en courant continu et d'impédance alternative) et spectroscopiques (spectroscopie Raman et XAS / EXAFS) à l'analyse en ligne de gaz (micro-GC, analyseurs de gaz FTIR, capteur O<sub>2</sub>) permet d'établir la corrélation entre l'activité du capteur et les données spectroscopiques obtenues dans les mêmes conditions et sur le même échantillon (Figure 5). Les informations suivantes pourraient être ainsi obtenues: (i) changements de phase gazeuse et produits de réaction (le cas échéant) issus de l'analyse de gaz en ligne, (ii) espèces de surface adsorbées, (iii) modifications de la surface et du volume de l'oxyde (le cas échéant) et corréler toutes ces données avec la détermination simultanée de la composition du gaz et de l'activité du capteur. Cette connaissance approfondie du fonctionnement des capteurs de gaz à base d'hybrides oxohydroxoorganoétains de fonctionnalité organique contrôlée pourrait aider à une meilleure compréhension des réactions de surface et en volume responsables des effets de détection des gaz et conduira finalement au développement de meilleurs capteurs avec une sélectivité et une sensibilité accrues.

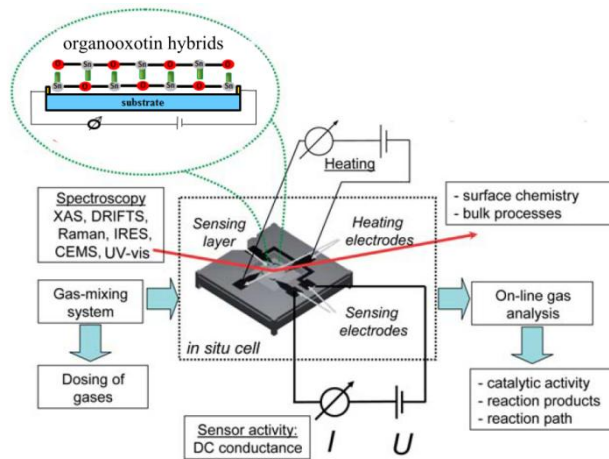


**Figure 5: Configuration idéale pour la caractérisation operando et in situ des propriétés de détection de gaz. Le système associe des techniques électriques (spectroscopie de conductance en courant continu et d'impédance alternative) et spectroscopiques (spectroscopie Raman et XAS / EXAFS) à une analyse de gaz en ligne (micro-analyseurs de gaz FTIR, FTIR, capteurs O<sub>2</sub>). Ce système permet d'établir la corrélation entre l'activité du capteur et les données spectroscopiques obtenues dans les mêmes conditions et sur le même échantillon.**

En résumé, ce travail de thèse a conduit à deux résultats originaux principaux: 1) l'impact des résidus de contre-ions issus de la suspension colloïdale commerciale sur les performances de détection de gaz des nanopoudres de SnO<sub>2</sub> malgré les effets de taille des cristallites et de surface spécifique, ce qui fournit une nouvelle vision de l'interprétation du comportement des nanopoudres de SnO<sub>2</sub> en détection des gaz ; 2) une voie de préparation simple et directe d'organoétains fonctionnels capables de produire des matériaux hybrides de classe II à base d'oxyde d'étain en trois étapes à partir de produits commerciaux ; les matériaux hybrides obtenus possèdent alors de bonnes propriétés de détection sélective des gaz pour H<sub>2</sub> et NO<sub>2</sub>, ce qui leur confère la possibilité de rivaliser avec les systèmes actuellement utilisés (Figure 6). En d'autres termes, l'avènement de ce type de matériaux hybrides organoétains pourrait révolutionner non seulement la formation de la liaison carbone-étain en chimie des organostanniques, mais également les applications possibles dans le domaine de la détection de gaz.

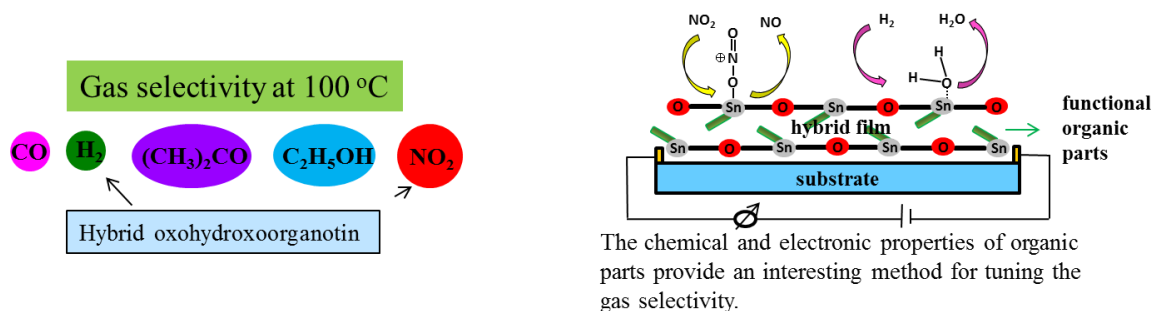


**Figure 6:** Couches hybrides OXT5a fournissant des réponses significatives au dihydrogène ( $H_2$ ) et au dioxyde d'azote ( $NO_2$ ) à une température relativement basse ( $100\text{ }^\circ\text{C}$ ) (gauche) ; mécanisme de détection plausible des couches hybrides OXT5a au dihydrogène ( $H_2$ ) et au dioxyde d'azote ( $NO_2$ ).

### References:

- [1] a) N. Yamazoe, K. Shimano, *J. Electrochem. Soc.*, **2008**, *155*, J85–J92. b) N. Yamazoe, K. Shimano, *J. Electrochem. Soc.*, **2008**, *155*, J93–J98.
- [2] a) N. Yamazoe, *Sens. Actuators, B*, **1991**, *5*, 7–19. b) B. Panchapakesan, D. L. DeVoe, M. R. Widmaier, R. Cavicchi, S. Semancik, *Nanotechnology*, **2001**, *12*, 336–349.
- [3] T. Kida, T. Doi, K. Shimano, *Chem. Mater.* **2010**, *22*, 2662–2667.
- [4] I.-S. Hwang, S.-J. Kim, J.-K. Choi, J.-J. Jung, D. J. Yoo, K.-Y. Dong, B.-K. Ju, J.-H. Lee, *Sens. Actuators, B* **2012**, *165*, 97–103.
- [5] Y.-X. Li, Z. Guo, Y. Su, X.-B. Jin, X.-H. Tang, J.-R. Huang, X.-J. Huang, M.-Q. Li, J.-H. Liu, *ACS Sens.* **2017**, *2*, 102–110.
- [6] S.-H. Lee, S.-H. Lee, V. Galstyan, A. Ponzoni, I. Gonzalo-Juan, R. Riedel, M.-A. Dourges, Y. Nicolas, T. Toupance, *ACS Appl. Mater. Interfaces* **2018**, *10*, 10173–10184.
- [7] (a) L. Renard, H. Elhamzaoui, B. Jousseume, T. Toupance, G. Laurent, F. Ribot, H. Saadaoui, J. Brötz, H. Fuess, R. Riedel, A. Gurlo, *Chem. Commun.* **2011**, *47*, 1464–1466. (b) L. Renard, J. Brötz, H. Fuess, A. Gurlo, R. Riedel, T. Toupance, *ACS Appl. Mater. & Interfaces* **2014**, *6*, 17093–17101.

# Contents

<b>Acknowledgements</b> .....	I
<b>Résumé</b> .....	III
<b>Chapter I Literature review of gas sensor technology</b> .....	5
<b>I.1 Definition and classification of chemical gas sensors</b> .....	7
(a) Optical gas sensor: .....	7
(b) Catalytic sensor: .....	8
(c) Electrochemical gas sensor: .....	8
(d) Thermal conductivity gas sensor: .....	8
(e) Semiconductor sensor: .....	8
(f) Acoustic wave gas sensor: .....	9
<b>I.2 Nanostructured materials for gas sensing</b> .....	10
I.2.1 Single element materials .....	10
I.2.2 Metal oxides.....	11
I.2.3 Organic semiconductors.....	11
I.2.4 Carbon nanostructures .....	13
<b>I.3 Gas sensing device structure</b> .....	13
<b>I.4 Mechanism principle</b> .....	14
(a) Oxygen Ionosorption Model.....	15
(b) Oxygen Vacancy Model (Reduction-reoxidation mechanism).....	16
<b>I.5 Applications</b> .....	16
(a) Automotive industry .....	17
(b) Food industry.....	17
(c) Environmental monitoring.....	17
(d) Fuel gas.....	18
(e) Industry process .....	18
<b>Chapter II Tin oxide based materials for gas sensing applications: Background and short literature review</b> .....	22
<b>II.1 Economic and societal issues</b> .....	22
<b>II.2 Prototype gas sensor - SnO<sub>2</sub> materials</b> .....	23
II.2.1 Structural (Crystallographic) properties .....	24
II.2.2 Electronic and optical properties .....	24
II.2.3 Applications .....	25
II.2.4 Gas sensors .....	29
II.2.5 Gas selectivity problem and general approaches.....	37
<b>II.3 Hybrid materials: definition, classification and applications</b> .....	38
II.3.1 Sol-gel process.....	42
II.3.2 Organotin hybrid.....	46

II.3.3 Hybrid organic-inorganic materials for gas sensing .....	49
<b>II.4 Main objectives and outline of the study</b> .....	53
II.4.1 Major objectives .....	53
II.4.2 General strategy .....	54
<b>Chapter III Characterization Techniques</b> .....	65
<b>III.1 <math>^1\text{H}</math>, <math>^{13}\text{C}</math> and <math>^{119}\text{Sn}</math> Nuclear Magnetic Resonance spectroscopies</b> .....	65
III.1.1 Principle .....	65
III.1.2 Instrumentation and experimental parameters .....	68
<b>III.2 Mass spectrometry (MS)</b> .....	68
III.2.1 Principle .....	68
III.2.2 Instrumentation and experimental parameters .....	70
<b>III.3 Fourier Transform Infrared Spectroscopy (FT-IR)</b> .....	71
III.3.1 Principle .....	71
III.3.2 Instrumentation and experimental parameters .....	71
<b>III.4 Raman Spectroscopy</b> .....	71
III.4.1 Principle .....	71
III.4.2 Instrumentation and experimental parameters .....	72
<b>III.5 Thermogravimetry Analysis (TGA-DTA)</b> .....	72
III.5.1 Principle .....	72
III.5.2 Instrumentation and experimental parameters .....	72
<b>III.6 Powder X-ray diffraction (XRD)</b> .....	72
III.6.1 Principle .....	72
III.6.2 Instrumentation and experimental parameters .....	74
<b>III.7 <math>\text{N}_2</math> sorption analysis</b> .....	74
III.7.1 Adsorption isotherm types .....	74
III.7.2 Brunauer, Emmett and Teller (B.E.T.) theory .....	76
III.7.3 Instrumentation and experimental parameters .....	77
<b>III.8 UV-Vis absorption</b> .....	77
III.8.1 Principle .....	77
III.8.2 Instrumentation and experimental parameters .....	79
<b>III.9 X-ray photoelectron spectroscopy (XPS)</b> .....	79
III.9.1 Principle .....	79
III.9.2 Instrumentation and experimental parameters .....	79
<b>III.10 Atomic Force Microscopy (AFM)</b> .....	80
III.10.1 Principle .....	80
III.10.2 Instrumentation and experimental parameters .....	80
<b>III.11 Transmission Electron Microscopy (TEM)</b> .....	81
III.11.1 Principle .....	81
III.11.2 Instrumentation and experimental parameters .....	82
<b>III.12 Scanning Electron Microscopy (SEM)</b> .....	82

III.12.1 Principle .....	82
III.12.2 Instrumentation and experimental parameters .....	83
<b>Chapter IV Synthesis and characterization of finely tuned SnO<sub>2</sub> nanoparticles .....</b>	<b>85</b>
<b>IV.1 Preparation of finely tuned SnO<sub>2</sub> nanoparticles.....</b>	<b>85</b>
IV.1.1 Introduction .....	85
IV.1.2 Synthesis of the SnO <sub>2</sub> nanoparticles.....	85
<b>IV.2 Characterization of SnO<sub>2</sub> nanoparticles.....</b>	<b>86</b>
IV.2.1 FTIR and Raman spectroscopy studies .....	86
IV.2.2 Crystallinity: Powder X-ray Diffraction studies.....	88
IV.2.3 Morphology and structure: Transmission Electron Microscopy studies .....	89
IV.2.4 Textural properties: N <sub>2</sub> sorption studies .....	92
IV.2.5 Surface composition and Debye length: X-ray photoelectron spectroscopy studies.....	94
<b>IV.3 Preparation and characterization of films processed from the SnO<sub>2</sub> nanoparticles.....</b>	<b>97</b>
IV.3.1 Fabrication of the SnO <sub>2</sub> nanoparticulate films.....	97
IV.3.2 Surface morphology: AFM studies.....	97
IV.3.3 Surface morphology: SEM studies .....	100
<b>IV.4 Conclusion.....</b>	<b>102</b>
<b>Chapter V Syntheses and characterization studies of tin-based hybrid materials .....</b>	<b>106</b>
<b>V.1 Design and synthesis of organotin-based hybrid material precursors.....</b>	<b>106</b>
V.1.1 Choice of the precursors and of their synthetic pathway.....	106
V.1.2 Selective alkylation to functional trialkynylorganotins .....	108
V.1.3 Synthesis of tetraphenylalkynyltin.....	109
V.1.4 Preparation of functional Grignard reagents for selective alkylation .....	109
V.1.5 Optimal experimental parameters for selective alkylation .....	110
<b>V.2 Preparation of organotin-based hybrid materials .....</b>	<b>111</b>
V.2.1 Hydrolysis-condensation of triphenylethynylorganotins .....	112
V.2.2 Preparation of oxohydroxoorganotin films and powders.....	112
<b>V.3 Preparation of organotin-based hybrid materials .....</b>	<b>113</b>
V.3.1 FTIR spectroscopy .....	113
V.3.2 Thermogravimetric studies .....	115
<b>V.4 Chemical composition of organotin hybrid materials .....</b>	<b>117</b>
V.4.1 Bulk chemical composition by EDX studies .....	117
V.4.2 Surface chemical composition by XPS studies.....	119
<b>V.5 Surface morphology of oxohydroxoorganotin films .....</b>	<b>121</b>
V.5.1 Surface morphology of <b>OXT5a</b> layers .....	121
V.5.2 Surface morphology of <b>OXT5b</b> layers.....	122
V.5.3 Surface morphology of <b>OXT5c</b> layers .....	124
V.5.4 Surface morphology of <b>OXT5d</b> layers.....	126



<b>V.6 Optical properties of oxohydroxoorganotin materials</b> .....	127
<b>V.7 Conclusion</b> .....	128
<b>Chapter VI Gas sensing properties of tin dioxide and hybrid oxohydroxoorganotin materials</b> .....	132
<b>VI.1 Gas sensing set-up and measurement principles</b> .....	132
VI.1.1 Structure of gas sensing substrates.....	134
VI.1.2 Selection of gas sensing parameters.....	135
<b>VI.2 Electrical and gas sensing characterization of SnO<sub>2</sub> nanoparticles</b> .....	136
VI.2.1 Preliminary tests carried out with TOa <sup>90</sup> and TOa <sup>600</sup> nanoparticles.....	136
VI.2.2 Characterization of the gas sensing properties of TOa and TOb samples...	139
VI.2.3 Discussion .....	143
<b>VI.3 Electrical and gas sensing characterization of oxohydroxoorganotin materials (OXT5a)</b> .....	145
<b>VI.4 Conclusion</b> .....	148
<b>Chapter VII General conclusion and outlook</b> .....	150
<b>Appendix</b> .....	156
<b>Experimental part</b> .....	159
<b>I. Organic and organometallic synthesis</b> .....	159
<b>II. NMR data of organic and organometallic materials</b> .....	167
<b>Publication</b> .....	181
<b>Curriculum Vitae</b> .....	194

# Chapter I Literature review of gas sensor technology

In recent years, gas sensors have received considerable attention driven by their practical applications in the detection of highly volatile and toxic gases. The pushing power behind is not only the strengthening of government regulations for safety at workplace and emission control but also the potential market to integrate those in smart phones and wearable devices (embedded electronics) thanks to the manufacturing processes improvement in sensor miniaturization and microfabrication, for instance in the case of metal-oxide sensors. As a result, the gas sensor market is expected to grow annually in the global point of view (Figures I-1 and I-2). This is highlighting the fact that the gas sensor is nowadays considered as an investable field. The global market for gas sensors was thus valued at USD 1,664.8 million in 2012 and is expected to grow at a CAGR<sup>1</sup> of 5.7% during the forecast period from 2012 to 2018 and reach USD 2,328.3 million by 2018 [1, 2].

Most gases in the atmosphere (N<sub>2</sub>, O<sub>2</sub>, CO<sub>2</sub>, H<sub>2</sub>O, CO, NO<sub>x</sub> etc...) are colorless and odorless, however, it is not possible to distinguish all types of gases based on body organs and especially, some of those are vital to our life while many others are harmful. Table I-1 illustrates the recommended exposure limits (RELs) of common toxic gases from NIOSH database<sup>2</sup> [3]. The vital gases like O<sub>2</sub> and H<sub>2</sub>O should be kept at adequate levels in living atmospheres, while the amount of hazardous gases, for example, CO should be controlled to be below a certain level leading to toxicity issues. As far as lighter hydrocarbons and H<sub>2</sub> are concerned, which are used as fuels, their explosion after leakage into air is one of the major concerns which is addressed by the use of gas sensor.



**Figure I-1: Global gas sensors market estimate and forecast, 2010 – 2018 (USD Million) (according to ref. [1]).**

<sup>1</sup> CAGR is the abbreviation of Compound Annual Growth Rate

<sup>2</sup> The National Institute for Occupational Safety and Health (NIOSH) is the United States federal agency responsible for conducting research and making recommendations for the prevention of work-related injury and illness.

The first commercial gas sensor device was developed in the 1960s using metal oxide as sensing layer. Since then, worldwide efforts have been made in order to improve the sensor sensitivity, selectivity, stability and speed (response and recovery rate), namely the 4s. Therefore, a large amount of research has been published in this area due to the fact that this sensor technology is broadly interdisciplinary, leading this metal-oxide type sensor to be the most investigated group in the gas sensing area.

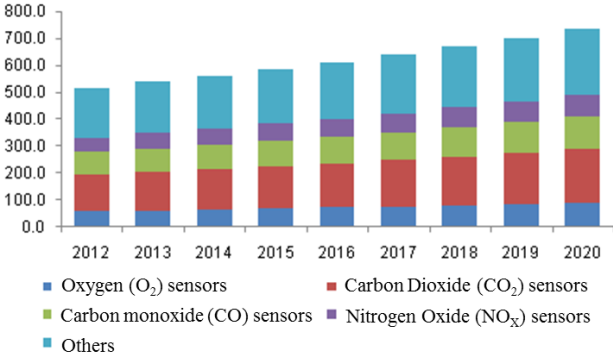


Figure I-2: Europe gas sensors market by product, 2012 – 2020 (USD Million) (according to ref. [2]).

Substance	NIOSH recommended Exposure Limit (TWA <sup>3</sup> , 8h)	
	ppm (vol.)	mg/m <sup>3</sup>
Ammonia (NH <sub>3</sub> )	25	17
Acetone	250	590
Carbon dioxide (CO <sub>2</sub> )	5000	9000
Carbon monoxide (CO)	35	40
Chlorine (Cl <sub>2</sub> )	0.5	1.5
Ethanol	1000	1900
Hydrogen sulfide (H <sub>2</sub> S)	10	14
Nitrogen dioxide (NO <sub>2</sub> )	1 (ST <sup>4</sup> )	1.8 (ST <sup>4</sup> )
Sulfur dioxide (SO <sub>2</sub> )	2	5

Table I-1: NIOSH Recommended Exposure Limits to Common Toxic Gases (according to ref. [3]).

<sup>3</sup> "TWA" indicates a time-weighted average concentration for up to a 10-hour workday during a 40-hour workweek.

<sup>4</sup> A short-term exposure limit (STEL) is designated by "ST" preceding the value; unless noted otherwise, the STEL is a 15-minute TWA exposure that should not be exceeded at any time during a workday.

## I.1 Definition and classification of chemical gas sensors

A chemical sensor, defined by the International Union of Pure and Applied Chemistry (IUPAC), “is a device that transforms chemical information, ranging from the concentration of a specific sample component to total composition analysis, into an analytically useful signal”. The chemical information may originate from a chemical reaction of the analyte or from a physical property of the system investigated [4]. This definition is quite general. Thus, there are many pragmatic descriptions which exist in the literatures. For instance, Prof. Wolfbeis defined a chemical sensor as a small-sized device comprising a recognition element, a transduction element, and a signal processor capable of continuously and reversibly reporting a chemical concentration [5]. Furthermore, this definition can be considered to be tasks of different units in chemical sensors that were expressed by IUPAC.

Generally speaking, chemical gas sensors usually contain two basic components connected in series: a chemical recognition system (receptor) and a physicochemical transducer as illustrated in Figure I-3. The former is provided with an active layer (a material or a combination of materials), which interacts with a target gas by changing in its own properties (work function, dielectric constant, electrode potential, mass, etc.), or by emitting energy (heat or light). The transducer is a device, which is able to transform such an effect into an electrical signal (sensor response). The construction of a sensor is determined by the transducer used, with the receptor appearing to be implanted within it.

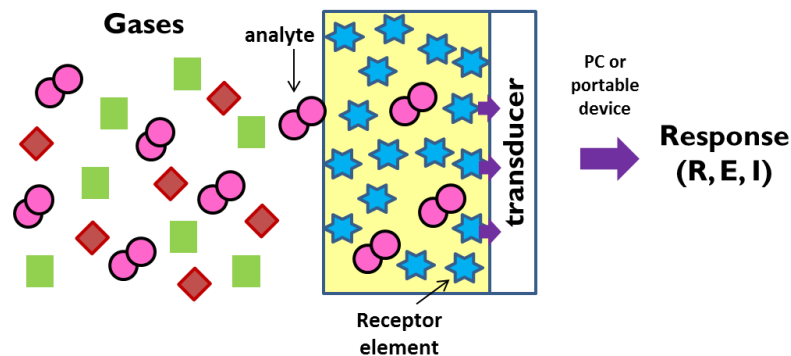


Figure I-3: Schematic diagram of a chemical gas sensor (adapted from ref. [6]).

Chemical sensors are classified as below according to the operating principle as described below [4,7]:

### (a) Optical gas sensor:

This type of sensors transform optical phenomenon, exploiting optical absorption, luminescence (fluorescence or phosphorescence emission) or light scattering of a gas species at defined optical wavelengths which normally consists of a light emitting element, a photo detecting element, a gas sensing element and a gas sensing element responding to light. One of the most common optical gas sensors is infrared gas sensor, which is the most expensive

since its cost is five times higher than that of electrochemical technology based gas sensors. However, recent technological advances, including the availability of powerful amplifiers and related electronic components, have opened a new frontier for infrared gas analysis. They are used for detecting methane, ethane, propane, butane, benzene, toluene, xylene and alcohols as methanol and ethanol.

(b) Catalytic sensor:

Catalytic sensors are relatively easy to install and calibrate, flexible in nature, and they can be used for monitoring emissions across different applications. Products based on this technology can operate over a wide temperature range and are extensively used for detecting combustible gases such as methane, hydrogen, butane and other light hydrocarbons. The first catalytic combustion type sensor was discovered by Jonson in 1923 [8] and was employed for the detection of methane in mines [9]. This kind of sensors usually contains a catalytic surface coated on a hot plate with Pt resistor. The gas concentrations can be detected by monitoring the resistance change of platinum contacts depending on the temperature.

(c) Electrochemical gas sensor:

A typical electrochemical gas sensor is made of a sensing electrode acting as the working electrode and a counter electrode [7, 9]. The operating principles are the same as liquid electrolytic fuel cells. They are based on the electrochemical oxidation or reduction of the gaseous analyte at a catalytic electrode surface. In principle, they detect gases by producing chemical reaction between the gas and oxygen contained in the sensor. The reaction produces a small current which is proportional to the concentration of the gas analyte.

(d) Thermal conductivity gas sensor:

Thermal conductivity measurements for gas analysis have been used for many decades [10]. They are usually used for the detection of the gases exhibiting thermal conductivity greater than that of air as hydrogen and methane while gases with conductivity close to that of air cannot be detected like ammonia and carbon monoxide. Not along to mention about the gases with thermal conductivity less than that of air as carbon dioxide (CO<sub>2</sub>) and butane (C<sub>4</sub>H<sub>10</sub>), which are even more difficult to detect due to interference issues. Thermal conductivity based sensors use filaments in order to sense any changes occurring in the thermal conductivity of the target substance.

(e) Semiconductor sensor:

The semiconductor gas sensor is one of the electrical sensors. Electrical sensor is based on the measurements where no electrochemical processes take place. Thus, the signal arises from the change of electrical properties of the active layer caused by the interactions with the analyte. Semiconductor gas sensors, is the device that is made up of metal oxides which is used for measurement of target gas concentration by measuring the electrical resistance of the

device, also known as semiconducting metal oxide sensor or Taguchi sensor (Figure I-4), can have different configuration but usually include one conducting electrode and one heating electrode [11]. The heater at the base is used for heating up the sensor to a constant temperature between 200 and 250 °C in order to speed up the reaction rate [9]. The conducting electrode is employed to detect resistance change in the active layer. The advantages offered by this type of sensor are high sensitivity, low production cost, easy maintenance, operation simplicity and potential for miniaturization. However, this type of sensor is less gas specific than electrochemical sensors, reacting with many gases and producing more false alarms.

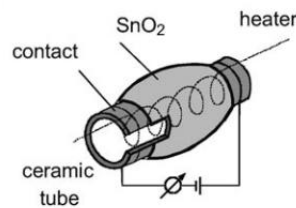


**Figure I-4: The Figaro-Taguchi-type (TGS) sensor (according to ref. [11]).**

(f) Acoustic wave gas sensor:

Their detection mechanism is based on the mechanical or acoustic wave. The first acoustic gas sensor was discovered by King [12] and was based on the measurement of bulk acoustic waves in a piezoelectric quartz crystal resonator which is sensitive to mass changes. Acoustic wave sensors (Figure I-5) have been found a variety of applications in the fields of temperature, pressure or mass measurements along with detection of chemicals or bacteria. They were used as gas sensors since 1964. Another advantage of this type of sensor is that the gas sensing can be made wireless and as shown by Lim *et al.* [13], which makes real online monitoring of the gas sensor.

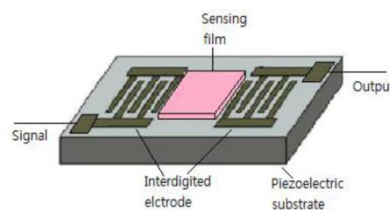


**Figure I-5: Surface acoustic wave (SAW) line (adapted from ref. [7]).**

At that stage, it is worthwhile to mention that this classification represents one of the possible ways to classify sensors. It is also conceivable to use various classifications of chemical sensors as long as they are based on clearly and logically arranged principles. However, this thesis mainly focuses on conductometric or resistive gas sensors based on semiconducting materials. As a consequence, the main sensing materials employed in this kind of sensors along with their working mechanisms are detailed in the following sections.

## I.2 Nanostructured materials for gas sensing

Nanostructured materials with small size, dimension and tailored structures have demonstrated great potential for use as active layer in gas sensors. In particular, the advantages of using nanostructured materials for gas sensing are from their large surface-to-volume ratio, high specific surface areas and more surface active sites, as well as the recently recognized effect of crystal facets showing high surface reactivity. Research endeavors have shown that a variety of nanomaterials which typically include single elements, metal oxides, organic semiconductors or carbon nanostructures reveal appealing features for room temperature gas sensors [14].

### I.2.1 Single element materials

Compared to the dominant metal oxides gas sensing materials, single element materials are not as widely studied for chemical sensors. This is due to the specific sensing mechanism that operates during the sensing reactions to some particular gases. The first case is **Palladium**. Palladium is an ideal sensor material for detecting H<sub>2</sub> at room temperature [15-19]. For example, Yu *et al.* have shown that Pd nanotubes with crystalline size of about 22-42 nm exhibited higher sensitivity and faster response time than the one based on a Pd film on exposure to H<sub>2</sub> at room temperature [15]. In another recent work, Favier *et al.* have successfully proved that a sensor including highly ordered Pd nanodots detect H<sub>2</sub> efficiently [20]. This kind of sensor was capable of detecting a full concentration range of H<sub>2</sub> between 0.1 % and 100 % with a detection limit of 0.1 %. The sensing mechanism is based on the lattice expansion of Pd on adsorption of H<sub>2</sub> functioning by break junction mechanism. This unique break junction mechanism gives Pd mesowire sensor a very high selectivity to H<sub>2</sub> against O<sub>2</sub>, CO and CH<sub>4</sub> [20, 21]. The second example is **Silicon-based materials**, which is a very important semiconductor commonly used in electronic industry. Bulk silicon is not suitable for a chemical sensor application because the electronic properties of bulk silicon are not easily modified due to the low surface activity. However, porous silicon (PS) was successfully used as a gas sensor to detect ethanol [22]. Particularly, porous silicon nanowires presented fast response and excellent reversibility to ppb-level NO gas at room temperature [23]. In this case, the NO sensing mechanism is attributed to the increasing charge density in porous silicon nanowires and the strong NO electron-donating nature results in an increase number of electron carriers. The last example of single element materials for gas sensing is **Tellurium**. Tellurium-based materials can detect different types of gases including NH<sub>3</sub> [24], H<sub>2</sub>S [25], CO [26] and NO<sub>2</sub> [27, 28]. Recently, tube-like structures of Te have been used as room temperature gas sensor materials due to their 1D structure, large surface-to-volume ratio and less agglomerated configuration. For instance, Te nanotubes showed fast response recovery to CO and NO<sub>2</sub> [29]. Raman spectroscopy studies revealed that the surfaces of Te nanotubes include TeO<sub>2</sub> layer and both showed p-type conductivity. In the presence of CO, the

TeO<sub>2</sub> layer is reduced to Te, leading to a decrease in resistance. On the other hand, when the sensor is exposed to NO<sub>2</sub>, the NO<sub>2</sub> molecules will induce the oxidation of Te and increase the hole concentrations in Te nanotubes. Thus, the resistance is reduced in both conditions.

### I.2.2 Metal oxides

Metal oxide-based gas sensors reversibly change their conductivity in response to changes in gas concentration and thus provide information about the composition of the ambient atmosphere. Their operating temperature range is usually comprised between 100 and 500 °C and they are the main source of gas sensor used in industry due to their compatibility in real world conditions (at atmospheric pressure in the presence of 20.5 vol% of oxygen). Many investigations on metal oxides are surrounded by studying their properties and methods of increasing the sensitivity and selectivity towards specific gases at different operating conditions. Specific metal oxides such as, SnO<sub>2</sub>, SrO, TiO<sub>2</sub>, ZnO, In<sub>2</sub>O<sub>3</sub>, WO<sub>3</sub>, CuO, Co<sub>3</sub>O<sub>4</sub>, GeO<sub>2</sub>, Ga<sub>2</sub>O<sub>3</sub>, CeO<sub>2</sub>, Cr<sub>2</sub>O<sub>3</sub>, Mn<sub>2</sub>O<sub>3</sub>, MoO<sub>3</sub>, NiO, Nb<sub>2</sub>O<sub>5</sub>, Nd<sub>2</sub>O<sub>3</sub>, V<sub>2</sub>O<sub>3</sub>, Fe<sub>2</sub>O<sub>3</sub>, Ta<sub>2</sub>O<sub>5</sub> and La<sub>2</sub>O<sub>3</sub> are suitable for sensing because of their electronic properties [30]. Metal oxides can be grouped as n-type or p-type depending on the main charge carriers which are present. The n-type (SnO<sub>2</sub>, ZnO, In<sub>2</sub>O<sub>3</sub> and WO<sub>3</sub>) and p-type (NiO, CuO, Co<sub>3</sub>O<sub>4</sub>, Cr<sub>2</sub>O<sub>3</sub> and TeO<sub>2</sub>) metal oxides are the most promising materials in sensing area [31].

### I.2.3 Organic semiconductors

The use of organic semiconductors as active layer in sensors has revolutionized modern technology in recent years due to their inherent capabilities arising from their lightness, low cost and high processability. Organic gas sensors have been successfully developed in many applications to detect humidity, various gases including ammonia, alcohol, nitrogen oxides, chlorine, hydrogen and nitroaromatic compounds based explosive vapors. The following section will mainly focus on conducting polymers, their nanocomposites and carbon nanostructures to discuss some recent advances in the domain of sensors operating at room temperature.

#### (a) Conducting polymers

Polyaniline, polypyrrole [32] or polythiophene are the conjugated organic polymers with either electrical insulator or semiconductor properties in their undoped state. The most effective way to achieve high conductivity consists in a doping of the polymers [32]. In the “doped” state, the backbone of conducting polymers is composed of delocalized  $\pi$ -electron system, which could increase the conductivity from low level ( $10^{-10}$  to  $10^{-5}$  S cm<sup>-1</sup>) up to high level ( $1$  to  $10^4$  S cm<sup>-1</sup>) falling in the metallic conducting region [33, 34]. This unique doping/dedoping chemistry makes conducting polymers very attractive for gas sensing applications. There has been a large research effort in exploring conducting polymers for room-temperature chemical sensors, among which polyaniline appears to be the most



extensively investigated candidate for such sensor materials. In particular, 1D nanostructured polyaniline nanofibers are a good sensing platform with superior performance owing to their high surface area compared to the bulk counterparts (conventional film). This phenomenon further approves the merits of nanofibers layer for use as NH<sub>3</sub>, saturated ethanol and NO<sub>2</sub> sensors [35][36]. On the other hand, polypyrrole nanowires exhibit fast gas sensing response to H<sub>2</sub> [37] and polythiophene is also an interesting room-temperature gas sensor for NH<sub>3</sub> and NO<sub>2</sub> detection [38, 39].

#### (b) Organic and inorganic nanocomposites

Over the past decades, there has been a growing interest in organic-inorganic hybrid materials from the viewpoints of both fundamental research and industrial applications. Indeed, hybrid nanocomposite structures, made of organic and inorganic components combined at the nanometer scale, offer novel systems showing enhanced mechanical or physical functionalities through synergic interactions between the two phases. The organic and inorganic phases can be connected through weak van der Waals or hydrogen bonding interactions, or strong covalent/iono-covalent bonds.

Individually, metal oxides and conducting polymers have been widely studied for their gas sensing applications. Sensor based on metal oxides usually suffer from limitations in terms of selectivity owing to a similar mechanism at the surface of the metal oxide layer taking place whatever the nature of the gas analyte and, also, a relatively high working temperature drawback. On the other hand, due to the unique doping/dedoping sensing mechanism of conducting polymers, the selectivity is generally higher than that of metal oxides. Nonetheless, their relative low sensitivity, irreversible recovery and poor long-term stability still require improvements and innovation.

A promising strategy to overcome the drawbacks of metal oxide and conducting polymers is to design and fabricate organic-inorganic composite materials. The inorganic phase can be diverse, ranging from metal oxides, metal nanoparticles to carbon nanotubes and graphene. Their incorporation into conducting polymers can increase the concentration of interacting sites with the analytes, improve the intra- and inter-chain mobility of charge carriers in the polymer chains or even modify the affinity between the composite and the electron-donor or -acceptor gases.

Conducting polymer metal oxide nanocomposites represent one of the major family of sensing materials that can be utilized for room temperature sensing purpose. For example, polypyrrole-SnO<sub>2</sub> nanocomposites have been used as ammonia sensors [40]. The improved sensor performance was attributed to the nanostructures, which provide a higher surface area to volume ratio with accessible pores and to the formation of p-n junctions at the interface between polypyrrole and SnO<sub>2</sub> nanoparticles. Swager *et al.* have also shown that the CNTs/polythiophene hybrids are highly sensitive and selective to organic vapors such as dimethylmethylphosphonate (DMMP), which is often used as a simulant to chemical warfare agents like sarin gas [41, 42].

## I.2.4 Carbon nanostructures

Carbon-based nanostructured materials such as carbon nanotubes (CNTs), graphene and carbon fibers have caught significant attention as a sensing material for chemical gas sensors. CNTs and graphene have been illustrated to detect  $\text{NH}_3$  and  $\text{NO}_2$  gases with very high sensitivity and low detection limit at low temperatures [43-45]. The single-walled CNT showed the changes in electrical resistance upon exposure to  $\text{NH}_3$  and  $\text{NO}_2$  gases. Although single-walled CNT sensors displayed a very high sensitivity to 200 ppm of  $\text{NO}_2$  [43], the sensor fabrication requires special techniques such as photolithography, complicated pattern growth, high production cost, low sensor yield, and poor reproducibility. In this respect, CNTs films are easier to fabricate but exhibit lower sensitivity compared to a single CNT device. As another allotrope of carbon, graphene has received more and more attention for chemical gas sensor applications in recent years. Several factors led to ultimate detection capability of graphene. Firstly, the complete exposures of carbon atom networks maximize the interaction with the target molecules. Secondly, graphene has low Johnson noise<sup>5</sup> due to its metallic conductivity. Even in the limit of no charge carriers, a small amount of extra electrons can cause a noticeable change in the conductance of graphene. Thirdly, the 2D crystal structure of graphene with few defects ensures a better screening of charge fluctuation than its 1D counterparts. CNTs and graphene are also very attractive materials for fabrication of nanocomposite gas sensors through chemical functionalization, providing more opportunities to optimize sensor selectivity.

<sup>5</sup> Johnson noise, roughly defined, is the random variation of voltage due to the thermal agitation of charge carriers in a resistor.

## I.3 Gas sensing device structure

In a typical metal-oxide-based gas sensor, the porous sensing layer is deposited on the transducer surface (e.g.  $\text{Si}_3\text{N}_4$ ,  $\text{Al}_2\text{O}_3$ ,  $\text{Si/SiO}_x$ ) carrying the electrodes and an integrated heater. The latter allows for tuning the sensor operation temperature in the 100-500 °C temperature range. Metal electrodes (usually Pt or Au) are fabricated to measure conductance or resistance changes of the sensing material layer.

Various structures have been designed in practice [46], as shown in Figure I-6. Originally such sensor was composed of a sintered block structure (about 0.5 cm in size) with a pair of Pt coil electrodes inserted (a) and one of the coils also served as a heater. Then a new architecture was developed involving a thin alumina tube within a heavy coating (b), a pair of wire electrodes was wound on the tube and a heater was set inside it. Currently a thick film structure is widely used (c), the thick film is screen-printed on an alumina substrate with a pair of electrodes and a heater printed in advance. A micro version of this structure, known as a MEMS (micro electro-mechanical system) sensor (d), is still under development. Apart from

these standard structures, bead-shaped structures have been engineered for practical use. Platinum coil and needle electrodes are inserted in a small bead made of sensing materials (about 0.5 mm in size) (e); the coil also works as a heater. A similar bead can also be inserted with a single coil (heater) in (f), the so-called ‘hot wire’ type; a change in the resistance of the sensing materials affects the composite resistance between the two terminals of the inserted coil. The resistance change is then measured precisely with a bridge circuit which yields the gas response. For actual use, each device is bonded to the connector pins and put inside a metal cap with a hole on top, in order to remove the risk of triggering gas explosions. In addition, an adsorbent such as active carbon (often referred to as a ‘filter’) is placed in a layer immediately behind the hole in order to remove unpleasant gases, as shown in (g).

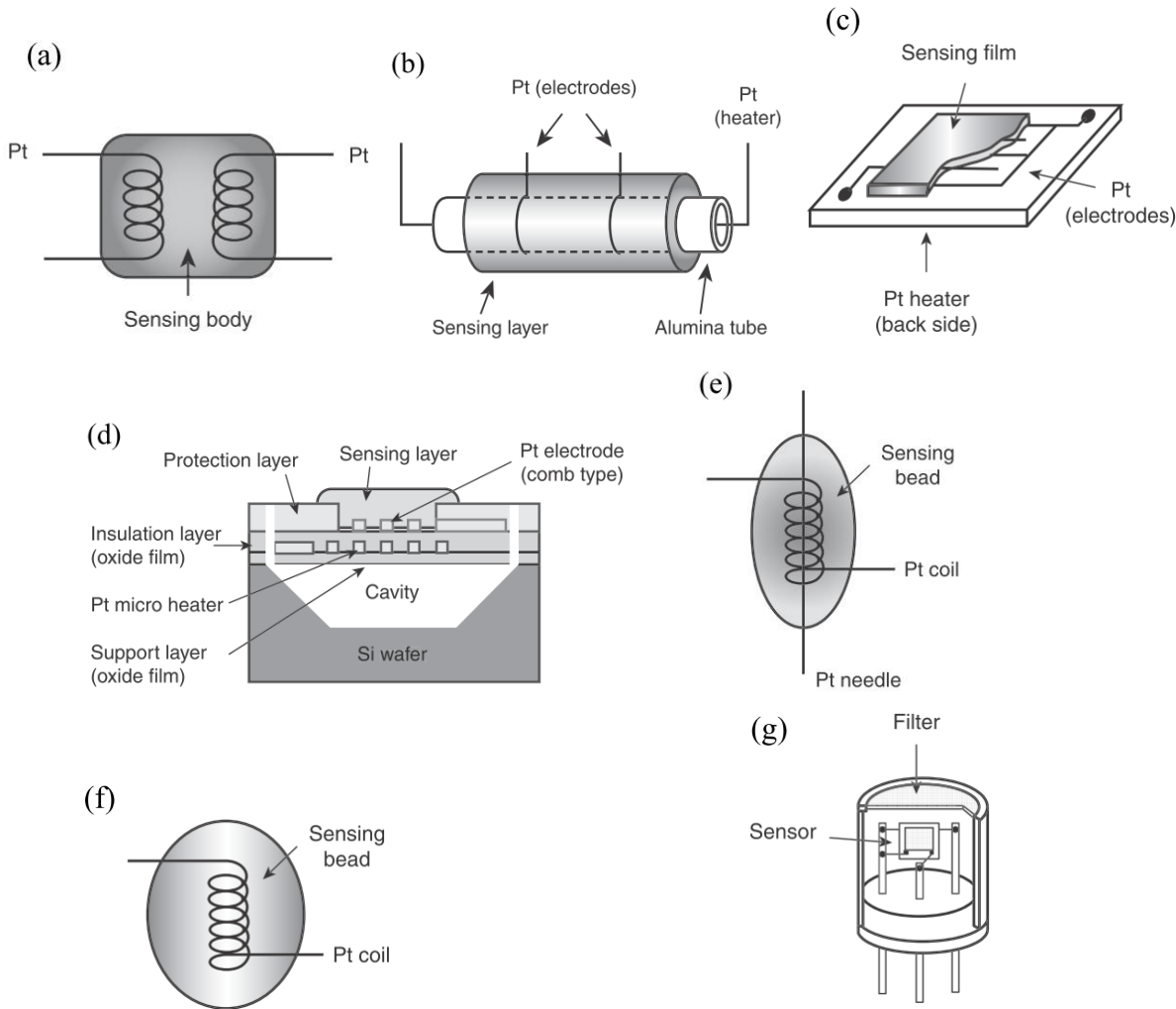


**Figure I-6: Device structures adopted for resistor type sensors in practice. (a) Sintered block, (b) thin alumina tube-coated layer, (c) screen printed thick film, (d) MEMs (e) small bead inserted with coil and needle electrodes, (f) small bead inserted with a single coil (heater and electrode), (g) practical sensor element assembling sensor device, metal cap and filter (adapted from ref. [46]).**

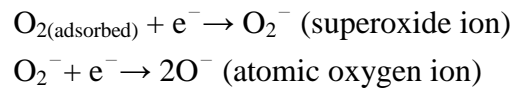
**I.4 Mechanism principle**

The basic working principle is the reversible change in the electrical conductivity caused

by the interaction between the sensing materials and gaseous species in the environment. Thus, an electrical output signal is generated once chemical reactions are initiated at the surface of the sensing layer. Although this process appears to be simple, the exact fundamental mechanisms that induce a gas response are still controversial. The sensor signal strongly depends on the pre-adsorbed oxygen on the sensing surface, which plays an important role upon exposure to the target gases. The operation of metal-oxide-based gas sensors is currently described by two main models [11]: (a) the oxygen ionosorption model; (b) the oxygen vacancy model

#### (a) Oxygen Ionosorption Model

This model is mainly supported by phenomenological measurements. All the processes involve electrons in the conduction band and thus influence the electrical conductivity. For instance, in a ZnO sensor,  $O_{2(gas)}$  is adsorbed onto the surface and different ionic forms of oxygen react with the current flow developing the following species:



$O^-$  is believed to be dominant at operating temperatures above 250 °C. It is one of the major reasons why sensing gases is a thermal-activated process for metal oxide gas sensors. It has been reported that the reaction between CO and the ZnO surface covered by ionic oxygen species take place as follows [47]:

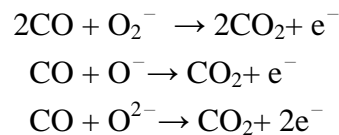
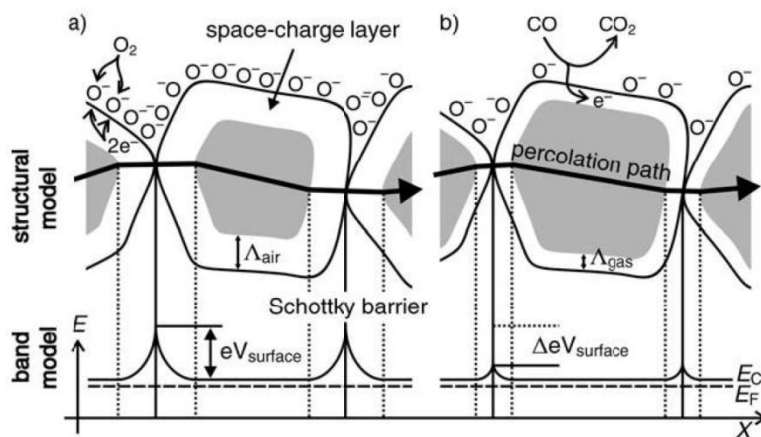


Figure I-7 schematically shows the structural and band model of conductive mechanism upon exposure to reference gas with or without CO [30]. When gas sensors are exposed to the reference gas containing CO, CO is oxidized by  $O^-$  and released electrons to the bulk materials, resulting in a decrease of the number of surface  $O^-$  and the thickness of space-charge layer. Then the Schottky barrier between two grains is lowered which facilitates electron migration through different grains and, therefore, enhance the conductivity of the sensing layer.



**Figure I-7: Structural and band models of conductive mechanism upon exposure to reference gas (a) without or (b) with CO (according to ref. [30]).**

Therefore, “Oxygen ionosorption” and “the reaction of reducing gases with ionosorbed oxygen ions” are the key descriptions of gas sensing mechanism in this model.

#### (b) Oxygen Vacancy Model (Reduction-reoxidation mechanism)

The second model rationalizes the sensing effects by changes in the oxygen stoichiometry. Literally it means that the determining factor is the amount of oxygen vacancies present at the surface. For example, tin dioxide ( $\text{SnO}_2$ ) as an n-type semiconductor gas sensor, is oxygen-deficient in nature, the oxygen vacancies of which act as electron donors. Reversible reduction and reoxidation of gases oxygen on the surface control the surface conductivity and therefore the whole sensing behavior. In this model, the mechanism of CO detection can be described as follows: 1) CO removes oxygen from the surface of the lattice to give  $\text{CO}_2$ , thus producing an oxygen vacancy; 2) the vacancy becomes ionized, thereby introducing electrons into the conduction band and increasing the conductivity; 3) in the presence of oxygen, it fills the vacancy; in this process one or more electrons are taken from the conduction band, which results in the decrease in conductivity.

As it has been underlined before, the amount of oxygen in the sensor surrounding plays a key role in both models. It must also be kept in mind that these mechanisms may be influenced significantly by the nature of materials and the operating conditions (e.g. temperature, composition of the gaseous phase, hydroxylation of the sensing layer surface).

## I.5 Applications

With a history of more than three decades, the market of gas sensors has become almost mature in some fields such as combustible gas monitoring, oxygen sensing for combustion exhaust control and humidity sensing for amenities of living spaces. Figure I-8 illustrates how a domestic house can be equipped with gas sensors in Japan [48]. Various kinds of sensors to monitor  $\text{CO}_2$ , air quality, odors and humidity are in increasing demand for various purposes. For example, a large number of air cleaners endowed with an air-quality sensor are produced

yearly to be installed not only in houses but also in car cabins.

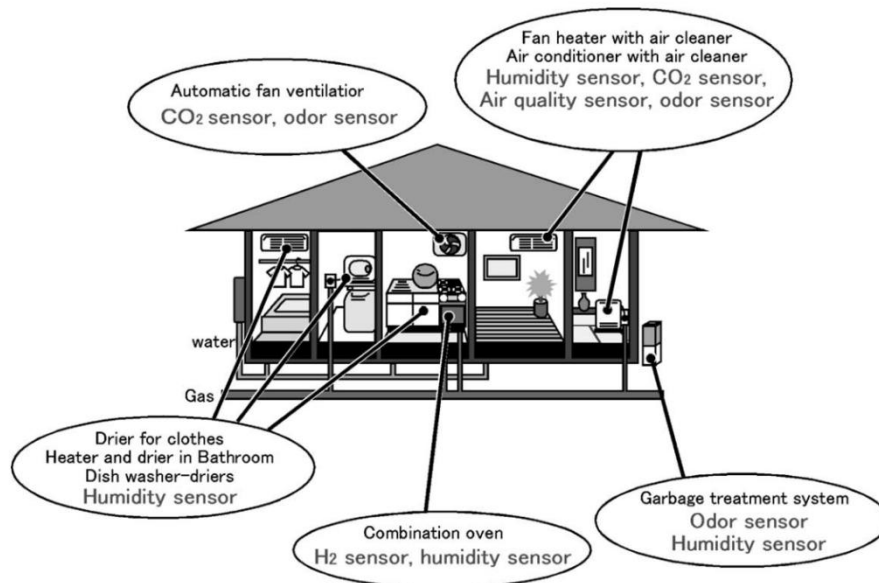


**Figure I-8: Various kinds of gas sensors equipped at various sites in a house (according to ref. [48]).**

There are several existing markets for gas sensors. A brief overview of the different markets as a function of the most significant gases to detect is outlined in the following section [47]:

(a) Automotive industry

A huge need of detecting gases exists in the automotive sector. Indeed, car ventilation control, filter control, combustion control, exhaust gases, and gasoline vapor detection are required to be monitored. Particularly, the by-products stemming from combustions in air like ( $\text{NO}_x$ :  $\text{NO}_2$ ,  $\text{NO}$ ) are the most troubling in regard to the environmental regulations. Moreover,  $\text{NO}_x$  are also produced through combustion from chemical plants, there are toxic at low concentrations and  $\text{NO}_2$  produces ground-level ozone.

(b) Food industry

Manufacturing monitoring and quality control in food industry are of utmost importance owing to the safety issue to human health. Thus, hydrogen sulfide ( $\text{H}_2\text{S}$ ) is formed due to bacterial breakdown of organic matter or wastes in food processing. At low concentrations this gas has a characteristic rotten-egg smell, however, the higher concentrations may cause instant paralysis and death in the case of an average adult (800 ppm for 5 minutes).

(c) Environmental monitoring

The air quality control, odor nuisance, and plant emissions are some examples of environmental monitoring. Ammonia ( $\text{NH}_3$ ) is produced in many sources as the animal manure decomposition. It is harmful to human eyes at low level of concentration and it is widely used in pharmaceutical processes. Therefore, it is necessary to effectively control its

concentrations [49].

(d) Fuel gas

CO is an environmentally hazardous gas which is emitted to the atmosphere due to incomplete combustion of fuels. On the other hand, methane is the main component of natural gas which is used in many chemical processes. It could be transported as liquefied phase and has been broadly used in electric generation by its burning as a fuel in gas turbines or steam boilers. Besides CO and methane, CH<sub>4</sub> emissions are severely regulated according to its powerful behavior as a green-house effect gas [50].

(e) Industry process

Sulfur dioxide (SO<sub>2</sub>) gas is the main source of acid rain in the global atmosphere. Henceforth, the control mechanisms of SO<sub>2</sub> emissions are a concerning matter of discussion. In the view of these environment and safety concerns, the development of sulfur dioxide sensor is very urgent and important [51].

Apart from the markets mentioned above, the gas sensors are also vastly used in other areas such as, humidity or oxygen sensing for home, early fire detection for public areas, cabin air monitoring and early fire detection in aerospace, explosive and warfare agents detection for national security [52], breath analysis in medical diagnostics[53].

## References:

- [1] Gas Sensors Market - Global Industry Size, Share, Trends, Analysis and Forecast 2012 – 2018. (<http://www.transparencymarketresearch.com/gas-sensors-market.html>)
- [2] Gas Sensors Market Analysis By Product (Oxygen, Carbon Dioxide, Carbon Monoxide, NO<sub>x</sub>), By Technology (Electrochemical, Semiconductor, Solid State, PID, Catalytic, Infrared), By End-Use (Medical, Building Automation & Domestic Appliances, Environmental, Petrochemical, Automotive, Industrial) And Segment Forecasts To 2020. (<http://www.grandviewresearch.com/industry-analysis/gas-sensors-market>)
- [3] The National Institute for Occupational Safety and Health. (<https://www.cdc.gov/niosh/>)
- [4] A. Hulanick, S. Glab, F. Ingman, *Pure & Appl. Chem.* **1991**, *63*, 1247-1250.
- [5] O.S. Wolfbeis, *Fresenius' J. Anal Chem.* **1990**, *337*, 522-527.
- [6] E. Zysman-Colman, in electronic book of “Iridium(III) in Optoelectronic and Photonics Applications”, John Wiley & Sons, Ltd, 2017, p.163.
- [7] S. Karthikeyan, H. M. Pandya, M. U. Sharma, K. Gopal, *J. Environ. Nanotechnol.* **2015**, *4*, 1-14.
- [8] J. G. Firth, A. Jones, T. Jones, *Combust. Flame* **1973**, *20*, 303-311.
- [9] Z. Yunusa, M. N. Hamidon, A. Kaiser, Z. Awang, *Sensors & Transducers* **2014**, *168*, 61-75.
- [10] T. Hubert, L. Boon-Brett, G. Black, U. Banach, *Sens. Actuators B Chem.* **2011**, *157*, 329-352.
- [11] A. Gurlo, R. Riedel, *Angew. Chem. Int. Ed.* **2007**, *46*, 3826-3848.
- [12] W. H. King, *Anal. Chem.* **1964**, *36*, 1735-1739.
- [13] C. Lim, W. Wang, S. Yang, K. Lee, *Sens. Actuators B Chem.* **2011**, *154*, 9-16.
- [14] J. Zhang, X. Liu, G. Neri, N. Pinna, *Adv. Mater.* **2016**, *28*, 795-831.
- [15] S. Yu, U. Welp, L. Z. Hua, A. Rydh, W. K. Kwok, H. H. Wang, *Chem. Mater.* **2005**, *17*, 3445-3450.
- [16] M. A. Lim, D. H. Kim, C.-O. Park, Y. W. Lee, S. W. Han, Z. Li, R. S. Williams, I. Park, *ACS Nano* **2012**, *6*, 598-608.
- [17] S. H. Lim, B. Radha, J. Y. Chan, M. S. Saifullah, G. U. Kulkarni, G. W. Ho, *ACS Appl. Mater. Interfaces* **2013**, *5*, 7274-7281.
- [18] F. Yang, D. K. Taggart, R. M. Penner, *Nano Lett.* **2009**, *9*, 2177-2182.
- [19] Y. Sakamoto, K. Takai, I. Takashima, M. Imada, *J. Phys.: Condens. Matter* **1996**, *8*, 3399-3411.
- [20] L. G. Villanueva, F. Fargier, T. Kiefer, M. Ramonda, J. Brugger, F. Favier, *Nanoscale* **2012**, *4*, 1964-1967.
- [21] F. Favier, E. C. Walter, M. P. Zach, T. Benter, R. M. Penner, *Science* **2001**, *293*, 2227-2231.
- [22] P. G. Han, H. Wong, M. C. Poon, *Colloids Surf. A* **2001**, *179*, 171-175.
- [23] K.-Q. Peng, X. Wang, S.-T. Lee, *Appl. Phys. Lett.* **2009**, *95*, 243112.
- [24] S. Sen, K. P. Muthe, N. Joshi, S. C. Gadkari, S. K. Gupta, Jagannath, M. Roy, S. K.



- Deshpande, J. V. Yakhmi, *Sens. Actuators B Chem.* **2004**, *98*, 154-159.
- [25] S. Sen, V. Bhandarkar, K. Muthe, M. Roy, S. Deshpande, R. Aiyer, S. Gupta, J. Yakhmi, V. Sahni, *Sens. Actuators B Chem.* **2006**, *115*, 270-275.
- [26] D. Tsiulyanu, S. Marian, H.-D. Liess, *Sens. Actuators B Chem.* **2002**, *85*, 232-238.
- [27] D. Tsiulyanu, S. Marian, V. Miron, H.-D. Liess, *Sens. Actuators B Chem.* **2001**, *73*, 35-39.
- [28] H. Park, H. Jung, M. Zhang, C. H. Chang, N. G. Ndifor-Angwafor, Y. Choa, N. V. Myung, *Nanoscale* **2013**, *5*, 3058-3062.
- [29] Y. C. Her, S. L. Huang, *Nanotechnology* **2013**, *24*, 215603.
- [30] C. Wang, L. Yin, L. Zhang, D. Xiang, R. Gao, *Sensors* **2010**, *10*, 2088-2106.
- [31] K. J. Choi, H. W. Jang, *Sensors* **2010**, *10*, 4083-4099.
- [32] G. Neri, *Chemosensors* **2015**, *3*, 1-20.
- [33] D. W. Hatchett, M. Josowicz, *Chem. Rev.* **2008**, *108*, 746-769.
- [34] A. G. MacDiarmid, *Angew. Chem. Int. Ed.* **2001**, *40*, 2581-2590.
- [35] J. Wang, S. Chan, R. R. Carlson, Y. Luo, G. Ge, R. S. Ries, J. R. Heath, H.-R. Tseng, *Nano Lett.* **2004**, *4*, 1693-1697.
- [36] Y. Zhang, J. J. Kim, D. Chen, H. L. Tuller, G. C. Rutledge, *Adv. Funct. Mater.* **2014**, *24*, 4005-4014.
- [37] L. Al-Mashat, C. Debiemme-Chouvy, S. Borensztajn, W. Wlodarski, *J. Phys. Chem. C* **2012**, *116*, 13388-13394.
- [38] J. Jang, M. Chang, H. Yoon, *Adv. Mater.* **2005**, *17*, 1616-1620.
- [39] S. T. Navale, A. T. Mane, G. D. Khuspe, M. A. Chougule, V. B. Patil, *Synth. Met.* **2014**, *195*, 228-233.
- [40] J. Zhang, S. R. Wang, M. J. Xu, Y. Wang, H. J. Xia, S. M. Zhang, X. Z. Guo, S. H. Wu, *J. Phys. Chem. C* **2009**, *113*, 1662-1665.
- [41] F. Wang, H. Gu, T. M. Swager, *J. Am. Chem. Soc.* **2008**, *130*, 5392-5393.
- [42] F. Wang, Y. Yang, T. M. Swager, *Angew. Chem. Int. Ed.* **2008**, *47*, 8522-8524.
- [43] J. Kong, N. R. Franklin, C. W. Zhou, M. G. Chapline, S. Peng, K. J. Cho, H. J. Dai, *Science* **2000**, *287*, 622-625.
- [44] J. D. Fowler, M. J. Allen, V. C. Tung, Y. Yang, R. B. Kaner, B. H. Weiller, *ACS Nano* **2009**, *3*, 301-306.
- [45] P. G. Collins, K. Bradley, M. Ishigami, A. Zettl, *Science* **2000**, *287*, 1801-1804.
- [46] N. Yamazoe, K. Shimanoe, O. K. Tan, in *Semiconductor Gas Sensors*, Woodhead Publishing, 2013, 3-34.
- [47] M. Gardon, J. M. Guilemany, *J. Mater Sci: Mater Electron*, 2013, *24*, 1410-1421.
- [48] N. Yamazoe, *Sens. Actuators B Chem.* **2005**, *108*, 2005, 2-14.
- [49] V.V. Petrov, T.N. Nazarova, A.N. Korolev, N.F. Kopilova, *Sens. Actuators B Chem.* **2008**, *133*, 291-295.
- [50] L. Francioso, D.S. Presicce, M. Epifani, P. Siciliano, A. Ficarella, *Sens. Actuators B Chem.* **2005**, *107*, 563-571.

- [51] W. Li, J. Guo, L. Cai, W. Qi, Y. Sun, J.-L. Xu, M. Sun, H. Zhu, L. Xiang, D. Xie, T. Ren, *Sens. Actuators B Chem.* **2019**, *290*, 443-452.
- [52] R. F. Kennedy, S. Nahavandi, *A Low-cost Intelligent Gas Sensing Device for Military Applications*, 2008 Congress on Image and Signal Processing.
- [53] N. Nasiri, C. Clarke, *Sensors*, **2019**, *19*, 462.

## Chapter II Tin oxide based materials for gas sensing applications:

### Background and short literature review

As described in the previous chapter, tin dioxide ( $\text{SnO}_2$ ) is the best understood prototype semiconductor material for gas sensing applications. According to a study made in 2014, it took more than 37% in the biggest market proportion among all the n- and p-type oxide semiconductor sensors (Figure II-1) [1]. Its gas sensitivity and selectivity have been widely studied and improved by various methods. To draw new insight in the improvement of both gas selectivity and sensitivity, this project aims to control the chemical structure and electronic properties of tin-oxide based materials through the acidity and basicity of preparation conditions and the introduction of organic functionalities. In this chapter, an overview of the main properties and applications of tin oxide based materials, with a special focus on gas sensing applications, is presented followed by some generalities about organic-inorganic hybrid materials which lead to the definition of the objectives of the project.

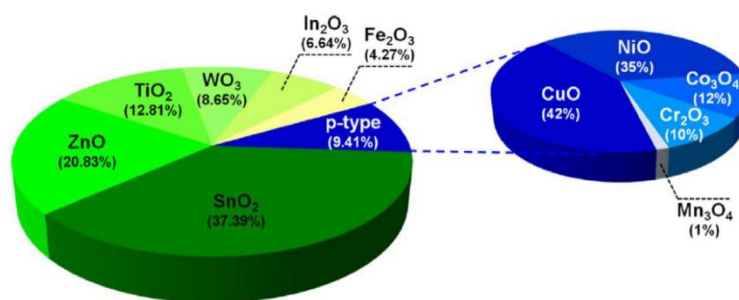


Figure II-1: Studies on n- and p-type oxide semiconductor gas sensors (internet search of Web of Knowledge [1]).

#### II.1 Economic and societal issues

Part of the scientific, technological and societal progress in the 21<sup>st</sup> century requires new functional materials. Indeed, the capability to design functional molecules and materials that substitute classical, more complex and bulky, structure and components will have a deep impact on many aspects of product development and supply. Furthermore, the intensive use of fossil fuels induces acute environmental issues, as global warming, but, also serious health problems related to the release of huge amount of undesirable gasses as carbon monoxide, nitrogen oxides or sulphur dioxide. Thus, air pollution is one of the most prominent problems that should be solved by our modern societies. On the other hand, the ever ongoing increase of the overall energetic demand has led to the emergence of alternative energy sources as fuel cells, atomic fission, nuclear fusion or solar light conversion.

Nonetheless, the advantages of such energies can be offset by the use of harmful or dangerous gases. For instance, it is generally admitted that the amount of energy produced by

hydrogen in fuel cells is three times the energy contained in equal weight of gasoline and about seven times that of coal [2]. Thus, hydrogen is considered as a future clean fuel as it is abundant, renewable and pollution free and as its product after combustion is water. However, hydrogen gas leaks easily from the lines and the systems and it is one of the most explosive gasses. Recently, the detection of volatile organic compounds (VOCs) using solid-state gas sensors has become particularly important because of their negative impacts on the environment and human health. However, their concentrations in the atmosphere are generally very low (below the ppm level) and thus are difficult to detect with conventional gas sensors.

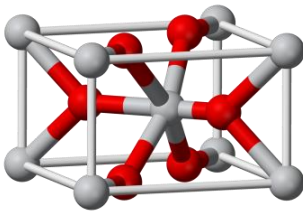
Consequently, the environmental issues due to the fossil fuels and the industrial use of dangerous gasses as hydrogen necessitate the availability of efficient devices to detect them at very low level and with a very high selectivity. The development of highly sensitive sensors is needed for the in situ detection of VOCs. Solid-state gas sensors therefore play a major role in semiconductor processing, medical diagnosis, environmental sensing, personal safety, and national security, with economic impact in agriculture, medicine, and in the automotive and aerospace industries [3]. However, in spite of the recent advances in the field of gas detection, namely by using semi-conducting oxide layers, the development of highly efficient new systems is still necessary.

## **II.2 Prototype gas sensor - SnO<sub>2</sub> materials**

Fabrication of nanostructured nanoporous semiconductors has attracted worldwide attention, stimulated by their outstanding chemical, electronic, magnetic and optical properties and their use as nanoscale devices, combined with the ever on-going miniaturization efforts. For instance, semi-conducting oxides are one of the most efficient families of materials to detect gas. Thus, metal-oxide-based gas sensors reversibly change their conductivity in response to changes in gas concentration and thus give information about the composition of the ambient atmosphere [4]. The operating temperatures are usually comprised between 100 and 500°C and they have been employed in real world conditions (at atmospheric pressure under air). The first example of detection of inflammable gases in air was reported for zinc oxide film and then SnO<sub>2</sub> appeared to be a very efficient system. Even though many different metal oxides have been investigated as sensing materials, SnO<sub>2</sub>, either alone or “activated” with small quantities of noble metals (Pd, Pt, Au), has remained the most commonly used and the best understood prototype material in commercial gas sensors as well as in basic studies of the gas-sensing mechanism because of its high gas sensitivity, good stability, and low cost [5]. As a matter of fact, SnO<sub>2</sub> or « stannic oxide » is a metal oxide semiconductor showing outstanding chemical and physical properties. It can be found in the nature as mineral cassiterite. Known and exploited since ancient times (3000 years BC), cassiterite is an oxide the color of which can varied from yellow to black. Its name, which comes from the Greek « kassiteros » (tin) was proposed by the French mineralogist Beudant in 1832.

## II.2.1 Structural (Crystallographic) properties

$\text{SnO}_2$  shows a unique stable polymorph at ambient pressure [6] named « cassiterite » and exhibit a tetragonal, i.e. rutile-like, crystalline structure (similar to the crystallographic structure of rutile  $\text{TiO}_2$ ). Each tin site  $\text{Sn}^{4+}$  is located at the center of an almost regular octahedron made of six oxygen ions,  $\text{O}^{2-}$ , each  $\text{O}^{2-}$  being surrounded by three  $\text{Sn}^{4+}$  ions positioned at the apices of an isosceles triangle (Table II-1).

Phase	Cassiterite
Cristalline phase	
System	Tetragonal
$\text{SnO}_2$ number per unit cell	2
Unit cell parameters (Å)	a = 4.737 c = 3.186
Ionic radius (Å)	r ( $\text{Sn}^{4+}$ ) = 0.71 r ( $\text{O}^{2-}$ ) = 1.14
Density ( $\text{g.cm}^{-3}$ )	6.92
Hardness (Mohs)	7.8
Refractive index	2.01
Band gap energy /eV	3.6

**Table II-1: Physical properties of  $\text{SnO}_2$ :  $\text{O}^{2-}$  ions: red spheres;  $\text{Sn}^{4+}$  ions: grey spheres.**

## II.2.2 Electronic and optical properties

In its stoichiometric form,  $\text{SnO}_2$  is an insulator, but in its deficient form in ambient conditions, tin dioxide is a n-type semiconductor with an energy bandgap of about 3.6 eV. As most of the n-type semiconductors,  $\text{SnO}_2$  crystals exhibit some discontinuities in the periodic lattice. These discontinuities are generally attributed on one hand to oxygen vacancies, which are considered as the main intrinsic defects in  $\text{SnO}_2$  rendering it sub-stoichiometric in oxygen, and on the other hand to the presence of interstitial tin atoms stemming from the reduction of some  $\text{Sn(IV)}$  ions into  $\text{Sn(II)}$  ions in order to compensate the charge imbalance. The electronic conductivity can then occur due to the electron mobility from  $\text{Sn(II)}$  sites towards  $\text{Sn(IV)}$  sites. Nonetheless, experimental data suggest that the origin of the non-stoichiometry in  $\text{SnO}_2$  materials is rather related to oxygen vacancies than to interstitial tin atoms [7].

Stannic ions  $\text{Sn}^{4+}$  possess 10 electrons in their external layer ( $4d^{10}$ ) and all internal layers are filled. As a consequence, the conduction band of  $\text{SnO}_2$  is mainly made of vacant 5s

orbitals of  $\text{Sn}^{4+}$  ions and shows a rather weak density of states, the effective mass of the electrons being  $0.3 m_e$  [8]. Furthermore, tin dioxide shows high electronic mobility both as single crystals (up to  $240 \text{ cm}^2 \cdot \text{V}^{-1} \cdot \text{s}^{-1}$ ) [9] and as nanomaterials (up to  $128 \text{ cm}^2 \cdot \text{V}^{-1} \cdot \text{s}^{-1}$ ) [10], and also unique resistivity change under a gas atmosphere [11].

### II.2.3 Applications

Among the binary and ternary oxides available, tetragonal  $\text{SnO}_2$  with a rutile-like structure, is one of the most important and functional materials for technological and industrial applications owing to its unique chemical and mechanical stabilities, and to two specific characteristics: variation in valence state and oxygen vacancies. Furthermore, its electronic conductivity can be easily enhanced by doping with fluorine or antimony which makes it as one of the most used transparent metal oxide conductors [12]. This wide band-gap semiconductor has therefore found a huge number of technologically important applications such as transparent conductive electrodes for optoelectronic devices, photocatalysis, solar energy conversion, and electrochemical storage of energy. Some examples are described more precisely in this section.

#### II.2.3.1 Optoelectronic devices

Fluorine and antimony-doped tin dioxide layers are widely used as transparent conductive oxide (TCO) in optoelectronic and photovoltaic devices due to its excellent transmittance and conductivity [12a-b, 13]. On the other hand, pure tin dioxide can be used in photodetectors. Thus, Chao *et al.* have reported a series of porous tin dioxide ( $\text{SnO}_2$ ) prepared by employing a method based on the calcination of tin sulfide precursors at different calcination conditions such as various annealing temperature and times, and zone heating [14]. The as-prepared porous tin dioxide samples were then deposited on PET (polyethylene terephthalate) substrates to yield flexible ultraviolet photodetectors which were further characterized (Figure II-2 e).

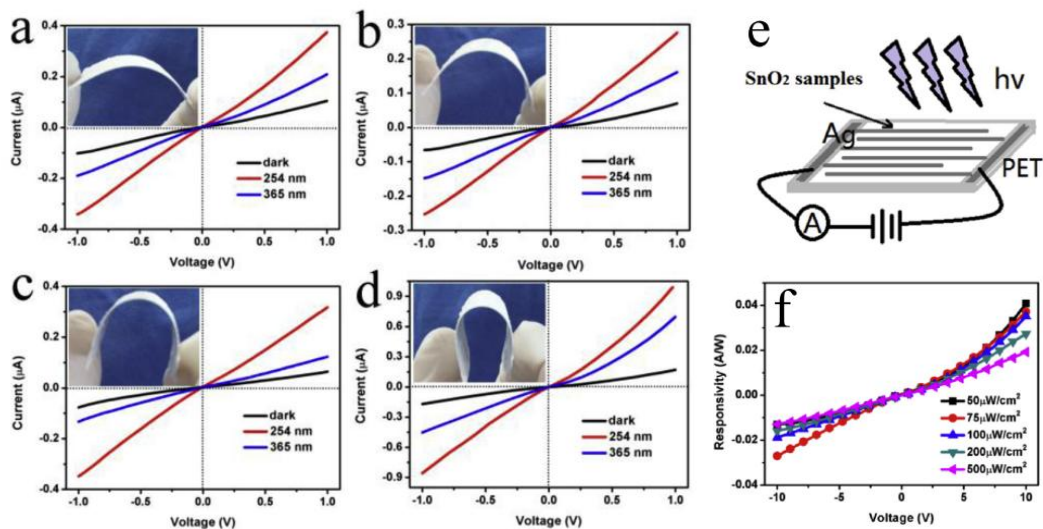


**Figure II-2:** I–V curves in the dark, and under light illumination of 254 nm and 365 nm for samples under four various bending (a) 400°C/1h, (b) 350°C/1h then 400°C/1h, (c) 350°C/1h then 450°C/0.5h, and (d) 380°C/6h; (e) schematic illustration of the flexible SnO<sub>2</sub> ultraviolet photodetector device; (f) responsivity versus applied-voltage characteristics of the sample treated at 380°C/6h under illumination of 254 nm ultraviolet light at different light intensity [14].

These devices showed linear photocurrent behaviors and good sensitivity to ultraviolet light at wavelengths of 254 nm and 365 nm. In addition, the performance of the flexible UV photodetectors can be further optimized by improving the crystallinity and prolonging the calcination times (Figure II-2 f). These systems based on porous SnO<sub>2</sub> materials open new avenues in the field of next-generation photodetectors and should be useful for creating high efficiency optoelectronic devices (Figure II-2 a-d).

### II.2.3.2 Photocatalysis

Due to current concerns in environmental issues, photodecomposition of organic pollutants represents one of the most interesting applications of tin dioxide based materials. Photocatalytic processes are based on the generation of electron-hole pairs by means of photons with energy higher than the band gap of the semiconductor material that, after charge separation and migration, can give rise to redox reactions with the species adsorbed on the surface of the oxide catalyst [15]. Nonetheless, the use of pure tin dioxide materials as photocatalyst still suffer from some limitations related to different factors as fast electron-hole recombination processes [16]. In this context, doping [17] and formation of SnO<sub>2</sub>-based heterostructures [18] have been successfully developed to circumvent these drawbacks. For instance, Mendoza-Damian *et al.* have developed a co-precipitation method providing boehmite(AlOOH)-SnO<sub>2</sub> composites including various Sn<sup>4+</sup> amounts which showed improved photocatalytic properties for phenol decomposition [18e]. As evidenced in Figure II-3, pure boehmite does not lead to the complete disappearance of the bands characteristic of phenol ( $\lambda_{\max} = 268$  nm) and its decomposition intermediates (hydroquinones,  $\lambda_{\max} = 287$  nm) after 2h

of irradiation. In contrast, when the Bhte-Sn10 composite was used, both phenol and hydroquinone absorption bands were completely removed after 2h of UV irradiation (Figure II-3B). This indicates that the boehmite( $\text{AlOOH}$ )- $\text{SnO}_2$  composite with 10 mol % of  $\text{Sn}^{4+}$  featured an improved photocatalytic activity eliminating phenol under UV light irradiation, where the photodegradation rate was found to be 2.9 times more active than that of boemite and bulk  $\text{SnO}_2$  (Figure II-3). The role of small  $\text{SnO}_2$  particles consists in extending the UV absorption of the boehmite particles and the composite materials favors the separation of photogenerated electron–hole charges.

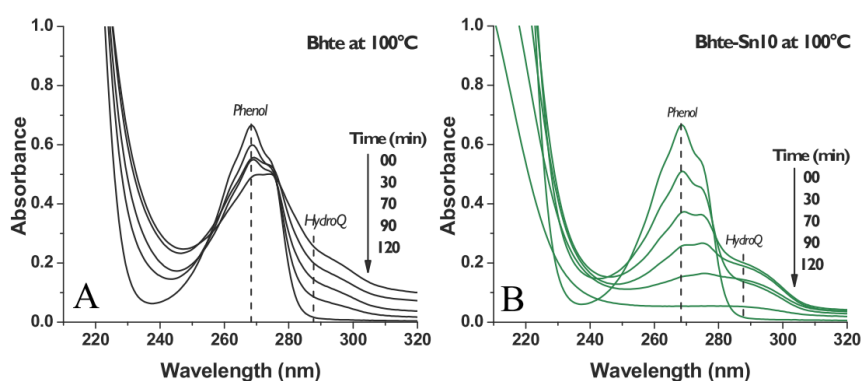


**Figure II-3: Absorbance spectra of phenol degradation using: (A) Bhte and (B) Bhte-Sn10 photocatalysts dried at 100 °C [18e].**

### II.2.3.3 Photovoltaics: Dye-sensitized solar cells (DSSCs)

A photovoltaic cell is a device that converts directly sunlight into electricity using semiconductor materials. Semiconductor materials enable electron flow when photons from sunlight are absorbed and eject electrons, leaving a hole that is filled by surrounding electrons. This phenomenon of electron flow by photon absorption is named photovoltaic effect. One of the emerging technologies in this field is dye-sensitized solar cells [19] which capture light with organic pigments anchored onto a mesoporous metal oxide semiconducting layer over a TCO substrate. These sensitized metal oxide photoanodes, playing the role of working electrode, is then put in contact with liquid redox [20] or solid electrolytes [21] and the system is completed by a counter electrode. Up to now, the most efficient devices involve mesoporous anatase titanium dioxide layers which have allowed reaching energy conversion efficiencies over 14% [22]. Along with zinc oxide ( $\text{ZnO}$ ), tetragonal  $\text{SnO}_2$  constitutes a promising alternative to  $\text{TiO}_2$  due to its higher electronic conductivity and photochemical stability [23]. The use of  $\text{SnO}_2$  particles with various sizes and well-defined morphologies led to efficiencies over 4% [24]. For example, Wang *et al.* have developed 0.35-1.60  $\mu\text{m}$  hierarchical  $\text{SnO}_2$  microspheres consisting of 5-10 nm of nanoparticles made through a facile hydrothermal route to be used as photoanode materials in DSSCs [24g]. The size and structure of samples thus play a huge influence on the photovoltaic performances of DSSCs (Figure II-4). Notably, the highest power conversion efficiency of 4.21% was achieved with the photoanode made of hierarchical  $\text{SnO}_2$  microspheres (thickness of  $\sim 15.9 \mu\text{m}$ ), and the



corresponding short-circuit current density ( $J_{sc}$ ) was  $9.38 \text{ mA cm}^{-2}$ , open-circuit voltage ( $V_{oc}$ ) was 692 mV, and the fill factor (FF) was 0.59.

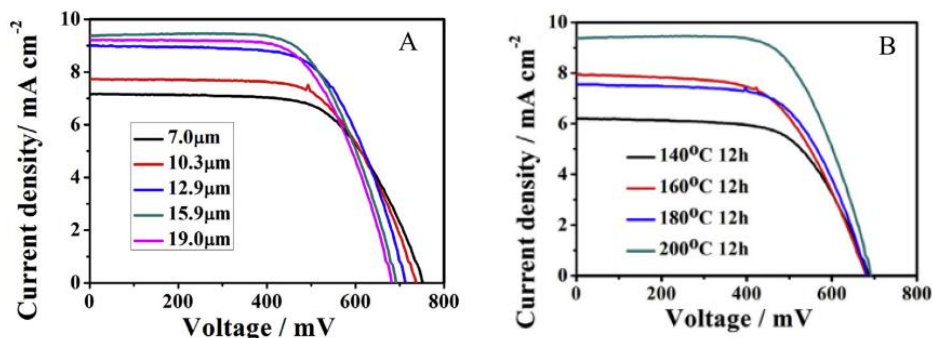


**Figure II-4: Photocurrent density-voltage (the J-V curves were plotted with the absolute values of current density) curves of DSSCs measured on (a) different film thicknesses of hierarchical SnO<sub>2</sub> photoanodes (200 °C, 12 h); (b) different sizes SnO<sub>2</sub> photoanodes with the film thickness of ~16.0 nm [24g].**

#### II.2.3.4 Electrochemical storage of the energy

Tin dioxide has also been widely used as electrode materials in supercapacitors [25] and lithium ion batteries [26]. Thus, in Li-ion batteries, SnO<sub>2</sub> is deemed to be a promising alternative for commercial graphite due to its higher storage capacity [26] even if the important volume expansion and contraction during alloying-delalloying cycles with Li<sup>+</sup> ions and related charge-transfer process have to be controlled [27]. That is the reason why polymer-SnO<sub>2</sub> based composites have been recently developed for this application. For instance, Wang *et al.* described a novel one dimensional and coaxial polyaniline@SnO<sub>2</sub>@multi-wall carbon nanotube (PANI@SnO<sub>2</sub>@MWCNT) composite as advanced conductive additive free anode material for the lithium ion battery [28]. Firstly, SnO<sub>2</sub> nanomaterials were self-assembled on the surface of MWCNT using Pluronic P123 triblock copolymer (PEO<sub>20</sub>-PPO<sub>70</sub>-PEO<sub>20</sub>) as template. The 1D MWCNT establishes a rigid conductive framework for SnO<sub>2</sub> nanoparticles. Then the PANI was further coated on the surface of SnO<sub>2</sub> by in situ polymerization to form a flexible protect layer to prevent the SnO<sub>2</sub> falling off from the surface of MWCNT (Figure II-5). Such hybrid structure ensures i) a stable interface between active materials and electrolyte; ii) provides effective conductive framework to enable the rapid Li ion diffusion; iii) offers the volume space by the soft and flexible PANI. Moreover, the one dimensional and coaxial PANI@SnO<sub>2</sub>@MWCNT can effectively accommodate the volume expansion of SnO<sub>2</sub> nanoparticles during lithiating and delithiating through the wrapping of the flexible coating layer of PANI and the buffer of the one dimensional MWCNT.

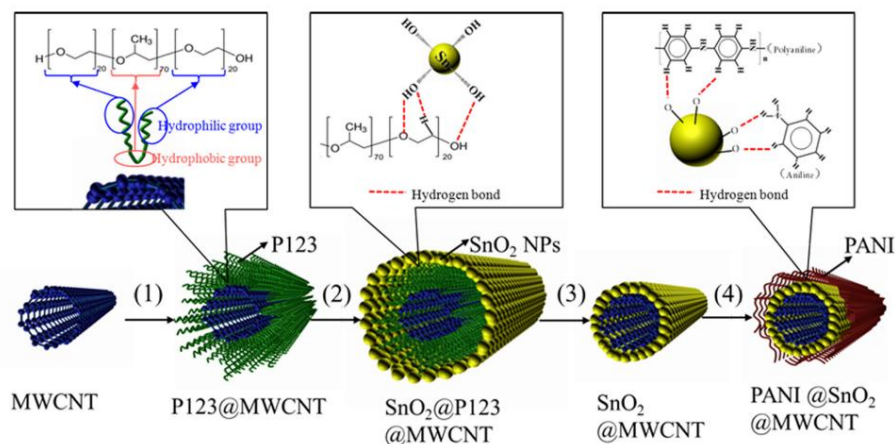


**Figure II-5: Preparation process of PANI@SnO<sub>2</sub>@MWCNT where steps (1), (2), (3) and (4) mean dissolving, self-assembly, heating, and in-situ polymerization, respectively [28].**

As a result, the electronic and lithium ionic conductivities of PANI@SnO<sub>2</sub>@MWCNT composite were improved via the synergistic effect of the conductive PANI and the MWCNT skeleton which could deliver a high reversible charge/discharge specific capacity of 878/888 mAh g<sup>-1</sup> at 0.2 A g<sup>-1</sup> over 100 cycles and 524/527 mAh g<sup>-1</sup> at 1.0 A g<sup>-1</sup> over 150 cycles without adding the conductive additive in the electrode (Figure II-6).

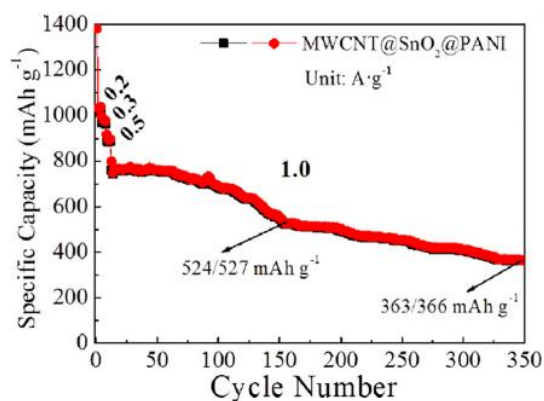


**Figure II-6: Charge/discharge performance of PANI@SnO<sub>2</sub>@MWCNT at a current density of 0.2, 0.3, 0.5 and 1.0 A g<sup>-1</sup> (the enlarge image is the ANI@SnO<sub>2</sub>@MWCNT composite) [28].**

## II.2.4 Gas sensors

Finally, the main application of SnO<sub>2</sub>-based materials appeared to be their use as active layers in chemiresistors for gas sensing. As mentioned above, surface reactions with a wide range of reducing and oxidizing gases cause change in the conductance of SnO<sub>2</sub> materials owing to charge transfer between the absorbate and the absorbent accounting for the sensing mechanism [4, 29]. As a result, SnO<sub>2</sub>-based sensors allowed the detection at the ppm level of many gases and volatile organic compounds including carbon monoxide (CO) [30], hydrogen (H<sub>2</sub>) [31], nitrogen oxides [32], ethanol [33], acetone [34] and, also, harmful gas such as hydrogen fluoride (HF) [35] or sulphide (HS) [36]. The sensing ability of SnO<sub>2</sub>-based devices

depends on many parameters including the operating temperature, the nature of the gas analyzed, the sensor geometry and the sensor enclosure. These factors indeed strongly influence the gas detection process which arises from a change in electrical resistance induced by a surface phenomenon. It is generally admitted that the oxygen adsorption on the surface of SnO<sub>2</sub>, in an oxygen atmosphere, produces an electron-depleted surface layer and, as a consequence, a barrier at the semiconductor surface [37]. In the presence of a reducing gas, the surface oxygen desorbs up to a steady level leading to a relaxation of the surface depletion region and barrier height that provoked a pronounced effect on the electrical conductance of the semi-conductor surface. In this context, it has been shown that both the conductivity and sensitivity of SnO<sub>2</sub>-based gas sensors are governed by the grain size. Indeed, in the case of a polycrystalline gas sensor, each crystallite of SnO<sub>2</sub> exhibits a space-charge layer of width L where L depends on the Debye length and the strength of the oxygen chemisorption. As the particle diameter D decreases to dimensions of the order of 2L, the whole crystallite can be depleted of electrons, and this causes the gas sensitivity of the element to change with D in the presence of a reducing gas. Consequently, the use of nanocrystals has enabled to reach high gas sensitivity and short response times [38]. Decreasing the crystalline size of SnO<sub>2</sub> is shown to be quite effective in improving its gas sensitivity. Thus, Xu *et al.* showed that the sensor response drastically increased as the crystal size decreased to less than 6 nm, which is twice as large as the thickness of the depletion layers in SnO<sub>2</sub> [39]. When the thickness of the depletion layers becomes comparable to the crystal radius, electron depletion layers form over the crystals, significantly increasing the difference in the electric resistance under air (O<sub>2</sub>) and under the target gases. On the other hand, as mentioned above, the loading of metal nanoparticles or dopants (Pd, Pt, Au...) on the SnO<sub>2</sub> surface enhances the sensitivity to reductive gas and decreases the operating temperature. Furthermore, owing to the importance of structure and morphology (crystallite size and shapes) of the particles as well as texture (porosity, surface-to-volume ratio) on the sensing properties of SnO<sub>2</sub> layers, nanostructured tin dioxide with various morphologies and structures, including nanoparticulate spheroids [40], nanotubes [41], nanorods [42], nanowires [30c, 43], nanoplates [44] and hollow spheres [45], has been designed to enhance the gas sensing performances. Some recent examples along with the corresponding gas sensing results are detailed below.

#### (a) SnO<sub>2</sub>-based Microfiber

Zou *et al.* have obtained hollow SnO<sub>2</sub> microfibers employing a unique sustainable biomass conversion strategy and shown that these microfibers can be used in a high-performance gas sensor [46]. By using alginate (sustainable seaweed) fiber as a template, the Sn atoms were introduced by a facile ion-exchange process in which the M<sup>2+</sup> cations were fixed in a novel “egg box” with coordination by  $\alpha$ -L-gulonate (G) blocks, which are negatively charged in the alginate macromolecule. When the Sn-alginate fibers were heated in air, the metal ions tended to aggregate on the surface of the fiber, and heterogeneous contraction of the fiber caused by the nonequilibrium heat treatment and carbon combustion led to the formation of a

hollow structure (Figure II-7 and II-8 A).

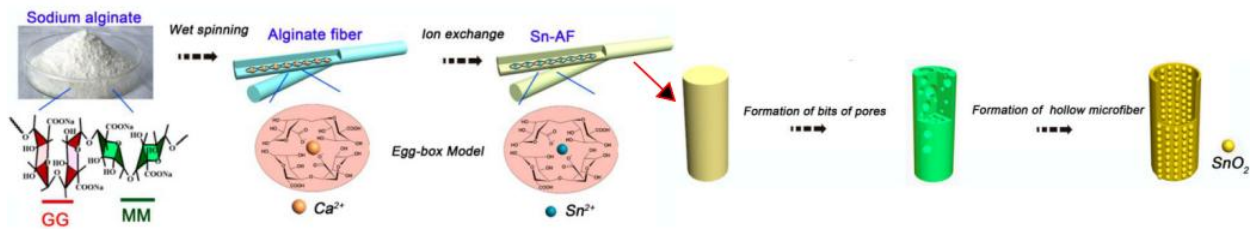


Figure II-7: Procedure used to fabricate hollow SnO<sub>2</sub> microfibers from sustainable alginate fiber [46].

The response of the hollow SnO<sub>2</sub> microfiber at 270°C to triethylamine (100 ppm TEA) is up to 49.5 with very fast response and recovery times, i.e. 14 and 12 s, respectively, (Figure II-8 B). The excellent sensing properties were attributed to the high sensitivity provided by SnO<sub>2</sub> and the good permeability and conductivity of the one-dimensional hollow structure (which can offer efficient channels for target gas diffusion). Furthermore, the sensitivity to TEA gas is much higher compared with the response to other gases: almost 15 times higher than that of *p*-xylene, 7 times that of acetone, 4 times that of benzene and isopropanol, and 3 times that of ethanol, indicating excellent selectivity for TEA (Figure II-8 C). Thus, these hollow SnO<sub>2</sub> microfibers are suitable for a unique TEA gas sensor and this work highlights their potential for future use in the gas sensor field.

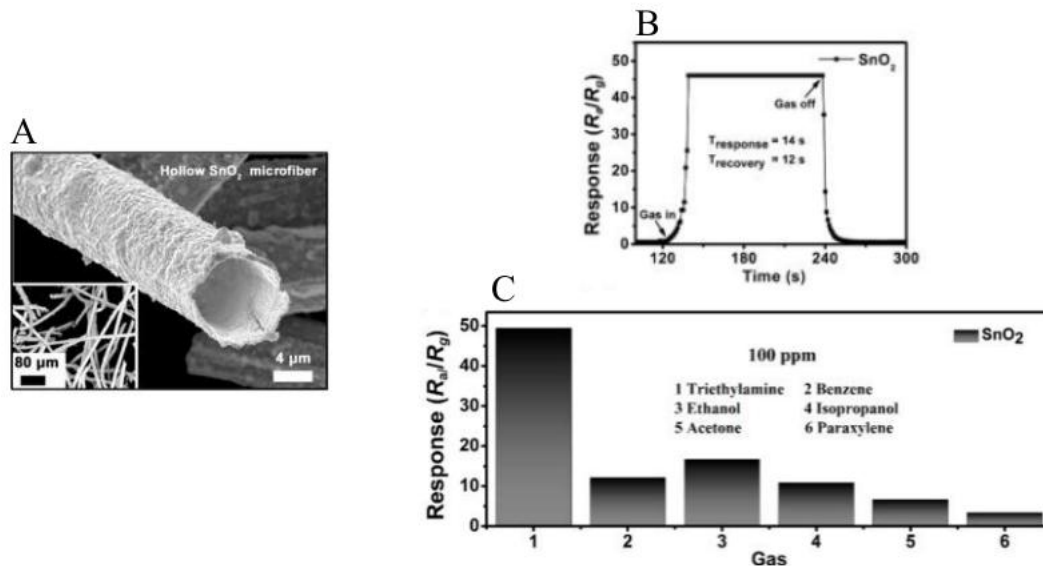
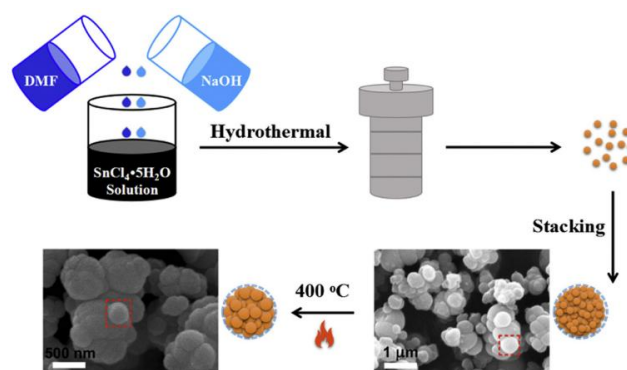


Figure II-8: (a) Cross-section SEM image of a single hollow SnO<sub>2</sub> microfiber (inserted photo is the cross-section SEM image of a single hollow SnO<sub>2</sub> microfiber); (b) Response/recovery curve of the hollow SnO<sub>2</sub> microfiber sensor to 100 ppm TEA at 270 °C; (c) Gas sensing selectivity of the hollow SnO<sub>2</sub> microfiber sensor to different gases at 270 °C at a concentration of 100 ppm [46].

#### (b) SnO<sub>2</sub>-Microsphere

Li *et al.* have synthesized SnO<sub>2</sub> microspheres by a facile hydrothermal method using the

chemical reaction solvents of water and DMF at a reaction temperature of 160 °C for 15 h, followed by thermal treatment at 400 °C for 1 h in air atmosphere (Figure II-9) [47]. The obtained SnO<sub>2</sub> are made of a large number of small spheres with average diameters of about 250 nm, and every small sphere consists of numerous primary nanocrystallites with average sizes of about 8 nm. The obtained SnO<sub>2</sub> microspheres were used to fabricate a gas sensor which shows good sensing performance in terms of selectivity and stability toward formaldehyde (HCHO). A best sensor response of 38.3 was thus found for 100 ppm HCHO at the operating temperature of 200 °C.



**Figure II-9: Preparation process of SnO<sub>2</sub> microspheres [47].**

The response time ( $\tau_{res}$ ) and recovery time ( $\tau_{recov}$ ) of the SnO<sub>2</sub> microspheres toward 100 ppm HCHO gas were approximately 17 s and 25 s (Figure II-10 A), respectively (the response time ( $\tau_{res}$ ) is defined as the time to reach 90% of the final equilibrium value and the recovery time ( $\tau_{recov}$ ) is defined as the time to decrease to 10% of the final equilibrium value). The  $\tau_{res}$  value and  $\tau_{recov}$  value of the sensor are far more rapid than most reported SnO<sub>2</sub> HCHO sensors [48]. As far as selectivity is concerned, sensors based on SnO<sub>2</sub> microspheres shows high response (38.28) to 100 ppm HCHO at 200 °C, while to 100 ppm of acetone, ammonia, xylene, methanol and toluene at 200 °C, the responses are 6.42, 1.74, 1.99, 19.38 and 1.55, respectively (Figure II-10 B). The response toward HCHO is around 6.0, 22.0, 19.2, 2.0, and 24.7 times higher than that toward acetone, ammonia, xylene, methanol and toluene, respectively. As a result, the gas sensor based on SnO<sub>2</sub> microspheres shows excellent gas response, good response-recovery properties, linear dependence, repeatability and selectivity, making it to be a promising candidate for practical detectors for HCHO.

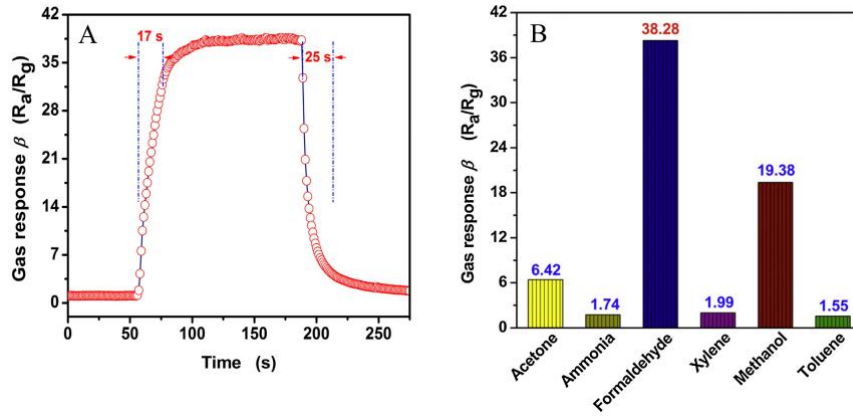


**Figure II-10: (A) Response and recovery characteristic of the gas sensor under HCHO concentration of 100 ppm at the operating temperature of 200 °C; (B) Selectivity of SnO<sub>2</sub> microspheres gas sensor to 100 ppm of different gases at 200 °C [47].**

The detection mechanism of HCHO can be interpreted in the following way (Figure II-11). When the sensor was exposed to the testing gas atmosphere, oxygen species adsorbed on the surface and captured free electrons from the sensing materials. The SnO<sub>2</sub> microspheres can ionize to adsorbed oxygen ions O<sub>x</sub><sup>-</sup> (O<sub>ads</sub><sup>-</sup> or O<sub>2ads</sub><sup>-</sup>) at grain boundaries. This process decreases the concentration of electrons, leads to the formation of a thick space-charge layer and a high resistance of the sensor. This process (Figure II-11 a) can be expressed as follows:

- (1) O<sub>2</sub>(gas) → O<sub>2</sub>(ads)
- (2) O<sub>2</sub>(ads) + e<sup>-</sup> → O<sub>2</sub><sup>-</sup>(ads)
- (3) O<sub>2</sub><sup>-</sup>(ads) + e<sup>-</sup> → 2O<sup>-</sup>(ads)
- (4) O<sup>-</sup>(ads) + e<sup>-</sup> → O<sup>2-</sup>(ads)

When the sensor is exposed to HCHO, the HCHO gas will react with the adsorbed oxygen ions and release the trapped electrons back to SnO<sub>2</sub> microspheres, leading to a thinner space-charge layer and lower potential barrier, and thus a decrease in resistance (Figure II-11 b), which can be described as follows:

- (5) HCHO(gas) → HCHO(ads)
- (6) HCHO(ads) + 2O<sup>2-</sup>(ads) → CO<sub>2</sub> + H<sub>2</sub>O(g) + 4e<sup>-</sup>



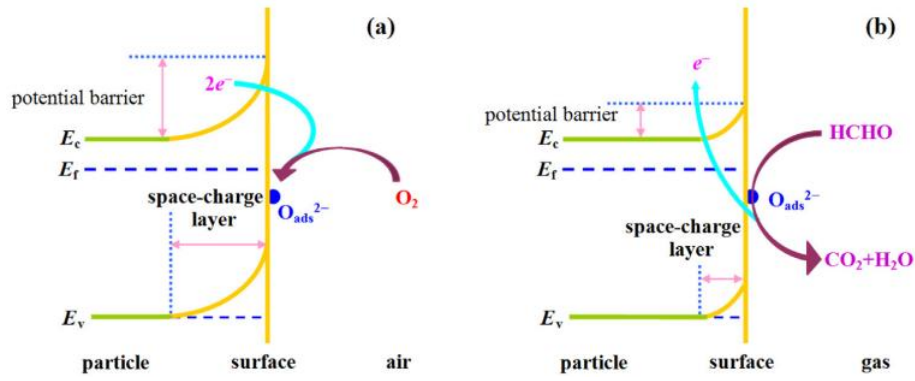


Figure II-11: Proposed sensing mechanism for HCHO on SnO<sub>2</sub> microspheres: (a) in air, (b) in HCHO [47].

### (c) SnO<sub>2</sub>-Nanorods

A gas sensor based on a regular array of SnO<sub>2</sub> nanorods on a bottom film was designed to demonstrate carrier mobility-dominated gas-sensing (CMDGS) by using it for room temperature gas sensing [49]. By applying ultrathin alumina membrane (UTAM) as a template, SnO<sub>2</sub> nanorod arrays with different lengths (340, 140, 110, and 40 nm) were prepared. In a plane view of the SnO<sub>2</sub> nanorod array, its SEM image depicts that the nanorods are vertically and hexagonally arranged with a period of 100 nm (Figure II-12 A). In cross-sectional views, different lengths of the nanorods can be observed, such as 140 nm of nanorod length (Figure II-12 A). It was found that the key parameter for determining the gas-sensing mode is adjusting the length of the arrayed nanorods. With the change in the nanorod length from 340 to 40 nm, the gas-sensing behavior changes from the conventional carrier density-dominated gas sensing (CDDGS) mode ( $I_t/I_0 > 1$ ) to a complete carrier-mobility mode ( $I_t/I_0 < 1$ ) (Figure II-12 B). The change from the positive to the negative response occurs when the nanorod length decreases from 110 to 80 nm, indicating that the CDDGS-CMDGS changing point of the nanorod length for ethanol is located within the range of 110-80 nm. Moreover, for the detection of 25 ppm acetone, the CMDGS-mode sensor (i.e., the 40 nm length sample) exhibited a current decrease of about 58% ( $1 - I_t/I_0 = 0.58$ ), whereas the CDDGS-mode sensor (i.e., the 340 nm length sample) showed a current increase of about 13% ( $I_t/I_0 - 1 = 0.13$ ), indicating that the sensitivity of the CMDGS mode was more than 4 times higher than that of CDDGS. Therefore, CMDGS proved to be an emerging gas-sensing mode for designing inorganic semiconductor gas sensors with high performances at room temperature. In addition, an optimum length of nanorods was achievable for obtaining the best CMDGS response, such as 40 nm of nanorod length as the best value for ethanol.

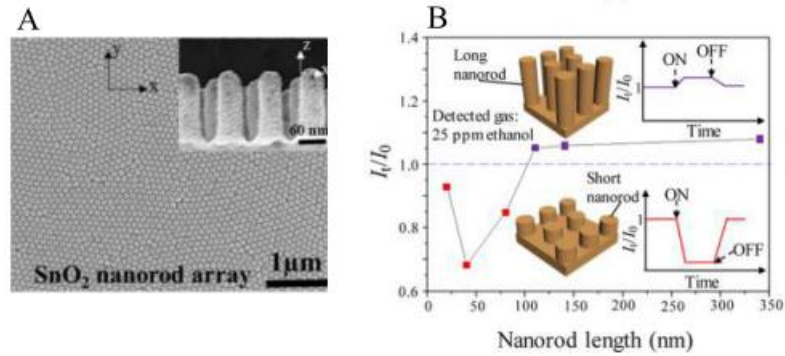


Figure II-12: (A) Plane view of SnO<sub>2</sub> nanorod array. The inset indicates the cross-sectional views of the SnO<sub>2</sub> nanorod arrays with 140 nm of nanorod length. (B)  $I_t/I_0$  of the SnO<sub>2</sub> nanorod array gas sensor versus the nanorod length (340, 140, 110, 80, 40, and 20 nm) in the detection of 25 ppm ethanol gas, describing that the CMDGS (i.e.,  $I_t/I_0 < 1$ ) substitutes the CDDGS (i.e.,  $I_t/I_0 > 1$ ) as the nanorod length is shorter than or equal to 80 nm [49].

(d) SnO<sub>2</sub>-Nanotubes (NTs)

To obtain high performance semiconductor metal oxide (SMO) gas sensors toward hydrogen sulfide (H<sub>2</sub>S) gas, Cho *et al.* have developed a facile fabrication method which effectively combines micro-electro-mechanical-systems (MEMS) heating platforms and porous SnO<sub>2</sub> nanotubes (Figure II-13 A). This method was based on sequential liquid-phase process consisting of localized hydrothermal synthesis and liquid-phase deposition (LPD). By using this sequential process, ZnO NWs could be locally synthesized in microscale area on freestanding MEMS device and then substituted to porous SnO<sub>2</sub> NTs through LPD. By controlling the LPD condition (i.e. pH), the amount of ZnO remaining in the SnO<sub>2</sub> tube could be modulated. As a result, SnO<sub>2</sub>-ZnO hybrid nanostructures as well as SnO<sub>2</sub> NTs were prepared. The SnO<sub>2</sub> NTs showed excellent sensitivity, response speed, and stability to H<sub>2</sub>S gas and exhibited the highest sensitivity at 5 mW heating power (Figure II-13 B). This study opens the way toward the development of a low-power electronic nose system by integrating a 1-D nanomaterial array (e.g., SnO<sub>2</sub>, CuO, ZnO, and TiO<sub>2</sub>) into a single chip through a sequential liquid-phase process for multiplexed detection of various gas species.

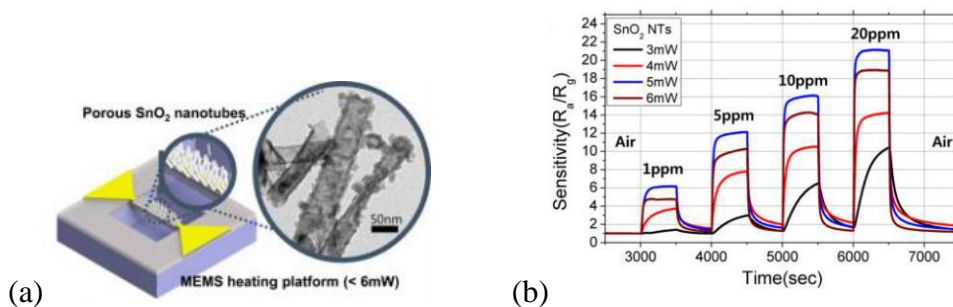
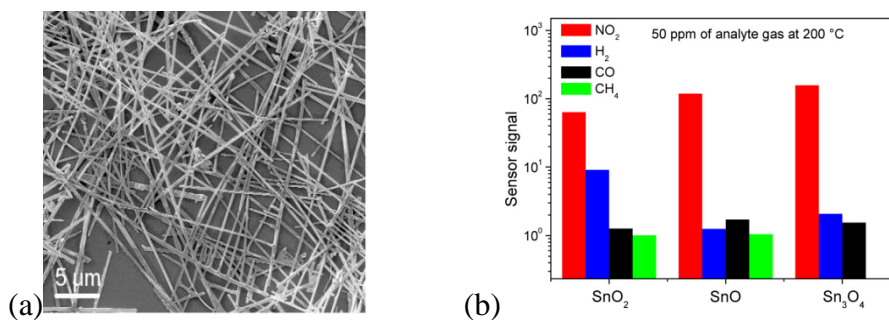


Figure II-13: (a) a TEM image of SnO<sub>2</sub> NTs synthesized by LPD at pH = 4; (b) The dynamic sensing response of H<sub>2</sub>S on SnO<sub>2</sub> NTs (synthesized at pH = 4) [50].



### (e) SnO<sub>2</sub>-Nanobelt

Tin oxide nanobelts including tin centers in various oxidation states (SnO<sub>2</sub>, SnO and Sn<sub>3</sub>O<sub>4</sub>) were synthesized by a carbothermal reduction method using a mixture of SnO<sub>2</sub> powder and carbon black as starting materials [51]. Gas sensing results revealed that Sn<sub>3</sub>O<sub>4</sub> nanobelts led to the highest sensor response to 50 ppm NO<sub>2</sub> at 200 °C. Moreover, at this operating temperature, Sn<sub>3</sub>O<sub>4</sub> nanobelts were found to display the highest selectivity to NO<sub>2</sub> relative to CO while SnO nanobelts showed the highest selectivity to NO<sub>2</sub> relative to H<sub>2</sub> and CH<sub>4</sub> (Figure II-14 B). As a result, tin oxide semiconducting nanomaterials, with unusual oxidation states for tin centers, appeared to be promising alternatives to SnO<sub>2</sub> for use in high performance gas sensor device.



**Figure II-14:** (a) FEG-SEM images of SnO<sub>2</sub> nanobelts synthesized by a carbothermal reduction method under controlled synthesis atmospheres; (b) Sensor signal of the three tin oxide nanobelts compositions for 50 ppm of NO<sub>2</sub>, H<sub>2</sub>, CO and CH<sub>4</sub> at 200 °C [51].

### (f) SnO<sub>2</sub>-Porous films

Kamble *et al.* have elaborated nanocrystalline tin oxide (SnO<sub>2</sub>) thin films by spray pyrolysis technique with varying the precursor concentration of the solution (0.1 M, 0.2 M, 0.3 M, 0.4 M and 0.5 M of SnCl<sub>4</sub>·5H<sub>2</sub>O solution) for NO<sub>2</sub> gas detection [52]. Spray pyrolysis is a chemical process in which a solution is sprayed on a heated substrate which is kept at a specific temperature. Thin films prepared from the 0.4 M solution showed a maximum gas response of 556 towards 10 ppm NO<sub>2</sub>. This is due to the adsorption of electrons on the surface of SnO<sub>2</sub> thin film by increasing the film thickness and hence the presence of porosity and the availability of free Sn sites for the interaction of oxidizing NO<sub>2</sub> gas molecules. Figure II-15 B shows the sensor response of these films toward 10 ppm of NO<sub>2</sub> gas as the function of the operating temperature in the 80-260°C range. The sensor response clearly increased with increasing the temperature and reached a maximum gas response value of 311.7 at 150 °C, a further increase in the operating temperature inducing a sensor response decrease. This trend at higher temperature was attributed to the dissociation of oxygen molecule into its atomic species due to which NO<sub>2</sub> gas molecules have to compete with oxygen atomic species for active sites on the metal oxide surface. This limits the adsorption of NO<sub>2</sub> gas molecules on the surface of SnO<sub>2</sub> and hence sensor response decreased with increasing in temperature. The maximum gas response was observed for NO<sub>2</sub> (556) gas rather than acetone (34), ammonia

(43), ethanol (46) and liquefied petroleum gas (59 for LPG) at 150 °C (Figure II-15 C), indicating the gas selectivity of the SnO<sub>2</sub> thin film prepared from the 0.4M solution. As a consequence, SnO<sub>2</sub> thin films deposited by spray pyrolysis can be used for selective and sensitive detection of NO<sub>2</sub> gas up to 5 ppm.

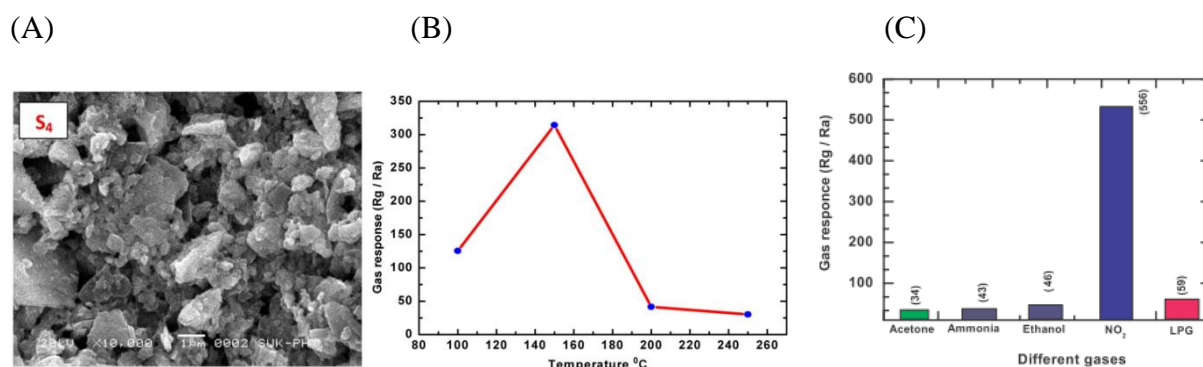


**Figure II-15: (A) SEM micrographs of thin films prepared from a 0.4 M solution; (B) Variation of sensor response of these thin films to 10 ppm of NO<sub>2</sub> gas at different temperatures; (C) Gas sensing performance of these thin films for various gases [52].**

In addition, the development of synthetic strategies providing materials with well-defined porosity is a key step toward efficient gas sensors as it should make easier the diffusion of gaseous species or into the porous materials [53].

## II.2.5 Gas selectivity problem and general approaches

Chemiresistors, conductometric or resistive gas sensors based on semiconducting materials, are indeed not selective since they can respond to several molecules in their surroundings. This is related to the modus operandi of the chemiresistors. The key process is the adsorption of the dioxygen and its subsequent reactions with gas molecules to be detected. As the same or similar changes in the conductivity may be caused by completely different molecules, these processes are not specific. For instance, any reducing gas (carbon monoxide, NH<sub>3</sub>, methane, ethylene, etc) is thought to be detected through its oxidation by adsorbed oxygen. Accordingly, specificity is lacking.

As an efficient gas sensor, selectivity is a crucial parameter. Metal oxide semiconductor (MOS) gas sensors are very attractive owing to their low cost simplicity of use, large number of detectable gases and various potential application fields. However, the MOS gas sensor has a serious shortcoming of low selectivity in the presence of a mixture of gases. Recent researches to improve semiconductor oxide-based gas sensors are mainly based on two ways: The first way is to dope the sensing layer with rare metal oxides (PdO, NiO, CdO, etc. [54]) or noble metals (Au, Ag, Pt, Pd, etc. [3a]). Even though the exact role of noble metal in the sensor response process is still subject to debate, two mechanisms have been proposed to rationalize the results. The “chemical” mechanism insists on the ability of the metal to dissociate oxygen, to spill over the SnO<sub>2</sub> surface and to catalyse the combustion of the target

gas and the reduction of the SnO<sub>2</sub> matrix, for instance Pt, Pd-SnO<sub>2</sub> [3a]. The “electronic” one involves the variation of contact potential on the Nanoparticle/SnO<sub>2</sub> interface caused by the change of the charge or the oxidation state of the nanoparticles, for example, Ag-SnO<sub>2</sub> [3a]. The second way is to prepare composite sensing materials, such as binary or ternary metal oxides and organic-inorganic materials. For example, SnO<sub>2</sub>/ZnO composite nanofibers were synthesized recently by Khorami *et al.*, who reported highly sensitive toward ethanol [55]. Moreover, an increase in the selectivity of metal oxide sensors could be also achieved in the following ways:

- appropriate tuning of operating temperature [56];
- tailoring the nanostructure (particle size, porosity, and crystallinity) of SnO<sub>2</sub>-based films using purely inorganic [57];
- application of filters and surface coating [58];
- simultaneous measurement of several physical values with the same sensor [59];
- non-stationary methods of measurement of electrical conductivity [60].

### **II.3 Hybrid materials: definition, classification and applications**

The field of hybrid materials is one of the most exciting research areas in science and technology which has known outstanding developments over the past three decades [61]. Many different routes to vary the composition and to control the structure of this materials class have been developed in fundamental research and transferred into technological applications [62]. Particularly, the synergetic combination of inorganic and organic components at the molecular level make this class of materials possibly the broadest playground for different disciplines in material science. Indeed, conventional materials such as metals, polymers or ceramics cannot fulfill the requirements for new applications which has initiated the birth of the hybrid material field. The history of mixing two compounds in one material to achieve improved properties is as old as mankind. One of the very old examples is the combination of straw (an organic fiber) and clay (an inorganic matrix) for the construction of houses. This mixture is not only solid, durable, non-toxic but also a good insulator and a thermal storage medium. However, this material is not called hybrid material from a scientific point of view, more likely it would belong to the composite materials. A more suitable example is the old dye Maya blue ( $x \cdot \text{indigo} \cdot (\text{Mg,Al})_4\text{Si}_8(\text{O,OH,H}_2\text{O})_{24}$ ) [63], which is a mixture of a clay mineral (palygorskite or more rarely sepiolite) and the organic dye indigo and shows impressive high stability which indigo alone does not [64]. The ancient Maya fresco paintings are characterized by bright blue colors that had been miraculously preserved (Figure II-16) [65]. It is a true example of hybrid materials which combines the resistance of an inorganic network and the color of an organic pigment in one material having properties well beyond those of a simple mixture of its components. In fact, the Maya blue pigment had withstood more than twelve centuries of a harsh jungle environment looking almost as fresh as when it was used in the 8th century. This material is often mentioned when it comes to the beginning of the history of hybrid materials.

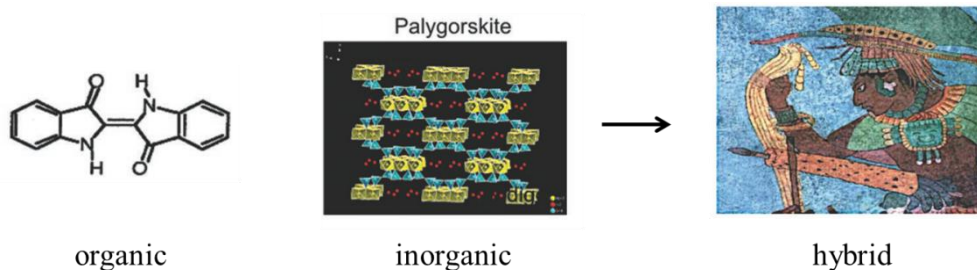
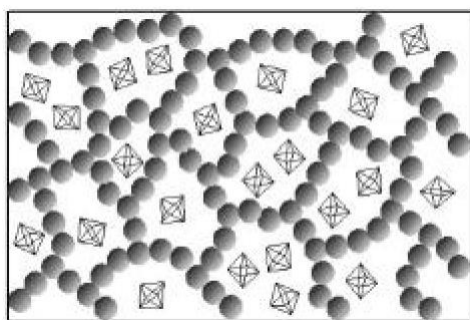
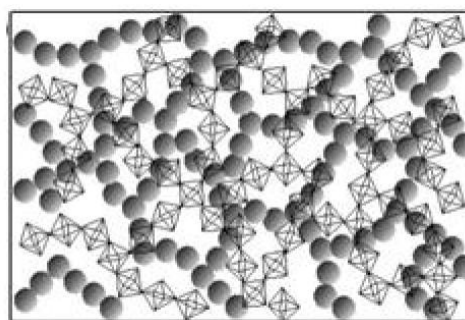


**Figure II-16: Ancient hybrid material for art: Maya blue [65].**

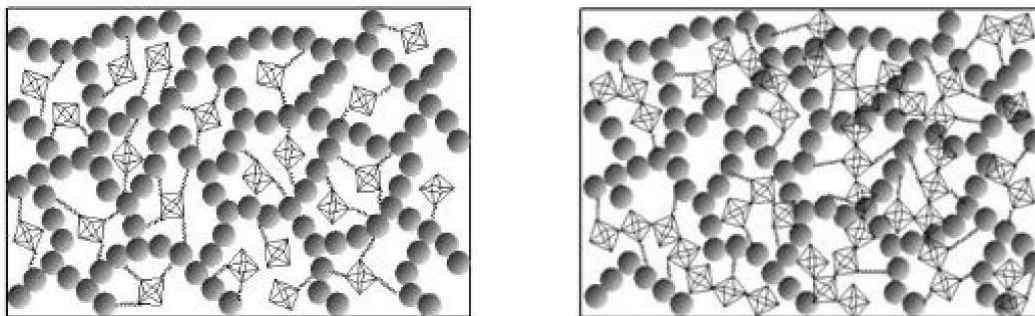
The current definition of hybrid material is given by the International Union of Pure and Applied Chemistry (IUPAC): A hybrid material is composed of an intimate mixture of both inorganic and organic components. Note: “The components usually interpenetrate on scale of less than 1  $\mu\text{m}$ . [66]” This definition is a very broad classification and has the disadvantage that it still covers a wide range of materials including many kinds of inorganic crystalline materials, polymer blends, and nanocomposites. A common and more specific definition would be: “A hybrid material consists of at least two components - usually an inorganic and an organic component – that are molecularly dispersed in the material.” Following this definition, hybrid materials are a special case of composites showing a mixture of the different components on the molecular length scale. Currently, a general classification of hybrid materials based on the interactions linking the inorganic and organic species has been proposed. In **Class I hybrid materials**, organic and inorganic components only exchange weak interaction (Figure II-17) to bond the whole structure. In **Class II hybrid materials**, parts of the two components are linked together through strong chemical bonds (Figure II-17).



(a) Blends



(b) Interpenetrating networks



(c) Building blocks covalently connected (d) Covalently connected polymers

**Figure II-17: The different types of hybrid materials: (a) blends (b) interpenetrating networks in class I; (c) building blocks covalently connectly (d) covalently connected polymer in class II [61b]. The grey spheres represent inorganic network and the polyhedrons represent the organic building blocks.**

### **Class I hybrids:**

In class I hybrid materials (Figure II-17), organic and inorganic components are linked together through weak bonds (van der Waals, hydrogen bonds, hydrophobic-hydrophilic balance,  $\pi$ - $\pi$  interactions, or electrostatic forces). They result from much research work emerging from sol-gel and polymer chemists and these materials will present a large diversity in their structures and final properties

### **Class II hybrids:**

Class II hybrid materials (Figure II-17) are the structures in which organic and inorganic components are grafted together through strong chemical bonds (covalent, ionic-covalent bonds, or Lewis acid/Lewis base bonds). The molecules used as starting building blocks for class II hybrids possess at least two distinct functionalities: alkoxy groups (R-OM bonds) which should experience hydrolysis-condensation reactions in the presence of water and lead to an oxo-polymer framework, and metal-to-carbon links which are stable in the hydrolysis reactions. The nature of the stable metal-to-carbon link depends on the nature of the metallic cation. Organometallic links (M-C bonds) are stable towards hydrolysis when M is silicon (Si), tin (Sn), mercury (Hg), lead (Pb) or phosphorus (P). On the contrary, M-C bonds are not stable when M is a transition-metal cation. Those M-O-C bonds which are stable upon hydrolysis could be the links between the organic and inorganic parts.

From the above mentioned points, it seems clear that hybrid materials are artificial systems developed in chemistry and materials science laboratories. In fact, the origin of hybrid materials, did not take place in the chemical laboratory but in nature. Typical examples are nacre (Figure II-18) which is a natural material made from platelets of aragonite glued together by biopolymers [67], crustacean carapaces, mollusc shells and bone or teeth tissues in vertebrates.



**Figure II-18: Iridescent nacre in a nautilus shell (left) and TEM image of nacre platelets (right) [68].**

Nowadays, most of hybrid materials that have already entered to the commercial markets owing to their applications ranging from sensors, dental filling, new generation of photovoltaic and fuel cells, smart microelectronic, functional smart coatings, micro-optical and photonic components [62a-b], but they only represent a small fraction of the tip of the iceberg. One of the main successful example are the class II hybrids named ORMOCERs (Organically Modified Ceramics) which was developed by the Fraunhofer Institute (Würzburg, Germany) since the eighties. The corresponding synthetic strategy involves the introduction of an organic group into an inorganic silica network by using organo-alkoxysilane molecular precursors or oligomers of general formula  $R'_nSi(OR)_{4-n}$  or  $(RO)_{4-n}Si-R''-Si(OR)_{4-n}$ . As mentioned above, the Si-C bond remains stable towards the hydrolysis-condensation yielding the silicate network and the organic moieties ( $R'$  and/or  $R''$ ) provide focused new properties to the inorganic network such as flexibility, hydrophobicity, refractive index modification and optical response. In addition, the co-condensation of these functional organosilanes with metal alkoxides, mainly  $Si(OR)_4$ ,  $Ti(OR)_4$ ,  $Zr(OR)_4$  or  $Al(OR)_3$ , allowed for modulating the characteristics (refractive index, mechanical resistance...) of the inorganic network. This approach has led to actual commercialized products in the numerous areas. Few selected examples of commercial applications of hybrid nanomaterials have been gathered in Figure II-19.



**Figure II-19: Examples of commercial applications of hybrid materials [62a].**

Indeed, numerous domains such as micro-optics, microelectronics, and photonics (curved



lenses, microlenses, waveguides based on hybrids coated on rigid substrates or on flexible foil, printed electro-optic circuits); protective/smart coatings (decorative, antidust, antiscratch, self-cleaning, antireflective, anticorrosion, antifogging, antirain); energy (photovoltaic cells, fuel cells, batteries, hybrid membranes for proton-exchange membrane (PEM) fuel cells, protective layers in photovoltaic solar cells, solid state dye-sensitized hybrid cell, ultrathin flexible batteries, etc.); environment (catalysis, photocatalysis, biocatalysis sensors, biosensors, membranes, etc.); human care, medical, and cosmetics domains (implants, imaging, therapeutic carriers, sensors, biosensors, dental cements, bioprotective coatings, hair and skin repair, etc.); car, and packaging industries (green tyres, weight lightening, polymer reinforcement, nanocomposite-based packaging, etc.); construction (organoclays paints), have been strongly impacted by the great versatility of hybrid material science.

### II.3.1 Sol-gel process

The main synthetic strategies towards functional organic-inorganic materials are based on sol-gel process [62c]. The sol-gel chemical process is a low temperature method to prepare oxides and ceramics based on the hydrolysis-condensation of molecular precursors. Thus, this hydrolysis-condensation process provide a sol which can evolve towards a gel or a precipitate leading to particles, monoliths, fibers or films depending on the drying and the material processing conditions [69] (Figure II-20).

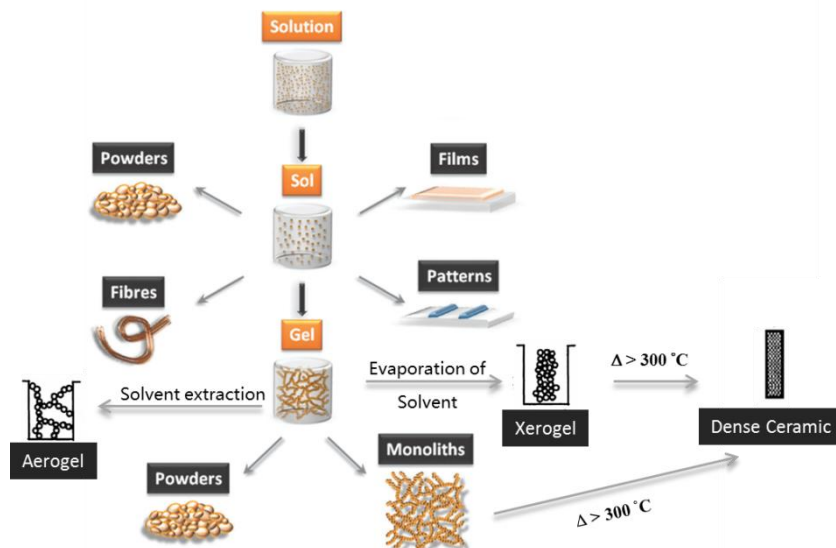


Figure II-20: Overview of the sol-gel process [71].

By definition, a sol is a colloidal dispersion of small particles in a liquid phase whereas a gel is usually a substance composed of a continuous network encompassing a continuous liquid phase [70]. Sol-gel reactions promote the growth of colloidal particles (sol) and their subsequent network formation (gel) through the hydrolysis and condensation reactions of inorganic alkoxide monomers. Shrinkage of a gel, as liquid evaporates during drying, involves

deformation of the network and transport of liquid through the pores. The resulting dried gel, called xerogel, is often reduced in volume by a factor of 5 to 10 compared to the original wet gel. If the wet gel is placed in an autoclave and dried under supercritical conditions, there is no interface between liquid and vapor, so there is no capillary pressure and relatively little shrinkage. This process is called supercritical drying, and the product is called an aerogel. This is indeed mostly air, having volume fractions of solids as low as ~1%. Xerogels and aerogels are useful in the preparation of dense ceramics, but they are also interesting in themselves because their high porosity and surface area. A ceramic is usually defined as nonmetallic and inorganic. The precursors for synthesizing these colloids consist of a metal or metalloid element surrounded by various reactive ligands, which form an inorganic 3D network over time. Metal alkoxides are most popular because they react readily with water. The most widely used metal alkoxides are the alkoxy silanes, such as tetramethoxysilane (TMOS) and tetraethoxysilane (TEOS). However, other alkoxides such as aluminates, titanates, zirconates, and borates are also commonly used in the sol-gel process, either alone or in combination with other alkoxides such as TEOS. Compared to classical solid state reactions, the sol-gel method has the advantage that the precursors react with each other in a liquid environment which reduces many diffusion problems that exist in solid state processes.

The basic reactions in the most investigated silicon-based sol-gel process are the hydrolysis of the precursor (silicon alkoxide:  $\text{Si}(\text{OR})_4$ ) and the condensation of the formed silanol groups (scheme II-1), which then leads to the formation of sol and after crosslinking the solid components in the sol to the formation of a gel. This solid product still contains water and alcohol in its pores. Further processing can lead to powders (xerogels), thin films or aerogels.

### II.3.1.1 Hydrolysis

Hydrolysis constitutes the first step of the sol-gel process in which Si-OR bonds are hydrolyzed into unstable silanols (Si-OH) with the concomitant release of alcohol molecules.



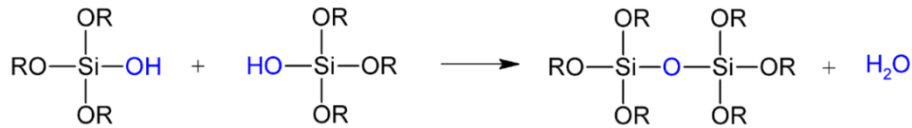
**Scheme II-1: Hydrolysis reaction in the sol gel process of silicon alkoxide.**

### II.3.1.2 Condensation

The unstable silanols (Si-OH) then condense together to form siloxane bridges (Si-O-Si) which serve as the inorganic network. The reaction can proceed in two manners, oxolation and alkoxolation.

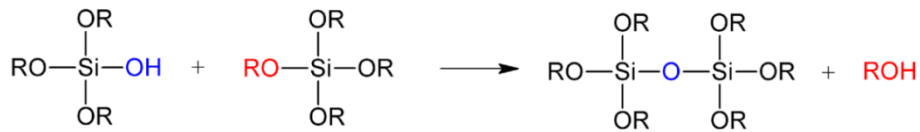
1. Oxolation: two silanols condense together and release water as a secondary product.





**Scheme II-2: Homocondensation in the sol-gel process of silicon alkoxide.**

2. Alkoxolation: a silanol group reacts with an alkoxy group to yield an alcohol molecule as a secondary product.

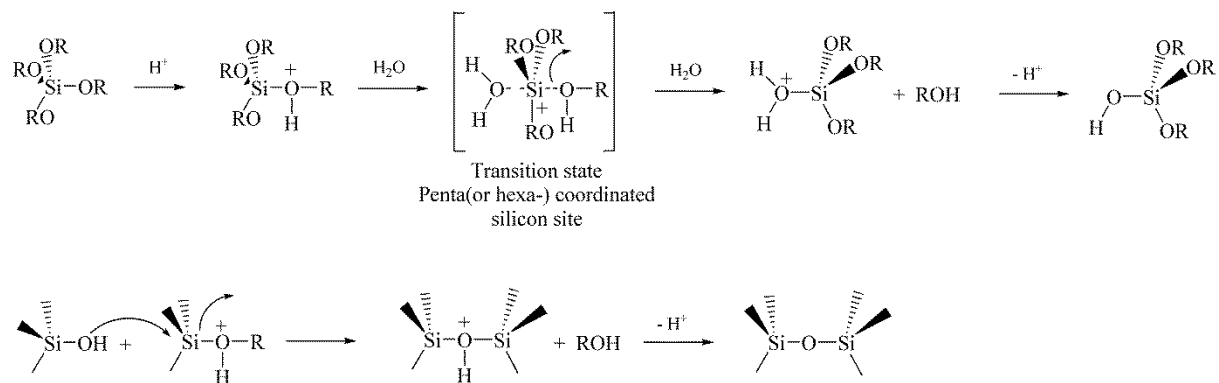


**Scheme II-3: Heterocondensation in the sol-gel process of silicon alkoxide.**

### II.3.1.3 Catalysis for hydrolysis and condensation

The catalysts play an important role in the sol-gel process by controlling the rate of hydrolysis and condensation. To complete the hydrolysis, it requires excess of water or the use of hydrolysis catalyst having an acidic or basic character; however, sometimes salts are employed as well. The most commonly used catalysts are mineral acids (HCl, H<sub>2</sub>SO<sub>4</sub>, HNO<sub>3</sub> etc.), alkali metal hydroxides (NaOH), and ammonium hydroxide (NH<sub>4</sub>OH).

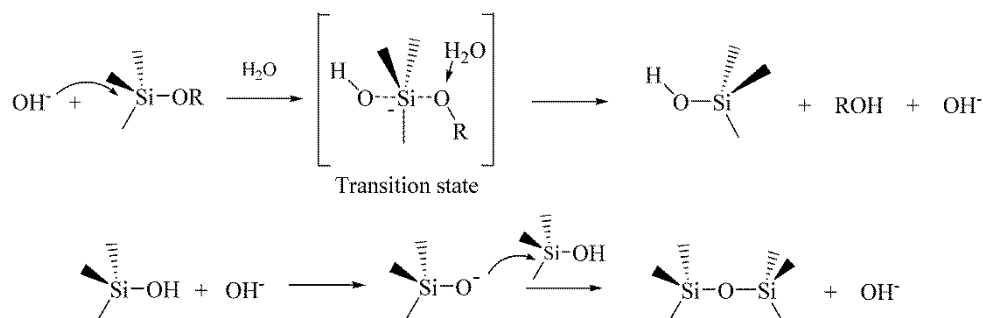
1. Acid-catalyzed: Under these conditions, the hydrolysis rate is much more increased than the condensation one, resulting in a less branched inorganic network (Figure II-21 A). The mechanism of acid catalyzed is an electrophilic reaction that can be expressed as below:



**Scheme II-4: The mechanisms of hydrolysis and condensation in acidic media.**

The silanol replaces either the alkoxy or the hydroxyl group of the neighboring alkoxide which results in the formation of a dimer.

2. Basic-catalyzed: In a basic catalyzed condition, the condensation rate is much more increased than the hydrolysis one, resulting in highly branched aggregates (Figure II-21 B). A nucleophilic substitution of alkoxide groups (OR) by hydroxyl ions occurs as below:



**Scheme II-5: The mechanisms of hydrolysis and condensation in basic media.**

3. High basic-catalyzed: no gelation will occur and monodisperse spherical particles (200 nm) formed (Figure II-21 C).

Therefore, different catalysts produce significant variations for the properties of silicon polymers as in Figure II-21.

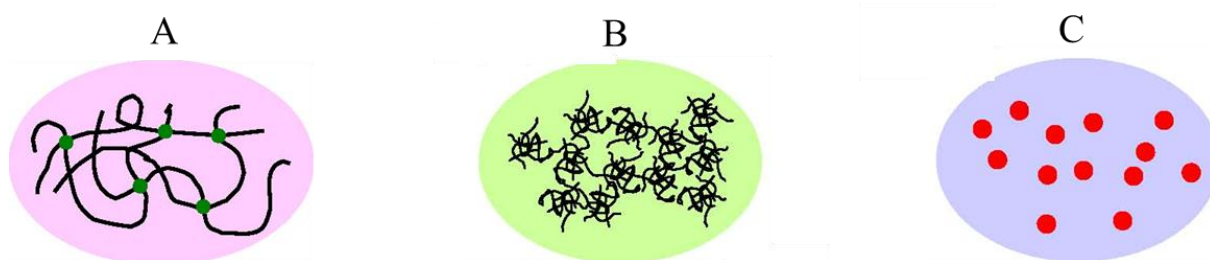


**Figure II-21: Catalysis control of the polymerization in the sol gel process of silicon alkoxide: (A) weakly branched polymers formed under acid catalyst; (B) highly branched aggregates formed under basic catalyst; (C) monodispersed spherical particles formed under highly basic catalyst.**

Sol-gel science and technology has the potential to make a significant impact in modification of the properties of materials. One of the most significant benefits of sol-gel science is the use of room temperature conditions and its insensitivity to the atmosphere. These features will allow its use with various materials, which cannot tolerate high temperatures and does not limit the researcher to using special precautions, such as a dry box. By assuming the load- and thermal-bearing phase in the material, sol-gel materials can increase thermal and mechanical properties of composites if the two systems are mixed homogeneously on the molecular level. A number of factors, including water content, modifiers, and solvent, can be altered in any sol-gel system, modifying the connectivity of the network and affecting the properties.

### II.3.2 Organotin hybrid

Among the various possible elements, tin is one of the rare metals showing Sn-C<sub>sp2</sub> or Sn-C<sub>sp3</sub> bonds stable under the hydrolysis conditions used in the sol-gel process. On the other hand, tin possesses a vacant 5d orbital that promotes hydrolysis-condensation processes by showing different coordination states during the transition state of the reaction. Considering the low number of organotin sol-gel precursors available, tin-based hybrid materials have not been widely developed as silicon-based analogues. It is mainly due to the fact that functional organotin trialkoxides precursors are not easily accessible due to handling and purification problems. There are two major methods which have been developed so far to construct organotin hybrid materials: i) the use of tin-oxo nanobuilding blocks as inorganic compact source [72] (Figure II-22a); ii) the development of di-metallic sol-gel precursors in which the two metal centers are bridged by an organic spacer (Scheme II-22b).

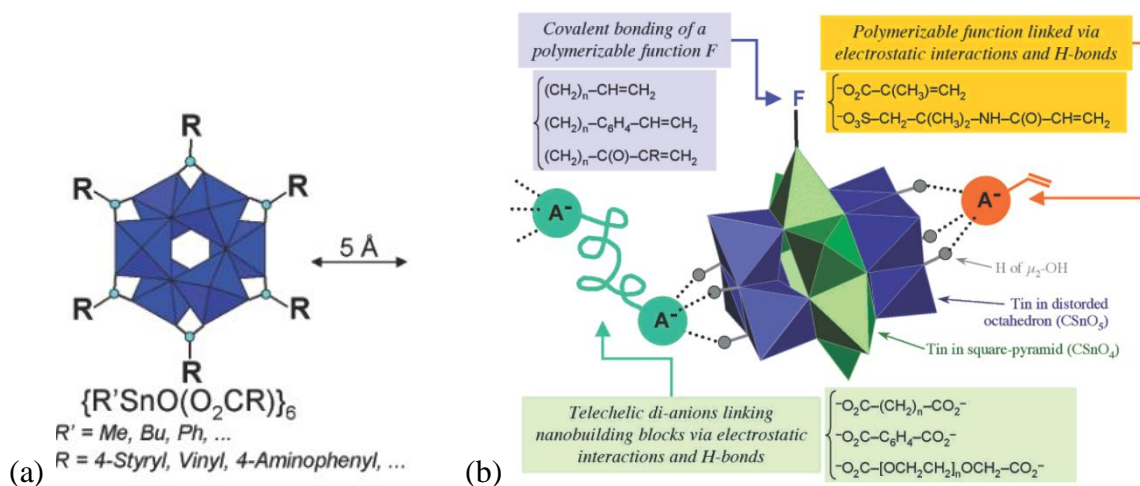


**Figure II-22: Two examples of tin-oxo clusters that can be used as nanobuilding blocks (NBBs): (a) tin-6; (b) schematic representation of the various possible strategies that can be used to assemble functionalized  $\{(R'Sn)_{12}O_{14}(OH)_6\}^{2+}$  clusters into hybrid materials [74].**

The first method is to use tin-oxo clusters as nanobuilding blocks to design new tin-based hybrid materials. In the first example, tin oxo-carboxylate clusters, such as  $\{R'SnO(O_2CR')\}_6$  ( $R = \text{methyl, phenyl, or butyl}$  and  $R' = \text{any organic function}$  [50e]), abbreviated as tin-6, represent a family of nanobuilding blocks in which the carboxylate groups can be used to provide the assembling functions [73]. Another interesting nanobuilding block is the oxo-hydroxo cluster  $\{(R'Sn)_{12}(\mu_3-O)_{14}(\mu_2-OH)_6\}^{2+}$ , abbreviated as tin-12 [74]. It can be prepared through several chemical pathways, including hydrolysis of organotin trichlorides [74f,h], trialkoxides [74d], trialkynides [74g] or refluxing in toluene butyltin hydroxide oxide and sulfonic acids [74b,i]. Depending on the preparation conditions different anions (e.g.,  $OH^-$ ,  $Cl^-$ ,  $R'SO_3^-$ ,  $R'CO_2^-$ ) balance the +2 charge of the cluster. These charge-compensating anions are situated at both cage poles, close to the hydroxy groups that bridge the six-coordinate tin atoms. Tin-12 clusters are versatile nanobuilding blocks for the synthesis of

well-defined tin–oxo-based hybrid materials that can be used as models; possible synthesis strategies associated with this cluster are depicted in Figure II-22 [74]. These clusters can be assembled through organic networks by using the covalent interface provided by the Sn–C bond, by using the ionic interface associated to the charge compensating anions  $X^-$ , or even by using both. In the first case, the organic moiety bound to tin should be polymerizable (e.g., R = butenyl, propyl methacrylate, propylcrotonate, 4-styryl) [75]. In the second case, charge-compensating organic dianions (dicarboxylates, or  $\alpha,\omega$ -telechelic macromonomers terminated by carboxylic or sulfonic groups) can be used to bridge the clusters [76].

As a typical example of the type of hybrid materials, hydrolysis of butenylSn(OAm)<sup>t</sup><sub>3</sub> first led to a tin oxo-hydroxo cluster surrounded by butenyl chains. Further radical polymerization of these butenyl groups in the presence of azobis(isobutyronitrile) (AIBN) yielded hybrid material in which tin-oxo clusters are linked to the organic network through Sn–C strong covalent bonds (Figure II-23).

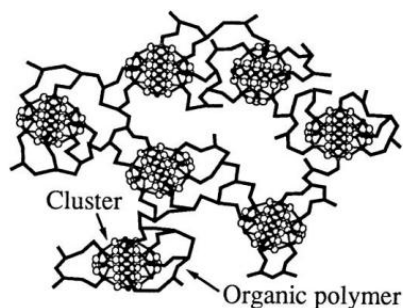
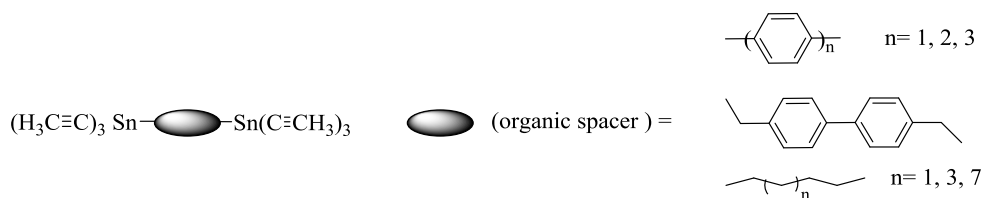


**Figure II-23: Schematic representation of a tin-based class II hybrid material [77].**

The second strategy was inspired from the works on the hydrolysis-condensation of bis(trialkoxysilyl)alkylene, arylene and benzylene derivatives in the presence or not of organic templates. Thus, this approach yielded bridged silsesquioxane hybrid materials exhibiting controlled texture and morphology, both at the mesoscopic and molecular levels [78]. Long-range ordered structures were also obtained when the organic bridge between the two silicon atoms contained urea functionalities able to induce the self-assembly of the organic linker via hydrogen bonding [79]. In the case of organotin-based hybrid materials, this route has been developed by Jousseume *et al.* in our institute [80] who have designed organodistannylated sol-gel precursors, also named as  $\alpha,\omega$ -bis(trialkynylstannylated) compounds, which led to nanostructured self-assembled organotin-based hybrid materials after hydrolysis-condensation processes. Due to the difficulty in purification and isolation of organotin alkoxides, organotin alkynides were used instead [81]. The precursors for these materials consist of two tin atoms, equipped with hydrolysable groups and separated from each other through an organic spacer (Scheme II-6) [80, 82].



**Scheme II-6: Examples of organotin compounds used as precursors of tin-based class II hybrid materials.**

A variety of spacers have been used ranging from long flexible aliphatic chains to rigid aromatic rings and their effect on the organization of the final materials has been studied [80, 82b]. After hydrolysis, the hydrolysable alkynyl groups left as a gas giving an inorganic network based on Sn-O-Sn bonds connected to the organic network via Sn-C stable bonds as a result of the beginning of the aging course. Then the resulting gels were applied to the subsequent drying process (condensation) which allowed the formation of self-assembled tin-based hybrid materials. Fundamental studies, performed by dynamic light scattering, of the hydrolysis-condensation processes of these new sol-gel precursors revealed that the particle growth rate strongly depends on the nature of the linker, a polymethylene spacer leading to the quicker process. This was attributed to a slower condensation process rather than a slower hydrolysis step in the case of aromatic and benzylic linkers [83].

Two kinds of organization have been evidenced by X-ray diffraction. The first organization involves the self-organization of the organic spacers at the nanometer scale through non-bonding interactions ( $\pi$ -stacking, van der Waals interactions, etc.) giving rise to a periodic spacing of tin oxide (Sn-O-Sn) planes [80b]. As a result, tin oxide planes are separated by layers of self-assembled organic spacer and a tilted angle (Figure II-24) was proposed to rationalize the interplanar distance deduced from XRD measurements depending on the expected length of the organic group.

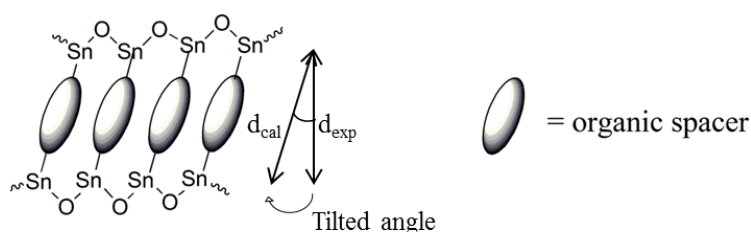
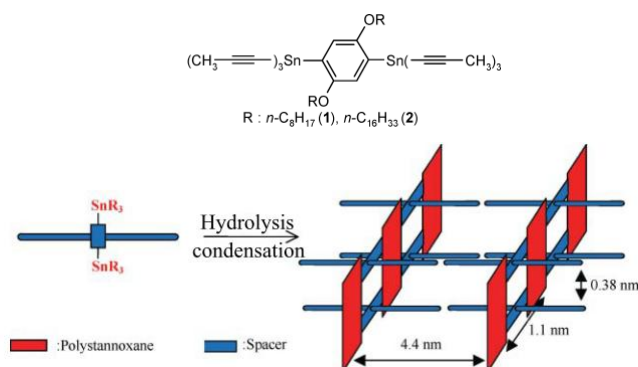


**Figure II-24: Model of organization in tin-based organic-inorganic hybrid materials.**

A second kind of organization was reached by the hydrolysis of cross-shaped bridged  $\alpha,\omega$ -bis(trialkynylstannylated) derivatives bearing long alkyl lateral chains of 8 or 16 carbons (Scheme II-7) [84]. In this case self-assembly of the organic moieties provided a well-organized hybrid material where planes of strips of polystannoxanes alternating with strips of aromatic rings are separated by thick layers of hydrocarbon chains ( $\text{OC}_8\text{H}_{17}/\text{OC}_{16}\text{H}_{33}$ ).



**Scheme II-7: Organization of the hybrid material (perpendicular to the main chains).**

Nonetheless, due to nature of the organic linker used so far, these organotin-based materials exhibited only few specific physical-chemical properties (hydrophobicity, tunable Lewis acidity) which have limited their potential application fields. Rare examples concern use as catalysts for transesterification [85] and gas sensing as develop in the following section.

### II.3.3 Hybrid organic-inorganic materials for gas sensing

A first class of hybrid materials for gas sensing applications concern the combination of tin dioxide particles with carbon materials as carbon nanotubes (CNTs) or graphene. These nanocomposites can be classified as class I hybrid materials. A sensing platform based on hybrid nanostructured consisting of discrete SnO<sub>2</sub> nanocrystals uniformly distributed on the surface of multiwalled CNTs (MWCNTs) has been reported for its high sensitivity to low concentration gases (NO<sub>2</sub>, H<sub>2</sub>, and CO) at room temperature in contrast to the high temperature operation required for SnO<sub>2</sub> nanocrystals alone and to the insensitivity to H<sub>2</sub> and CO for CNTs alone (Figure II-25) [86]. Discrete SnO<sub>2</sub> nanocrystals of ~2 to 3 nm in size uniformly decorated the external surface of the MWCNT. The dependence of the sensor response on the different NO<sub>2</sub> concentrations (100, 50, and 25 ppm) shows higher sensitivity with increasing NO<sub>2</sub> concentration. For 1% H<sub>2</sub>, the average sensitivity was ~0.17; for 1000 ppm H<sub>2</sub>, the average sensitivity was ~0.10; and for 100 ppm CO, the sensitivity was ~0.11. The sensing performance of the hybrid nanostructure sensor could be attributed to the effective electron transfer between SnO<sub>2</sub> nanocrystals and MWCNTs and to the increase in the specific surface area of hybrid nanostructures.



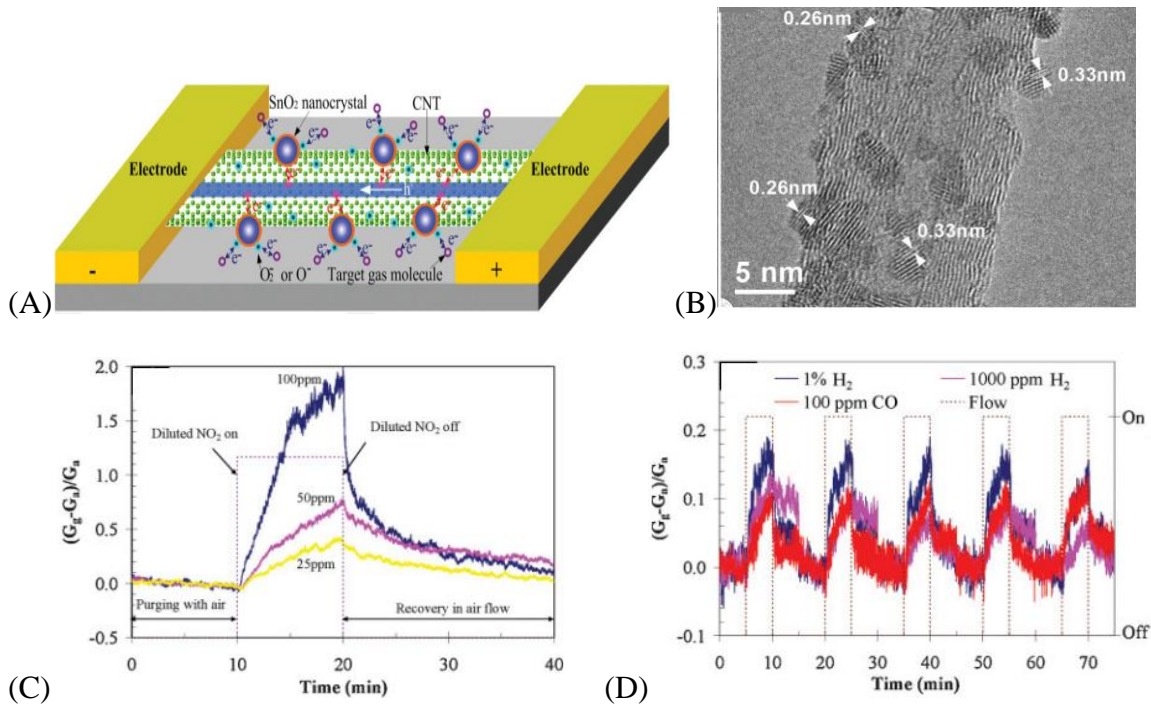


**Figure II-25: (A) SnO<sub>2</sub>-CNT sensing platform; (B) HRTEM image of a MWCNT uniformly coated with SnO<sub>2</sub> nanocrystals; (C) the dependence of the sensor response on NO<sub>2</sub> concentrations of 100, 50, and 25 ppm; (D) room temperature sensing responses of the SnO<sub>2</sub> nanocrystal-MWCNT sensor to 1% and 1000 ppm H<sub>2</sub>, and 100 ppm CO diluted in air.**

Compared to CNTs, graphene has four main advantages in the field of chemical gas sensors: (1) the larger specific surface area; (2) more interfacial contacts in hybrids; (3) lower noise level; (4) larger carrier mobility. Among intrinsic graphene and its derivatives, reduced graphene oxide (rGO) prevails over graphene and graphene oxide on account of its various functional groups and excellent conductivity, respectively. One of the examples for gas sensing application is the SnO<sub>2</sub>-rGO nanocomposites prepared by hydrothermal treatment of aqueous dispersion of GO in the presence of Sn salts (Figure II-26) [87]. During the hydrothermal reaction process, GO was reduced to rGO, and simultaneously different amount of SnO<sub>2</sub> nanoparticles were formed on the graphene sheets. The size of the SnO<sub>2</sub> nanoparticles in the composite was around 10 nm. It is found that SnO<sub>2</sub>-rGO-2 nanocomposites (0.024 g of SnCl<sub>4</sub>·5H<sub>2</sub>O used) exhibit high response of 3.31 at 5 ppm NO<sub>2</sub> at the operating temperature of 50 °C, which is higher than that of rGO (1.13). All the observations indicate that addition of SnO<sub>2</sub> nanoparticles achieved twofold goals: fabrication of peculiar heterostructure between the SnO<sub>2</sub> and the rGO in order to attract more electrons from the rGO toward SnO<sub>2</sub> and to significantly enhance more active sites for the adsorption of gaseous molecules. Moreover, SnO<sub>2</sub>-rGO-2 nanocomposites exhibit response to NO<sub>2</sub> and no obvious response to the other gases (Cl<sub>2</sub>, NO, CO, H<sub>2</sub>O (25%RH) and NO<sub>2</sub>), indicating that SnO<sub>2</sub>-rGO-2 has high selectivity for NO<sub>2</sub> sensing.

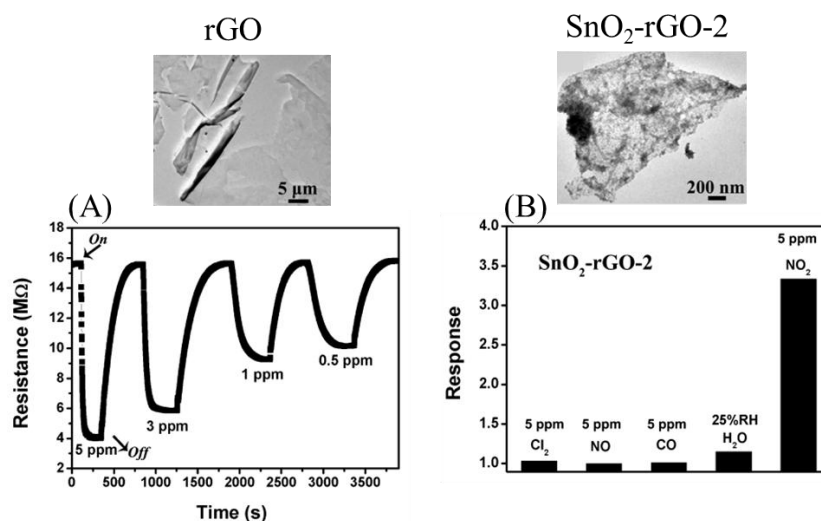


**Figure II-26:** TEM images of rGO and SnO<sub>2</sub>-rGO-2 and (A) the dynamic NO<sub>2</sub> sensing transients of SnO<sub>2</sub>-rGO-2 at 50 °C; (B) the responses of SnO<sub>2</sub>-rGO-2 to different gases (Cl<sub>2</sub>, NO, CO, H<sub>2</sub>O (25%RH) and NO<sub>2</sub>) at 50 °C.

For the class II hybrid material, an interesting gas sensing investigation example on an innovative organic–inorganic hybrid material, referred to as ECS-14 (where ECS = Eni carbon silicates) (Figure II-27), revealed the possibility to use them as selective gas sensors [88]. Indeed, ECS-14 phase was used as functional material in screen-printable compositions and was deposited by drop coating for morphological, structural, thermal, and electrical characterizations. Electrical characterization of the sensors based on ECS-14 versus concentrations of gaseous analytes gave significant results at room temperature in the presence of humidity whereas the response for other gases (methane, acetaldehyde, ammonia, acetone, toluene, ethanol, and benzene) was negligible, thereby demonstrating fundamental properties for a good quality sensor (speed, reversibility, and selectivity) that make them competitive with respect to systems currently in use. The sensing mechanism for humidity was investigated by spectroscopic analysis: both absorption and emission spectroscopy of ECS-14 mainly point to rings in a non-interacting state, with optical properties changing reversibly upon dehydration/ rehydration due to a varied environment of the rings. The near-IR result suggests that the benzene rings constitute a scaffolding bridge between inorganic layers during the dehydration/rehydration process, providing robustness to the ECS structure.

A model for the reaction mechanism has been proposed: ECS-14 channels allow access of water molecules, which, due to their high polarity, are coordinated by sodium atoms (receptors) belonging to inorganic layers. The interaction of adsorbed water molecules with hydroxyl groups, by hydrogen bridges, gives rise to protonic transport (Grotthuss mechanism) along the ECS-14 phase. This sensing mechanism finds analogy with the behavior of chemoresistive gas sensors based on p-type semiconductors. In addition, the benzene rings participate in the sensing mechanism of humidity as transduction element. Therefore, the rare



behavior of functionality exchange between the organic and inorganic components have been observed; that is, in contrast to other hybrids, the functional site of ECS-14 has been ascribed to the inorganic phase while the organic component provided structural stability to the material, leading the possible operation at room temperature and avoiding high power consumption of most common sensors based on metal oxide semiconductors.

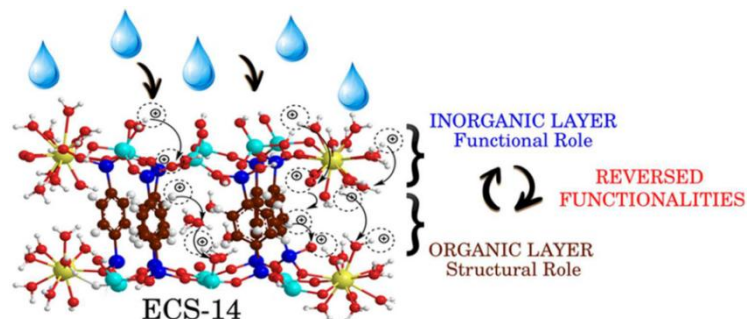


**Figure II-27: Representation of protonic conduction ( $H^+$  ions) along [010] in ECS-14 phase. Si atoms are shown in blue, Al atoms in cyan, benzene rings in brown, oxygen atoms in red, Na atoms in yellow, and H atoms in white.**

Finally, organotin class II hybrid materials also showed gas sensing properties, especially for hydrogen. The first example was reported for self-assembled nanoporous tin-based hybrid thin films prepared by the sol-gel method from organically-bridged ditin hexaalkynides [89]. According to XRD and AFM investigations, these hybrid films exhibited hierarchical organization as depicted in Figure II-28 and, remarkably, they were active in gas detection possessing a near room-temperature gas sensitivity to  $H_2$ . Thus they were able to detect hydrogen gas from 50 to 200 °C at the 200 - 10000 ppm level. These results were very surprising since the hybrid films do not have crystalline  $SnO_2$  structure which is thought to be responsible for gas sensing activity in  $SnO_2$  chemiresistors. According to the results of the dc conductance measurements the organic spacers contribute in an indirect way to the conduction as well as to the sensing mechanism of organized hybrid films.

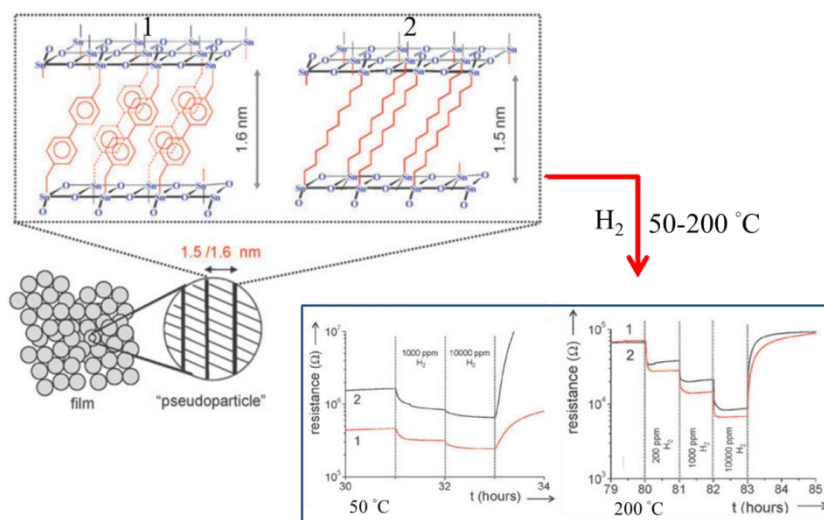


**Figure II-28: Short range hierarchical order in organic–inorganic pseudoparticles containing SnO<sub>x</sub> networks and their gas sensing performance on H<sub>2</sub> at 50 °C and 200 °C [modified from ref. 89].**

In addition, the simpler bis(tri-prop-1-ynylstannyl)butylene precursor also led to hybrid layers detecting hydrogen at moderate temperature. Thus, homogeneous organotin-based hybrid thin films can be processed by the spin-coating deposition technique using a solution of this precursor in presence of water and an acid catalyst [90]. These films showed significant resistance changes in the presence of H<sub>2</sub> at a 150 °C (Figure II-29).

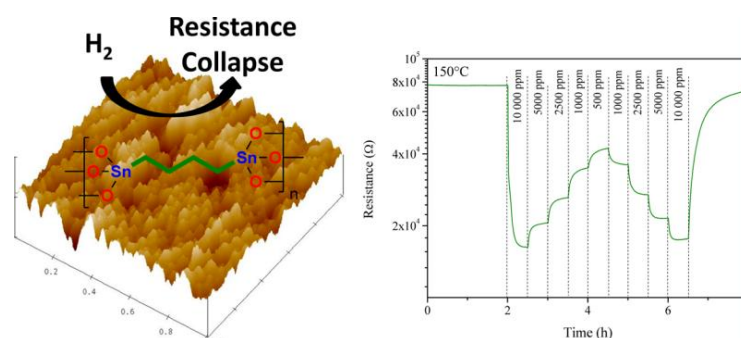


**Figure II-29: AFM image (3D morphology) of an organotin based thin layer (left) and its resistance change in the presence of CO (right) [90].**

Hereafter, these findings open a fully new class of gas-sensing materials as well as a new opportunity to integrate organic functionality in gas sensing metal oxides. Moreover, the question arises about the possibility to use monostannylated precursors to produce these kinds of hybrid layer able to detect gases.

## II.4 Main objectives and outline of the study

### II.4.1 Major objectives

As mentioned in the previous sections, the use of functional hybrid metal oxide based materials that associate at the nanometre level active inorganic and organic components in a single material, is very promising since it allows taking advantage of the outstanding chemical and electronic properties of nanostructured oxide materials and, on the other hand, of the flexibility offered by the organic component. In this context, the aim of this project of fundamental research is to draw new prospects in the field of gas sensing by finely tuning of the chemical nature, the texture and the morphology of the active layer to develop selective gas sensors. Our approach is based on the design of molecular single precursors which contain all the functionalities required to get stable hybrid material showing selective detection of harmful/toxic gasses. The novelty relies on the use of the tool box offered by the organotin chemistry to design original gas sensor operating at low temperature and consuming low energy. This approach associates tightly organometallic chemistry, chemistry of materials, structural characterizations, fabrication and characterization of the target devices, and gathers the complementary skills of University of Bordeaux, Technische Universität Darmstadt (TUD), and University of Brescia. To broaden the scope of the possible applications of these new hybrid and oxide materials, our goal is to apply the previous synthetic route or develop a new synthetic strategy to prepare organotin-based hybrid thin films which can be converted into oxide thin films after various post-treatment. The aim of this project is therefore to develop new hybrid organic-inorganic nanostructured architectures able to selectively detect target gas by exploiting three expected breakthroughs since the use of organic functionality in metal oxide-based sensors has not been explored so far:

- 1) the design of hybrid films involving organotin oxide planes and layers of organic spacers;
- 2) to exploit self-assembly phenomena in organotin-based hybrids to control the nanostructuring of the hybrid active layer;
- 3) to increase the selectivity of the active tin-oxide layers by using functional organic group in the organic spacers.

## II.4.2 General strategy

To attain the previous goals, this project has been divided into three main tasks:

Task 1: Synthesis and characterization of tin dioxide particles used as reference materials for gas sensing

Task 2: Synthesis and preparation of organotin class II hybrid materials using monostannylated precursors

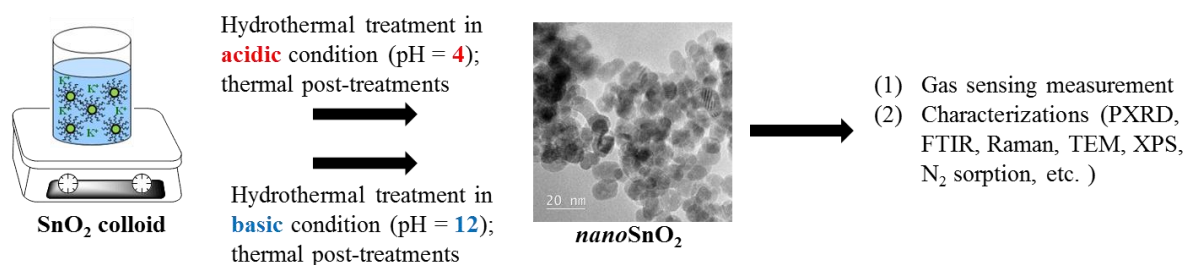
Task 3: Device fabrication and characterization of the gas sensing properties of the materials prepared

### II.4.2.1 Description of task 1

Gas selectivity of SnO<sub>2</sub>-based sensors is one of the most critical issues for purpose applications. Several strategies have been proposed to control gas selectivity as mentioned

above. Nonetheless, these methods usually involve the use of noble metals or long synthetic strategies or processing and do not allow the preparation of large quantities of materials. To circumvent this limitation, we have adapted a hydrothermal method developed to obtain large amount of 18-nm  $\text{SnO}_2$  colloids employed to fabricate porous photoanodes for dye-sensitized solar cells [23, 24d].

In a first part reported in chapter 4, we investigated a similar approach using hydrothermal treatment of a commercial colloid by tuning the pH conditions and the thermal post-treatment used. Indeed, the gas sensitivity and selectivity of these  $\text{SnO}_2$  nanoparticles are expected to be altered by this pH modification. This approach, which can be easily scaled up, provided well-defined tin dioxide nanoparticles which were used as reference materials for gas sensing tests. The obtained nanoparticles were characterized by FTIR, Raman, XRD, TEM, XPS and  $\text{N}_2$  sorption analysis and the films processed from colloidal dispersion of these nanoparticles were characterized by AFM and SEM (Scheme II-8).



**Scheme II-8: Task I in this project.**

#### II.4.2.2 Description of task 2

The promising results obtained at institut des Sciences Moléculaires (ISM, University of Bordeaux) with organotin hybrid layers [89, 90] validate the approach proposed and prompt us to generalize it to new systems involving monostannylated precursors and organic functionalities bearing heteroatoms. The main issue will rely on the introduction of the organic group as thiophene or benzyl groups in the hybrid layers to improve the selectivity of the tin oxide-based hybrid gas sensor. To do so, new organotin precursors have to be synthesized and then used to process hybrid layers by the sol-gel which will be characterized. The corresponding works are reported in Chapter 5.

##### II.4.2.2.1 Task 2-1: Design, Synthesis and Characterisation of Organotin Precursors

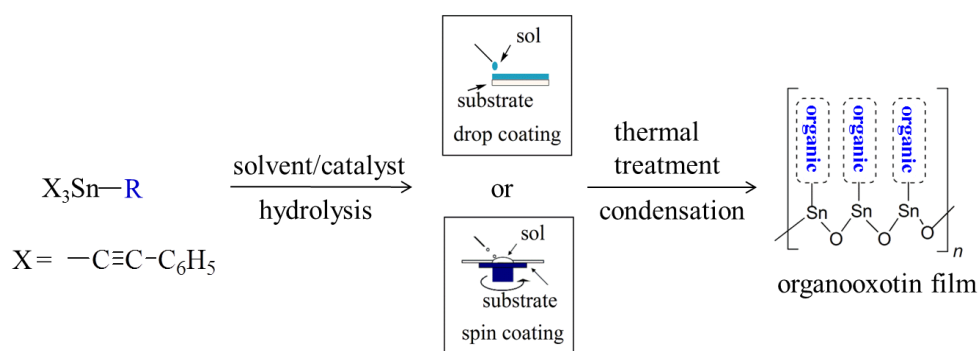
The first goal of this task will be the design, the synthesis and the characterisation of sol-gel precursors able to give class II organotin hybrid materials by the sol-gel process. Alkynylorganotins appeared to be very suitable precursors for different fundamental and practical reasons: (i) the alkynyl functionality is removed upon hydrolysis as an inert gas or liquid which prevents any pollution or decomposition of the resulting hybrids; (ii) their hydrolysis rate lies between the chloride and alkoxide ones favouring the formation of gels;

(iii) their reaction with hydroxylated species can be easily monitored by IR spectroscopy. As the tin-aryle and tin-benzyle bonds are less chemically and thermally stable than the tin-alkyle bond, the latter will be chosen in all the target structures. However, organically-bridged organoditins which include various kinds of organic linker between the two tin atoms will not be chosen as the synthetic route due to the shortage of the key chemicals and multi-steps syntheses, instead another direct and exquisite way has been chosen in this project as the synthetic strategy of trialkynylorganotin which contain one tin linked to functional organics. In order to induce the selectivity expected, heterosystems as sulfur, benzene or nitrobenzene will be introduced in the organic spacer as thiophene, benzyl groups or functions.

To avoid long synthetic procedure, one step preparation method was developed adapting previously reported based on a selective alkylation of tetraalkynyltin with a Grignard reagent [91]. The structure of these precursors will be assessed by multinuclear ( $^1\text{H}$ ,  $^{13}\text{C}$ ,  $^{119}\text{Sn}$ ) 1D and 2D NMR spectroscopy, FTIR spectroscopy and high resolution mass spectrometry. Furthermore, their electronic properties will be determined in solution by UV-visible absorption data that could be used to interpret the gas sensing properties of the target films.

#### II.4.2.2.2 Task II-2: Processing of Nanostructured Tin-based Hybrid Layers

Once the synthesis and the characterization of the target precursors achieved, they will be hydrolyzed and coated over different substrates, for instance, glass and silicon wafer substrates by various deposition techniques such as spin-coating or drop-coating (Scheme II-9).



**Scheme II-9: General strategy to produce organotin hybrid thin films in this project.**

The hydrolysis conditions (solvent, concentration) will be varied in order to get the desired hybrid films, with no remaining hydrolyzable groups to ensure the formation of the more condensed inorganic network, with various thicknesses. In the same way, acidic catalysts will be added to speed up the hydrolysis in case it would be too slow. Acidic hydrolysis conditions will be also employed to perform simultaneously the hydrolysis-condensation process. Finally, these hybrid layers will be dried around  $150^\circ\text{C}$  to remove the organic solvents and to prepare nanostructured tin oxide hybrid layers. Then, the thermal stability of these hybrid layers will be determined by thermogravimetry analysis.

#### II.4.2.2.3 Task 2-3: Structural Characterisation of Nanostructured Tin-based Hybrid Layers

As the use of functional organics is expected to “decorate” the nanostructuring of the hybrid layers, much attention will be paid to the determination of the structure, the texture and the morphology of the obtained films. Thus, the hybrid materials will be characterized with respect to their structure by SEM which will give information on the structural properties of the materials. Infrared spectroscopy will be used to obtain the information about the active surface/ bulk groups. Moreover, their morphology will be studied by SEM and AFM microscopy. On the other hand, the composition will be determined by XPS that will yield the content in Sn, O, C, S or N. The EDX will provide additional information about chemical composition.

#### II.4.2.3 Description of task 3

The tin dioxide particles and organotin-based hybrid materials synthesized and characterized under activities in the previous tasks will be tested in respect of their gas sensing properties. To do this, the materials will be deposited as films on  $\text{Al}_2\text{O}_3$  substrates provided with integrated electrodes and heater, and exposed to gases with different properties: (i) reducing ( $\text{H}_2$ , CO, and volatile organic compounds such as ethanol and acetone) and (ii) oxidizing ( $\text{NO}_2$ ) in different concentration ranges. The spin-coating technique allows for the deposition of continuous layers whereas the microdropping will be used for site-selective deposition. The key component in gas-sensing studies is the experimental facility of gas sensing, and electrical properties which was developed at University of Brescia. The current system couples (DC conductance and AC electrical response) with ten sensors and six different gases in the presence of relative humidity and controlled temperature, and a MS spectrometer monitors the outlet of the test chambers. Each of the systems is equipped with one special module designed for ozone characterization, Kelvin probe measurement and photoactivated characterization. This system is controlled by a Personal Computer. Using this system we could establish the sensor activity data obtained under the same conditions but on different samples (Figure II-30). We will analyze: (i) conductance changes ( $\Delta G$ ) and resistance change ( $\Delta R$ ), (ii) response time (speed), (iii) sensor response (S). As aforementioned, we have already shown the principal applicability of hybrid materials for gas sensing studies as well as confirmed their thermal stability.

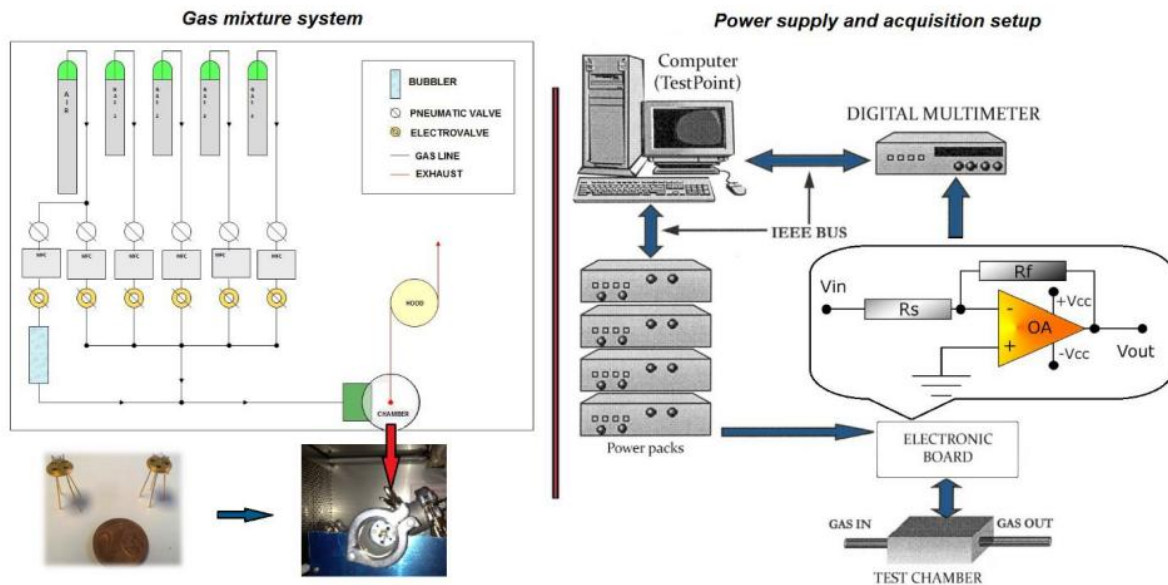


**Figure II-30: Schematic representation of experimental setup used for the electrical characterization (used from ref. [88]).**

For tin dioxide nanoparticles, the gas sensing sensibility and selectivity will be rationalized in terms of chemical composition, structural, textural and electronic properties of the nanopowders obtained. The influence of the organic moieties and the quality of the films obtained on these gas sensing properties will be also investigated in the case of the hybrid layers.

## References:

- [1] H.-J. Kim, J.-H. Lee, *Sens. Actuators B Chem.* **2014**, *192*, 607-627.
- [2] S. Shukla, S. Seal, L. Ludwig, C. Parish, *Sens. Actuators B*, **2004**, *97*, 256-265.
- [3] (a) N. Yamazoe, *Sens. Actuators B*, **1991**, *5*, 7-19. (b) G. Sberveglieri, *Sens. Actuators B*, **1995**, *23*, 103-109.
- [4] A. Gurlo, R. Riedel, *Angew. Chem. Int. Ed.*, **2007**, *46*, 3826-3848.
- [5] (a) M. E. Franke, T. J. Koplín, U. Simon, *Small* **2006**, *2*, 36-50. (b) M. Tiemann, *Chem. Eur. J.* **2007**, *13*, 8376-8388.
- [6] S. R. Shief, *Phys. Rev. B* **2006**, *73*, 014105
- [7] K. G. Godinho, A. Walsh, G. W. Watson, *J. Phys. Chem. C* **2009**, *113*, 439-448.
- [8] J. B. Asbury, E. Hao, Y. Wang, H. N. Ghosh, T. Lian, *J. Phys. Chem. B* **2001**, *105*, 4545-4557.
- [9] M. Nagasawa, S. Shionoya, S. Makishima, *Jpn. J. Appl. Phys.* **1965**, *4*, 195-202.
- [10] H. Liu, Q. Wan, *Nanoscale* **2012**, *4*, 4481-4484.
- [11] N. Barsan, M. Schweizer-Berberich, W. Göpel, *J. Anal. Chem.* **1999**, *365*, 287-304.
- [12] (a) K. L. Chopra, S. Major, D. K. Pandya, *Thin Solid Films* **1983**, *102*, 1. (b) R. G. Gordon, *MRS Bulletin* 2000, **25**, 52. (c) J. Montero, J. Herrero, C. Guillen, *Sol. Energy Mater. Sol. Cells* **2010**, *94*, 612-616. (d) J. E. N. Swallow, B. A. D. Williamson, T. J. Whittles, M. Birkett, T. J. Featherstone, N. Peng, A. Abbott, M. Farnworth, K. J. Cheetham, P. Warren, D. O. Scanlon, V. R. Dhanak, T. D. Veal, *Adv. Funct. Mater.* **2018**, *28*, 1701900.
- [13] (a) M. Esro, S. Georgakopoulos, H. Lu, G. Vourlias, A. Krier, W. I. Milne, W. P. Gillin, G. Adamopoulos, *J. Mater. Chem. C* **2016**, *4*, 3563-3570. (b) P. Tang, C. Liu, J. Zhang, L. Wu, W. Li, L. Feng, G. Zeng, *Appl. Surf. Sci.* **2018**, *436*, 134-140.
- [14] J. Chao, X. Sun, S. Xing, X. Zhang, S. Gao, Z. Du, *J. Alloys Compd.* **2018**, *753*, 212-218.
- [15] (a) T. Uddin, PhD Thesis, University of Bordeaux 1, **2013**. (b) W. Ben Soltan, S. Ammar, C. Olivier, T. Toupance, *J. Alloys Compd.* **2017**, *729*, 638-647.
- [16] S. P. Kim, M. Y. Choi, H. C. Choi, *Appl. Surf. Sci.* **2015**, *357*, 302-308.
- [17] (a) T. Jia, W. Wang, F. Long, Z. Fu, H. Wang, Q. Zhang, *J. Phys. Chem. C* **2009**, *113*, 9071-9077. (b) X. Jia, Y. Liu, X. Wu, Z. Zhang, *Appl. Surf. Sci.* **2014**, *11*, 609-613. (c) N. Shanmugam, T. Sathya, G. Viruthagiri, C. Kalyanasundaram, R. Gobi, S. Ragupathy, *Appl. Surf. Sci.* **2016**, *360*, 283-290.
- [18] (a) W. Cun, Z. Jincai, W. Xinming, M. Bixian, S. Guoying, P. Ping'an, F. Jiamo, *Appl. Catal. B: Environmental* **2002**, *39*, 269-279. (b) Liu, D.D. Sun, P. Guo, J.O. Leckie, *Nano Lett.* **2007**, *7*, 1081-1085. (c) Z. Zhang, C. Shao, X. Li, L. Zhang, H. Xue, C. Wang, Y. Liu, *J. Phys. Chem. C* **2010**, *114*, 7920-7925. (d) J. Yuan, X. Zhang, H. Li, K. Wang, S. Gao, Z. Yin, H. Yu, X. Zhu, Z. Xiong, Y. Xie, *Catal. Commun.* **2014**, *60*, 129-133. (e) G. Mendoza-Damián, F. Tzompantzi, R. Pérez-Hernández, R. Gómez, A. Hernández-Gordillo, *Catal. Today* **2016**, *266*, 82-89.



- [19] (a) A. Hagfeldt, G. Boschloo, L. Sun, L. Kloo, H. Pettersson, *Chem. Rev.* **2010**, *110*, 6595. (b) A. Fakharuddin, R. Jose, T. M. Brown, F. Fabregat-Santiago, J. Bisquert, *Energy Environ. Sci.* **2014**, *7*, 3952.
- [20] M. Grätzel, *Acc. Chem. Res.* **2009**, *42*, 1788-1798.
- [21] H. J. Snaith, L. Schmidt-Mende, *Adv. Mater.* **2007**, *19*, 3187-3200.
- [22] K. Kakiage, Y. Aoyama, T. Yano, K. Oya, J. Fujisawa, M. Hanaya, *Chem. Commun.*, **2015**, *51*, 15894-15897.
- [23] A. N. M. Green, E. Palomares, S. Haque, J. M. Kroon, J. R. Durrant, *J. Phys. Chem. B* **2005**, *109*, 12525-12533.
- [24] (a) E. Easwaramoorthi, J. Lee, *J. Phys. Chem. C* **2010**, *114*, 22032-22037. (b) E. N. Kumar, R. Jose, P. S. Archana, C. Vijila, M. M. Yusoff, S. Ramakrishna, *Energy Environ. Sci.* **2012**, *5*, 5401-5407. (c) A. Birkel, Y.-G. Lee, D. Koll, X. Van Meerbeek, S. Frank, M. J. Choi, Y. S. Kang, K. Char, W. Tremel, *Energy Environ. Sci.* **2012**, *5*, 5392-5340. (d) L. Cojocaru, C. Olivier, T. Toupance, E. Sellier, L. Hirsch, *J. Mater. Chem. A* **2013**, *1*, 13789-13799. (e) Y. Wang, J. Tian, C. Frei, L. Lv, X. Liu, Z. Zhao, G. Cao, *J. Phys. Chem. C* **2014**, *118*, 25931-25938. (f) M. Abd-Ellah, S. Bazargan, J. Thomas, Md. A. Rahman, S. Srivastava, X. Wang, N. F. Heinig, K. T. Leung, *Adv. Electron. Mater.* **2015**, *1*, No. 1500032. (g) Y.-F. Wang, Q.-P. Luo, Y. Ding, X. Wang, X.-F. Li, D.-J. Li, *Mater. Chem. Phys.* **2018**, *207*, 141-146.
- [25] Y. Zhang, Z. Hu, Y. Liang, Y. Yang, N. An, Z. Li, H. Wu, *J. Mater. Chem. A* **2015**, *3*, 15057-15067.
- [26] (a) Y. Wang, J. Y. Lee, H. C. Zeng, *Chem. Mater.* **2005**, *17*, 3899-3903. (b) X. W. Lou, Y. Wang, C. Yuan, J. Y. Lee, L. A. Archer, *Adv. Mater.* **2006**, *17*, 2325-2329. (c) H.-W. Ha, K. Kim, M. de Borniol, T. Toupance, *J. Solid State Chem.*, **2006**, *179*, 689-694. (d) Y. Han, X. Wu, Y. Ma, L. Gong, F. Qu, H. Fan, *CrystEngComm* **2011**, *13*, 3506-3510. (e) R. Hu, Y. Ouyang, T. Liang, H. Wang, J. Liu, J. Chen, C. Yang, M. Zhu, *Adv. Mater.* **2017**, *29*, 1605006.
- [27] (a) W. Winter, J. O. Besenhard, *Electrochim. Acta* 1999, **45**, 31-50. (b) J. M. Tarascon, M. Armand, *Nature* **2001**, *414*, 359-367. (c) J. H. Kang, S.-M. Paek, J.-H. Choy, *Chem. Commun.* **2012**, *48*, 458-460.
- [28] M.-S. Wang, Z.-Q. Wang, Z. Chen, Z.-L. Yang, Z.-L. Tang, H.-Y. Luo, Y. Huang, X. Li, W. Xu, *Chem. Eng. J.* **2018**, *334*, 162-171.
- [29] A. Gurlo, *ChemPhysChem* **2006**, *7*, 2041-2052.
- [30] (a) P. G. Harrison, M. J. Willett, *Nature* **1988**, *332*, 337-339. (b) Z. L. Wang, *Adv. Mater.* **2003**, *15*, 432-436. (c) A. Kolmakov, Y. Zhang, G. Cheng, M. Moskovits, *Adv. Mater.* **2003**, *15*, 997-1000.
- [31] (a) G. Tournier, C. Pijolat, *Sens. Actuators, B* **2005**, *106*, 553-562. (b) C-W. Han, S-H. Han, I. Singh, T. Toupance, *Sens. Actuators, B* **2005**, *109*, 264-269.
- [32] (a) E. Leblanca, L. Perier-Cambya, G. Thomasa, R. Gibert, M. Primetb, P. Gelinb, *Sens. Actuators, B* **2000**, *62*, 67-72. (b) T. Hyodo, K. Sasahara, Y. Shimizu, M. Egashira, *Sens.*

- Actuators, B* **2005**, *106*, 580-590.
- [33] (a) T. Brousse, D. Beutier, D. M. Schleich, *Ionics* **1995**, *1*, 499-503. (b) E. R. Leite, I. T. Weber, E. Longo, J. A. Varela, *Adv. Mater.* **2000**, *12*, 965-968.
- [34] (a) N. V. Hieu, H.-R. Kim, B.-K. Ju, J.-H. Lee, *Sens. Actuators B Chem.* **2008**, 133, 228-234. (b) Y.-X. Li, Z. Guo, Y. Su, X.-B. Jin, X.-H. Tang, J.-R. Huang, X.-J. Huang, M.-Q. Li, J.-H. Liu, *ACS Sensors* **2017**, *2*, 102-110.
- [35] (a) J-B. Sanchez, F. Berger, M. Fromm, M.-H. Nadal, *Sens. Actuators B* **2005**, *106*, 823-831. (b) F. Berger, J-B. Sanchez, O. Heintz, *Sens. Actuators B* **2009**, *143*, 152-157. (c) J-B. Sanchez, F. Berger, *Talanta* **2009**, *80*, 385-389.
- [36] J. Zhao, S. Wu, J. Liu, H. Liu, S. Gong, D. Zhou, *Sens. Actuators B* **2010**, *145*, 788-793.
- [37] (a) W. Göpel, K.D. Schierbaum, *Sens. Actuators, B* **1995**, *26-27*, 1-12. (b) A. Dieguez, A. Romano-Rodriguez, J. R. Morante, U. Weimar, M. Schweizer-Berberich, W. Göpel, *Sens. Actuators, B* **1996**, *31*, 1-8.
- [38] L. Zhou, F. Shen, X. Tian, D. Wang, T. Zhang, W. Chen, *Nanoscale*. **2013**, *5*, 1564-1569.
- [39] C. Xu, J. Tamaki, N. Miura, N. Yamazoe, *Sens. Actuators, B* **1991**, *3*, 147-155.
- [40] (a) C. Nayral, T. Ould-Ely, A. Maisonnat, B. Chaudret, P. Fau, L. Lescouzères, A. Peyre-Lavigne, *Adv. Mater.* **1999**, *11*, 61-63. (b) C. Nayral, E. Viala, P. Fau, F. Senocq, J.-C. Jumas, A. Maisonnat, B. Chaudret, *Chem. Eu. J.* **2000**, *6*, 4082-4090. (c) J. Ba, J. Polleux, M. Antonietti, M. Niederberger, *Adv. Mater.* **2005**, *17*, 2509-2512. (d) T. Kida, T. Doi, K. Shimanoe, *Chem. Mater.* **2010**, *22*, 2662-2667.
- [41] I. Cho, K. Kang, D. Yang, J. Yun, I. Park, *ACS Appl. Mater. & Interfaces* **2017**, *9*, 27111-27119.
- [42] T. Li, W. Zeng, *Ceramics Int.* **2017**, *43*, 728-735.
- [43] I.-S. Hwang, S.-J. Kim, J.-K. Choi, J.-J. Jung, D.-J. Yoo, K.-Y. Dong, B.-K. Ju, J.-H. Lee, *Sens. Actuators B Chem.* **2012**, *165*, 97-103.
- [44] F. Li, Y. Chen, J. Ma, *J. Mater. Chem. A* **2014**, *2*, 7175-7178.
- [45] (a) J. Zhang, X. Liu, S. Wu, M. Xu, X. Guo, S. Wang, *J. Mater. Chem.* **2010**, *20*, 6453-6459. (b) R. Von Hagen, M. Sneha, S. Mathur, *J. Am. Ceram. Soc.* **2014**, *97*, 1035-1040.
- [46] Y. Zou, S. Chen, J. Sun, J. Liu, Y. Che, X. Liu, J. Zhang, D. Yang, *ACS Sens.* **2017**, *2*, 897-902.
- [47] Y. Li, N. Chen, D. Deng, X. Xing, X. Xiao, Y. Wang, *Sens. Actuators B* **2017**, 238, 264-273.
- [48] (a) Y. Lin, Y. Wang, W. Wei, L. H. Zhu, S. P. Wen, S. P. Ruan, *Ceram. Int.* **2015**, *41*, 7329-7336. (b) H. Y. Du, J. Wang, P. Yu, N. S. Yu, Y. H. Sun, J. L. Tian, *J. Nanopart. Res.*, **2014**, *16*, 2216.
- [49] S. Xu, H. Zhao, Y. Xu, R. Xu, Y. Lei, *ACS Appl. Mater. Interfaces* **2018**, *10*, 13895-13902.
- [50] I. Cho, K. Kang, D. Yang, J. Yun, I. Park, *ACS Appl. Mater. Interfaces* **2017**, *9*,

27111-27119.

- [51] P. H. Suman, A. A. Felix, H. L. Tuller, J. A. Varela, M. O. Orlandi, *Sens. Actuators B* **2015**, *208*, 122-127.
- [52] D. L. Kamble, N. S. Harale, V. L. Patil, P. S. Patil, L. D. Kadam, *J. Anal. Appl. Pyrolysis* **2017**, *127*, 38-46.
- [53] T. Brezesinski, A. Fisher, K. Iimura, C. Sanchez, D. Grosso, M. Antonietti, B. M. Smarlsy, *Adv. Funct. Mater.* **2006**, *16*, 1433-1440.
- [54] C. Wang, P. Zhao, S. Liu, *Physica status solidi A*, **2015**, *212*, 1789-1794.
- [55] H. A. Khorami, M. Keyanpour-Rad and M. R. Vaezi, *Appl. Surf. Sci.*, **2011**, *257*, 7988-7992.
- [56] J. Zakrzewski, W. Domanski, P. Chaitas, T. Laopoulos, *IEEE Trans. Instrum. Meas.* **2006**, *55*, 14-20.
- [57] (a) Y. Li, D. Deng, X. Xing, N. Chen, X. Liu, X. Xiao, Y. Wang, *Sens. Actuators B* **2016**, *237*, 133-141. (b) D. Hu, B. Han, S. Deng, Z. Feng, Y. Wang, J. Popovic, M. Nuskol, Y. Wang, I. Djerdj, *J. Phys. Chem. C* **2014**, *118*, 9832-9840.
- [58] J. R. Stetter, M. W. Findlay, G. J. Maclay, J. Zhang, S. Vaihinger, W. Gopel, *Sens. Actuators B* **1990**, *1*, 43-47.
- [59] H. Fritze, D. Richter, H. L. Tuller, *Sens. Actuators B* **2005**, *111-112*, 200-206.
- [60] S. Nakata, K. K. Takemura, K. Neya, *Sens. Actuators B* **2001**, *379*, 1-6.
- [61] (a) P. Gomez-Romero, C. Sanchez, in “*Functional Hybrid Materials*”, Wiley-VCH, Weinheim, **2003**. (b) G. Kickelbick, in “*Hybrid Materials: Synthesis, Characterization and Applications*”, Wiley-VCH, Weinheim, **2007**. (c) M. Faustini, L. Nicole, E. Ruiz-Hitzky. Sanchez, *Adv. Funct. Mater.* **2018**, *28*, 1704158.
- [62] (a) M. Faustini, L. Nicole, E. Ruiz-Hitzky, C. Sanchez, *Adv. Funct. Mater.* **2018**, *28*, 1704158. (b) C. Sanchez, P. Belleville, M. Popall, L. Nicole, *Chem. Soc. Rev.* **2011**, *40*, 696-753. (c) C. Sanchez, C. Boissiere, S. Cassaignon, C. Chaneac, O. Durupthy, M. Faustini, D. Grosso, C. Laberty-Robert, L. Nicole, D. Portehault, F. Ribot, L. Rozes, C. Sassoeye, *Chem. Mater.* **2014**, *26*, 221-238. (d) S. Parola, B. Julian-Lopez, L. D. Carlos, C. Sanchez, *Adv. Funct. Mater.* **2016**, *26*, 6306-6344.
- [63] H. Berke, *Chem. Soc. Rev.*, **2007**, *36*, 15-30.
- [64] (a) O. H. Van, *Science* **1966**, *154*, 645-646. (b) M. Jose-Yacaman, L. Rendon, J. Arenas, M. C. S. Puche, *Science* **1996**, *273*, 223-225.
- [65] P. Gomez-Romero, C. Sanchez, *New J. Chem.*, **2005**, *1*, 57-58.
- [66] G. Kickelbick, *Hybrid Mater.* **2014**, *1*, 39-51.
- [67] L. J. Bonderer, A. R. Studart, L. J. Gauckler, *Science*, **2008**, *319*, 1069-1073.
- [68] N. Nassif, N. Pinna, N. Gehrke, M. Antonietti, C. Jager, H. Colfen, *PNAS*, **2005**, *102*, 12653-12655.
- [69] C. J. Brinker, G. W. Scherer, in the book of “*Sol-gel science: the physics and chemistry of sol-gel processing*”, Academy Press Inc., **2013**.
- [70] S. K. Young, in the book of “*Overview of sol-gel science and technology*”, army

research laboratory, **2002**.

- [71] P. G. Kudryavtsev, O. L. Figovsky, N. P. Kudryavtsev, *J. Sci. Israel-technological advantages*, **2016**, *18*, 112-133.
- [72] C. Sanchez, G. J. de A. A. Soler-Illia, F. Ribot, T. Lalot, C. R. Mayer, V. Cabuil, *Chem. Mater.*, **2001**, *13*, 3061-3083.
- [73] F. Ribot, D. Minoux, C. Sanchez, *Mater. Res. Soc. Symp. Proc.*, **2000**, *628*, CC2.2.
- [74] (a) F. Ribot, C. Eychenne-Baron, C. Sanchez, *Phosphorus Sulfur Silicon Relat. Elem.*, **1999**, *150*, 41-58. (b) C. Eychenne-Baron, F. Ribot, C. J. Sanchez, *Organomet. Chem.*, **1998**, *567*, 137-142. (c) F. Ribot, C. Eychenne-Baron, C. Sanchez, *Mater. Res. Soc. Symp. Proc.*, **1998**, *519*, 29. (d) F. Banse, F. Ribot, P. Toledano, J. Maquet, C. Sanchez, *Inorg. Chem.*, **1995**, *34*, 6371-6379. (e) R. R. Holmes, *Acc. Chem. Res.*, **1989**, *22*, 190-197. (f) D. Dakternieks, H. Zhu, E. R. T. Tiekink, R. J. Colton, *J. Organomet. Chem.*, **1994**, *476*, 33-40. (g) P. Jaumier, B. Jousseaume, M. Lahcini, F. Ribot, C. Sanchez, *Chem. Commun.*, **1998**, 369-370. (h) H. Puff, H. J. Reuter, *Organomet. Chem.*, **1989**, *373*, 173-184. (i) C. Eychenne-Baron, F. Ribot, N. Steunou, C. Sanchez, *Organometallics*, **2000**, *19*, 1940-1949. (j) J. Beckmann, K. Jurkshat, U. Kaltenbrunner, S. Rabe, M. Schürmann, D. Dakternieks, A. Duthie, D. Müller, *Organometallics*, **2000**, *19*, 4887-4898.
- [75] B. Jousseaume, M. Lahcini, M.-C. Rasclé, F. Ribot, C. Sanchez, *Organometallics*, **1995**, *14*, 685-689.
- [76] F. Ribot, C. Eychenne-Baron, F. Banse, C. Sanchez, *MRS. Proceedings.*, **1996**, *435*, 43.
- [77] C. Sanchez, F. Ribot, *New J. Chem.*, **1994**, *18*, 1007-1047.
- [78] (a) S. Inagaki, S. Guan, Y. Fukushima, T. Ohsuna, O. Terasaki, *J. Am. Chem. Soc.* **1999**, *121*, 9611-9614. (b) B.J. Melde, B. Hollande, C.F. Blanford, A. Stein, *Chem. Mater.*, **1999**, *11*, 3302-3308. (c) T. Asefa, M.J. MacLachlan, N. Coombs, G.A. Ozin, *Nature*, **1999**, *402*, 867-869.
- [79] (a) J.J.E. Moreau, L. Vellutini, M. Wong Chi Man and C. Bied, *J. Am. Chem. Soc.*, **2001**, *123*, 1509-1510. (b) J.J.E. Moreau, L. Vellutini, J-L. Bantignies, M. Wong Chi Man, C. Bied, P. Dieudonné, J-L. Sauvajol, *J. Am. Chem. Soc.* **2001**, *123*, 7957-7958. (c) J.J.E. Moreau, B.P. Pichon, M. Wong Chi Man, C. Bied, H. Pritzkow, J-L. Bantignies, P. Dieudonné, J-L. Sauvajol, *Angew. Chem. Int. Ed.* **2004**, *43*, 203-206.
- [80] (a) B. Jousseaume, H. Riague, T. Toupance, M. Lahcini, P. Mountford, B. R. Tyrell, *Organometallics*, **2002**, *21*, 4590-4954. (b) H. Elhamzaoui, B. Jousseaume, H. Riague, T. Toupance, P. Dieudonné, C. Zakri, M. Maugey, H. Allouchi, *J. Am. Chem. Soc.* **2004**, *126*, 8130-8131. (c) H. Elhamzaoui, B. Jousseaume, T. Toupance, C. Zakri, M. Biesemans, R. Willem, H. Allouchi, *Chem. Commun.* **2006**, 1304-1306. (d) H. Elhamzaoui, B. Jousseaume, T. Toupance, C. Zakri, *J. Sol-Gel Sci. Technol.*, **2008**, *48*, 6-10.
- [81] (a) M. Lahcini, P. Jaumier, B. Jousseaume, *Angew. Chem., Int. Ed.*, **1999**, *38*, 402-404. (b) M. Biesemans, R. Willem, S. Damoun, P. Geerlings, E. R. T. Tiekink, M. Lahcini, P.

- Jaumier, B. Jousseume, *Organometallics*, **1998**, *17*, 90-97. (c) P. Jaumier, B. Jousseume, E. R. T. Tiekink, M. Biesemans, R. Willem, *Organometallics*, **1997**, *16*, 5124-5126. (d) M. Biesemans, R. Willem, S. Damoun, P. Geerlings, M. Lahcini, P. Jaumier, B. Jousseume, *Organometallics*, **1996**, *15*, 2237-2245. (e) B. Jousseume, M. Lahcini, M.-C. Rasclé, C. Sanchez, F. Ribot, *Organometallics*, **1995**, *14*, 685-689.
- [82] (a) H. Elhamzaoui, T. Toupance, B. Jousseume, H. Allouchi, *Organometallics* **2007**, *26*, 3908-3917. (b) T. Toupance, M. de Borniol, H. Elhamzaoui, B. Jousseume, *Appl. Organometal. Chem.* **2007**, *21*, 514-520.
- [83] H. Elhamzaoui, T. Toupance, M. Maugey, C. Zakri, B. Jousseume, *Langmuir* **2007**, *23*, 785-789.
- [84] H. Elhamzaoui, B. Jousseume, T. Toupance, C. Zakri, *Dalton Trans.* **2009**, 4429-4431.
- [85] (a) B. Jousseume *unpublished results*. (b) T. Toupance, L. Renard, B. Jousseume, C. Olivier, V. Pinoie, I. Verbruggen, R. Willem, *Dalton Trans.* **2013**, *42*, 9764-9770.
- [86] G. Lu, L. E. Ocola, J. Chen, *Adv. Mater.* **2009**, *21*, 2487-2491.
- [87] H. Zhang, J. Feng, T. Fei, S. Liu, T. Zhang, *Sens. Actuators B* **2014**, *190*, 472-478.
- [88] B. Fabbri, L. Bonoldi, V. Guidi, G. Crusiani, D. Casotti, C. Malagu, G. Bellussi, R. Millini, L. Montanari, A. Carati, C. Rizzo, E. Montanari, S. Zanardi, *ACS Appl. Mater. Interfaces*, **2017**, *9*, 24812-24820.
- [89] L. Renard, H. Elhamzaoui, B. Jousseume, T. Toupance, G. Laurent, F. Ribot, H. Saadaoui, J. Broetz, H. Fuess, R. Riedel, A. Gurlo, *Chem. Commun.*, **2011**, *47*, 1464-1466.
- [90] L. Renard, J. Broetz, H. Fuess, A. Gurlo, R. Riedel, T. Toupance, *ACS Appl. Mater. Interfaces*, **2014**, *6*, 17093-17101.
- [91] (a) P. Jaumier, M. Lahcini, B. Jousseume, F. Ribot, *Angew. Chem. Int. Ed.* **1999**, *42*, 402-404. (b) B. Jousseume, in book of “*ChemInform Abstract: Monoorganotin Precursors for Hybrid Materials*”, WILEY-VCH Verlag GmbH & Co, **2010**, p.367.

## Chapter III Characterization Techniques

In the context of the elaboration of organic-inorganic hybrid and metal oxide based materials for gas sensing purpose, it is of paramount importance to draw a detailed picture of their chemical composition, structure, texture and morphology. In addition, the chemical structure and the purity of the new organometallic precursors used to process hybrid powders and films had to be determined.

The current chapter describes a brief and general overview, i.e. working principles, machine types, and characterization parameters, of the main analytic methods employed throughout this work that enabled a complete characterization of the different molecular compounds and oxide materials prepared in this work. Thus, Nuclear Magnetic Resonance (NMR) and Mass spectroscopies were mainly used to identify molecular compounds, Fourier Transform Infra-Red spectroscopy providing complementary information about the presence of specific functional groups. Powder X-ray Diffraction (PXRD) combined with Raman spectroscopy allowed for phase identification and crystallinity study of inorganic samples. Texture, morphology and topology of the different films and powders prepared were determined by N<sub>2</sub> sorption analysis, Scanning or Transmission Electron Microscopy (SEM or TEM) and Atomic Force Microscopy (AFM). Electronic structure and chemical states of the different materials synthesized were investigated by UV-visible absorption and X-ray Photoelectron spectroscopies. Finally, thermal stability and thermal decomposition pathways were characterized by Thermogravimetry and Differential Thermoanalysis (TG-DTA) coupled or not to mass spectrometry.

### III.1 <sup>1</sup>H, <sup>13</sup>C and <sup>119</sup>Sn Nuclear Magnetic Resonance spectroscopies

#### III.1.1 Principle [1]

Of the important spectroscopic aids that are at the disposal of the chemist for use in structure elucidation, dynamics of molecules, reaction state, and chemical environment of molecule compounds, nuclear magnetic resonance (NMR) spectroscopy is one of the most powerful and widely employed tools. Even though a large variety of NMR spectrometers using various techniques of detection exists, the basic principle of NMR is common to all experiments and all nuclei. This analytic method exploit the magnetic properties of certain atomic nuclei endowed with a nuclear spin (*I*) different from zero such as <sup>1</sup>H, <sup>13</sup>C, <sup>29</sup>Si, <sup>31</sup>P or <sup>119</sup>Sn with *I* = ½ in units of  $h/2\pi$  (*h* : Planck constant). As atomic nucleus is a spinning charge particles, a nuclear magnetic moment directly proportional to the spin is associated to each nucleus. When a strong external magnetic field *H*<sub>0</sub> is applied, the nuclear moments orient themselves with only given allowed orientations according to quantum mechanics. The energy of interaction is proportional to the nuclear magnetic moment (which depends on the magnetogyric ratio  $\gamma$  of the nucleus and the spin value) and the applied field. For instance, for

$I = \frac{1}{2}$ , two states can be defined: a)  $\alpha$ -state when the nuclei align with the external magnetic field  $H_0$ ; b)  $\beta$ -state when the nuclei align against the external field  $H_0$ . If the gyromagnetic ratio is positive as for  $^1\text{H}$  and  $^{13}\text{C}$ , the  $\alpha$ -state is more stable than the  $\beta$ -state, and  $\Delta E$  is the energy difference between the  $\alpha$ - and  $\beta$ -spin states given by the following relationships:  $\Delta E = (\gamma h H_0)/2$ . This difference therefore depends on the applied magnetic field as shown in Figure 3.1., the greater the strength of the applied magnetic field, the larger the energy difference between two spin states.

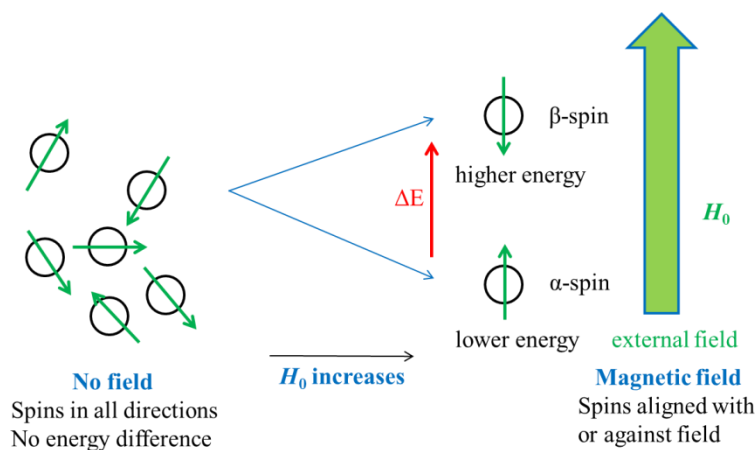


Figure III.1: External field applied to nuclear spins [adapted from ref. 1].

When the sample is irradiated with an electromagnetic wave having the same energy as  $\Delta E$ , the spin flips from  $\alpha$ - to  $\beta$ -spin states. The conditions of resonance are satisfied which leads to an absorption of the electromagnetic wave. Then, the excited nuclei undergo relaxation and they progressively return to their original state. During this process, they emit electromagnetic signals whose frequencies depend on  $\Delta E$  as well. In modern Pulsed Fourier Transform NMR spectroscopy, the spectrometer records these desexcitation signals, also named Free Induction Decay, and Fourier transformation provides the experimental spectra plotting the absorption intensity as a function of the signal frequency.

The exact resonant frequency of the energy transition depends on the effective magnetic field at the nucleus. This effective field is affected on one hand by electron shielding, which is in turn dependent on the chemical environment of the nucleus, and, on the other hand, by the spin state of the neighboring magnetically active nuclei, which is related to the nuclei connectivity. The measurement is therefore very sensitive to the features of molecular structure. Advanced methods, including double resonance (homonuclear or heteronuclear decoupling, spin-echo or Distortionless Enhancement by Polarization Transfer (DEPT) etc...) or two-dimensional (through-bonds homonuclear or heteronuclear correlations, through-space homonuclear correlations) techniques have been developed to determine the 3D-structure of molecules and for structure determination of biopolymers, for example proteins or nucleic acids. NMR is also used in medicine for magnetic resonance imaging (MRI).

### (a) $^1\text{H}$ NMR

$^1\text{H}$  nuclei are the easiest nuclei to observe due to high magnetogyric ratio and natural abundance. For simple molecules, simple one-dimensional experiments allow the rough assignments of main resonances using chemical shift, integration waves and coupling constant considerations. For more complex structures, two-dimensional homonuclear  $^1\text{H}$ - $^1\text{H}$  correlation spectroscopy experiments (COSY or NOESY) can be used to establish the connectivity between the different nuclei.

### (b) $^{13}\text{C}$ NMR [2]

As both natural abundance, i.e. 1.1 %, and magnetogyric ratio of  $^{13}\text{C}$  nuclei are low,  $^{13}\text{C}$  NMR spectroscopy is much less sensitive than  $^1\text{H}$  NMR spectroscopy.  $^1\text{H}$ -decoupled  $^{13}\text{C}$  NMR experiments have therefore been developed to enhance the signal intensities and to simplify the spectra. Thus, in such experiments, each chemically different or set of equivalent carbons give rise to single signals, the chemical shift of which provide information about the hybridization ( $\text{sp}^3, \text{sp}^2, \text{sp}$ ) of each carbon. Double resonances techniques as J-modulated  $^{13}\text{C}$  NMR spectroscopy or DEPT ( $90^\circ$  and  $135^\circ$ ) reveal how many hydrogens are attached to each carbon. Finally, two-dimensional  $^1\text{H}$ - $^{13}\text{C}$  heteronuclear NMR techniques as HSQC (Heteronuclear single-quantum correlation) and HMBC (Heteronuclear Multiple Bond Correlation) experiments can be exploited to highlight the 1-bond (HSQC) or 2,3-bond (HMBC) connectivity between  $^1\text{H}$  and  $^{13}\text{C}$  nuclei.

### (c) $^{119}\text{Sn}$ NMR

The  $^{115}\text{Sn}$ ,  $^{117}\text{Sn}$ , and  $^{119}\text{Sn}$  nuclei each possess spin 1/2 and are in principle suitable for NMR studies. Their characteristics are shown in Table 3.1.

Table 3.1 Properties of  $^{115}\text{Sn}$ ,  $^{117}\text{Sn}$ , and  $^{119}\text{Sn}$  nuclei

Property	$^{115}\text{Sn}$	$^{117}\text{Sn}$	$^{119}\text{Sn}$
Natural abundance (%)	0.35	7.61	8.58
Magnetic moment ( $\mu/\mu_N$ )	-1.590	-1.732	-1.8119
Magnetogyric ratio ( $\gamma/10^7 \text{ rad T}^{-1}\text{s}^{-1}$ )	-8.792	-9.578	-10.021
NMR frequency (MHz) <sup>a</sup>		35.632295	37.290662
Receptivity towards D <sup>b</sup>	$1.24 \times 10^{-4}$	$3.49 \times 10^{-3}$	$4.51 \times 10^{-3}$
Receptivity D <sup>c</sup>	0.705	19.8	25.6

<sup>a</sup> With respect to  $^1\text{H} = 100 \text{ MHz}$ . <sup>b</sup> Relative to  $^1\text{H}$ . <sup>c</sup> Relative to  $^{13}\text{C}$ .

It can be seen that the receptivity of  $^{117}\text{Sn}$  and  $^{119}\text{Sn}$  isotopes is some powers of ten lower than that  $^1\text{H}$  but about 20 times higher than that of  $^{13}\text{C}$ . With respect to both receptivity and relative abundance,  $^{119}\text{Sn}$  presents some advantages compared to  $^{117}\text{Sn}$ , and most measurements have been made with  $^{119}\text{Sn}$  even though  $^{117}\text{Sn}$  has been used when external circumstances have rendered  $^{119}\text{Sn}$  inconvenient or when coupling by tin isotopes has been studied.[3] Satellites due to coupling by the  $^{117}\text{Sn}$  and  $^{119}\text{Sn}$  isotopes can be observed both in



$^1\text{H}$  and  $^{13}\text{C}$  NMR spectra and can be definitely established by checking that the coupling constant ratio  $J(^{117}\text{Sn})/J(^{119}\text{Sn})$  is equal to that of the two magnetogyric ratios, i.e. 1.0462.

### III.1.2 Instrumentation and experimental parameters

In this work,  $^1\text{H}$ ,  $^{13}\text{C}$  and  $^{119}\text{Sn}$  NMR spectra were recorded on Bruker Avance III 600 ( $^1\text{H}$ : 600.16 MHz,  $^{13}\text{C}$ : 150.93 MHz and  $^{119}\text{Sn}$ : 223.74 MHz) spectrometer equipped with a 5 mm BBI probe with Z-gradients and ATM accessory.  $^1\text{H}$  and  $^{13}\text{C}$  NMR spectra were obtained at 600.16 MHz and 150.93 MHz respectively, with chemical shifts reported in ppm downfield from tetramethylsilane (TMS), using the peak for  $\text{CHCl}_3$  ( $\delta = 7.26$  ppm for  $^1\text{H}$  and 77 ppm for  $^{13}\text{C}$ ) as an internal reference.

$^{119}\text{Sn}$  spectra were obtained at 223.74 MHz with chemical shifts reported in ppm downfield relative to the external reference  $\text{SnMe}_4$  in  $\text{CDCl}_3$ .  $^{119}\text{Sn}$  NMR parameters were follows: pulse width = 24.8  $\mu\text{s}$  ( $90^\circ$ ), sweep width = 178 kHz.

This spectrometer is intended for liquid NMR and gels. It is equipped with two types of probe:

1. A BBI probe of 5 mm diameter allows the analysis of liquid samples with low concentration and very high sensitivity for the proton. This probe is also suitable for recording 2D / 3D spectra in multinoyals.
2. An HR-MAS probe to analyze the spectra of gels in high resolution by detection of  $^1\text{H}$  and  $^{13}\text{C}$ .

A cold group of type BCU-05 makes it possible to record spectra between  $-80$  and  $180^\circ\text{C}$ . It is controlled under TOPSPIN 3.

## III.2 Mass spectrometry (MS)

### III.2.1 Principle

The working principle of mass spectrometry is based on acceleration and deviation of charged particles (ions) in a vacuum due to the forces by applying electric and magnetic fields. A compound must be therefore charged or ionized to be analyzed with a mass spectrometer. Besides, the ions have to be introduced in the gas phase into the vacuum system of the mass spectrometer which can be achieved for gaseous or heat-volatile samples. However, many (thermally labile) analytes decompose upon heating. These kinds of samples require either desorption or desolvation methods if they have to be analyzed by mass spectrometry. Although desorption/desolvation and ionization are usually separate processes, the term "ionization method" is commonly used to refer to both ionization and desorption (or desolvation) methods. The choice of ionization method depends on the nature of the sample and the type of information required from the analysis. So-called "soft ionization" methods such as field desorption (FD), electrospray ionization (ESI) and matrix-assisted laser desorption ionization (MALDI) tend to produce mass spectra with little or no fragment-ion content. On the other hand, hard ionization techniques are the processes which bring high

quantities of residual energy in the subject molecule resulting in large degrees of fragmentation (i.e. the systematic rupturing of bonds acts to remove the excess energy, restoring stability to the resulting ion). Resultant ions tend to have  $m/z$  lower than the molecular mass other than in the case of proton transfer and not including isotope peaks. The main example of hard ionization is electron ionization (EI). The mass spectroscopy can be therefore classified according to the ionization method used the main ones of which are described in the following [4]:

**Electron ionization (EI)**, also known as electron impact ionization, is the oldest and best-characterized of all the ionization methods. A beam of electrons passes through the gas-phase sample. An electron that collides with a neutral analyte molecule can knock off another electron, resulting in a positively charged ion. The ionization process can either produce a molecular ion which will have the same molecular weight and elemental composition as the starting analyte, or it can produce a fragment ion which corresponds to a smaller piece of the analyte molecule. This method gives a high degree of fragmentation, yielding highly detailed mass spectra whose skillful analysis can provide important information for structural elucidation/characterization and facilitate identification of unknown compounds by comparison to mass spectral libraries obtained under identical operating conditions. However, EI is not suitable for coupling to HPLC (High-Performance Liquid Chromatography), i.e. LC-MS, since at atmospheric pressure, the filaments used to generate electrons burn out rapidly. Thus, EI is coupled predominantly with GC (Gas Chromatography), i.e. GC-MS, where the entire system is under high vacuum.

**Field desorption (FD)** is a method of ion formation used in mass spectrometry (MS) in which a high-potential electric field is applied to an emitter with a sharp surface, such as a razor blade, or more commonly, a filament from which tiny "whiskers" have been formed. This results in a high electric field which can provoke ionization of gaseous molecules of the analyte. Mass spectra produced by FD have little or no fragmentation because FD is a soft ionization method. They are dominated by molecular radical cations  $M^+$  and less often, protonated molecules  $[M+H]^+$ . The technique was first reported by Beckey in 1969. It is also the first ionization method to ionize nonvolatile and thermally labile compounds. One major difference of FD with other ionization methods is that no primary beam to bombard a sample is required.

In the case of **Electrospray Ionization (ESI)**, the sample solution is sprayed across a high potential difference (a few kilovolts) from a needle into an orifice in the interface. Heat and gas flows are used to desolvate (evaporate the solvent) the ions existing in the sample solution. Electrospray ionization can produce multiply charged ions with the number of charges tending to increase as the molecular weight increases.

For **Matrix-assisted Laser Desorption Ionization (MALDI)**, the analyte is dissolved in a solution containing an excess of a matrix such as sinapinic acid or dihydroxybenzoic acid that has a chromophore that absorbs at the laser wavelength. A small amount of this solution is placed on the laser target. The matrix absorbs the energy from the laser pulse and produces a

plasma that results in vaporization and ionization of the analyte.

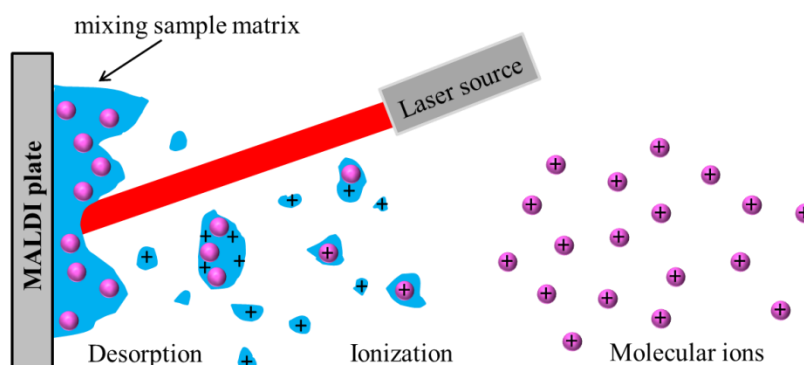


Figure III.2: MALDI spectrometer.

### III.2.2 Instrumentation and experimental parameters

Regardless the ionization method employed, MS spectra were recorded at the CESAMO (“Centre d’Etude Structurale et d’Analyse des Molécules Organiques”, Bordeaux, France).

FD measurements were carried out on a TOF mass spectrometer AccuTOF GCv using an FD emitter with an emitter voltage of 10 kV. One to two microliters solution of the compound is deposited on a 13  $\mu\text{m}$  emitter wire.

GC-MS analyses were performed on a Agilent 7890A GC ultra gas chromatograph coupled to a TOF mass spectrometer AccuTOF GCv by JEOL. Capillary GC analysis was performed on a TG-5MS (30 m  $\times$  0.32 mm  $\times$  0.25  $\mu\text{m}$ ) capillary column with helium as carrier gas. GC conditions were 50  $^{\circ}\text{C}$  at rate of 15  $^{\circ}\text{C}/\text{min}$  to 310  $^{\circ}\text{C}$ , carrier gas (He) flow rate of 1.2 mL/min. Injection temperature was 200  $^{\circ}\text{C}$  with split mode. The transfer line and source temperatures were maintained at 220  $^{\circ}\text{C}$  and 180  $^{\circ}\text{C}$ . A solvent delay of 2 min was selected. In the full-scan mode electron ionization (EI) mass spectra in the range 60-900(m/z) at 70 eV.

ESI spectra were carried out using a QStar Elite mass spectrometer (Applied Biosystems). The instrument is equipped with an ESI source and spectra were recorded in the negative/positive mode. The electrospray needle was maintained at 4500 V and operated at room temperature. Samples were introduced by injection through a 20  $\mu\text{L}$  sample loop into a 400  $\mu\text{L}/\text{min}$  flow of methanol from the LC pump.

MALDI-MS studies were performed on a Voyager mass spectrometer (Applied Biosystems). The instrument is equipped with a pulsed  $\text{N}_2$  laser (337 nm) and a time-delayed extracted ion source. Spectra were recorded in the positive-ion mode using the reflectron and with an accelerating voltage of 20 kV. Samples were dissolved in  $\text{CH}_2\text{Cl}_2$  at 10 mg/ml. The DCTB matrix (Trans-2-(3-(4-*tert*-butylphenyl)-2-methyl-2-propénylidene)malononitrile) solution was prepared by dissolving 10 mg in 1 ml of  $\text{CH}_2\text{Cl}_2$ . A MeOH solution of cationisation agent (NaI, 10 mg/ml) was also prepared. The solutions were combined in a 10:1:1 volume ratio of matrix to sample to cationisation agent. One to two microliters of the obtained solution was deposited onto the sample target and vacuum-dried.

### III.3 Fourier Transform Infrared Spectroscopy (FT-IR)

#### III.3.1 Principle [5]

Fourier Transform Infrared (FT-IR) spectroscopy is one of the most common spectroscopic techniques used in organic and inorganic chemistry for structural elucidation and compound identification. The principle of FT-IR spectroscopy is based on the absorption of infrared light at different functional group by a sample submitted to an infrared beam. At ambient temperature, atoms in organic molecules and inorganic solids are in continuous vibration with respect to each other. The IR radiation is absorbed by a molecule or a material provided its frequency matches the frequency of a specific molecular or materials vibration. The absorbed energy (usually expressed as wave number, in  $\text{cm}^{-1}$ ) is directly connected to the molecular or materials composition: nature of the atoms involved in the bond, nature of the bond (single, double, triple), environment (hydrogen bonding, etc...), structure (Sn-C, Sn-O,  $\text{C}\equiv\text{C}$ , etc...), etc... Consequently, since every molecule has a unique chemical composition, IR spectra can be considered as fingerprints for each compound. Infrared spectrum usually represents the light transmittance (T%) or absorbance (A) as a function of the wavenumber ( $\text{cm}^{-1}$ ). Analysis of the spectral mid-IR region, covering range of wavenumbers between 4000 and  $400\text{ cm}^{-1}$ , can therefore provide useful information with regard to molecular precursor and the materials prepared from these precursors.

#### III.3.2 Instrumentation and experimental parameters

IR spectra were recorded on a FTIR Perkin-Elmer spectrophotometer 1600, equipped with a temperature-stabilized heated wire source operating at 1300 K and a temperature-stabilized FR-DTGS (fast recovery deuterated triglycine sulfate) detector using 200 mg dry KBr pellets containing about 2-3 mg of sample. Spectra were recorded by collecting 16 scans at  $4\text{ cm}^{-1}$  resolution.

### III.4 Raman Spectroscopy

#### III.4.1 Principle

Raman spectroscopy also addresses transitions between vibrational or rotational energy levels in molecular compounds or materials. However, in contrast to IR spectroscopy which detects vibrations involving a change in the permanent dipole moment of the chemical bond, Raman spectroscopy is associated with changes in polarisability to produce Raman (inelastic) scattering of monochromatic light, usually from a laser in the visible, near infrared, or near ultraviolet range. The laser light interacts with molecular vibrations, phonons, or other excitations in the system, resulting in the energy of the laser photons being shifted up or down. The shift in energy supplies information about the vibrational modes in the system.

Typically, a sample is illuminated with a laser beam. Electromagnetic radiation from the illuminated spot is collected with lens and sent through a monochromator. Elastic scattered

radiation at the wavelength corresponding to the laser line (Rayleigh scattering) is filtered out by either a notch filter, edge pass filter, or a band pass filter, while the rest of the collected light is dispersed onto a detector. Spontaneous Raman scattering is typically very weak, and as a result the main difficulty of Raman spectroscopy is separating the weak inelastically scattered light from the intense Rayleigh scattered laser light.

#### III.4.2 Instrumentation and experimental parameters

Raman measurements were performed using a Jobin-Yvon Horiba XploRA confocal spectrometer with a resolution of  $4.3 \text{ cm}^{-1}$  in the spectral range  $200\text{-}1900 \text{ cm}^{-1}$ . The laser source is a laser diode giving access to two laser wavelengths with a maximum power of 45 mW. Experiments were carried out using an incident wavelength of  $\lambda = 532 \text{ nm}$  and the laser beam power was fixed at 100% of the maximum power. To improve the signal-to-noise ratio, each spectrum was the result of 2 accumulated spectra with an acquisition time of 60 seconds for each spectrum.

### III.5 Thermogravimetry Analysis (TGA-DTA)

#### III.5.1 Principle

Thermogravimetric analysis (TGA) enables the weight loss of a material to be monitored as a function of a selected temperature program. Differential Thermal Analysis (DTA) is an associated technique for recording the difference in temperature between a substance and a reference material as a function of time or temperature as the two specimens are subjected to identical temperature regimes in an environment heated or cooled at a controlled rate, providing the information of phase transformation (endothermic/exothermic reaction). Moreover, when the evolved species are analyzed by a mass spectrometer, this technique gives further insight about the composition of the materials and reaction mechanisms. As a consequence, TGA-DTA coupled to mass spectrometry method is usually used to acquire information about the thermal stability of the materials prepared and to get some clues about decomposition, oxidation or reduction mechanisms. In addition, in the case of hybrid materials, it provides some information about the composition of the materials.

#### III.5.2 Instrumentation and experimental parameters

In this work, thermogravimetric analyses were performed with a NETZSCH STA 409 C/CD (Erich NETZSCH GmbH & Co. Holding KG, Selb, Germany) thermogravimetric analyzer under synthetic air ( $\text{N}_2/\text{O}_2 = 80/20$ ). The temperature range was 30 to 600 °C with a heating rate of  $5 \text{ °C min}^{-1}$ .

### III.6 Powder X-ray diffraction (XRD)

#### III.6.1 Principle

Powder XRD is an analytical technique which is primarily used to identify crystal phase and provide information about unit cell dimensions. XRD relies on the formation of constructive interference when a monochromatic X-ray beam interacts with a crystalline material. These X-rays are generated by a cathode ray tube and then filtered to produce monochromatic radiation. They are then collimated to concentrate toward the sample. The interaction of the incident rays with a powder sample produces a unique constructive interference diagram, also named as diffraction diagram, when the conditions satisfy Bragg's law:

$$n\lambda = 2d \sin \theta$$

where  $n$  is an integer,  $\lambda$  is the wavelength of the X-ray,  $d$  is the interplanar spacing between lattice planes and  $\theta$  is the angle between the incident X-ray beam and the lattice planes. The diffracted rays are detected, counted and processed. By scanning the sample through a range of  $2\theta$  angles, all the possible diffraction directions of the sample atomic lattices are gathered.

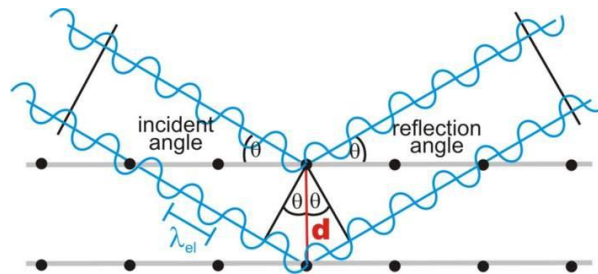


**Figure III.3: Bragg's law.**

The conversion of the position of the diffraction peaks to  $d$ -spacing leads to the identification of the sample as  $d$  is a unique parameter. The lattice spacing,  $d$ , is then deduced from Bragg's formula:

$$d = \frac{\lambda}{2 \sin \theta}$$

where  $\lambda$  is the wavelength of the X-ray source (Cu  $K\alpha$  radiation) and  $\theta$  is the Bragg diffraction angle. The lattice parameter can be then calculated using the formula (e.g. for a tetragonal lattice):

$$\frac{1}{d^2} = \frac{h^2 + k^2}{a^2} + \frac{l^2}{c^2}$$

where  $h$ ,  $k$  and  $l$  are the Miller indices of the lattice plane. Moreover, the average crystallite size can be inferred from Scherrer formula:

$$\tau = \frac{K\lambda}{\beta \cos \theta}$$

where K is the shape factor that was taken to be 0.9 and  $\beta$  is the full width at half maximum of the peak.

### III.6.2 Instrumentation and experimental parameters

Powder X-ray diffraction patterns were herein recorded with a Bruker AXS Advance diffractometer (D2 PHASER A26-X1-A2B0D3A) equipped with a source delivering a monochromatic Cu anode ( $K\alpha$  radiation,  $\lambda = 1.54056 \text{ \AA}$ ). The  $\theta$ -2 $\theta$  scans were recorded in an angular range between 10 and 90° with a step of 0.02°.

### III.7 N<sub>2</sub> sorption analysis [6]

Along with mercury intrusion/extrusion porosimetry, gas sorption analysis is one of the most powerful methods to assess the porosity of materials. Adsorption takes place when a solid surface is exposed to a gas or a liquid which induces, under certain conditions, an enrichment of fluid molecules or increase in the density of fluid in the neighborhood of an interface. The amount of adsorbed species is then closely related to the extent and the shape of the interfacial area which provides useful information about pore size distribution and surface area.

The relationships between the amount of gas adsorbed ( $x$ ) by unit of mass of adsorbent ( $m$ ) and the equilibrium pressure at a fixed temperature is named adsorption isotherm and is usually depicted in graphical form as shown in Figure III.4.



**Figure III.4: Basic adsorption isotherm.**

At this stage, it is worth mentioning that, at a given pressure named saturation pressure  $P_s$ , all the sites are occupied by the adsorbate and a further pressure increase does not cause any difference in adsorption process.

#### III.7.1 Adsorption isotherm types

Most of isotherms resulting from gas physical adsorption on solids can be grouped into six main types according to the IUPAC classification (Figure III.5).

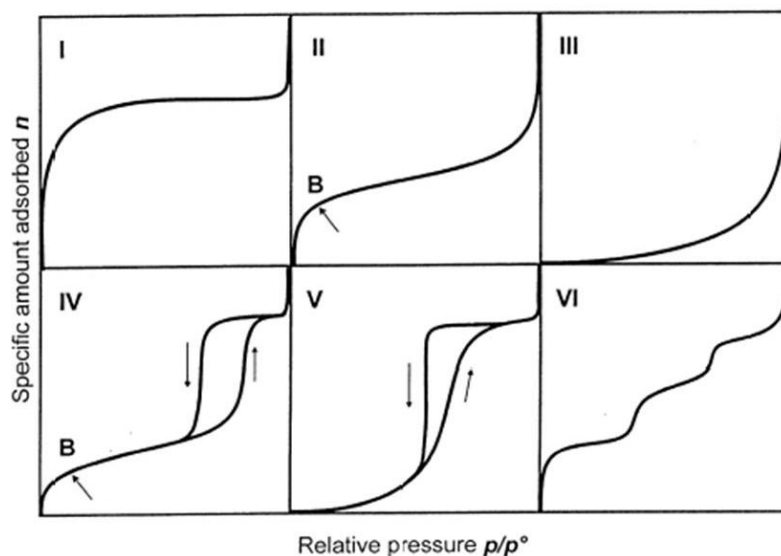


**Figure III.5: The different classes of gas physisorption isotherms according to the IUPAC classification.**

The reversible Type I isotherm is concave to the  $p/p^\circ$  axis and approaches a limiting value as  $p/p^\circ \rightarrow 1$ . Type I isotherms are given by microporous solids having relatively small external surfaces (e.g. activated carbons, molecular sieve zeolites and certain porous oxides), the limiting uptake being governed by the accessible micropore volume rather than by the internal surface area.

The reversible Type II isotherm is the normal form of isotherm obtained with a non-porous or macroporous adsorbent. The Type II isotherm represents unrestricted monolayer-multilayer adsorption. Point B, the beginning of the almost linear middle section of the isotherm, is often taken to indicate the stage at which monolayer coverage is complete and multilayer adsorption about to begin.

The reversible Type III isotherm is convex to the  $p/p^\circ$  axis over its entire range and therefore does not exhibit a Point B. Isotherms of this type are not common, but there are a number of systems (e.g. nitrogen on polyethylene) which give isotherms with gradual curvature and an indistinct Point B. In such cases, the adsorbate-adsorbate interactions play an important role.

Characteristic features of the Type IV isotherm are its hysteresis loop, which is associated with capillary condensation taking place in mesopores, and the limiting uptake over a range of high  $p/p^\circ$ . The initial part of the Type IV isotherm is attributed to monolayer-multilayer adsorption since it follows the same path as the corresponding part of a Type II isotherm obtained with the given adsorptive on the same surface area of the adsorbent in a non-porous form. Type IV isotherms are given by many mesoporous industrial adsorbents.

The Type V isotherm is uncommon; it is related to the Type III isotherm in that the adsorbent-adsorbate interaction is weak, but is obtained with certain porous adsorbents.



The Type VI isotherm, in which the sharpness of the steps depends on the system and the temperature, represents stepwise multilayer adsorption on a uniform non-porous surface. The step-height represents the monolayer capacity for each adsorbed layer and, in the simplest case, remains nearly constant for two or three adsorbed layers. Amongst the best examples of Type VI isotherms are those obtained with argon or krypton on graphitised carbon blacks at liquid nitrogen temperature.

### III.7.2 Brunauer, Emmett and Teller (B.E.T.) theory

The determination of the specific area of solid materials is one of the key points to rationalize the properties of materials. Different models have been applied to interpret gas sorption isotherms which allow the evaluation of specific surface area of solids. In particular, Langmuir model allows for explaining the monolayer formation whereas Brunauer, Emmett and Teller (B.E.T.) theory rationalizes the multilayer formation during the physical adsorption of a gas.

For monolayer adsorption, Langmuir adsorption equation is applicable at low pressure conditions. In this case, gaseous molecules possess high thermal energy and high escape velocity which results in fewer gaseous molecules available near the surface of adsorbent. By contrast, at high pressure and low temperature conditions, thermal energy of gaseous molecules decreases and more and more gaseous molecules are available per unit surface area inducing multilayer formation. Using some assumptions, Brunauer, Emmett and Teller have extended the Langmuir theory to multilayer adsorption and have proposed the BET equation, which give rise to a type-II isotherm, that can be written as:

$$\frac{P}{V_{total}(P - P_0)} = \frac{1}{V_{mono}C} + \frac{c - 1}{V_{mono}C} \left(\frac{P}{P_0}\right)$$

where  $V_{total}$  is the specific volume of gas adsorbed at the equilibrium pressure  $P$ ,  $V_{mono}$  is the volume of gas corresponding to a monolayer and  $C$  is a constant.

$$C = \frac{K_1}{K_L}$$

$K_1$  is the equilibrium constant when single molecule adsorbed per vacant site and  $K_L$  is the equilibrium constant to the saturated vapor liquid equilibrium.

The BET theory applies to systems showing multilayer adsorption and usually utilizes probing gases that do not chemically react with material surfaces as adsorbates to quantify specific surface area. Nitrogen is the most commonly employed gaseous adsorbate for surface probing by the BET methods. For this reason, standard BET analysis is most often conducted at the boiling temperature of  $N_2$  (77 K). Further probing adsorbates are also utilized, albeit with lower frequency, allowing the measurement of surface area at different temperatures and

measurement scales. These include argon, carbon dioxide, and water. Specific surface area is a scale-dependent property, with no single true value of specific surface area definable, and thus, quantities of specific surface area determined through BET theory depend on the adsorbate molecule utilized and its adsorption cross section.

### III.7.3 Instrumentation and experimental parameters

In this work, data collection was performed with N<sub>2</sub> by the static volumetric method, using an ASAP2010 (Micromeritics) apparatus. Prior to each measurement, the samples were degassed at 120 °C *in vacuo* for a time interval high enough to reach a constant pressure (< 10 mHg). The BET equation was applied between 0.05 and 0.3 relative pressures to provide specific surface areas. Total pore volumes were determined by the amount of nitrogen adsorbed at a 0.99 relative pressure. Pore size distributions were evaluated by the Barrett, Joyner, Halenda (BJH) method for mesopores (pores of diameter 2-50 nm). The adsorption isotherm was used to determine the overall pore size distribution and the calculation was performed by the Micromeritics software package which uses the recurrent method and applies the Harkins and Jura equation for the multilayer thickness.

## III.8 UV-Vis absorption

### III.8.1 Principle

According to quantum mechanics theory, energies of electrons in atoms, molecules or materials are quantified. In this context, electronic absorption phenomena in molecular compounds or materials generally lie within the ultraviolet to the visible region, thus, the corresponding spectroscopy is named “UV-Visible absorption spectroscopy”.

For instance, inorganic semiconductors are transparent to photons whose energies lie below their bandgap whereas they are strongly absorbing for photons whose energies exceed the bandgap energy. In the case of organic semiconductors, many systems absorb ultraviolet or visible light depending on the electronic orbitals that are involved. Their absorption spectra generally show a number of absorption bands corresponding to the structural units of the molecule.

In an absorption measurement, the absorbance depicts the attenuation of the transmitted radiant power in a material. Due to this absorption, the amount of light that is transmitted through a material diminishes as it travels through the material. For inorganic semiconductors, the bandgap could be determined from the transmission of the light of various wavelengths. The intensity of the light that is transmitted through the semiconductor,  $I_T$ , follows the Beer-Lambert law, according to:

$$I_T = I_0 e^{-\alpha d}$$

where  $\alpha$  is the absorption coefficient,  $d$  is the thickness of the semiconductor material and  $I_0$

the intensity of the incident light. The absorption coefficient strongly depends on the wavelength of the incident light, and it can be in the range of  $10^5 \text{ cm}^{-1}$  for photons whose energies are larger than the bandgap of the semiconductor. The transmittance,  $T$ , and the optical density,  $OD$ , can be then defined as:

$$T = \frac{I_T}{I_0} \quad \text{and} \quad OD = -\log T$$

The absorption coefficient can, thus, be directly determined from the measurement. For a large number of inorganic semiconductors in both crystalline and amorphous forms, the dependence of the absorption coefficient upon the photon energy  $h\nu$  for optically induced transitions is usually expressed as:

$$\alpha h\nu = A(h\nu - E_g)^m$$

Where  $E_g$  is the energy gap,  $A$  is a constant and  $m = 1/2$  for an allowed direct energy gap and  $m = 3/2$  for a forbidden direct energy gap. Plotting  $(\alpha h\nu)^2$  versus  $h\nu$  gives an approximate value of  $E_g$  by taking the intercept of the extrapolation to the zero absorption with the photon energy axis.

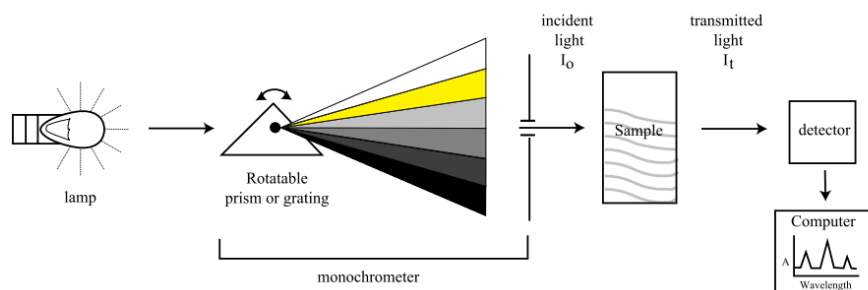


**Figure III.6: Schematic diagram of a typical UV-Vis Spectrometer.**

A basic experimental setup for absorption spectroscopy is given by the schematic diagram in Figure III.6. The transmission spectrum of a semiconductor could be observed with the use of a monochromator and a photodetector. Light from a source that passes through the monochromator will be reflected at different angles for different wavelengths by a grating placed inside the monochromator. By rotating the grating it is possible to tune the wavelength of the incident light through the exit slit of the monochromator for the recording at the photodetector of the transmitted light intensity through the sample as a function of the wavelength. Plotting the optical density (or absorbance) as a function of the wavelength of the incident light yields the absorption spectrum.

### III.8.2 Instrumentation and experimental parameters

In this work, solution UV-visible spectra in chloroform were recorded in quartz cuves with a 1650 PC Shimadzu spectrophotometer.

## III.9 X-ray photoelectron spectroscopy (XPS)

### III.9.1 Principle

XPS is a quantitative spectroscopy technique that utilizes photoionization and analysis of the kinetic energy distribution of the emitted photoelectrons through the core levels analysis for the determination of the electronic structure, elemental composition, chemical state and bonding interactions of materials. When a material is irradiated with a monochromatic electromagnetic X-ray wave with energy  $h\nu$ , electrons are ejected with a kinetic energy ( $E_k$ ) toward the analyzer. This principle is illustrated in Figure III.7. The energy conservation law (equation III.1), relates the kinetic energy of the photoemitted electron to its binding energy ( $E_B$ ) and the x-ray photon energy:

$$E_k = h\nu - |E_B| \quad (\text{Equation III.1})$$

Where  $E_k$ : kinetic energy of the photoelectron (eV);  $h\nu$ : photon energy;  $E_B$ : binding energy (eV). The electrons are ejected only if their binding energy ( $E_B$ ) is less than the energy of the incident photons.

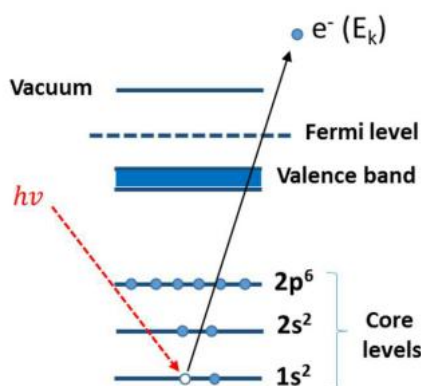


Figure III.7: Schematic diagram of photoelectric process.

It differs from conventional spectroscopic methods as it detects electrons rather than photons. It is an indispensable powerful technique employed in the study of surfaces and interfaces due to its high surface sensitivity.

### III.9.2 Instrumentation and experimental parameters

XPS spectra were recorded with a 220i-XL ESCALAB from VG. Powders were pressed onto indium foils and put under UHV to reach the  $10^{-8}$  Pa range. The non-monochromatized Mg X-Ray source was used at 200 W, as well as a flood gun to compensate the

non-conductive samples. The spectra were calibrated in relation to the C1s binding energy (285 eV) which was applied as an internal standard. Fitting of the high resolution spectra were provided through the ECLIPSE program from VG.

### III.10 Atomic Force Microscopy (AFM)

#### III.10.1 Principle [7]

AFM uses a cantilever with a very sharp tip to scan over a sample surface. As the tip approaches the surface, the close-range, attractive force between the surface and the tip cause the cantilever to deflect towards the surface. However, as the cantilever is brought even closer to the surface, such that the tip makes contact with it, increasingly repulsive force takes over and causes the cantilever to deflect away from the surface. A laser beam is used to detect cantilever deflections towards or away from the surface. By reflecting an incident beam off the flat top of the cantilever, any cantilever deflection will cause slight changes in the direction of the reflected beam. A position-sensitive photo diode (PSPD) can be used to track these changes. Thus, if an AFM tip passes over a raised surface feature, the resulting cantilever deflection (and the subsequent change in direction of reflected beam) is recorded by the PSPD. AFM images the topography of a sample surface by scanning the cantilever over a region of interest. The raised and lowered features on the sample surface influence the deflection of the cantilever, which is monitored by the PSPD. By using a feedback loop to control the height of the tip above the surface (maintaining constant laser position), the AFM can generate an accurate topographic map of the surface features (Figure III.8).

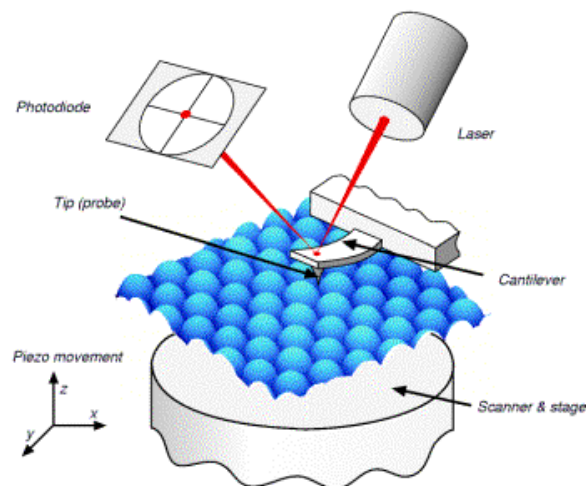


**Figure III.8:** Schematic illustration of AFM. The tip is attached to a cantilever, and is raster-scanned over a surface. The cantilever deflection due to tip-surface interactions is monitored by a photodiode sensitive to laser light reflected at the tip backside. For microscopy applications, the position of the reflected beam is kept centered in the diode through feedback-controlled z-changes in the stage [7].

#### III.10.2 Instrumentation and experimental parameters

In this work, AFM images were recorded in the standard tapping-mode using NSC11/AIBS cantilevers (typical resonance frequency: 325 kHz, typical force constant: 40 N/m) on a commercial atomic force microscope (Dimension Icon, Bruker, Santa Barbara, CA) and cypher AFM (asylum research, Santa Barbara, CA).

### **III.11 Transmission Electron Microscopy (TEM)**

#### **III.11.1 Principle**

Transmission Electron Microscopy allows for producing high-resolution, black and white images from the interaction occurring between suitably prepared samples and energetic electrons in the vacuum chamber. Air needs to be pumped out of the vacuum chamber, creating a space where electrons are able to move. The electrons then pass through multiple electromagnetic lenses constituted of solenoids fabricated with coil wrapped around them. The beam passes through the solenoids, down the column, makes contact with the screen where the electrons are converted to light in order to form an image. The image can be manipulated by adjusting the voltage of the gun to accelerate or decrease the speed of electrons as well as changing the electromagnetic wavelength via the solenoids. The coils focus images onto a screen or photographic plate. During transmission, the speed of electrons directly correlates to electron wavelength; the faster electrons move, the shorter wavelength and the greater the quality and detail of the image. The lighter areas of the image represent the places where a greater number of electrons were able to pass through the sample and the darker areas reflect the dense areas of the object. These differences provide information on the structure, texture, shape and size of the sample. To carry out TEM analyses, samples need to have certain properties. They need to be sliced thin enough for electrons to pass through, a property known as electron transparency. Samples need to be able to withstand the vacuum chamber and often require special preparation before viewing.

From a practical point of view, a transmission electron microscope includes three essential systems as figure III.9: (1) an electron gun, which produces the electron beam, and the condenser system, which focuses the beam onto the object, (2) the image-producing system, consisting of the objective lens, movable specimen stage, and intermediate and projector lenses, which focus the electrons passing through the specimen to form a real, highly magnified image, and (3) the image-recording system, which converts the electron image into some form perceptible to the human eye.

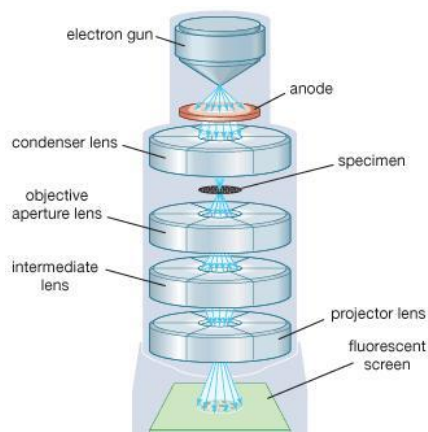


**Figure III.9: Schematic diagram of TEM.**

The image-recording system usually consists of a fluorescent screen for viewing and focusing the image and a digital camera for permanent records. In addition, a vacuum system, consisting of pumps and their associated gauges and valves, and power supplies are required.

### III.11.2 Instrumentation and experimental parameters

Low-resolution TEM and High-resolution-TEM images were recorded on JEOL JEM-2100 and JEOL JEM-2200FS microscopes, respectively, after dispersing the powders in ethanol and coating a small droplet of the suspension on holey carbon (Cu) grid.

## III.12 Scanning Electron Microscopy (SEM)

### III.12.1 Principle

SEM is also a topographic technique, designed for directly studying the surfaces of solid materials. It involves a beam of focused electrons with relatively low energy as an electron probe that is scanned in a regular pattern over the specimen. The electron source and electromagnetic lenses that generate and focus the beam are similar to those described for the transmission electron microscope (TEM). The action of the electron beam stimulates emission of high-energy backscattered electrons and low-energy secondary electrons from the surface of the specimen. There are no elaborate specimen-preparation techniques required for examination in the SEM, thus, large and bulky specimens could be accommodated. It is desirable that the specimen is electrically conducting; otherwise, a sharp picture cannot be obtained. Conductivity is usually achieved by evaporating a film of metal, such as gold, 50–100 angstroms thick onto the specimen in a vacuum. However, the SEM can be operated at 1–3 kilovolts of energy, thus, even nonconducting specimens may be examined without the need for a metallic coating.

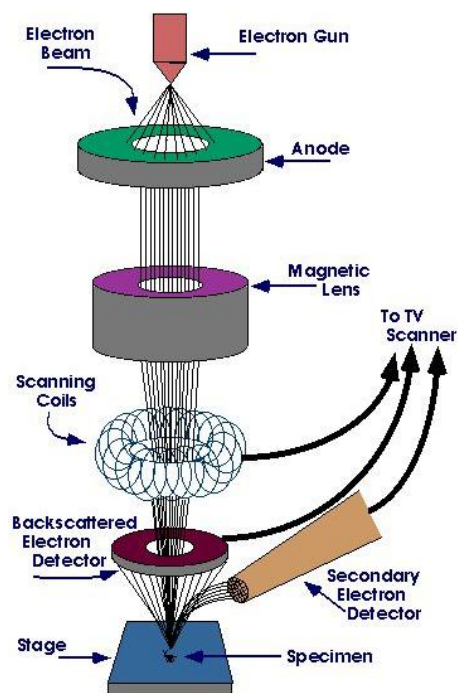


**Figure III.10: Schematic diagram of SEM.**

### III.12.2 Instrumentation and experimental parameters

In this work, some of the morphologies of the tin-oxide layers (Figure V-7) were observed by scanning electron microscopy (SEM) in a Hitachi TM-1000 microscope at University of Bordeaux. Micrographs were taken at several different magnifications ranging from  $\times 180$  to  $\times 70000$ . (sample section of about  $0.5 \text{ cm}^2$  were mounted on a carbon tab, which ensured a good conductivity). A thin layer of gold-palladium was sputtered on the foam fragment prior to analysis.

The other SEM images (Figure IV-18 to IV-20, Figure V5, V-11 and V-14) were taken at a Philips XL30 FEG (Philips, Netherlands) at Darmstadt. The samples were coated with a thin layer of gold using a Quorum Q300T D (Quorum Technologies Ltd, United Kingdom) for 20 s at 30 mA. Imaging was performed at an acceleration voltage of 10 kV with a secondary electron detector.



## References:

- [1] H. Gunther, in book of NMR Spectroscopy: Basic Principles, Concepts, and Applications in Chemistry, third Edition, **2013**, Wiley-VCH Verlag GmbH & Co. KGaA.
- [2] W. Voelter, E. Breitmaier, in book of Carbon-13 NMR Spectroscopy, third edition, **1987**, VCH Verlagsgesellschaft mbH.
- [3] A.G. Davies, in book of Organotin Chemistry, **1997**, VCH Verlagsgesellschaft mbH.
- [4] J. H. Gross, in Textbook of Mass Spectrometry, second Edition, **2011**, Springer-Verlag Berlin Heidelberg.
- [5] B. C. Smith, in book Fundamentals of Fourier Transform Infrared Spectroscopy, second Edition, **2011**, CRC Press.
- [6] K. S. W. Sing, D. H. Everett, R. A. W. Haul, L. Moscou, R. A. Pierotti, J. Rouquerol, T. Siemieniewska, *Pure & App. Chem.*, **1985**, 57(4), 603-619.
- [7] C. Zeng, C. Vitale-Sullivan, X. Ma, *Minerals* **2017**, 7(9), 158.

# Chapter IV Synthesis and characterization of finely tuned SnO<sub>2</sub> nanoparticles

As underlined in the previous chapters, tin dioxide constitutes one of the most attractive binary oxides for both technological and commercial applications due to its outstanding physicochemical properties such as excellent transparency in the visible range, high electronic conductivity, remarkable chemical and photochemical stability, and mechanical hardness. In addition, tin dioxide exhibits two specific properties, change in valence state and presence of oxygen vacancies, leading to unique resistivity variation under gas atmosphere which makes tin dioxide as the best understood prototype materials for gas sensing.

Our first aim was therefore to develop a method leading to well-defined SnO<sub>2</sub> nanoparticles which can be scaled up easily. In this context, we investigated an approach based on the hydrothermal treatment of a commercial colloid by varying the pH conditions and the thermal post-treatment used. The nanopowders obtained were characterized by FTIR, Raman spectroscopy, powder X-ray diffraction (PXRD), transmission electron microscopy (TEM), X-ray photoelectron spectroscopy (XPS) and nitrogen sorption porosimetry. Their ability to detect a series of reductive and oxidative gases is further discussed in chapter VI.

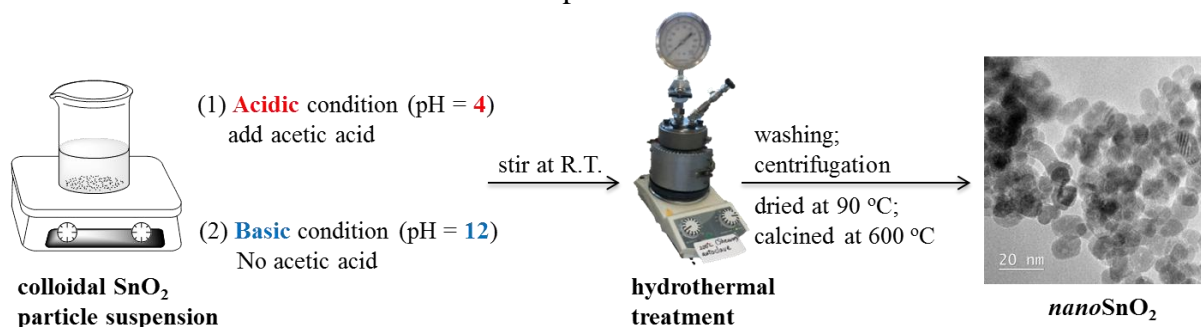
## IV.1 Preparation of finely tuned SnO<sub>2</sub> nanoparticles

### IV.1.1 Introduction

Many routes have been explored to prepare tin dioxide materials of various shapes and morphologies, including oxidation [1] or evaporation [2] under stringent conditions, hydrothermal [3], conventional sol-gel precipitation [4], hydrothermal crystallization [5], pyrolysis of organotins [6] or electrochemical deposition [7] followed by thermal oxidation, hydrolytic [8] and non-hydrolytic [9] sol-gel, ionic liquid assisted [10], microwave [11] and sonochemical methods [12]. However, these methods usually involve long synthetic strategies or processes and do not allow the production of large quantities of materials. To break through this limitation, hydrothermal treatments under acidic conditions of available commercial SnO<sub>2</sub> suspension have been developed to obtain large amount of 18-nm SnO<sub>2</sub> colloids employed to fabricate porous photoanodes for dye-sensitized solar cells [13]. Although the work was mainly focused on the application of dye-sensitized solar cells, the simple hydrothermal operating conditions and clean synthesis of nanoparticulate tin dioxide materials, also named *nano*SnO<sub>2</sub> [14], has drawn our attention for the synthesis of SnO<sub>2</sub> nanoparticles for gas sensing applications. The pH conditions and the temperature of the thermal post-treatment were varied to tune the properties of the particles.

### IV.1.2 Synthesis of the SnO<sub>2</sub> nanoparticles

Tin dioxide particle growth was achieved by hydrothermal treatment of a commercial SnO<sub>2</sub> particle suspension (Alfa Aesar, SnO<sub>2</sub>, 15% w/v in water, pH = 11-12, counter-ion K<sup>+</sup>) [15] under either acidic or basic conditions as depicted in Scheme 1:



**Scheme IV-1: SnO<sub>2</sub> nanoparticles prepared under two experimental conditions.**

#### IV.1.2.a Preparation under acidic condition (pH = 4)

In first procedure, 37 g of the colloidal SnO<sub>2</sub> particle suspension and 1 g of glacial acetic acid (Fisher Scientific) were mixed in a closed vessel and stirred for 48 h at room temperature (RT). The resulting acidic slurry (pH = 4.0) in a homemade vessel was placed into a stainless steel autoclave (300 mL) and kept at 240°C (29 Bars) for 90 hours. After naturally returning to RT, the obtained solids were isolated by centrifugation and then cleaned by several cycles of redispersion, sonication, and centrifugation using water and ethanol as solvents (each time: 6500 rpm, 10 minutes). Drying with a nitrogen flow in air and heating at 90°C overnight yielded 5.6 g of a light greenish powder, hereafter named TOa<sup>90</sup>. Further calcination in air at 300 °C, 500 °C and 600 °C, respectively, for 96 hours yielded white powders, hereafter named TOa<sup>300</sup>, TOa<sup>500</sup> and TOa<sup>600</sup>.

#### IV.1.2.b Preparation under basic condition (pH = 12)

As far as the synthesis under basic conditions is concerned, the same procedure was employed with solely 37 g of the commercial SnO<sub>2</sub> particle suspension (pH = 12, ammonia solution). After the hydrothermal treatment, washings, centrifugation and drying at 90°C overnight, 4 g of a light yellowish powder, hereafter named TOb<sup>90</sup>, was obtained. Further calcination in air at 500 °C and 600 °C for 96 hours yielded white powders, hereafter named TOb<sup>500</sup> and TOb<sup>600</sup>.

## IV.2 Characterization of SnO<sub>2</sub> nanoparticles

### IV.2.1 FTIR and Raman spectroscopy studies

First of all, it is necessary to mention that the commercial colloid used as precursor in this research includes polypyrrole and K<sup>+</sup> counterions.[15] The evolution in composition depending on the preparation conditions were first studied by FTIR and Raman spectroscopy. The FTIR spectra of the SnO<sub>2</sub> nanoparticles assessed as a function of the synthetic conditions are shown in Figure IV-1. Regardless of the preparation conditions, no characteristic band of

organics were observed in the FTIR spectra indicating that most organic polymers have been removed during the purification processes. In the case of TOa samples, typical features of adsorbed water or surface hydroxyl groups (broad bands centered at 3430 ( $\nu_{\text{O-H}}$ ) and 1634 ( $\nu_{\text{O-H}}$ )  $\text{cm}^{-1}$ ), and tin oxide moieties (675-650 and 575 (sh) ( $\nu_{\text{Sn-O-Sn}}$  and  $\nu_{\text{Sn-O}}$ )  $\text{cm}^{-1}$ ) [16] were observed. Furthermore, a significant shift, i.e. from 651 for TOa<sup>90</sup> to 677  $\text{cm}^{-1}$  TOa<sup>600</sup>, of the  $\nu_{\text{Sn-O-Sn}}$  vibration mode was observed which accounts for change in crystallite size upon calcinations [17]. Similar features were detected for TOb samples with some additional bands in the 1200-900  $\text{cm}^{-1}$  region that could be attributed to hydroxyl-metals bonds [18].

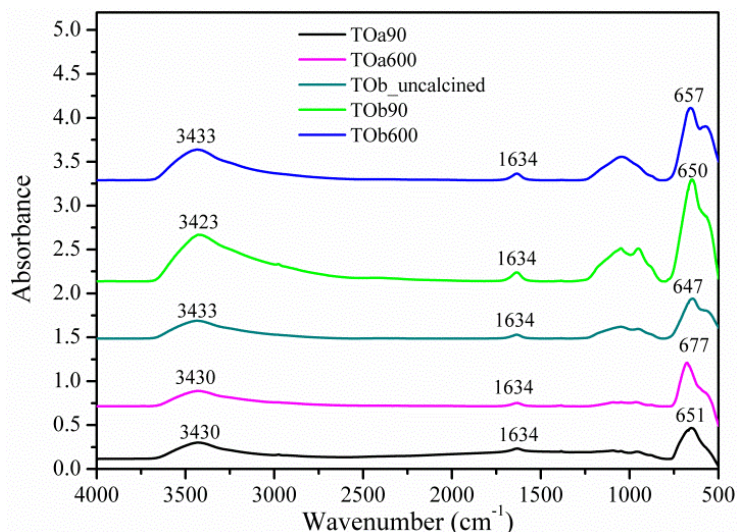


**Figure IV-1: FTIR absorbance spectra of SnO<sub>2</sub> particles: TOa90 (black), TOa600 (pink), TOb\_uncalcined (dark cyan), TOb90 (green), TOb600 (blue).**

On the other hand, the rutile-type phase of SnO<sub>2</sub> can be sensitively detected by Raman spectroscopy. According to group theory analysis, rutile SnO<sub>2</sub> has four Raman active modes ( $A_{1g} + B_{1g} + B_{2g} + E_g$ ) [19] and rutile-type SnO<sub>2</sub> single crystal shows vibrational bands at 123 ( $B_{1g}$ ), 473 ( $E_g$ ), 633 ( $A_{1g}$ ) and 773  $\text{cm}^{-1}$  ( $B_{2g}$ ) [20]. The Raman spectrum of the dried commercial colloid exhibits no clear evidence of crystalline SnO<sub>2</sub> species (Figure IV-2). By contrast, after hydrothermal treatment in acidic or basic medium, with or without further calcination, Figure IV-2 shows the Raman bands of SnO<sub>2</sub> nanoparticles at 632 ( $A_{1g}$ ) and 773  $\text{cm}^{-1}$  ( $B_{2g}$ ) along with a very broad band centered around 550  $\text{cm}^{-1}$  which can be attributed to modes related to local order disorder and vacant site [19], or to oxo-hydroxotin species [21]. It is generally admitted that  $A_{1g}$  and  $B_{2g}$  are relative to the expansion and contraction vibrational modes of Sn-O bonds and the tetragonal rutile structure of SnO<sub>2</sub> is assessed by the presence of these Raman features [22]. Moreover, the relative intensity of the sharp peak at 632  $\text{cm}^{-1}$  with respect to this at 550  $\text{cm}^{-1}$  increases after calcination suggesting an improved crystallization of the nanoparticles. In addition, no feature was detected in the 900-1800  $\text{cm}^{-1}$  wavenumber range confirming that the remaining organics and polymers have been removed.

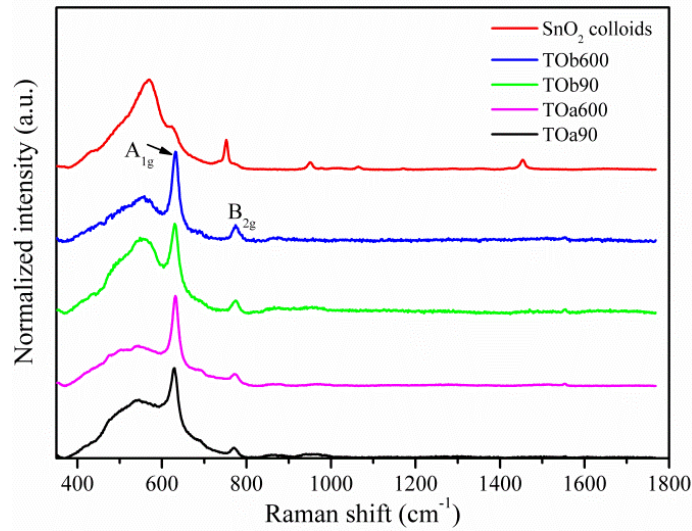


**Figure IV-2: Raman spectra of SnO<sub>2</sub> particles: TOa<sup>90</sup> (black), TOa<sup>600</sup> (pink), TOB<sup>90</sup> (green), TOB<sup>600</sup> (blue). The spectrum of the dried commercial colloid is given as a reference (red).**

#### IV.2.2 Crystallinity: Powder X-ray Diffraction studies

Powder X-ray Diffraction confirmed the crystalline structure of the particles formed (Figure IV-3). No matter what kind of the preparation condition used, the tetragonal, i.e. rutile-like, tin dioxide phase was obtained as revealed by the X-ray diffraction pattern of each sample studied with main features at  $d$  (Å) values of {110} (3.347), {101} (2.6427), {200} (2.369), {211} (1.7641), {220} (1.675), {002} (1.5934), {310} (1.4984), {112} (1.4392), {301} (1.4155), {202} (1.322), {321} (1.2147) and {222} (1.1544) in good agreement with the reported data (JCPDS File No. 41-1445). The average crystallite size was the calculated from the Scherrer relation [23]:

$$t = (0.9\lambda)/(\beta \cos \theta) \quad \text{where} \quad \lambda \text{ is the wavelength,}$$

$$\beta \text{ is the angular half-width of the hkl peak for the}$$

$$\text{studied sample,}$$

$$\theta \text{ is the Bragg angle for the chosen hkl reflection.}$$

The average crystallite size was estimated to be 8.0, 9.0, 9.3, 9.6, 7.9, 7.5 and 7.5 nm for TOa<sup>90</sup>, TOa<sup>300</sup>, TOa<sup>500</sup>, TOa<sup>600</sup>, TOB<sup>90</sup>, TOB<sup>500</sup> and TOB<sup>600</sup>, respectively (Table IV-1). As a consequence, the calcination step induced a slight increase in the mean crystallite size for samples prepared in acidic condition but has no influence for those synthesized in basic medium.

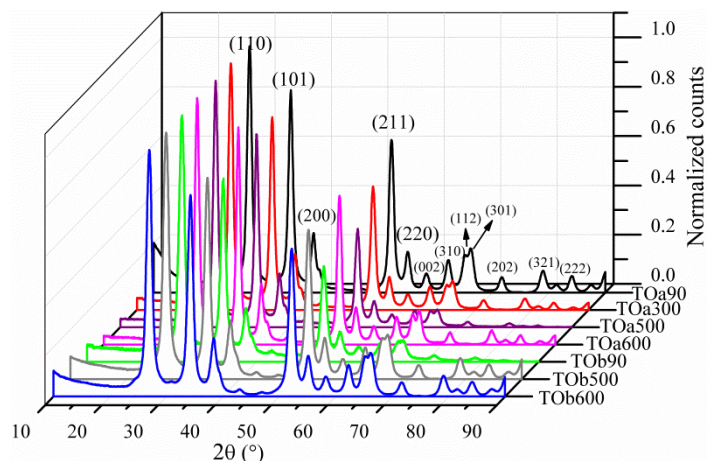


**Figure IV-3: PXRD patterns of SnO<sub>2</sub> particles: TOa<sup>90</sup> (black), TOa<sup>300</sup> (red), TOa<sup>500</sup> (violet), TOa<sup>600</sup> (pink), TOb<sup>90</sup> (green), TOb<sup>500</sup> (grey), TOb<sup>600</sup> (blue).**

Sample	Mean crystallite size from XRD <sup>a</sup> (nm)	Mean particle size from TEM <sup>b</sup> (nm)
TOa <sup>90</sup>	8.0 ± 0.5	10.7 ± 1.0
TOa <sup>300</sup>	9.0 ± 0.5	-
TOa <sup>500</sup>	9.3 ± 0.5	-
TOa <sup>600</sup>	9.6 ± 0.5	11.6 ± 1.0
TOb <sup>90</sup>	7.9 ± 0.4	8.5 ± 0.5
TOb <sup>500</sup>	7.5 ± 0.4	-
TOb <sup>600</sup>	7.5 ± 0.4	8.4 ± 0.5

**Table IV-1: Average crystallite size and average particle size for SnO<sub>2</sub> nanopowders. <sup>a</sup>Estimated from full width at half- maximum of the diffraction peak using the Scherrer equation. <sup>b</sup>Deduced from TEM images.**

### IV.2.3 Morphology and structure: Transmission Electron Microscopy studies

#### IV.2.3.1 Low-resolution TEM

TEM micrographs along with particle size histograms for TOa and TOb samples are showed in Figures IV- 4 and IV- 5, respectively. In each case, TOa and TOb samples are composed of a network of aggregated pseudo-spherical nanocrystallites with a rather narrow particle size distribution. The average particle size was found to be  $10.7 \pm 1$  nm and  $11.6 \pm 1$  nm for TOa<sup>90</sup> and TOa<sup>600</sup>, respectively (Figure IV-4) and was estimated to be 8.52 and 8.37 nm for TOb<sup>90</sup> and TOb<sup>600</sup>, respectively. As a result, these data confirm that the calcination step does not influence the average particle size for particles prepared in basic conditions whereas it induces a slight increase of the mean particle size in the case of particles synthesized in acidic medium. These values are in good agreement with the crystallite sizes estimated from XRD pattern (Table IV-1).



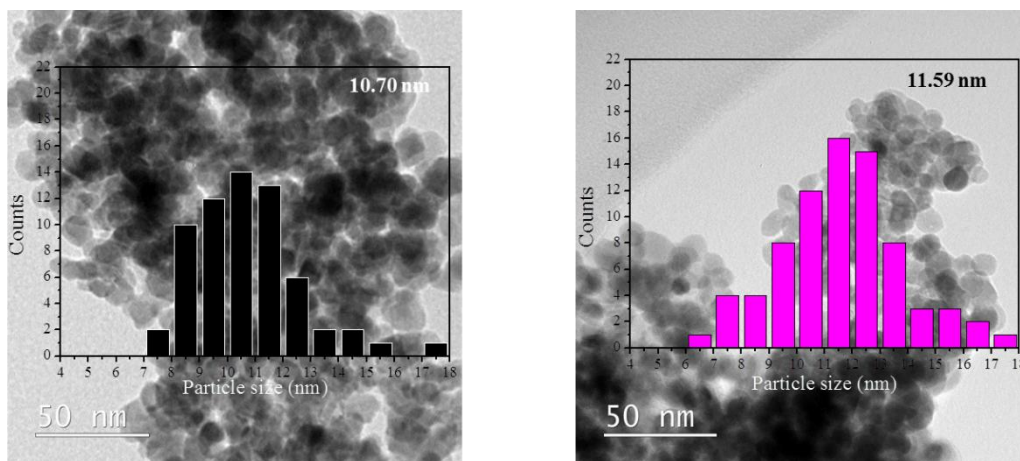


Figure IV-4: TEM micrographs and particle size distribution of TOa<sup>90</sup> (left) and TOa<sup>600</sup> (right).

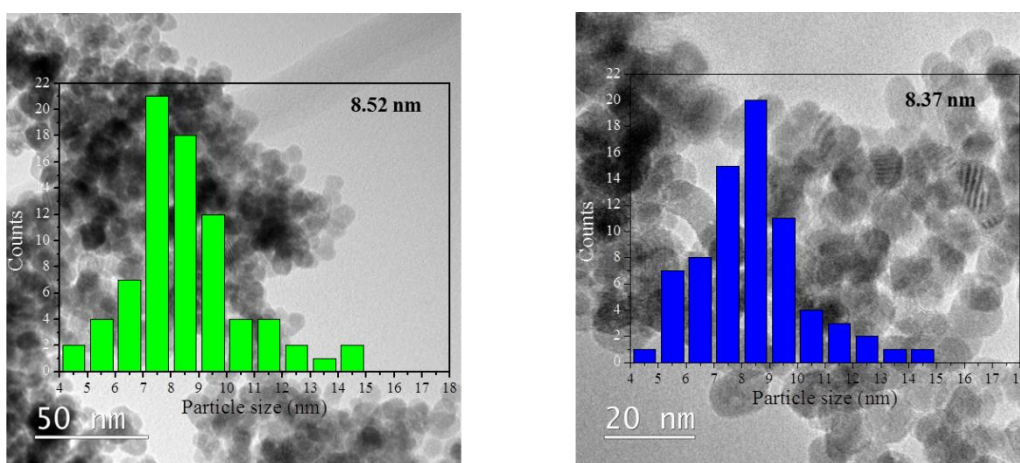


Figure IV-5: TEM micrographs and particle size distribution of TOB<sup>90</sup> (left) and TOB<sup>600</sup> (right).

Nonetheless, the particle sizes inferred from TEM images are slightly larger than the crystallite sizes deduced from powder X-ray diffraction patterns. This may be explained by taking into account that the Scherrer relationships can provide an underestimation of the average crystallite size because the contribution of smaller size components in a crystallite-size distribution dominates the line-broadening in the XRD patterns. As a consequence, the actual crystallite size might be larger than that estimated by XRD measurements and be closer to the mean particle size determined from the TEM micrographs [24].

#### IV.2.3.2 High-resolution TEM

HR-TEM micrographs and selected-area electron diffraction (SAED) pattern of each samples showed the formation of well-crystallized SnO<sub>2</sub> particles exposing well-defined facets which is typical the formation of rutile-like tin dioxide (Figure IV-6 to IV-9). First of all, TOa<sup>90</sup> showed particles exposing lattice fringes with d-spacings of 3.2, 2.1 and 1.7 Å corresponding to (110), (200) and (211) planes of cassiterite (Figure IV-6), i.e. rutile-like, SnO<sub>2</sub>.

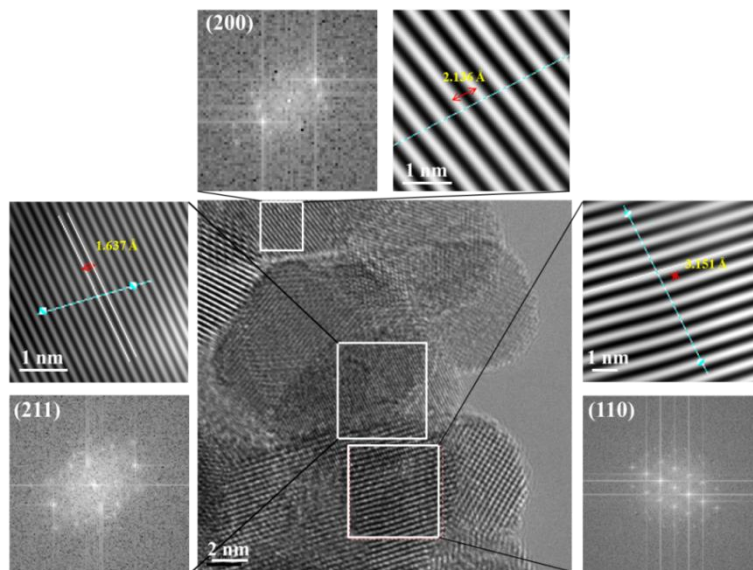


Figure IV-6: HR-TEM images of TOa<sup>90</sup> and selected area electron diffraction (SAED) patterns.

After calcination in air at 600 °C, TOa<sup>600</sup> showed particles exposing lattice fringes with d-spacings of 3.3 and 2.2 Å corresponding to (110) and (200) planes of cassiterite (Figure IV-7).

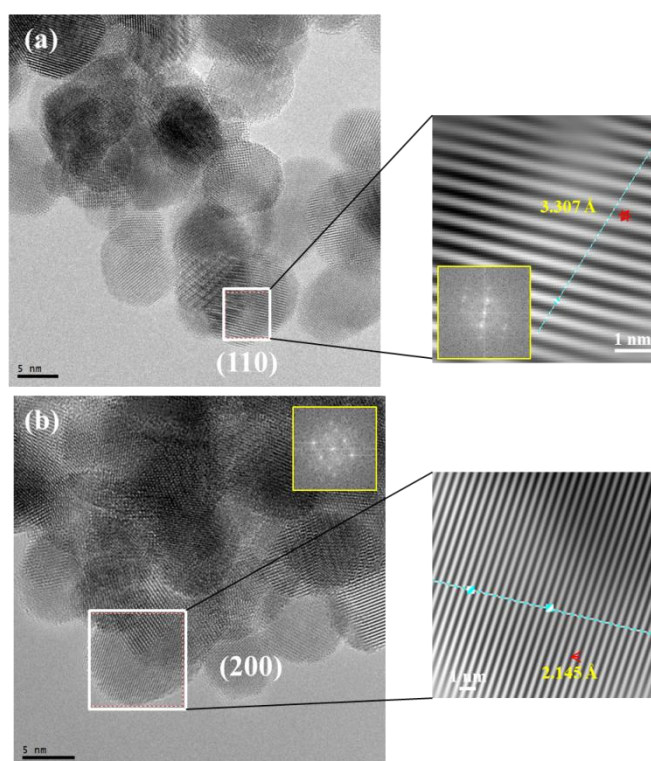
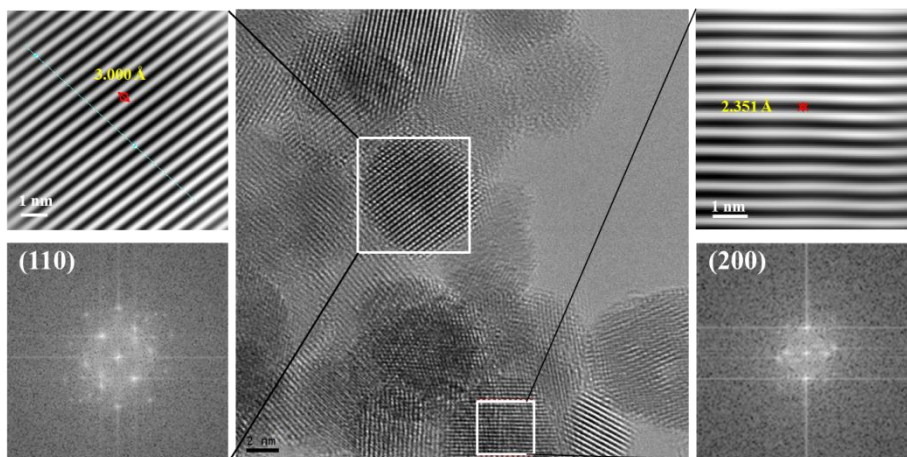


Figure IV-7: HR-TEM images and selected area electron diffraction (SAED) patterns of TOa<sup>600</sup>. (a) d-spacing is 3.31 Å corresponding to (110) plane; (b) d-spacing is 2.15 Å corresponding to (200) plane.

As for the samples which have been prepared under basic conditions, TOb<sup>90</sup> is made of particles exposing lattice fringes with d-spacings of 3.0 and 2.4 Å corresponding to (110) and (200) planes of cassiterite (Figure IV-8).





**Figure IV-8: HR-TEM images of TOB90 and selected area electron diffraction (SAED) patterns.**

The same features were observed for the corresponding calcined sample. Thus, TOB<sup>600</sup> sample showed particles exposing lattice fringes with d-spacings of 3.1, 2.5 and 1.7 Å corresponding to (110), (101) and (211) planes of cassiterite.

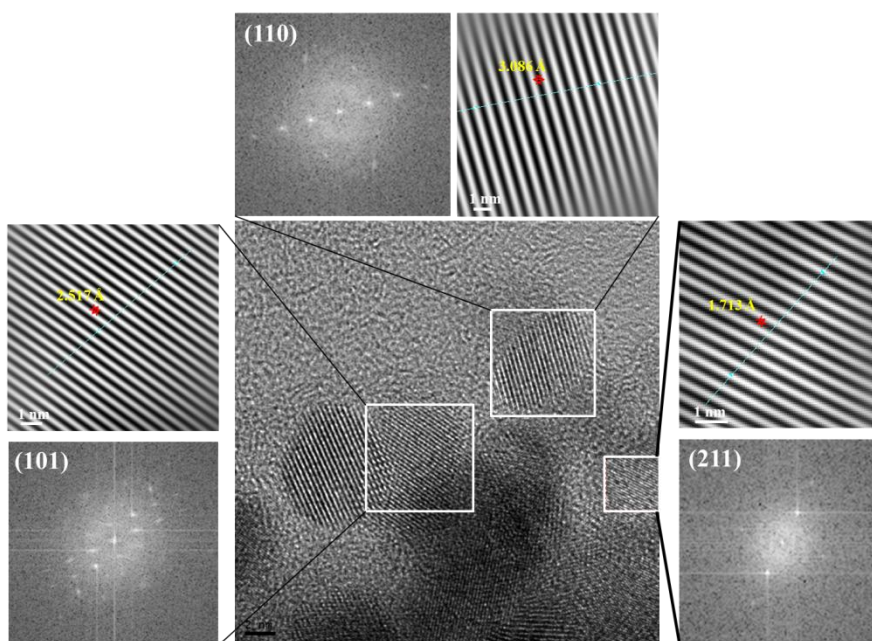


**Figure IV-9: HR-TEM images of TOB<sup>600</sup> and selected area electron diffraction (SAED) patterns.**

In summary, the same exposed facets were observed in the HR-TEM micrographs of all samples studied. In particular, the nanopowders obtained just after hydrothermal treatment already expose low-surface-energy facets as (110) (surface energy: 1.554 J.m<sup>-2</sup>) [5b], explaining the absence of change in the nature of the exposed facets after calcination.

#### IV.2.4 Textural properties: N<sub>2</sub> sorption studies

Textural properties of the different SnO<sub>2</sub> nanopowders were determined by N<sub>2</sub> adsorption–desorption analysis (Figure IV-10). Each sample led to a type IV sorption

isotherm showing a type H<sub>2</sub> hysteresis loop which is characteristic of mesoporous solids according to the IUPAC classification [25]. Furthermore, all powders exhibit a well-defined and rather narrow pore size distribution with an average pore size of about 16 and 21 nm for TOa and TOb, respectively (Table IV-2). As a consequence, the detected mesoporosity can be attributed to the interparticle space that can be seen in the porous network of aggregated cassiterite SnO<sub>2</sub> nanoparticles evidenced by TEM studies [24]. Nonetheless, a strong influence of the use of acetic acid was observed on the BET surface areas and total pore volumes. Thus, S<sub>BET</sub> values collapse from 106-98 m<sup>2</sup>.g<sup>-1</sup> for TOb samples to 79-61 m<sup>2</sup>.g<sup>-1</sup> for TOa samples. Similarly, total pore volumes found for powder synthesized under acidic conditions are 1.7 lower than those of the samples prepared in basic medium. Moreover, the calcination step affects more the textural properties of the powders prepared in acidic conditions as it was already mentioned for the mean crystallite and particle sizes deduced from XRD and TEM analyses. This trend might be related to the higher potassium amount present in the sample prepared in basic medium that would inhibit particle growth and specific surface area.

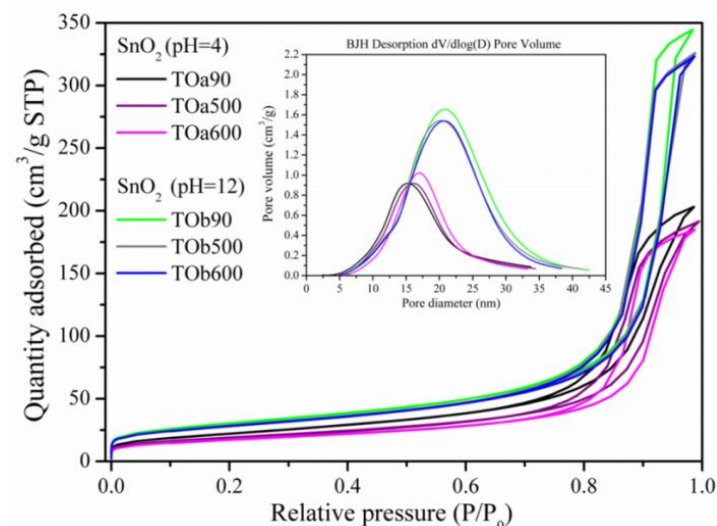


**Figure IV-10: Nitrogen adsorption-desorption isotherms and pore size distribution (insert) of TOa<sup>90</sup> (black), TOa<sup>500</sup> (violet), TOa<sup>600</sup> (pink), TOb<sup>90</sup> (green), TOb<sup>500</sup> (grey), TOb<sup>600</sup> (blue).**

Sample	Specific surface area $S_{\text{BET}}$ ( $\text{m}^2 \cdot \text{g}^{-1}$ ) <sup>a</sup>	Total pore volume ( $\text{cm}^3 \cdot \text{g}^{-1}$ ) <sup>b</sup>	Average pore diameter <sup>b</sup> (nm) <sup>c</sup>
TOa <sup>90</sup>	79.0 ± 2.5	0.31 ± 0.02	15.6 ± 0.5
TOa <sup>300</sup>	74.5 ± 2.0	0.32 ± 0.02	15.7 ± 0.5
TOa <sup>500</sup>	67.5 ± 2.0	0.30 ± 0.02	17.5 ± 0.5
TOa <sup>600</sup>	61.5 ± 2.0	0.29 ± 0.02	19.7 ± 0.5
TOb <sup>90</sup>	106.5 ± 3.0	0.53 ± 0.03	20.7 ± 0.5
TOb <sup>500</sup>	100.0 ± 3.0	0.50 ± 0.03	20.5 ± 0.5
TOb <sup>600</sup>	99.0 ± 3.0	0.50 ± 0.03	20.6 ± 0.5

**Table IV-2: Nitrogen sorption porosimetry data of SnO<sub>2</sub> nanopowders. <sup>a</sup>Surface areas were determined by BET. <sup>b</sup>Pore volumes estimated by single-point analysis. <sup>c</sup>Mean pore diameters calculated by BJH theory (applied to the desorption branch).**

#### IV.2.5 Surface composition and Debye length: X-ray photoelectron spectroscopy studies

The commercial colloid used as precursor includes polypyrrole and K<sup>+</sup> counter-ions. Surface chemical elements and chemical states of the SnO<sub>2</sub> particles were then investigated by X-ray Photoelectron Spectroscopy. Apart from weak C 1s and Si 2p peaks located around 285 and 102 eV respectively, which might be attributed to environmental carbon and silicon contaminations, only Sn (Sn 3p, Sn 3d, Sn 4d and Sn LMM Auger), oxygen (O 1s and O KLL Auger) and potassium (K 2p) elements were observed in the survey of the TOa and TOb samples (Figure IV-11). Table IV-3 gathers the energies of the typical lines detected. In each case, the Sn 3d spectrum exhibited two peaks at  $487.0 \pm 0.1$  eV and at  $495.4 \pm 0.1$  eV arising from spin-orbit coupling of the 3d state. The splitting between the Sn 3d doublets was found to be  $8.4 \pm 0.1$  eV, which is consistent with that reported for SnO<sub>2</sub> and the presence of Sn(IV) states [26]. On the other hand, the O 1s spectrum of TOa showed a main component at  $530.9 \pm 0.1$  eV, which can be attributed to the lattice oxygen O<sup>2-</sup> (Figure IV-11C, O 1s). Additional shoulders located at 531.9 and  $533.0 \pm 0.1$  eV next to the main peak indicate that several other chemical states are present according to the measured binding energy. They are caused by air contamination (water, OH, O-C), which is typical for ex-situ samples, the calcination step diminishing the amount of these chemical states (Table IV-4). Finally, surface K/Sn atomic ratios were found to be 0.01-0.02 and 0.08-0.09 for TOa and TOb samples, respectively, which are significantly lower than that of the dried commercial colloid (Table IV-4). As a consequence, acidic treatment favors the elimination of potassium counterions in the starting colloid (Table IV-4).

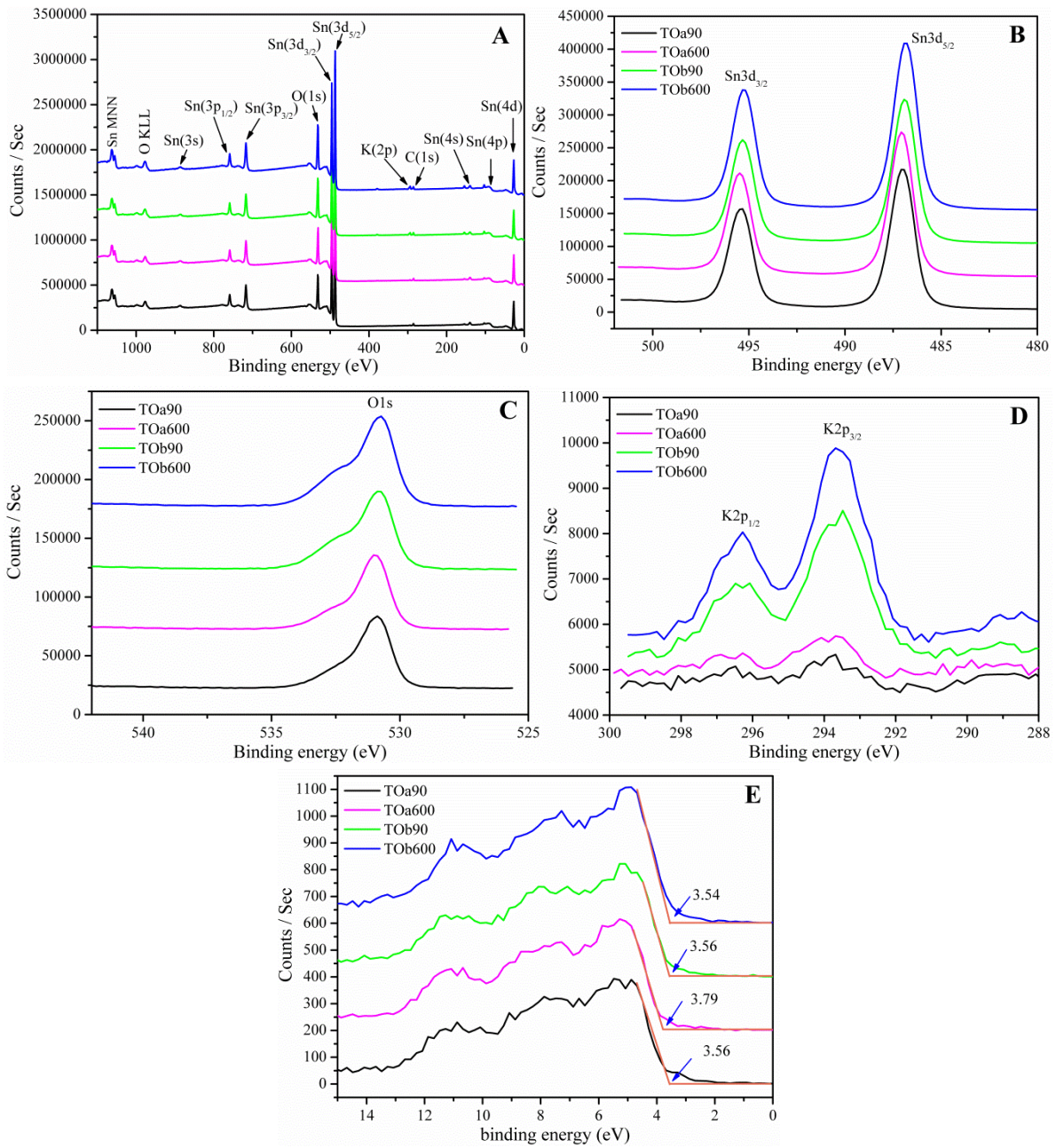


**Figure IV-11: XPS patterns of TOa<sup>90</sup> (black), TOa<sup>600</sup> (pink), TOb<sup>90</sup> (green) and TOb<sup>600</sup> (blue) particles (A) XPS full survey spectra; (B) Sn 3d region; (C) O 1s region; (D) K 2p region (full); (E) valence band XPS spectra.**



Sample	Sn 3d <sub>3/2</sub> (eV) <sup>a</sup>	Sn 3d <sub>5/2</sub> (eV) <sup>a</sup>	O 1s (eV) <sup>a</sup>	K 2p <sub>3/2</sub> (eV) <sup>a</sup>	VBE (eV) <sup>b</sup>	L <sub>D</sub> (nm) <sup>c</sup>
TOa <sup>90</sup>	495.4	487.0	530.9	293.9	3.56	6.4
TOa <sup>600</sup>	495.5	487.1	531.0	293.8	3.79	0.7
TOb <sup>90</sup>	495.5	487.1	530.9	293.6	3.56	6.4
TOb <sup>600</sup>	495.4	486.9	530.8	293.7	3.54	76

**Table IV-3: Energies values of the peaks from XPS spectra and related estimation of Debye lengths (L<sub>D</sub>).**

<sup>a</sup>Calibration has been done by fixing C 1s at 285 eV. <sup>b</sup>Valence Band Energy (VBE): Energy difference between the valence-band maximum and the Fermi level (E<sub>vf</sub>) determined by extrapolating the linear portion of the absorption jump to the spectrum baseline. <sup>c</sup>Debye length (L<sub>D</sub>) has been calculated at room temperature from equation (1).

Sample	O/Sn (at. %)	K/Sn (at. %)	OH/O <sup>2-</sup> (at. %) <sup>a</sup>	OC/O <sup>2-</sup> (at. %) <sup>b</sup>
TOa <sup>90</sup>	1.75	0.01	0.41	0.15
TOa <sup>600</sup>	1.76	0.02	0.26	0.09
TOb <sup>90</sup>	2.12	0.08	0.37	0.37
TOb <sup>600</sup>	2.12	0.09	0.43	0.14

**Table IV-4: Quantitative analysis of the surface composition deduced from XPS data. <sup>a</sup>Ratio between the contributions at 531.9 and 530.9 eV. <sup>b</sup>Ratio between the contributions at 533.0 and 530.9 eV.**

Figure IV-11E also shows the valence-band XPS spectra of the TOa and TOb samples with and without calcination. The upper valence band is predominantly composed of O 2p states with some contributions of Sn-O states [27]. The binding energy of the valence band maximum with respect to the Fermi level (E<sub>vf</sub>) (Table IV-3) was determined as reported in the literature [28]. Whatever the thermal post-treatment used, the values are comprised between 3.4-3.7 eV, which match well with the band gap energy of SnO<sub>2</sub> (3.6 eV at 300K) and are in good accordance with those described for undoped SnO<sub>2</sub> films fabricated by in situ sputter deposition [28, 29]. These features suggest a Fermi-level position near the bottom of the conduction band and the presence of few oxygen vacancies in the tin dioxide particles prepared [27]. In addition, the spectra of the annealed samples exhibit no further band gap emission above the valence-band maximum, evidencing the stoichiometric termination of the SnO<sub>2</sub> nanoparticle surface, where each tin surface atom exists as Sn<sup>4+</sup> centers [26, 30]. Such a surface termination is conventionally observed for tin oxide materials thermally treated in an oxidizing atmosphere [31].

On the other hand, the observed differences in the E<sub>vf</sub> values (Table IV-3) have deep implications from an electrical point of view. Based on E<sub>vf</sub> values, the density of charge carriers (n<sub>b</sub>) has been calculated through the Fermi integral using an energy gap value E<sub>g</sub> = 3.6 eV [32].

On the basis of  $n$ , the Debye length ( $L_D$ ) has been further calculated as an essential parameter controlling the gas sensing performance of metal oxide chemiresistors:

$$L_D = \sqrt{\frac{\epsilon kT}{q^2 n_b}} \quad (1)$$

where  $\epsilon$  is the dielectric constant of the semiconductor ( $\epsilon \approx 10^{-10}$  F/m for SnO<sub>2</sub>) [30],  
 $k$  is the Boltzmann constant ( $1.381 \times 10^{-23}$  J/K),  
 $T$  is the temperature (in K),  
 $q$  is the electron charge ( $1.602 \times 10^{-19}$  C).

$L_D$  values calculated for  $T = 300$  K are reported in Table IV-3. Although the vacuum condition of the XPS measurement could induce oxygen desorption from SnO<sub>2</sub>, being XPS data acquired at room temperature, oxygen removal is expected to occur only to a small extent, thus suggesting that  $L_D$  values reported in Table IV-3 could be reasonably adopted to compare the electrical properties of the prepared materials.

### IV.3 Preparation and characterization of films processed from the SnO<sub>2</sub> nanoparticles

The characterization of the gas sensing properties of the SnO<sub>2</sub> nanoparticles prepared above requires thin film processing. Due to its easy implementation, the drop-coating deposition technique, which consists in dropping several droplets of a dispersion of the nanoparticles on a substrate followed by drying, was chosen. The SnO<sub>2</sub> nanoparticles were dispersed in a mixture of solvents adapting a previously reported procedure [33].

#### IV.3.1 Fabrication of the SnO<sub>2</sub> nanoparticulate films

The colloidal suspensions were prepared as follows: 0.25 g of the *nano*SnO<sub>2</sub> particles were dispersed into a mixture of water (1.5 mL) and acetone (1 mL) in the presence of Triton X-100 (1 drop) and acetic acid (1 drop). The whole solution was stirred at room temperature for 34 h-54 h. The drop coating (3 droplets, each is 0.3  $\mu$ L) technique is chosen to fabricate SnO<sub>2</sub> films on the glass slide (1x1 cm) or Si (100) wafer substrates for further characterizations while those on the Al<sub>2</sub>O<sub>3</sub> substrate are for gas sensing measurement. Finally, each film was dried in air at 200 °C for 3 days.

#### IV.3.2 Surface morphology: AFM studies

The surface morphology of the nanocrystalline SnO<sub>2</sub> films processed on glass slides was first studied by AFM with two scanning sizes which are 10 and 1  $\mu$ m. These films were fabricated from the different SnO<sub>2</sub> nanoparticles (TOa<sup>90</sup>, TOa<sup>500</sup>, TOa<sup>600</sup>, TOb<sup>90</sup>, TOb<sup>300</sup> and TOb<sup>600</sup>) which have been treated previously at different calcination temperatures (Figure IV-12 to IV-17). The surface of the film composed of the TOa<sup>90</sup> particles shows of cloudy

assembly of aggregated SnO<sub>2</sub> nanoparticles, the size of the aggregates was about 180 nm (Figure IV-12, 1 μm scale). The mean roughness (Ra) was found to be 28.7 nm at 1 μm scale.

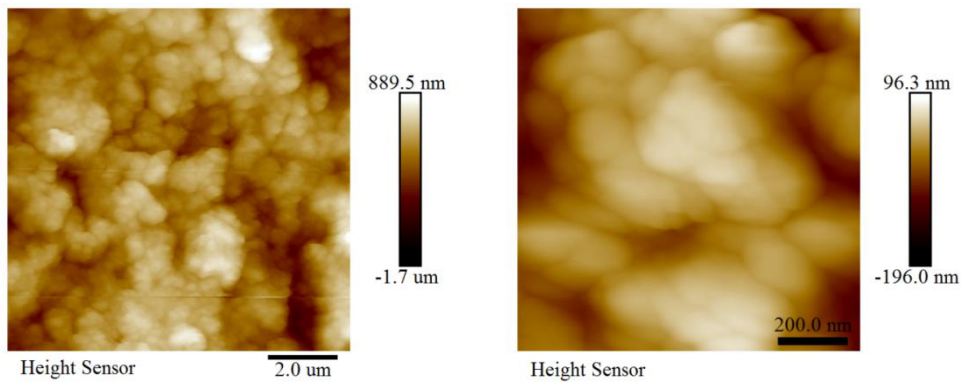


**Figure IV-12: Height AFM tapping images of TOa<sup>90</sup> films at: 10 μm scale (left); 1 μm scale (right).**

For the films processed from TOa<sup>500</sup> sample (Figure IV-13), the aggregate size was quite similar, i.e. 180 nm, and the mean roughness (Ra) is slightly lower (22.3 nm at 1 μm scale).

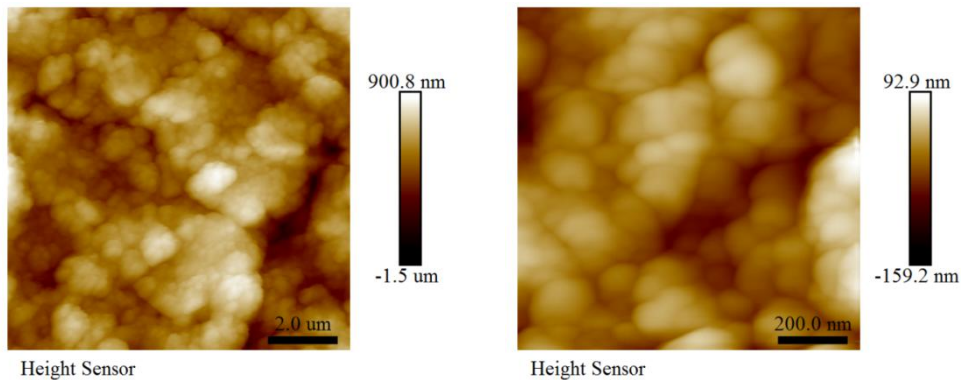


**Figure IV-13: Height AFM tapping images of TOa<sup>500</sup> films at: 10 μm scale (left); 1 μm scale (right).**

By contrast, the particles prepared under acidic conditions and calcined at 600 °C led to slightly bigger aggregated SnO<sub>2</sub> nanoparticles the size of which was about 200 nm (Figure IV-14). In this case, the mean roughness (Ra) is 33.6 nm at 1 μm scale.

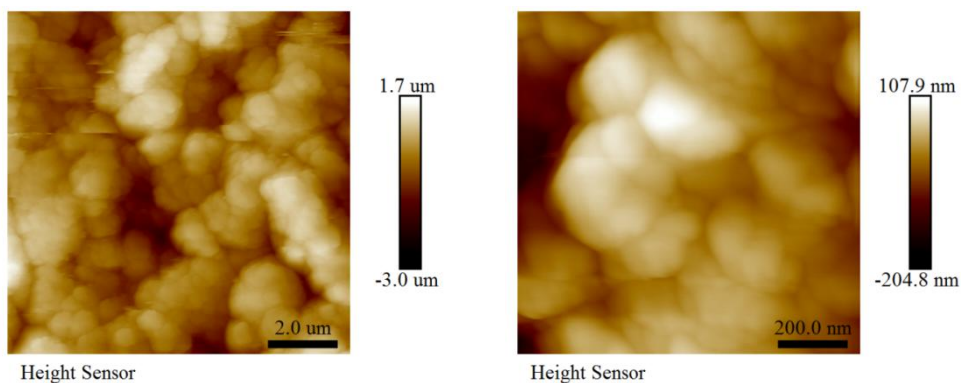


**Figure IV-14: Height AFM tapping images of TOa<sup>600</sup> films at: 10 μm scale (left); 1 μm scale (right).**

As far as the films from TOB<sup>90</sup> sample are concerned, the surface exhibited aggregates the size of which was clearly smaller, i.e. about 100 nm, than those of films prepared from particles obtained in acidic condition (Figure IV-15). The mean roughness (Ra) is then 40 nm at 1  $\mu$ m scale.

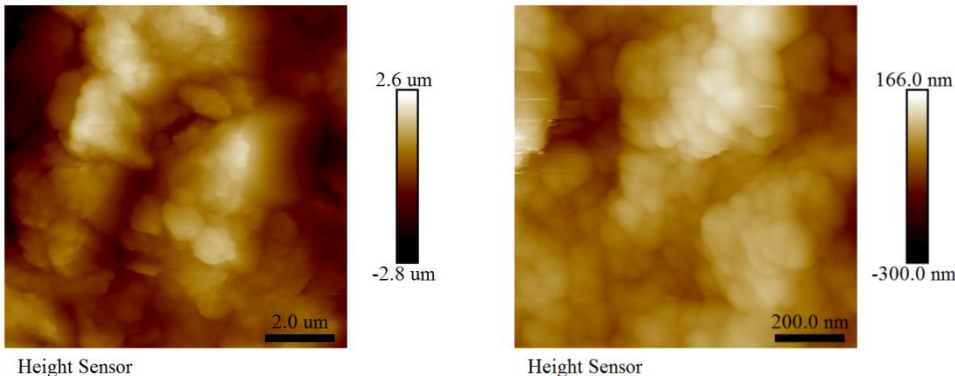


Figure IV-15: Height AFM tapping images of TOB<sup>90</sup> at: 10  $\mu$ m scale (left); 1  $\mu$ m scale (right).

With the TOB<sup>300</sup> nanoparticles, the size of the aggregates slightly grew to 180 nm whereas the mean roughness (Ra) was lower, i.e. 29 nm at 1  $\mu$ m scale (Figure IV-16).

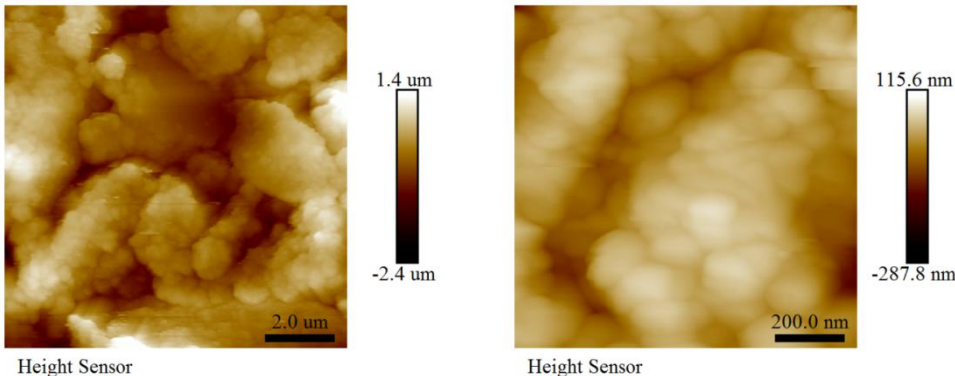


Figure IV-16: Height AFM tapping images of TOB<sup>300</sup> at: 10  $\mu$ m scale (left); 1  $\mu$ m scale (right).

Finally, the films processed from TOB<sup>600</sup> showed the higher roughness (Ra), i.e. 71.7 nm at 1  $\mu$ m scale, the largest particle aggregates, with a size estimated to be around 200 nm (Figure IV-17).

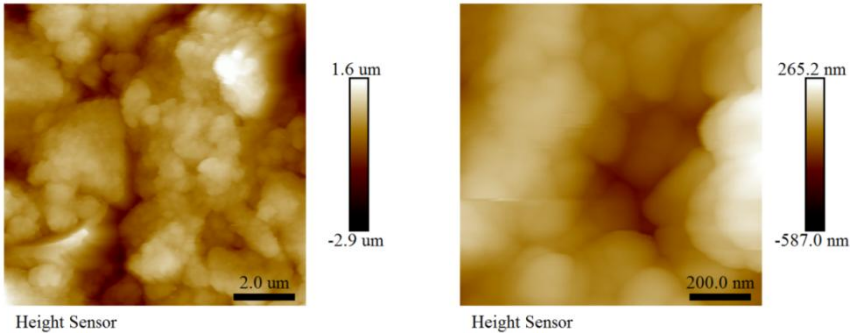


Figure IV-17: Height AFM tapping images of TOB<sup>600</sup> at: 10  $\mu$ m scale (left); 1  $\mu$ m scale (right).



In summary, a granny surface topography observed at 1  $\mu\text{m}$  scale was found for each film regardless the preparation conditions (pH, temperature of the thermal post-treatment) of  $\text{SnO}_2$  nanoparticles. The size of the nano-objects detected by AFM, i.e. 180-200 nm for most films, did not correspond to the size of the nanoparticle constituting the films but to this of aggregates. It can be therefore concluded that, in this study, AFM did not allow to characterize the actual size of the individual nanoparticles. Moreover, these aggregated nanoparticles lead to the thick (more than 1  $\mu\text{m}$ )  $\text{SnO}_2$  films in each case which could be attributed to the drop coating manipulation. On the other hand, the AFM images of  $\text{TOb}^{90}$ ,  $\text{TOb}^{300}$  and  $\text{TOb}^{600}$  at 10  $\mu\text{m}$  scale show different surface features compared to the other  $\text{SnO}_2$  samples prepared in acidic conditions. This suggests that the surface features may be related to the preparation conditions without acid treatment which leads to the presence of a large amount of  $\text{K}^+$  cations. Finally, all films showed a rather larger mean roughness, comprised between 22 and 70 nm, which offers an important surface at the solid-gas interface. This feature should therefore be favorable for the use of these films in gas sensing applications.

### IV.3.3 Surface morphology: SEM studies

Like AFM images, SEM images reveal the surface morphology evolution of the  $\text{SnO}_2$  films prepared from particles synthesized under acidic conditions and thermally post-treated at different temperatures; i.e. 90  $^\circ\text{C}$ , 300  $^\circ\text{C}$  and 600  $^\circ\text{C}$  (Figure IV-18 to IV-20). The images were recorded at magnifications of 200x, 2000x and 10000x.

At low magnification of 200x, the films prepared from  $\text{TOa}_{\text{uncalcined}}$  and  $\text{TOa}^{90}$  samples both exhibited branched and irregular cracks. This could be attributed to the preparation procedure of  $\text{SnO}_2$  films and to residual water remained in the nanoparticulate  $\text{SnO}_2$  sample. By contrast, the films processed from particles calcined at higher temperature,  $\text{TOa}^{300}$  and  $\text{TOa}^{600}$ , showed the best smooth and homogeneous surface layers without obvious cracks.

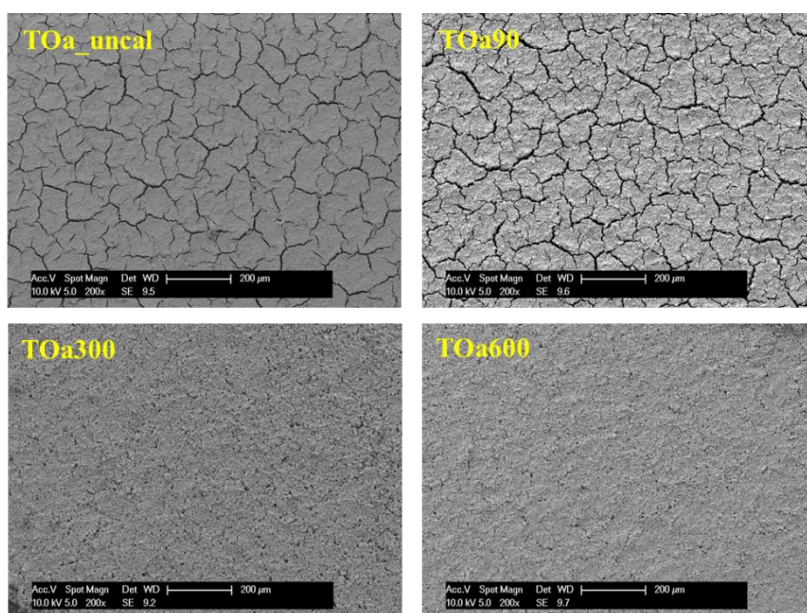


**Figure IV-18: SEM images of  $\text{SnO}_2$  films at magnification of 200 prepared from:  $\text{TOa}_{\text{uncalcined}}$  (upper-left);  $\text{TOa}^{90}$  (upper-right);  $\text{TOa}^{300}$  (lower-left);  $\text{TOa}^{600}$  (lower-right).**

The large crack lines for films prepared from TOa\_uncalcined and TOa<sup>90</sup> samples are more clearly observed at 2000x of magnification (Figure IV-19). These images also confirmed that films including TOa<sup>300</sup> and TOa<sup>600</sup> nanoparticles presented a more compact morphology without significant cracks on the surfaces.

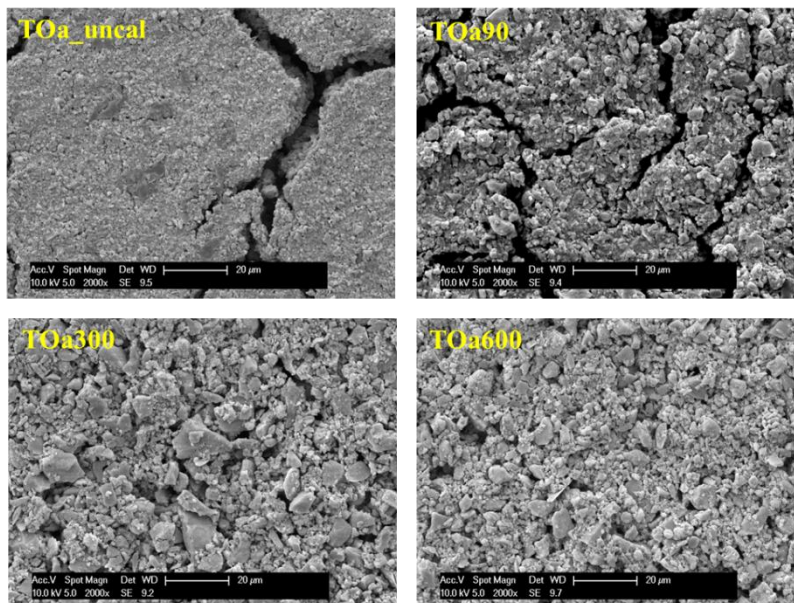


**Figure IV-19: SEM images of SnO<sub>2</sub> films at magnification of 2000 prepared from: TOa\_uncalcined (upper-left); TOa<sup>90</sup> (upper-right); TOa<sup>300</sup> (lower-left); TOa<sup>600</sup> (lower-right).**

Finally, micrographs recorded at 10000x of magnification indicated that the TOa\_uncalcined film contained more sticky aggregates and was composed of rather small size aggregates. By contrast, films made of TOa<sup>300</sup> and TOa<sup>600</sup> samples were made of larger and irregular aggregates (Figure IV-20). The evolution of the surface morphology therefore suggests that the aggregate sizes grew as the calcination temperature of the nanoparticles was increased.

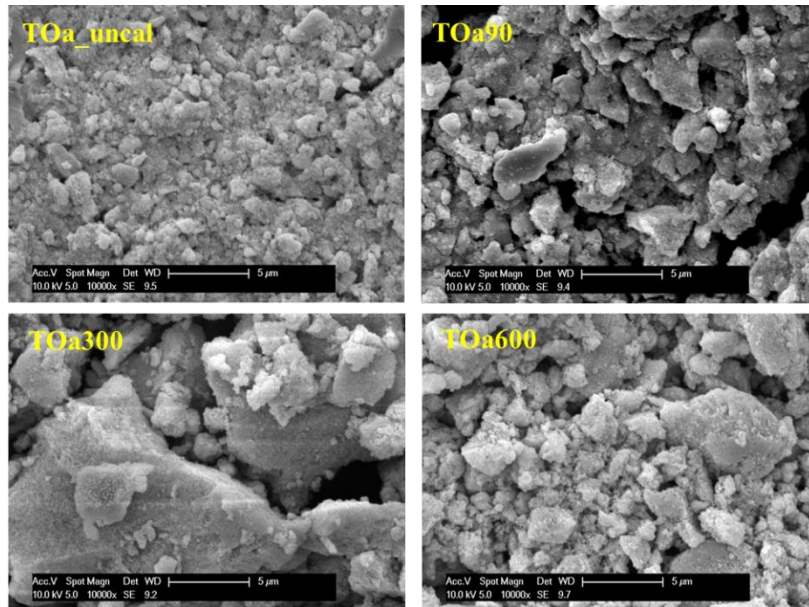


**Figure IV-20: SEM images of SnO<sub>2</sub> films at magnification of 10000 prepared from: TOa\_uncalcined (upper-left); TOa<sup>90</sup> (upper-right); TOa<sup>300</sup> (lower-left); TOa<sup>600</sup> (lower-right).**

In summary, particles calcined at a temperature higher than 300 °C yielded crack-free and more homogeneous films composed of large aggregates. These results are consistent with the PXRD studies indicating that the calcination process slightly increased the SnO<sub>2</sub> particle size and also help for stabilizing the surface condition of SnO<sub>2</sub> films.

#### **IV.4 Conclusion**

Tin dioxide (SnO<sub>2</sub>) nanoparticles were straightforwardly synthesized using an easily scaled-up liquid route that involves the hydrothermal treatment, either under acidic or basic conditions, of a commercial tin dioxide particle suspension including potassium counter-ions. After further thermal post-treatment, the nanomaterials have been thoroughly characterized by Fourier transform infrared (FTIR) and Raman spectroscopy, powder X-ray diffraction (PXRD), transmission electron microscopy (TEM), X-ray photoelectron spectroscopy (XPS) and nitrogen sorption porosimetry. Varying pH conditions and temperature of the thermal treatment provided cassiterite SnO<sub>2</sub> nanoparticles with crystallite sizes ranging from 7.3 to 9.7 nm and Brunauer-Emmett-Teller surface areas ranging from 61 to 106 m<sup>2</sup>.g<sup>-1</sup>, acidic conditions favouring potassium cation removal. Moreover, the drop-coating method allowed for preparing crack-free and rough films from the nanoparticles obtained, namely from nanoparticles prepared under acidic conditions and calcined in air.

Moreover, this study suggests that acidic conditions favored the elimination of K<sup>+</sup> ions decrease which gave slightly larger crystallite/particle sizes. On the other hand, SnO<sub>2</sub> nanoparticles prepared in basic condition includes a significant amount of K<sup>+</sup> ions which hampers particle growth during the calcinations step leading to higher surface area and to smaller crystalline/particle sizes. Thus, the as-determined morphological (XRD, TEM), electronic (E<sub>vf</sub> and L<sub>D</sub> from XPS data) and textural (specific surface area (S<sub>BET</sub>)) properties

clearly suggest the basic medium as the most effective synthesis condition to achieve a microstructure suitable for gas sensing. In particular, the material treated at low temperature (TOb<sup>90</sup>) features *a priori* the optimal structure and is expected to be the most efficient for gas sensing applications. Nonetheless, the results of gas sensing tests described in chapter VI will reveal an unexpected behavior for the nanoparticles prepared in this study.

## References:

- [1] J. Duan, S. Yang, H. Liu, J. Gong, H. Huang, X. Zhao, R. Zhang, Y. Du, *J. Am. Chem. Soc.* **2005**, *127*, 6180-6181.
- [2] (a) Z. R. Dai, Z. W. Pan, Z. L. Wang, *J. Am. Chem. Soc.* **2002**, *124*, 8673-8680. (b) Z. R. Dai, J. L. Gole, J. D. Stout, Z. L. Wang, *J. Phys. Chem. B* **2002**, *106*, 1274-1279.
- [3] D-F. Zhang, L-D. Sun, J-L. Yin, C-H. Yan, *Adv. Mater.* **2003**, *15*, 1022-1025.
- [4] R. Yogamalar, V. Mahendran, R. Srinivasan, A. Beitollahi, R. P. Kumar, A. C. Bose, A. Vinu, *Chem.-Asian J.* **2010**, *5*, 2379-2385.
- [5] (a) G. Xi, J. Ge, *Inorg. Chem.* **2010**, *49*, 2302-2309. (b) X. Wang, X. Han, S. Xie, Q. Kuang, Y. Jiang, S. Zhang, X. Mu, G. Chen, Z. Xie, L. Zheng, *Chem.-Eur. J.* **2012**, *18*, 2283-2289. (c) K. Sato, Y. Yokoyama, J. C. Valmalette, K. Kuruma, H. Abe, T. Takarada, *Cryst. Growth Des.* **2013**, *13*, 1685-1693.
- [6] C. Nayral, T. Ould-Ely, A. Maisonnat, B. Chaudret, P. Fau, L. Lescouzères, A. Peyre-Lavigne, *Adv. Mater.* **1999**, *11*, 61-63. (b) C. Nayral, E. Viala, P. Fau, F. Senocq, J-C. Jumas, A. Maisonnat, B. Chaudret, *Chem. Eu. J.* **2000**, *6*, 4082-4090. (c) C. Nayral, E. Viala, V. Collière, P. Fau, F. Senocq, A. Maisonnat, B. Chaudret, *Appl. Surf. Sci.* **2000**, *164*, 219-226.
- [7] M. Zheng, G. Li, X. Zhang, S. Huang, Y. Lei, L. Zhang *Chem. Mater.* **2001**, *13*, 3859-3861.
- [8] (a) S. de Monredon, A. Cellot, F. Ribot, C. Sanchez, L. Armelao, L. Gueneau, L. Delattre, *J. Mater. Chem.* **2002**, *12*, 2396-2400. (b) L. Broussous, C. V. Santilli, S. H. Pulcinelli, A.F. Craievich, *J. Phys. Chem. B* **2002**, *106*, 2855-2860. (c) T. Toupance, O. Babot, B. Jousseume, G. Vilaça, *Chem. Mater.* **2003**, *15*, 4691-4697. (d) V. Briois, S. Belin, M. Zucolotto Chalaça, R. H. A. Santos, C.V. Santilli, S. H. Pulcinelli, *Chem. Mater.* **2004**, *16*, 3885-3894.
- [9] (a) N. Pinna, G. Neri, M. Antonietti, M. Niederberger *Angew. Chem. Int. Ed.* **2004**, *43*, 4345-4349. (b) J. Ba, J. Polleux, M. Antonietti, M. Niederberger, *Adv. Mater.* **2005**, *17*, 2509-2512.
- [10] (a) L.-L. Li, W-M. Zhang, Q. Yuan, Z-X. Li, C.-J. Fang, L-D. Sun, L-J. Wan, C-H. Yan, *Cryst. Growth & Des.* **2008**, *8*, 4165-4172. (b) S. Bellayer, L. Viau, Z. Tebby, T. Toupance, J. Le Bideau, A. Vioux, *Dalton Trans.* **2009**, 1307-1313.
- [11] (a) A. Birkel, F. Reuter, D. Koll, S. Frank, R. Branscheid, M. Panthöfer, E. Rentschler, W. Tremel, *CrystEngComm* **2011**, *13*, 2487-2493. (b) L. C. Nehru, C. Sanjeeviraja, *J. Adv. Ceram.*, **2014**, *3*, 171-176.
- [12] G. Pang, S. Chen, Y. Koltypin, A. Zaban, S. Feng, A. Gedanken, *Nano Lett.* **2001**, *12*, 723-726.
- [13] (a) S. Chappel, A. Zaban, *Sol. Energy Mater. Sol. Cells* **2002**, *71*, 141-152. (b) A. N. M. Green, E. Palomares, S. Haque, S.; J. M. Kroon, J. R. Durrant, *J. Phys. Chem. B* **2005**, *109*, 12525-12533.
- [14] L. Cojocar, C. Olivier T. Toupance, E. Sellier, L. Hirsch, *J. Mater. Chem. A* **2013**, *1*,

13789-13799.

- [15] S. Maeda, S. P. Armes, *Chem. Mater.* **1995**, *7*, 171–178
- [16] (a) P. G. Harrison, A. Guest, Tin Oxide Surfaces. Part 17. *J. Chem. Soc. Faraday Trans 1* **1987**, *83*, 3383–3397. (b) P. G. Harrison, N. C. Lloyd, W. Daniell, C. Bailey, W. Azelee, *Chem. Mater.* **1999**, *11*, 896–909.
- [17] M. Ocaña, C. J. Serna, E. Matijevic, *Colloid Polym. Sci.* **1995**, *273*, 681–686.
- [18] R. S. Hiratsuka, S. H. Pulcinelli, C. V. Santilli, *J. Non-Cryst. Solids* **1990**, *121*, 76–83.
- [19] P. Sangeetha, V. Sasirekha, V. Ramakrishnan, *J. Raman Spectrosc.* **2011**, *42*, 1634–1639.
- [20] S. G. Ansari, M. A. Dar, M. S. Dhage, Y. S. Kim, Z. A. Ansari, A. Al-Hajry, H. S. Shin, *Rev. Sci. Instrum.* **2009**, *80*, No. 045112
- [21] S. M. Vock, L. M. Sharygin, Y. S. Bobovich, V. F. Gonchar, E. N. Loguntsev, *J. Appl. Spectrosc.* **1986**, *44*, 636–639.
- [22] J. X. Wang, D. F. Liu, X. Q. Yan, H. J. Yuan, L. J. Ci, Z. P. Zhou, Y. Gao, L. Song, L. F. Liu, W. Y. Zhou, G. Wang, S. S. Xie, *Solid State Commun.* **2004**, *130*, 89–94.
- [23] R. Jenkins, R. L. Snyder, Introduction to X-ray Powder Diffractometry; Winefordner, J. D., Ed.; John Wiley and Sons Inc.: New York, 1996; Chapter 3, pp 89–91.
- [24] T. Toupance, H. Elhamzaoui, B. Jousseau, H. Riague, I. Sadeddin, G. Campet, J. Broetz, *Chem. Mater.* **2006**, *18*, 6364–6372.
- [25] K. S. W. Sing, *Pure Appl. Chem.* **1985**, *57*, 603–619.
- [26] J. F. Moulder, W. F. Stickle, P. E. Sobol, K. D. Bomben, Handbook of X-ray Photoelectron Spectroscopy; Physical Electronics, Inc.: Eden Prairie, 1995.
- [27] L. Renard, O. Babot, H. Saadaoui, H. Fuess, J. Brötz, A. Gurlo, E. Arveux, A. Klein, T. Toupance, *Nanoscale* **2012**, *4*, 6806–6813.
- [28] C. Körber, P. Ágoston, A. Klein, *Sens. Actuators, B* **2009**, *139*, 665–672.
- [29] C. Körber, S. P. Harvey, T. O. Mason, A. Klein, *Surf. Sci.* **2008**, *602*, 3246–3252.
- [30] M. Batzill, U. Diebold, *Prog. Surf. Sci.* **2005**, *79*, 47–154.
- [31] C. Körber, A. Wachau, P. Ágoston, K. Albe, A. Klein, *Phys. Chem. Chem. Phys.* **2011**, *13*, 3223–3226.
- [32] Sze, S. M.; Kwok, K. N. G. Physics of Semiconductor Devices, 3rd ed.; Wiley: Hoboken, NJ, 2007; Chapter 1.
- [33] Z. Tebby, T. Uddin, Y. Nicolas, C. Olivier, T. Toupance, C. Labrugère, L. Hirsch, *ACS Appl. Mater. & Interfaces* **2011**, *3*, 1485–1491.



# Chapter V Syntheses and characterization studies of tin-based hybrid materials

As mentioned in chapter II, the second objective of this work was the preparation and the characterization of organotin oxide films to be tested in gas sensors. Compared to previously reported studies [1], this work aims at establishing faster synthetic routes towards the targeted organotin oxide films by sol-gel process from hydrolysable organotins synthesized only in few steps from commercial precursors. In this context, four functional trialkynylorganotins including alkyl, benzyl or thiophenylalkyl units were straightforwardly synthesized through a selective alkylation process of tetraphenylalkynyltin using suitable Grignard reagents. The results enlighten new experimental conditions for preparing trialkynylorganotin compounds from tetraalkynyltins in the presence of suitable Grignard reagents. Then, oxohydroxo organotin-based powders or thin films were processed by the sol-gel method from four functional trialkynylorganotins including alkyl, benzyl or alkylthiophene units. Composition and thermal properties of bulk materials were characterized by FTIR and TG analyses while composition and surface morphologies of oxohydroxoorganotin-based thin films were highlighted by a combination of AFM, SEM, EDX and XPS studies. Furthermore, optical properties and band gap energies were determined by UV-visible spectroscopy and discussed as a function of the organic functionality nature.

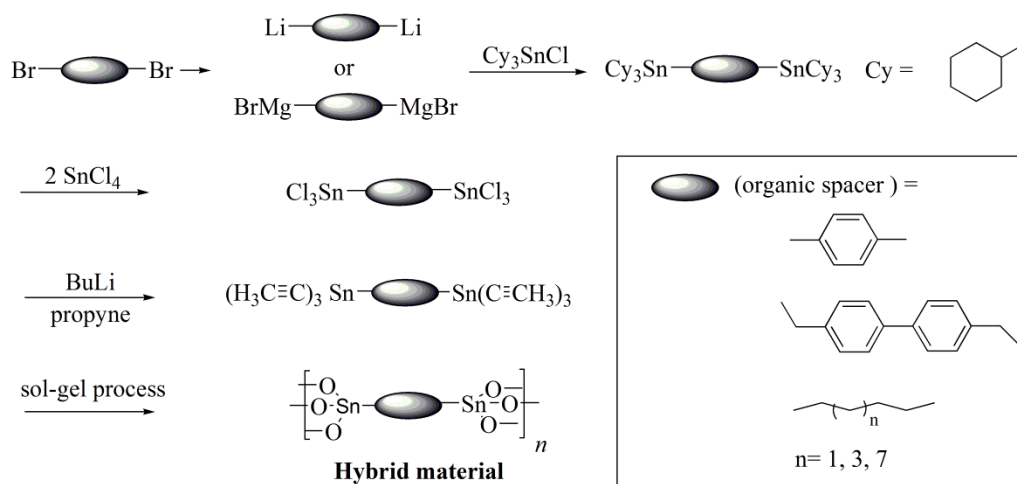
## V.1 Design and synthesis of organotin-based hybrid material precursors

### V.1.1 Choice of the precursors and of their synthetic pathway

Inorganic sol-gel materials can be processed by employing nearly all metals [2]. By contrast, class II hybrid materials in which organic and inorganic components are linked through strong covalent bonds are mainly obtained from organosilicon derivatives, which include hydrolytically stable silicon-carbon bonds [3]. Besides silicon, tin also leads to metal-carbon bonds stable under the experimental conditions of the sol-gel process. Nonetheless, the chemistry of tin-based hybrid materials is not as developed as the chemistry of silicon-based hybrid materials due to less easily accessible precursors. By analogy with organosilane chemistry, tin precursors for class II hybrid materials should be functional organotin trialkoxides. However, the synthesis of this kind of derivatives is tricky and they are difficult to purify and to handle owing to stability issues [4]. In this context, the chemistry of trialkynylorganotins was developed in our group. The alkynyl group was selected due to the following reasons: (1) tin-alkynyl bond is easily cleaved by water, leading to the inorganic network of hybrid materials; (2) the alkynyl group is easy to introduce onto tin through a lithium alkynide; (3) trialkynylorganotins are often solid compounds relatively uncomplicated to purify. In addition, functional trialkynylorganotins are stable enough to be handled in air

for a short period of time, and can be chromatographed over  $\text{MgSO}_4$ .

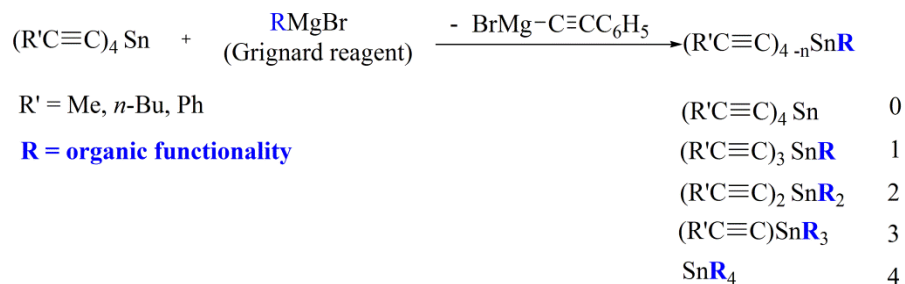
Since their first report at the beginning of the 1960s [5], different synthetic routes have been developed to fabricate alkynylstannanes. Thus, the high acidity of the acetylenic proton renders the alkynylstannanes readily accessible either directly from the terminal alkynes or through their metal derivatives [6]. Along with the reaction of terminal alkyne with distannoxanes in the presence of drying salts [7] or tin chlorides in the presence of  $\text{CuI}/\text{Et}_3\text{N}$  [8], the conventional reactions between tin halides and alkynyl lithium or alkynyl Grignard reagents are the more versatile and straightforward methods to obtain alkynyltins [9]. Thus, this strategy was exploited by Jousseau *et al.* to synthesize functional trialkynylorganotin which provided oxo-hydroxo organotin clusters or polymers after hydrolysis-condensation [10]. This strategy was extended to the preparation of hydrolyzable distannylated derivatives for sol-gel and material chemistry [11]. Thus, the synthesis of alkylene-, arylylene-, and benzylene-bridged ditin hexaalkynides was successfully achieved (scheme V-1) [11a], which led to self-assembled tin-based hybrid materials under certain hydrolytic conditions [12].



**Scheme V-1: Previous study of synthetic route toward bridged ditins derivatives from sol-gel precursors.**

This synthetic route involves four steps from commercial products. At first, tricyclohexyltin chloride was obtained from the reaction between the chlorotrimethylsilane and the tricyclohexyltin hydroxide. Then, a nucleophilic substitution reaction between tricyclohexyltin chloride and a dilithium or di-Grignard reagent of  $\alpha,\omega$ -dibromohalides yielded the hexacyclohexyl derivatives. The electrophilic cleavage of the latter provided the hexachloride compounds which were converted into the hexaalkynyl derivatives by reaction with the suitable alkynyllithium. This synthetic scheme is therefore rather long for application purposes. That is the reason why we have decided to use the transmetallation reaction of tetraalkynyltins by Grignard reagents to give unsymmetrical substituted trialkynylorganotin (Scheme V-2).





**Scheme V-2: Selective alkylation of tetraalkynyltins with Grignard reagents (0: tetrakisalkynyltin; 1: trialkynylorganotin; 2:dialkynyldiorganotin; 3: alkynyltriorganotin; 4: organotin).**

It has been indeed shown that when methyl- or butylmagnesium bromide was reacted with tetraphenylethynyltin, a smooth transmetallation takes place and leads selectively to the corresponding alkynylorganotin derivative in good yields [13]. Moreover, the course of the reaction can be easily followed by <sup>119</sup>Sn NMR as typical chemical shifts for tetrakisalkynyltins, trialkynylorganotins, dialkynyldiorganotins, alkynyltriorganotins and tetraorganotins (Table V-1). [14]

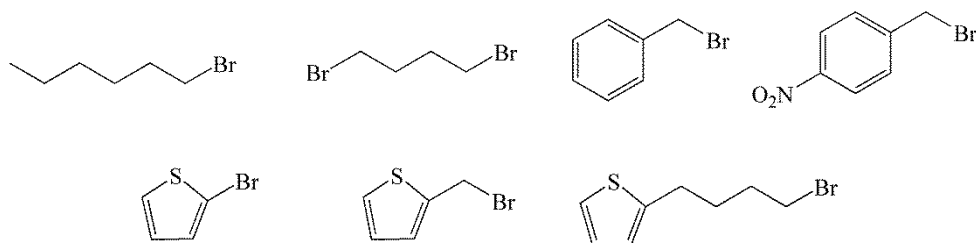
Compound	0	1	2	3	4
<sup>119</sup> Sn (ppm)	- 335	- 240 to 250	- 150 to 180	- 60 to 80	Various values

**Table V-1: <sup>119</sup>Sn-NMR chemical shifts for alkynylorganotin derivatives (0: tetrakisalkynyltin; 1: trialkynylorganotin; 2:dialkynyldiorganotin; 3: alkynyltriorganotin; 4: tetraorganotin).**

As a consequence, this method has been investigated to prepare functional trialkynylorganotins including alkyl, benzyl, thiophenyl or thiophenylalkyl units, the <sup>119</sup>Sn NMR chemical shifts being expected to be comprised between -240 to -250 ppm.

### V.1.2 Selective alkylation to functional trialkynylorganotins

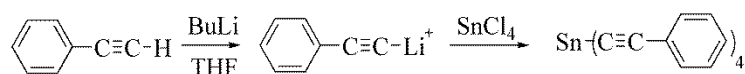
The good reaction selectivity to obtain the functional trialkynylorganotins, defined as no presence of a disubstituted compound or their derivatives, depends on the nature of the alkynyl group linked to the tin atom. The best selectivity (100%) was obtained with the phenylethynyl group rather than with the propynyl or hexynyl groups (85-90%) [13]. However, the appropriate working conditions to reach high selectivity are strongly dependent on the property of each applied Grignard reagent resulting in the most challenging part of this synthesis. To introduce various organic functionalities in the targeted organotin oxide materials, we aimed at making this reaction with tetraphenylalkynyltin and different organomagnesium bromides (Scheme V-3).



**Scheme V-3: Chemical structure of the various bromide derivatives employed.**

### V.1.3 Synthesis of tetraphenylalkynyltin

Tetraphenylethynyltin was first synthesized according to a previously reported procedure (Scheme V-4) [14]. Deprotonation of phenylacetylene by butyllithium yielded phenylethynyl lithium. Then the nucleophilic substitution reaction between tin tetrachloride and an excess of phenylethynyl lithium gave tetraphenylethynyltin in high yields (81%) after purification. The obtained product showed a single resonance located at - 335 ppm in  $^{119}\text{Sn}$  NMR spectroscopy which is a characteristic of a tetraalkynylorganotin.

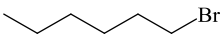
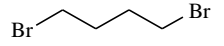
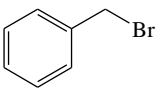
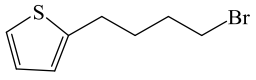
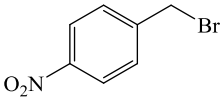
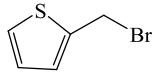
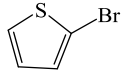


**Scheme V-4: Direct synthetic route toward tetraphenylalkynyltin.**

### V.1.4 Preparation of functional Grignard reagents for selective alkylation

Both quality and yield of the Grignard reagent are the key factors ruling the selective alkylation process of tetraphenylethynyltin. The whole reaction has to be carried out under strict anhydrous conditions, i.e. under a nitrogen gas flow and with carefully dried glass vessels, to obtain high quality of Grignard reagent. The relative amount of activated magnesium and bromide derivative both have decisive impacts on the Grignard reagent's quality and yield which governs the efficiency of the second step. After optimization, the best molar ratio between magnesium and organic bromide was found to be 1.5-2 including a magnesium amount comprised between 1.5 and 3.0 g. Furthermore, as the control of the stoichiometry is essential to favor the monosubstitution of the tetraalkynylstannane, the Grignard reagent has to be titrated precisely. In this aim, the amount of anhydrous diethyl ether was fixed to about 50 mL in total to have a sufficient amount of solution for performing the second step. After considering different titration method, the one involving benzyl alcohol as titrant ( $1 \text{ mol. L}^{-1}$ ) and 1,10-phenanthroline as color indicator was selected. Optimal titration conditions include drying of a two-necked flask under a constant  $\text{N}_2$  gas flow and holding the testing Grignard solution with the color indicator for 30 minutes at room temperature before adding the titrant. This waiting time is necessary in order to stabilize the whole testing Grignard solution and to obtain the accurate yield of Grignard reagent. It turned out that a minimum yield of 50% for the Grignard reagent was required to obtain high

selectivity during the second step. Different bromide derivatives were thus tested (Table V-2). It was found that the bromide compounds where at least one CH<sub>2</sub> was linked to the bromine atom were the more suitable choice to favor the selective alkylation of tetraphenylethynylstannane in order to get pure trialkynylorganotin. By contrast, 4-nitrobenzylmagnesium bromide, 2-thiophenylmethylmagnesium bromide and 2-thiophenylmagnesium bromide cannot be prepared in good yields due to solubility or stability issues.

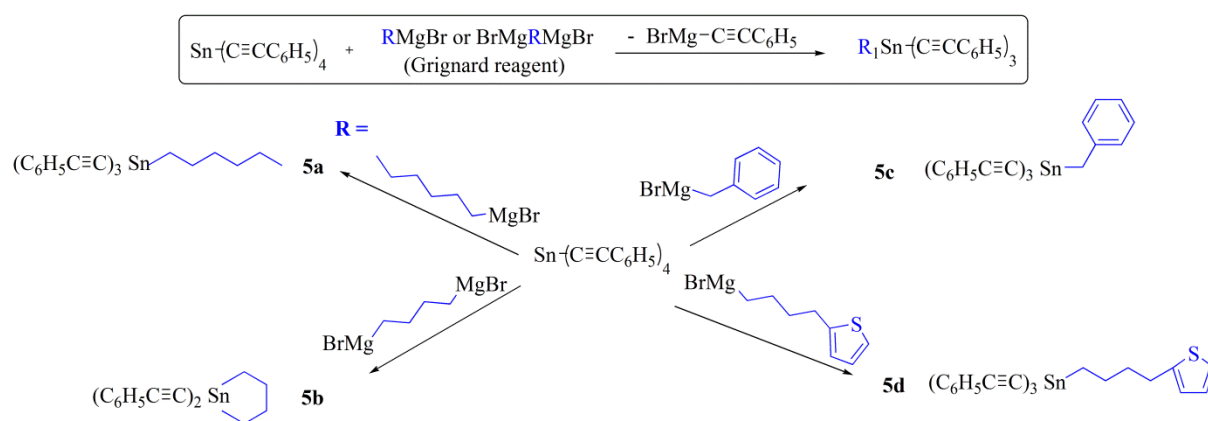
Entry	R'	R-Br	Toluene:Ether ratio (mL)	Temperature conditions (Grignard:Addition:Holding)
1	C <sub>6</sub> H <sub>5</sub>		30:10	55°C for 2 h -78°C for 30 min 40°C for 17 h
2	C <sub>6</sub> H <sub>5</sub>		40:20	55°C for 1.5 h -78°C for 30 min 50°C overnight
3	C <sub>6</sub> H <sub>5</sub>		25:10	55°C for 2 h -78°C for 30 min 40°C for 17 h
4	C <sub>6</sub> H <sub>5</sub>		43.5:19	55°C for 2 h -78°C for 30 min 40°C for 18 h
5	C <sub>6</sub> H <sub>5</sub>		-	Very low solubility in ether
6	C <sub>6</sub> H <sub>5</sub>		-	Unstable bromide and difficult to preserve
7	C <sub>6</sub> H <sub>5</sub>		30:10	Titration cannot be performed and mixture of products

**Table V-2: Optimized experimental conditions for the preparation of Grignard reagents and its further coupling with tetraphenylethynyltin.**

### V.1.5 Optimal experimental parameters for selective alkylation

The preparation of functional trialkynylorganotin using a Grignard reagent and tetraphenylethynyltin is trickier than the reaction itself. B. Jousseau *et al.* in the group have previously studied this reaction but experimental parameters were still remaining to be

optimized for making pure trialkynylorganotin. Among the many different experimental parameters which have to be taken into account before and during the synthesis, the main one is the reaction temperature chosen before and after adding the Grignard reagent. It was the trickiest part of this synthetic work since many trials have failed. Finally, after playing with varying reacting temperature and duration period, the best working temperature conditions were found. Thus, the reaction medium should be kept to  $-78\text{ }^{\circ}\text{C}$  when adding the Grignard reagent to the tetraphenylethynyltin solution and held until the temperature goes back to room temperature naturally. Then, the whole solution should be heated at  $40\text{ }^{\circ}\text{C}$  overnight. A temperature of  $40\text{ }^{\circ}\text{C}$  was found to be an optimal temperature for synthesizing the trialkynylorganotins since three functional alkynylorganotins have been effectively obtained at this temperature. Another important factor is the choice of anhydrous solvents for making the tetraphenylethynyltin solution. The best anhydrous solvent for the tetraphenylethynyltin solution was found to be a mixture of toluene and diethyl ether in a 2:1 ratio. Luckily, this experiment has successfully overcome many challenges from countless trials to find the best working condition and four of functional trialkynylorganotins have been obtained as shown in scheme V-5.



**Scheme V-5: The synthesis of four functional trialkynylorganotins.**

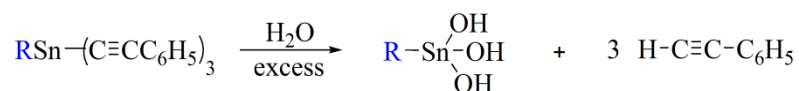
The  $^1\text{H-NMR}$ ,  $^{119}\text{Sn-NMR}$  spectroscopy and mass spectrometry data of these phenylethynyl- organotins are detailed in Annex. In particular, compounds **5a**, **5c** and **5d** led to a single resonance in  $^{119}\text{Sn}$  NMR located at  $-242$ ,  $-252$  and  $-242$  ppm which is typical of trialkynylorganotins [15]. Furthermore, a single peak at  $-103$  ppm was detected in the  $^{119}\text{Sn}$  NMR spectrum of **5b** which is consistent with the formation of a dialkynyldiorganotin derivative.

In summary, the best experimental parameters have been found for the very first time for highly selective alkylation reaction without obtaining dialkynyldiorganotin or alkynyltriorganotin derivatives at the same time.

## V.2 Preparation of organotin-based hybrid materials

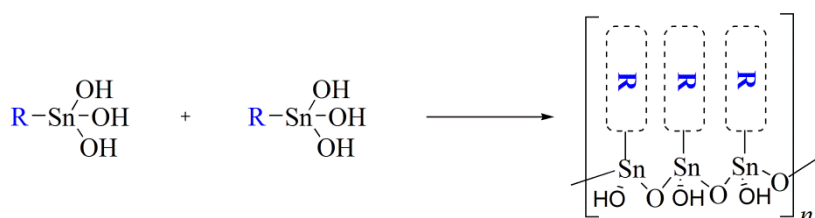
## V.2.1 Hydrolysis-condensation of triphenylethynylorganotins

The previous phenylethynylorganotin derivatives were then hydrolyzed in acidic conditions as reported in the literature [16]. The hydrolysis process can be represented as depicted in scheme V-6 for trialkynylorganotins. Protonation of the alkynyl group favors the nucleophilic attack of the water molecule at the tin center yielding the formation of hydroxyl group after elimination of alkyne and regeneration of the acidic catalyst.



**Scheme V-6: Hydrolysis of trialkynylorganotins.**

Then, the hydroxyl groups react with another alkynyltin or hydroxytin compound to yield Sn-O-Sn linkage with the concomitant elimination of alkyne or water molecules through oxolation-like mechanisms. Further condensation then provides oxohydroxoorganotin species (Scheme V-7).



**Scheme V-7: Polycondensation to oxohydroxoorganotin.**

## V.2.2 Preparation of oxohydroxoorganotin films and powders

Fabrication of oxohydroxoorganotin thin films required three main steps: (a) substrate cleaning process: this process guarantees a good adhesion of the organooxotin layer onto the substrate without any contamination; (b) sol preparation: this step corresponds to hydrolysis-condensation of the trialkynylorganotin in the presence of water and an acidic catalyst; (c) film fabrication and thermal treatment: this step allows for the film formation through further condensation of the oxohydroxoorganotin species activated by the drying process.

### (a) Substrate cleaning process

The substrates for film characterizations were either microscopy glass slides or 100 silicon wafers. The substrates were cleaned by deionized water to remove the dust. Then, the glass slides/wafers were put into an acetone bath and sonicated for 15 mins. Finally, the substrates were dried with nitrogen gas and washed with isopropanol.

### (b) Sol preparation

0.16 mmol of alkynylorganotin compound was dissolved in 1 mL THF and sonicated for 5 minutes. Then, 0.23 g of water containing 1vol.% of 1N HCl was added to the previous solution. The resulting mixture was then sonicated for 10 minutes to give a yellow transparent solution.

(c) Film fabrication

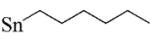
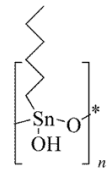
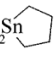
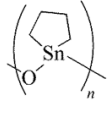
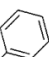
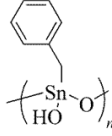
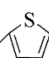
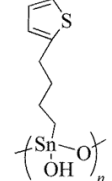
1 drop (0.04 g) of the sol prepared in step (b) was drop-casted at the center of the substrates and the resulting layer was dried in the air for 15 minutes. Further heating at 140 °C for 2 hours in the air yielded the expected hybrid organotin films.

Fabrication of hybrid powders for FTIR and TGA characterizations were also performed from the sol described in step (b). This sol was dried in an oven at 140 °C for 2 hours in air and cooled to room temperature naturally.

### **V.3 Characterization of organotin-based hybrid materials**

#### **V.3.1 FTIR spectroscopy**

One of the main advantages of alkynylorganotins relies on the fact that their reaction with hydroxylated species can be readily monitored by FTIR spectroscopy and the leaving group is released as a gas or liquid [16]. Thus, hydrolysis-condensation processes of trialkynylorganotins led to hybrid tin oxides as summarized in table V-3. They were then characterized by FTIR spectra in order to confirm the formation of oxohydroxoorganotin structures (Figure V-1).

trialkynylorganotins	hydrolysis-condensation	oxohydroxoorganotins
$(C_6H_5C\equiv C)_3Sn$  <b>5a</b>	<div style="display: flex; justify-content: space-around; align-items: center;"> <div style="text-align: center;"> <p>hydrolysis</p> <p><math>H_2O/H^+</math></p> <p>THF</p> </div> <div style="text-align: center;"> <p>condensation</p> <p>coating</p> <p>thermal treatment</p> </div> </div>	 <b>OXT5a</b>
$(C_6H_5C\equiv C)_2Sn$  <b>5b</b>		 <b>OXT5b</b>
$(C_6H_5C\equiv C)_3Sn$  <b>5c</b>		 <b>OXT5c</b>
$(C_6H_5C\equiv C)_3Sn$  <b>5d</b>		 <b>OXT5d</b>

**Table V-3: Hydrolysis-condensation process of trialkynylorganotins (5a, 5b, 5c and 5d) led to oxohydroxoorganotins (OXT5a, OXT5b, OXT5c and OXT5d).**

First of all, regardless of the precursor nature, the disappearance of the stretching vibration band of the triple bond  $\nu(C\equiv C)$ , located around  $2140\text{ cm}^{-1}$ , revealed that the three phenylethynyl groups of each precursor have been entirely substituted after the drying step along with the complete removal of phenylacetylene. In addition, the strong broad absorption band, ranging from  $3600$  to  $2500\text{ cm}^{-1}$  with a maximum around  $3360\text{ cm}^{-1}$ , which appeared after hydrolysis can be attributed to the stretching vibration band  $\nu(O-H)$  of hydroxyl moieties linked to tin or of adsorbed water. This finding confirms that phenylethynyl groups were completely replaced by hydroxyl groups during the hydrolysis process. Moreover, broad bands located between  $700$  and  $500\text{ cm}^{-1}$  appeared below sharp resonances stemming from the organic groups that can be assigned to the Sn-O-Sn and Sn-O stretching vibrations which indicate the formation of Sn-O-Sn linkages [17].

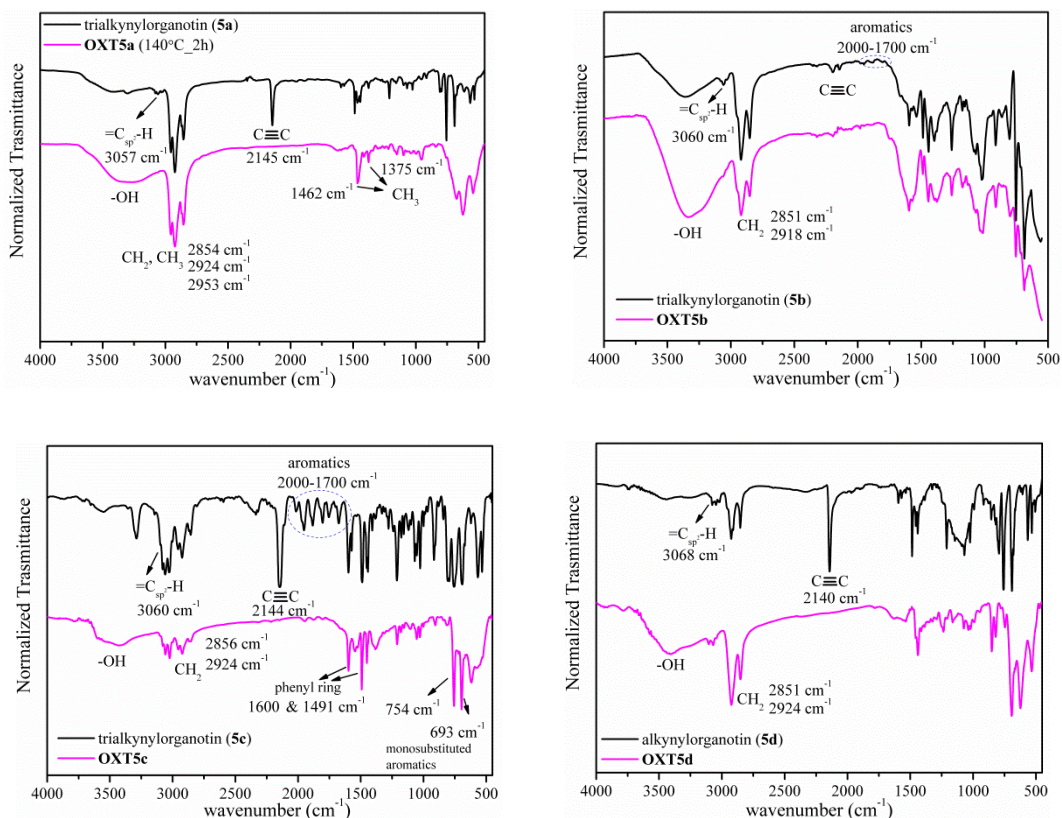


**Figure V-1: FTIR transmission spectra of trialkynylorganotins 5a, 5b, 5c and 5d before and after hydrolysis.**

In addition, FTIR spectroscopy proved that the organic functions are still present in the hybrid materials. Thus, all hybrid xerosols (**OXT5a**, **OXT5b**, **OXT5c** and **OXT5d**) showed resonances at  $2854$  and  $2924\text{ cm}^{-1}$  (for **OXT5a**),  $2851$  and  $2918\text{ cm}^{-1}$  (for **OXT5b**),  $2856$  and  $2924\text{ cm}^{-1}$  (for **OXT5c**) and  $2851$  and  $2924\text{ cm}^{-1}$  (for **OXT5d**) which can be assigned to the symmetric and asymmetric  $\text{CH}_2$  stretching vibration modes. The deformation band of methylene groups was also observed at  $1460\text{ cm}^{-1}$  in each sample. For **OXT5a**, additional features were detected at  $2953$  and  $1375\text{ cm}^{-1}$  which can be attributed respectively to the stretching and the deformation mode of the methyl group. Furthermore, the stretching vibration mode of  $\text{C}_{\text{ar}}\text{-H}$  bonds ( $\nu(\text{C}_{\text{ar}}\text{-H})$ ) were detected in the  $3020\text{-}3080\text{ cm}^{-1}$  wavenumber range for **OXT5c** and **OXT5d** confirming the presence of benzyl and thiophenyl units. In addition, the presence of phenyl ring in **OXT5c** was assessed by the two strong resonances at  $693$  and  $754\text{ cm}^{-1}$  assigned to the deformation vibration mode of  $\text{C}_{\text{ar}}\text{-H}$  bond, the position of which is characteristic of monosubstituted benzene rings. As a consequence, regardless of the organic moiety nature, these FTIR spectroscopy data are consistent with the formation of oxo-hydroxy organotin species since the organic functionalities appeared to be not damaged after the hydrolysis and condensation process.

### V.3.2 Thermogravimetric studies

As thermal activation is usually performed to evaluate gas sensing properties of materials, it was crucial to determine the thermal stability of the different hybrid powders. TG-DTG



curves of oxohydroxoorganotin **OXT5a**, **OXT5b**, **OXT5c** and **OXT5d** materials recorded between 25 and 600 °C under an air flow are shown in Figure V-2. Although the tin-carbon bond (Sn-C) is weaker than the C-C or Si-C bond, it is relatively non-polar and is, therefore, stable in the presence of water, atmosphere O<sub>2</sub> and at temperature up to 200 °C. This was experimentally checked thanks to these TGA studies. Indeed, the TGA curves of the four materials revealed that they were thermally stable up to 200 °C under an air flow. It must be also noted that each hybrid material (**OXT5a**, **OXT5b**, **OXT5c** and **OXT5d**) showed a slight mass loss (0.46-1.68 %) around 140 °C which was ascribed to the desorption of the physisorbed water. Moreover, the pyrolytic process occurred in two main steps at 278 and 387 °C for **OXT5a**, 247 and 489 °C for **OXT5b**, 297 and 517 °C for **OXT5c** and, 330 °C for **OXT5d**. In the case of **OXT5a**, the total mass loss was exploited to determine a tentative chemical formula for this hybrid material assuming a complete conversion into SnO<sub>2</sub> after pyrolysis at 600°C in air. Thus, the mass loss expected for the theoretical molecular formula [(C<sub>6</sub>H<sub>13</sub>)SnO(OH)]<sub>n</sub> · 0.22 H<sub>2</sub>O were 1.65 wt % for water loss and 37.43 % for organic loss which was in close agreement with the experimental values (water loss: 1.68 % and mass loss: 36.96 %). It will be shown in the following paragraph that this tentative chemical formula is rather consistent with further characterization performed by EDX analyses. However, the theoretical calculations of **OXT5b**, **OXT5c** and **OXT5d** were not applicable due to the interference of adsorbed water, multifarious decomposition pathways of organic units, and the uncertainty of final pyrolysis product.

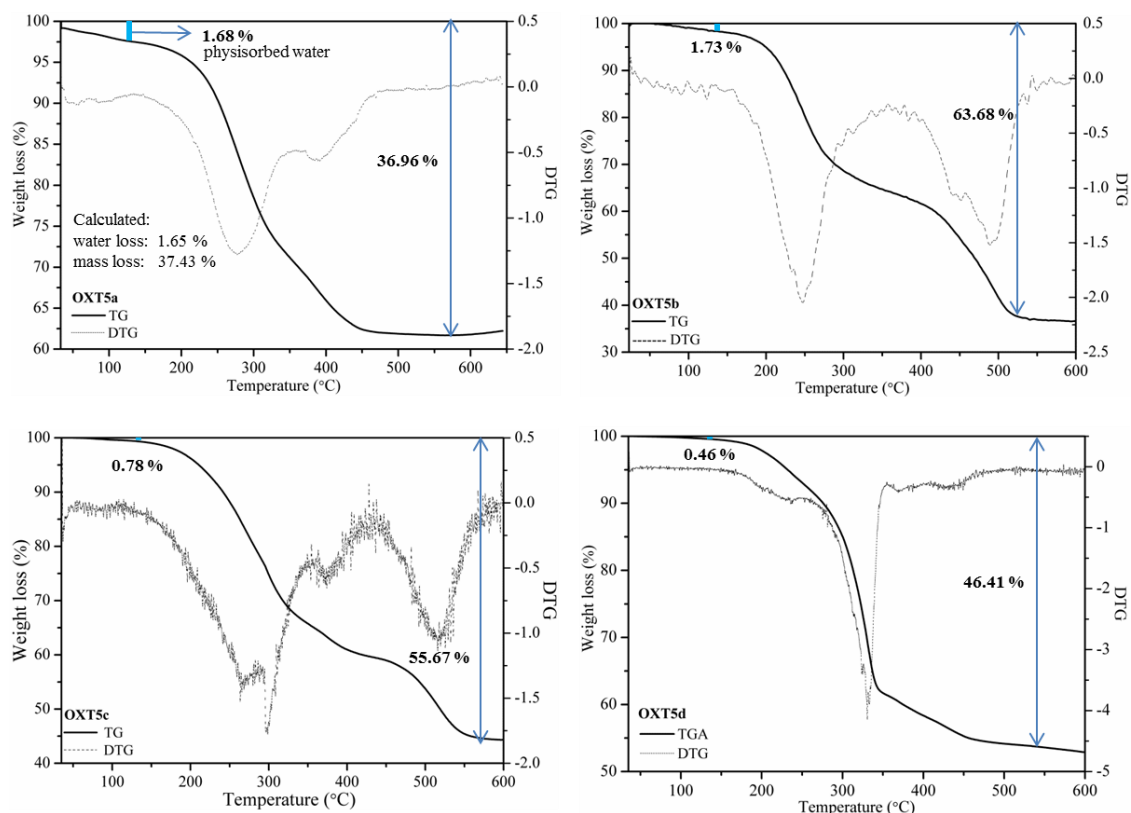


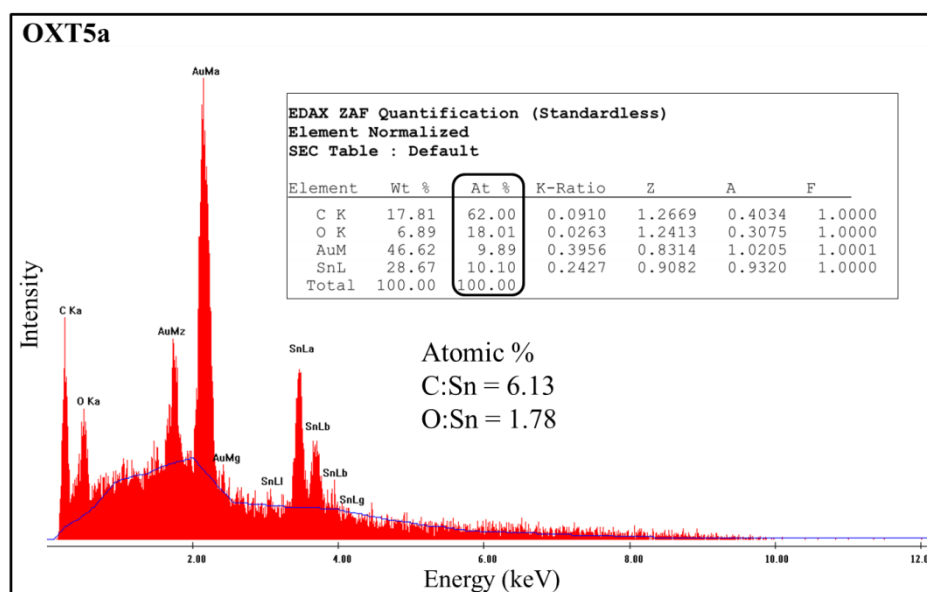
**Figure V-2: TGA-DTG curves of trialkynylorganotins (5a, 5b and 5d in black) and oxohydroxoorganotins (OXT5a, OXT5b, OXT5c and OXT5d in red).**

## V.4 Chemical composition of organotin hybrid materials

Bulk and surface chemical composition and chemical states of oxohydroxoorganotin layers (**OXT5a**, **OXT5c** and **OXT5d**) prepared according to the procedure described in paragraph V.2.2 were investigated by Energy-Dispersive X-ray (EDX) and X-ray Photoelectron Spectroscopy (XPS).

### V.4.1 Bulk chemical composition by EDX studies

EDX spectra and quantification analysis are given in Figure V-3. For **OXT5a**, an experimental C/Sn atomic ratio of 6.13 was determined which is fully consistent with the presence of the  $\text{Sn}(\text{C}_6\text{H}_{13})$  fragment without additional adventitious carbon species. Furthermore, the experimental O/Sn atomic ratio was found to be 1.78 which is rather close to the one expected, i.e. 1.5, for a fully condensed sol-gel network. These data therefore confirm the formation of films made of oxohydroxohexyltin entities and the tentative formula  $(\text{C}_6\text{H}_{13})\text{SnO}_{1.2}(\text{OH})_{0.58}$  may be proposed by postulating only Sn(IV) centers. As a consequence, the hydrolysis and condensation process of tri(phenylethynyl)hexyltin (**5a**) actually occurred and was rather completed leading to oxohydroxyltin compounds without loss of the organic functionality.



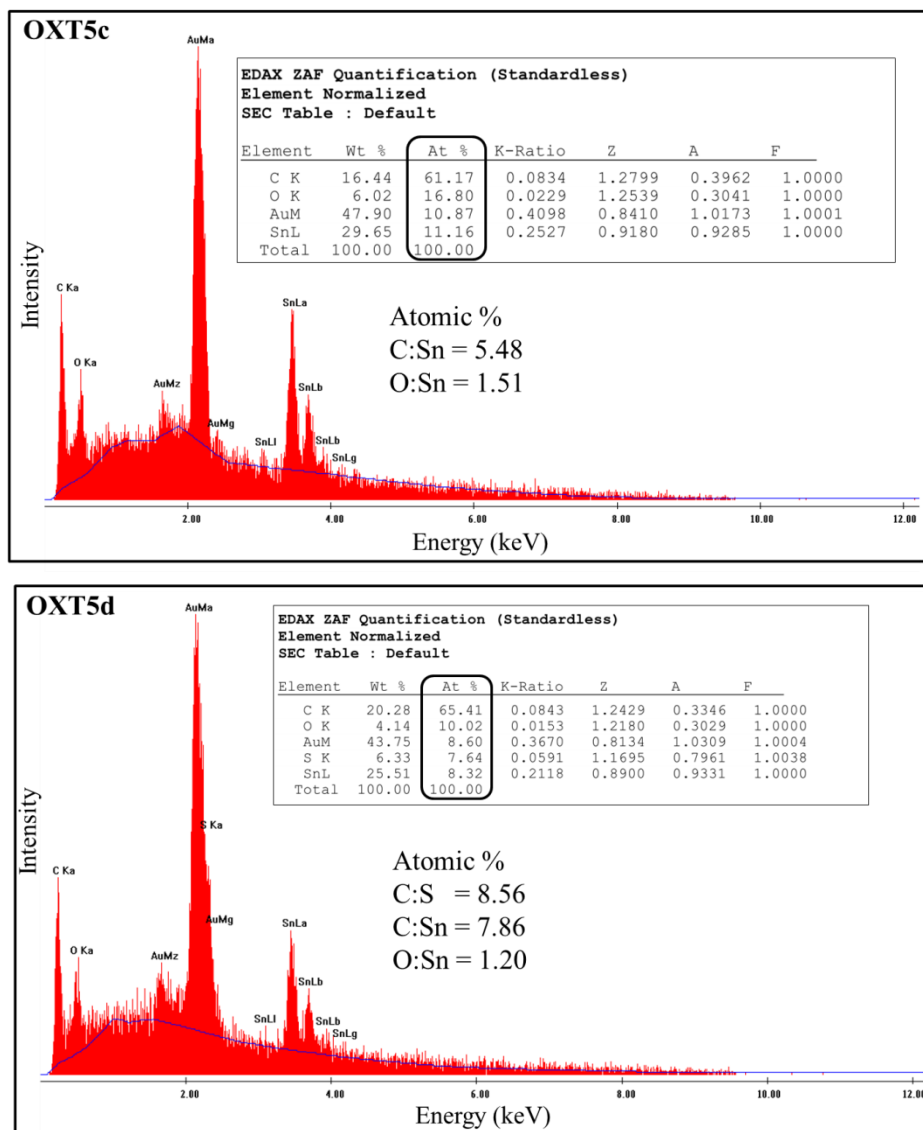


Figure V-3: EDX spectrum and quantification table (inserted) for OXT5a (top), OXT5c (middle) and OXT5d (bottom) films.

A good agreement between the EDX data and the expected atomic ratio was also found in the case of **OXT5d**. Thus, experimental C/Sn and C/S atomic ratios of 7.86 and 8.56 were obtained respectively which fits very well with the presence of the  $\text{Sn}(\text{C}_4\text{H}_8\text{-C}_4\text{H}_3\text{S})$  fragment. On the other hand, the experimental O/Sn atomic ratio was found to be 1.2 which is a little bit lower than that expected, i.e. 1.5, for a fully condensed sol-gel network. These data therefore confirm the formation of films made of oxohydroxothiophenylbutyltin entities by hydrolysis-condensation of precursor **5d** without a loss of the organic functionality during the hydrolysis process.

By contrast, a slight carbon deficiency was found for **OXT5c**. Thus, the experimental C/Sn atomic ratio, i.e. 5.48, was lower than the one expected, i.e. 7, whereas the O/Sn atomic ratio of 1.51 suggests an almost fully condensed network. These data indicate the formation of films containing oxohydroxobenzyltin entities by hydrolysis-condensation of precursor **5c** but with a slight loss of the organic function. This might be due to the higher sensitivity of the

tin-benzyl bond to hydrolysis under acidic conditions compared to the tin-C<sub>sp<sup>3</sup></sub><sup>butyl</sup> bond involved in **OXT5a** and **OXT5d**. Notably, the EDX data of **OXT5b** is not attainable due to the difficulty of the reproducibility of **5b**.

#### V.4.2 Surface chemical composition by XPS studies

XP survey spectra along with expands of the most informative regions for **OXT5a**, **OXT5c** and **OXT5d** hybrid layers are reported in Figure V-4, while corresponding binding energies and quantitative analysis results are gathered in Table V-4 and V-5.

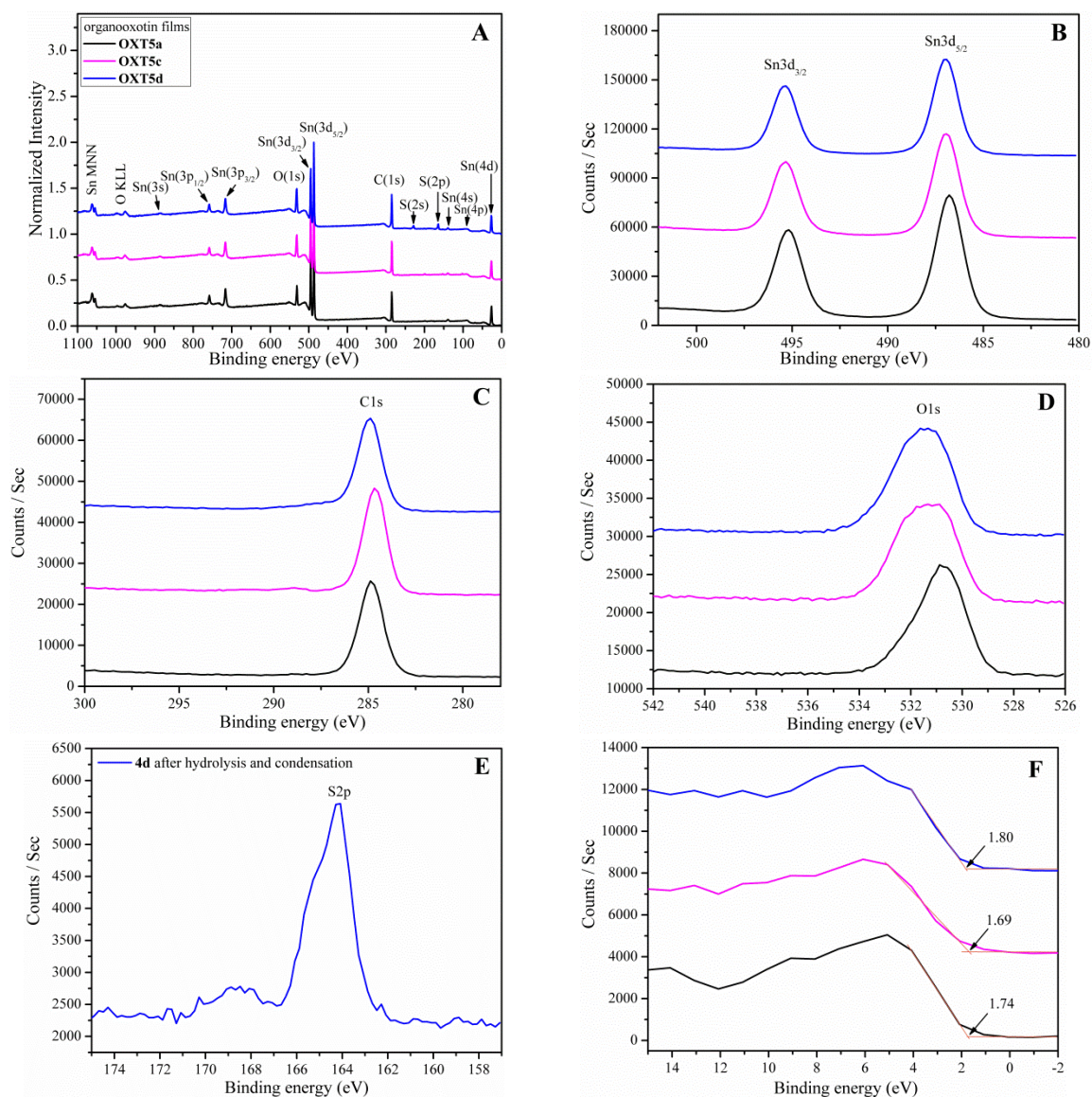


**Figure V-4 :** XPS patterns of organooxotin layers (**OXT5a**:black; **OXT5c**: pink; **OXT5d**: blue) (A) XPS full survey spectra; (B) Sn 3d region; (C) C 1s region; (D) O 1s region; (E) S 2p region (full); (F) valence band XPS spectra.

Apart from weak Cl 2p and Si 2p peaks observed at 199 and 102 eV, respectively, for **OXT5a** and **OXT5c** hybrid layers, which might be attributed to some residual HCl traces from hydrolysis process and silicon contaminations, Sn (Sn 3s, Sn 3p, Sn 3d, Sn 4s, Sn 4p, Sn

4d and Sn LMM Auger), carbon (C 1s) and oxygen (O 1s and O KLL Auger) related emissions were detected in the survey of **OXT5a**, **OXT5c** and **OXT5d** hybrid layers. Moreover, sulfur (S 2s and S 2p) emission was detected in the survey of **OXT5d** (blue) indicating the presence of sulfur atoms in the hybrid layers. In each case, the Sn 3d spectrum exhibited two peaks at  $487.0 \pm 0.1$  eV and at  $495.4 \pm 0.1$  eV due to spin-orbit coupling of the 3d state (Table V-4). The spin-orbit separation was found to be  $8.5 \pm 0.1$  eV. The Sn  $3d_{5/2}$  region exhibited a single feature at a binding energy of  $486.8 \pm 0.1$  eV, confirming that the sample was composed of only Sn (IV) states, with no noticeable Sn (II), which was expected at 485.8 eV, nor Sn(0), which was at 484.5 eV [18]. In addition, the main feature in the O 1s region (Figure V-4D, black line) of **OXT5a** was located at 530.8 eV and was attributed to the lattice oxygen  $O^{2-}$  confirming the formation of Sn-O-Sn linkages. The shoulders located at 531.9 and  $533.0 \pm 0.1$  eV next to the main peak indicate that there are several chemical states according to the measured binding energy. They can be attributed to functions stemming from the hydrolysis process (water and OH) and air contamination (O-C) which is typical for ex-situ samples. The O 1s peaks of **OXT5c** and **OXT5d** were slightly shifted toward higher energies. In particular, the O 1s peak for **OXT5d** was found to be at higher binding energy than for **OXT5a**, indicating the presence of more surface hydroxyl groups or oxygen-carbon. In addition, the S 2p region showed two features at -165.2 and -164.1 eV in a 1:2 ratio due to the spin-orbit coupling which can be assigned to S  $2p_{1/2}$  and S  $2p_{3/2}$  states. These values are consistent with those reported for unbounded sulfur atoms in thiophene units [19] and revealed that only one type of sulfur exists in the hybrid layer. Moreover, the measured C/S atomic ratio was found to be 8.53 which is close to the expected one, i.e. 8, for the 2-thiophenylbutyl unit. These data confirm the presence of the thiophene unit at the surface of the films. It must be also underlined that, regardless of the organic functionality nature, the experimental C/Sn atomic ratio is lower than the expected one which suggests that the surface is enriched in tin atoms (Table V-5).

Hybrid layer	Sn $3d_{3/2}$ (eV) <sup>a</sup>	Sn $3d_{5/2}$ (eV) <sup>a</sup>	C 1s (eV) <sup>a</sup>	O 1s (eV) <sup>a</sup>	S $2p_{3/2}$ (eV) <sup>a</sup>	VBE <sup>b</sup> (eV)
<b>OXT5a</b>	495.2	486.8	284.7	530.8	-	1.74
<b>OXT5c</b>	495.4	487.0	284.7	531.3	-	1.69
<b>OXT5d</b>	495.4	487.0	284.7	531.5	164.1	1.80

**Table V-4: Binding Energy and Valence Band Energy values for OXT5a, OXT5c and OXT5d hybrid layers.** <sup>a</sup>Calibration has been done by fixing C 1s at  $284.7 \pm 0.1$  eV. <sup>b</sup>Valence Band Energy (VBE): Energy difference between the valence-band maximum and the Fermi level ( $E_{vf}$ ) determined by extrapolating the linear portion of the absorption jump to the spectrum baseline.

Hybrid layer	O/Sn (at%)	C/Sn (at%)	C/S (at%)	OH/O <sup>2-</sup> (at%) <sup>a</sup>
<b>OXT5a</b>	1.24	3.63	-	0.2
<b>OXT5c</b>	1.71	4.81	-	0.88
<b>OXT5d</b>	1.98	5.34	8.53	1.28

**Table V-5: Quantitative analysis of the surface composition deduced from XPS data. <sup>a</sup>Ratio between the contributions at 532.3 and 530.7 eV.**

Furthermore, Figure V-4F shows the valence-band XPS spectra for **OXT5a**, **OXT5c** and **OXT5d** hybrid layers. Extrapolating the linear portion of the valence band emission to the spectrum baseline yielded the energy gap between the valence-band maximum and the Fermi level ( $E_{vf}$ ) (Table V-4). Whatever the organic functionality, the value was found to be in the range 1.7-1.8 eV which is very different from those reported for pure SnO<sub>2</sub> layers as described in chapter IV [20]. As a result, the hybrid layers obtained exhibited electronic properties very different from those of tin dioxide but further discussion can be hardly carried out due to surface charging effects that might occur in the case of hybrid layers [21].

## V.5 Surface morphology of oxohydroxoorganotin films

The surface morphology of organooxotin layers prepared according to the procedure described in paragraph V.2.2 was then studied by Scanning Electron Microscopy (SEM) and Atomic Force Microscopy (AFM). All the films were dried in air at 140 °C for 2h.

### V.5.1 Surface morphology of **OXT5a** layers

The SEM images of **OXT5a** showed a smooth and flat surface with some irregular shapes of cracks (Figure V-5A).

At magnification of 1000x (Figure V-5B), a certain number of small bubbles was observed inside each crack. The size of the crack edges suggests that the film thickness is rather weak, i.e. below 1 μm. Besides, increasing the magnification up to 2000x and 10000x (Figure V-5C and Figure V-5D), revealed that the surface of **OXT5a** films is rather uniform which might open the way towards applications in the fields of coatings and gas sensing.



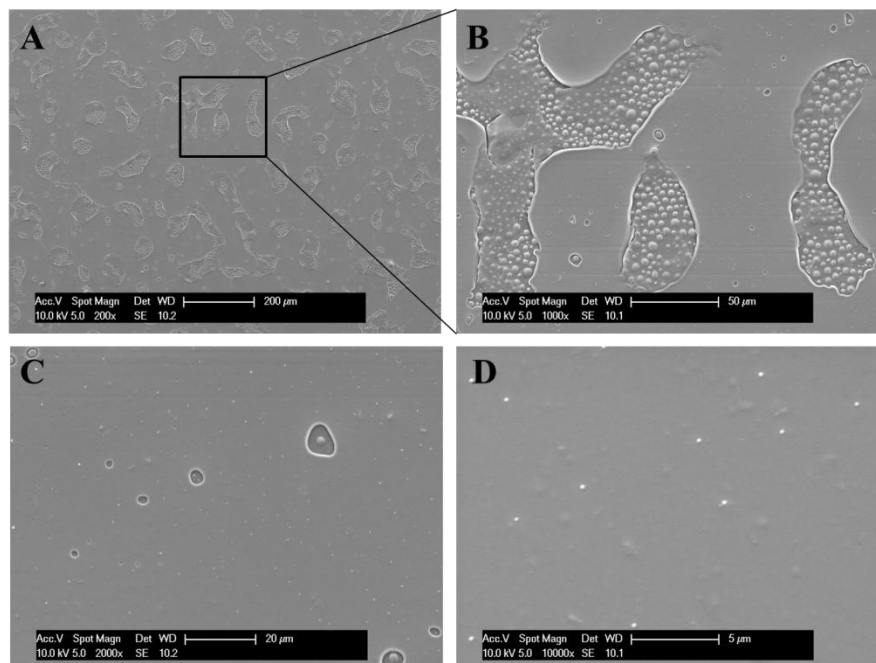


**Figure V-5: SEM images of OXT5a: (A) magnification of 200x; (B) magnification of 1000x; (C) magnification of 2000x; (D) magnification of 10000x.**

This regular surface morphology was further confirmed by AFM studies as depicted in Figure V-6. AFM images recorded in the tapping mode revealed the formation of **OXT5a** layers composed of nanoparticles which are densely packed (Figure V-4 A and B). The 3D images (Figure V-6C) showed that the surface was quite homogeneous and made of a dense network of aggregated particles. Finally, the rms roughness of the layer was found to be about 0.2 nm which is remarkably thin for a sol-gel layer and is comparable to the one of high quality self-assembled organic monolayer processed from organosilanes on silicon wafer [22].

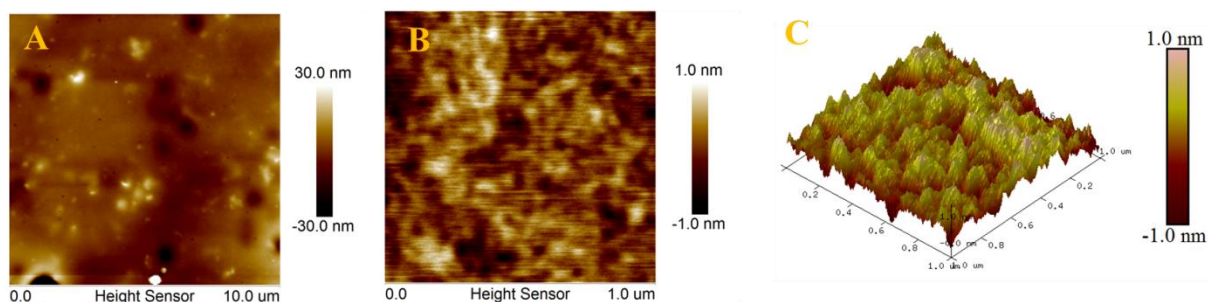


**Figure V-6: Height AFM images of OXT5a: (A) scan size: 10  $\mu$ m; (B) scan size: 1  $\mu$ m; (C) 3D morphology.**

### V.5.2 Surface morphology of **OXT5b** layers

The morphology of **OXT5b** layers was strongly dependent upon the quality of the sol used. The surface images of the layers processed from sols containing precipitates are shown in Figure V-7 A and B whereas those of films prepared from sol without precipitation are depicted in Figure V-7 C, D and E. Two different behaviors were thus evidenced. The first family of films, obtained from sols including precipitates, shows a rather rough surface

morphology with a macroporous texture organized randomly layer by layer (Figure V-7 A and B). The second family of layers exhibited a rather homogeneous surface with some bubble defects and showed an interesting organization within the bubble layers (Figure V-7 C to E).

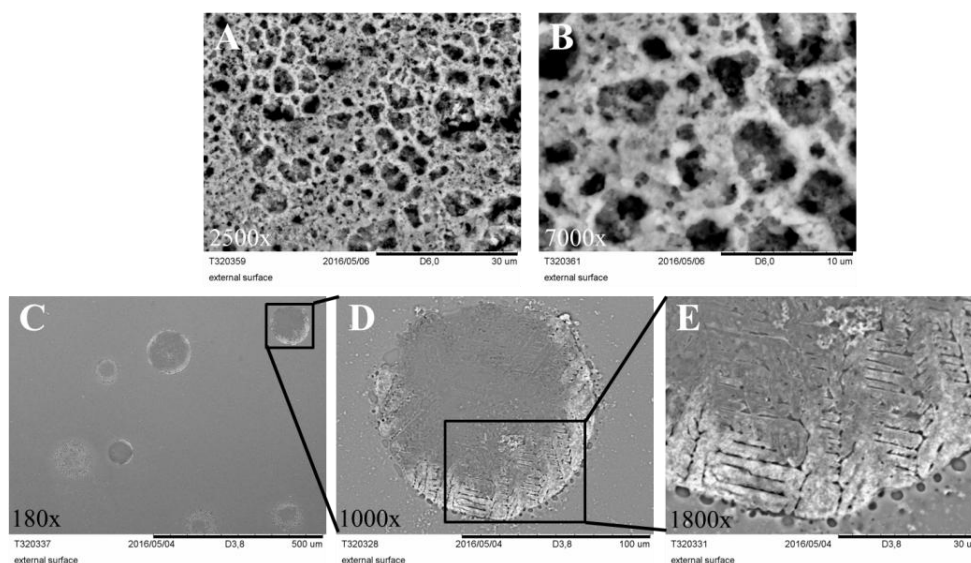


**Figure V-7: SEM images of OXT5b: magnification of (A) 2500x; (B) 7000x; (C) 180x; (D) 1000x; (E) 1800x.**

AFM studies also confirm the existence of two kind of surface topology. Thus, AFM images of the layers prepared from the sol containing precipitates showed a porous structure (Figure V-8) while the second kind of films shows linear organization of the hybrid materials (Figure V-9). The 3D morphologies (Figure V-8C and Figure V-9C) clearly indicated two different topologies resulting from the characteristics of the sol prepared: a unique macroporous architecture formed by the spontaneous layer by layer self-assembly of aggregated particles as depicted in Figure V-8C and striped lines parallel to each other as shown in Figure V-9C. The presence of these striped lines, which was not observed in any other samples, might be related to the linear shape of the oxohydroxoorganotin species formed from the diorganotin **5b** which cannot reticulate in three-dimension. Compared to films processed from precursor **5a**, roughness of **OXT5b** is much higher as suggested by SEM and AFM images. Thus, the rms roughness of the layer prepared from sol solution with precipitates was about 10 nm ( $R_a = 7.01$  nm) and that of the layer prepared from sol solution without precipitation was estimated to be 8.3 nm ( $R_a = 6.6$  nm). In the latter case, the roughness slightly decreased likely due to smaller particles formed at the sol step.



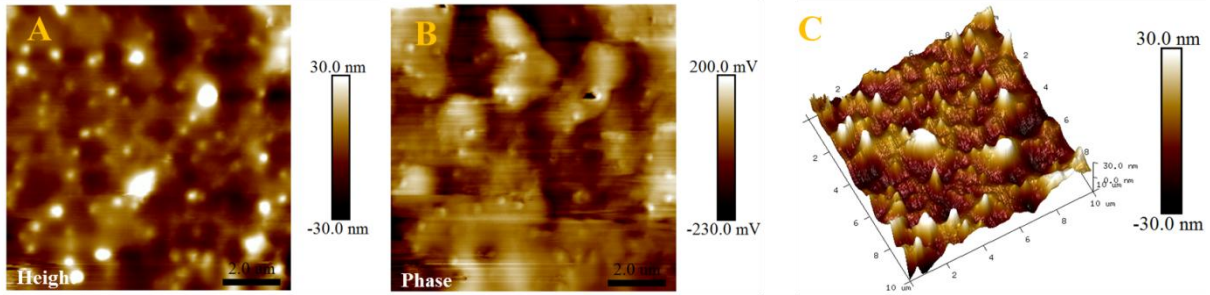


Figure V-8: Height AFM images of OXT5b: (A) scan size: 10  $\mu\text{m}$ ; (B) phase image; (C) 3D morphology.

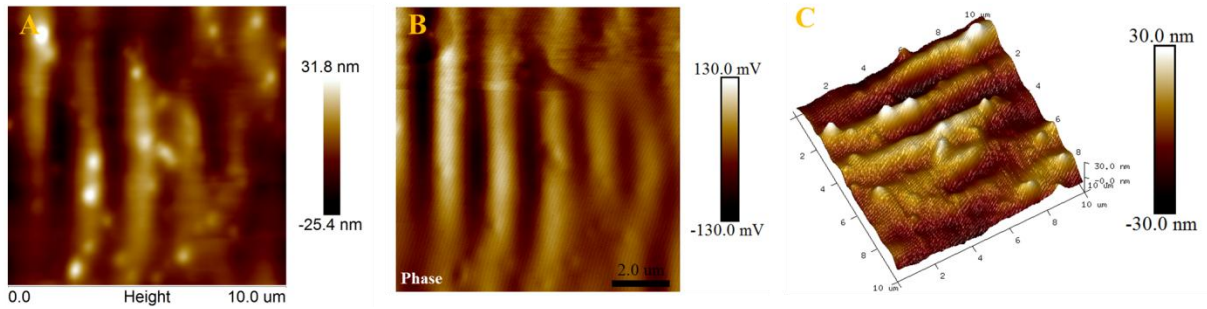


Figure V-9: Height AFM images of OXT5b: (A) scan size: 10  $\mu\text{m}$ ; (B) phase image; (C) 3D morphology.

On the other hand, the film surface was slightly scratched into a straight line by a syringe with 0.64 mm of needle diameter size (Figure V-10A) in order to measure the film thickness. The thickness of the film (Figure V-10B) was determined by the step analysis of AFM software (NanoScope Analysis 1.8). This analysis led to a thickness of about 30 nm which is remarkably thin. This result confirms that the sol-gel route is an efficient way to process ultra-thin tin oxide-based films as it was reported for the first time by our group several years ago [23].

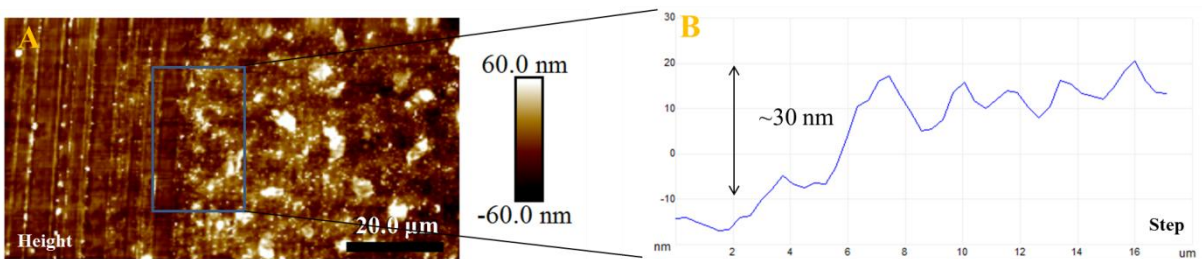


Figure V-10: Height AFM images of OXT5b: (A) scan size: 95.3  $\mu\text{m}$ ; (B) film thickness by step analysis.

### V.5.3 Surface morphology of OXT5c layers

The OXT5c layer exhibits a porous network with irregular vacancies in between (Figure V-11). However, it turns out that the hybrid layer did not fully cover the substrate surface.

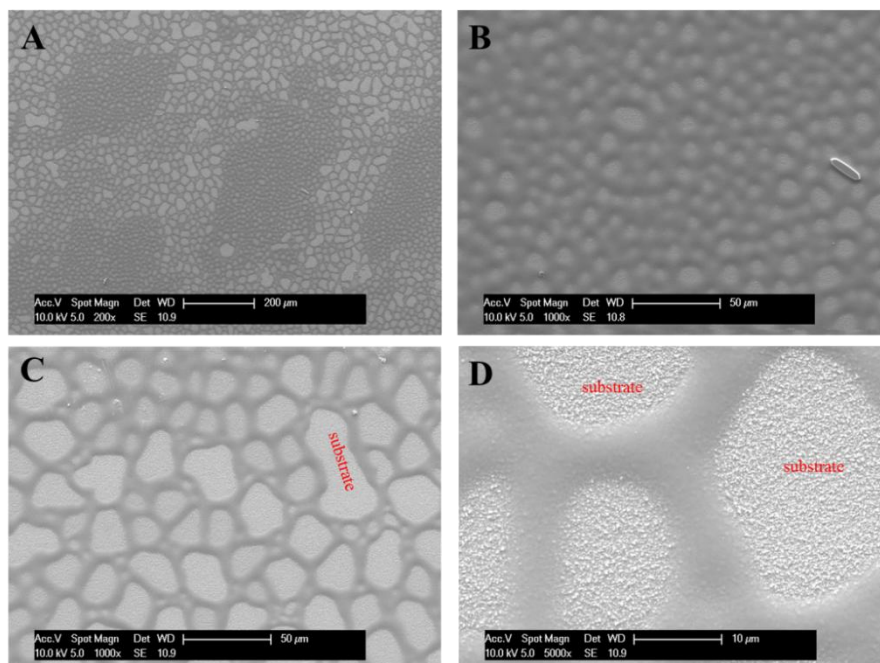


Figure V-11: SEM images of OXT5c: magnification of (A) 200x; (B) 1000x; (C) 1000x; (D) 5000x.

On the other hand, the 3D AFM images of **OXT5c** indicates that the surface of this hybrid layer is rather flat (Figure V-12B) with an estimated rms roughness of about 0.316 nm ( $R_a = 0.247$  nm). The 3D phase image exhibited as in Figure V-12C. Finally, the film thickness of **OXT5c** was found to be about 150 nm by the step analysis (Figure V-13).

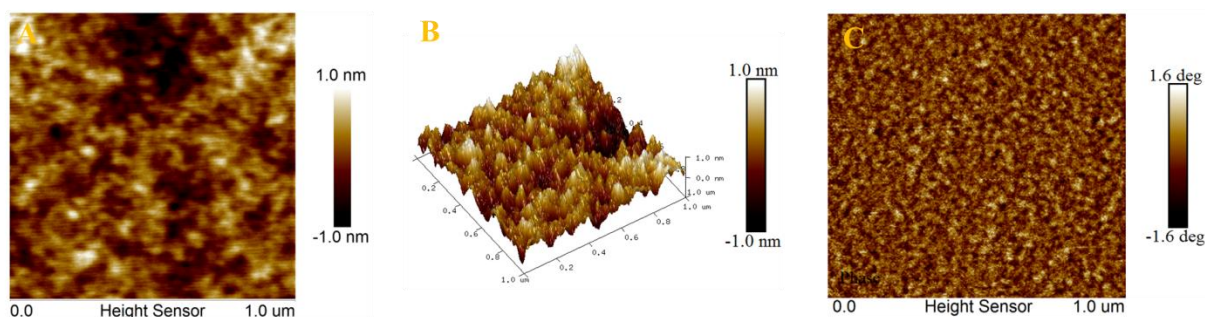


Figure V-12: Height AFM images of OXT5c: (A) scan size: 1  $\mu$ m; (B) 3D morphology; (C) 3D phase image of 1  $\mu$ m scan size.

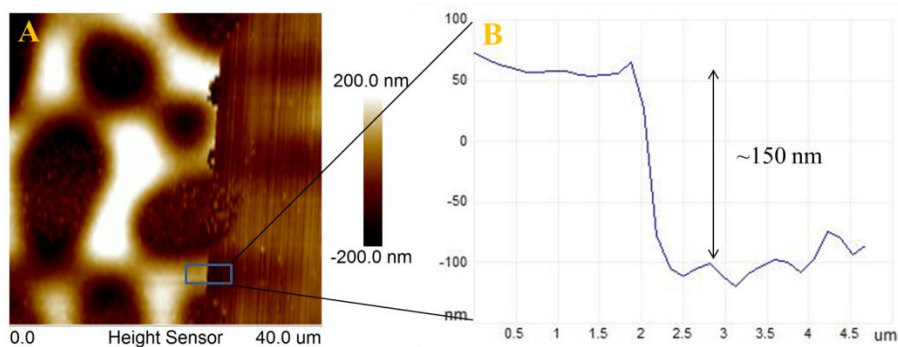
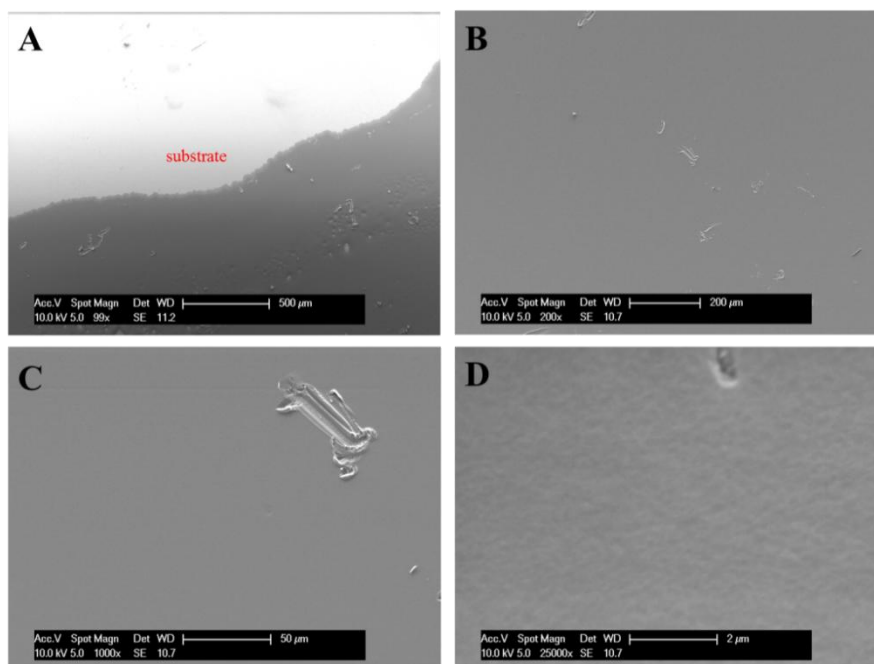


Figure V-13: Height AFM images of OXT5c: (A) scan size: 40.0  $\mu$ m; (B) film thickness by step analysis.

#### V.5.4 Surface morphology of **OXT5d** layers

The SEM images of **OXT5d** shown in Figure V-14 revealed a denser and more homogeneous surface than that of the layers prepared from **5a**, **5b** and **5c** (AFM and SEM images of **OXT5a**, **OXT5b** and **OXT5c** from Figure V-5 to Figure V-13). Figure V-14A showed the frontier between substrate (bright side) and **OXT5d** layer (dark side) and the film showed in Figure V-14C was scratched on purpose in order to prove the film surface.



**Figure V-14: SEM images of OXT5d: magnification of (A) 99x; (B) 200x; (C) 1000x; (D) 25000x.**

The AFM images of **OXT5d** showed interesting needle-tip shape surface topology at scan size of 10  $\mu\text{m}$  (Figure V-15 A) and phase image also indicated the formation of a rather flat surface (Figure V-15 B). The 3D profile of the surface (Figure V-15 C) indicated that rms roughness of the layer was about 6.78 nm ( $R_a = 5.43$  nm). When the scan size narrowed down to 1  $\mu\text{m}$ , the surface showed an aggregated morphology and 3D phase image exhibited its surface feature (Figure V-15 D and Figure V-15E).



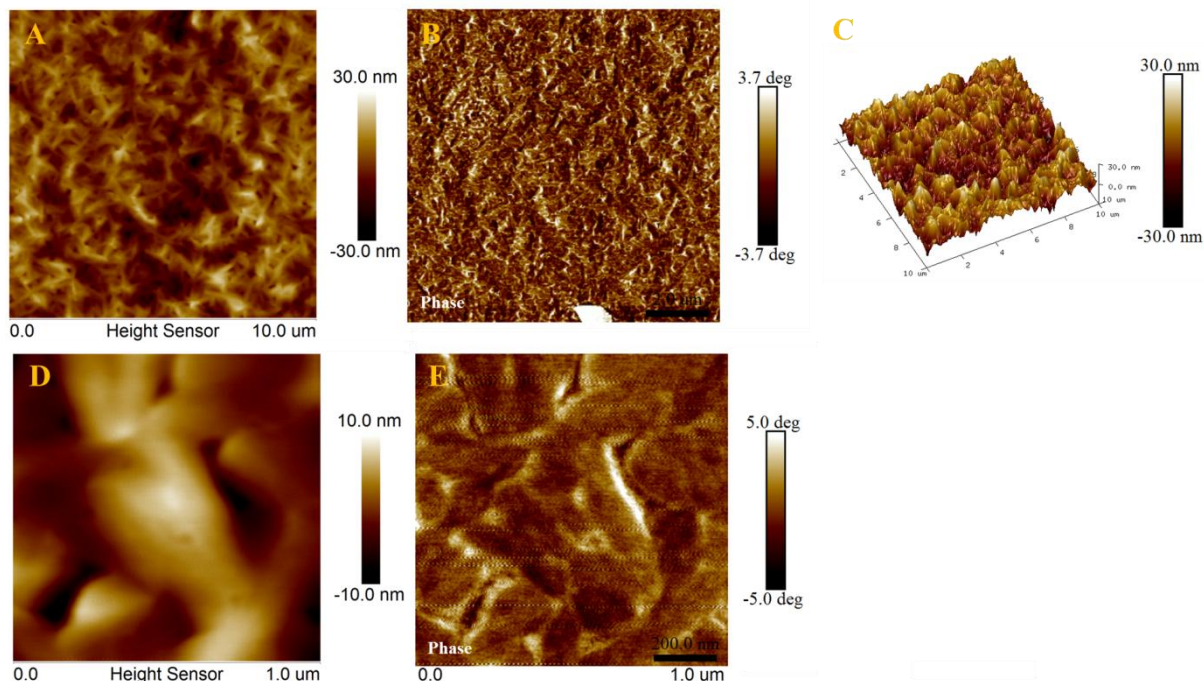


Figure V-15: Height AFM images of OXT5d: (A) scan size: 10  $\mu\text{m}$ ; (B) phase scan: 10  $\mu\text{m}$ ; (C) 3D morphology; (D) scan size: 1  $\mu\text{m}$ ; (E) phase scan: 1  $\mu\text{m}$ .

## V.6 Optical properties of oxhydrooorganotin materials

The four hybrid powders prepared according to the procedure indicated in paragraph V.2.2 were dispersed in chloroform and the UV-visible absorption spectra of the resulting dispersion were recorded (Figure V-16).

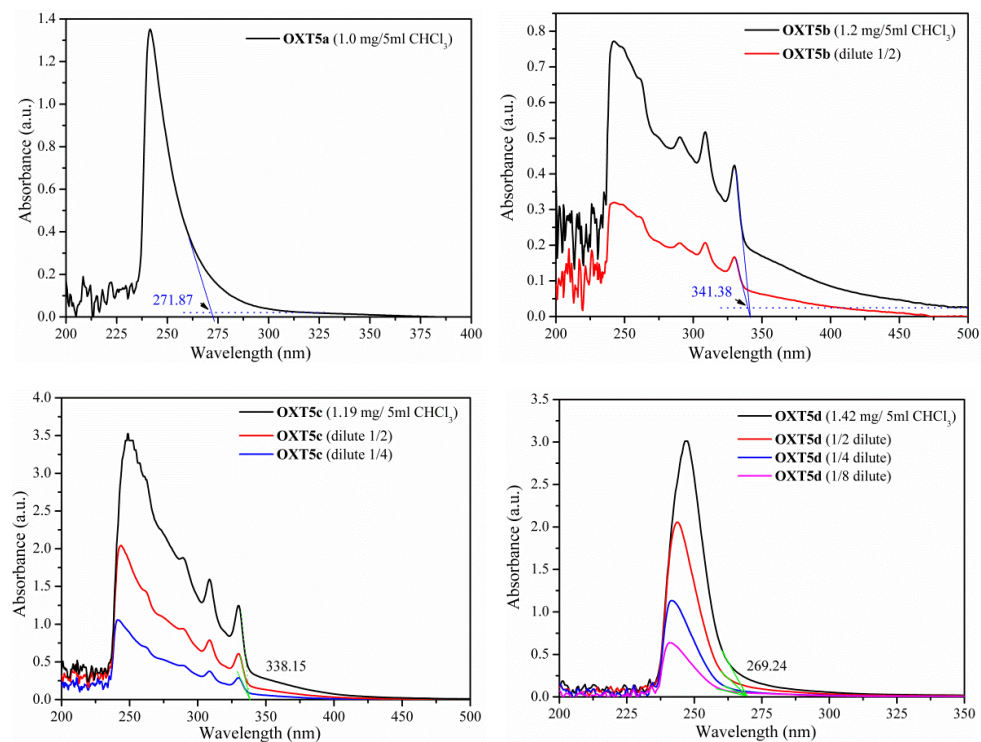


Figure V-16: Room temperature UV-Vis absorption spectrum of OXT5a (top, left), OXT5b (top, right),

**OXT5c (bottom, left) and OXT5d (bottom, right). Each sample was dispersed in anhydrous CHCl<sub>3</sub> (5 mL).**

The energy band gap values were estimated by extrapolating the absorption band edge to the spectrum baseline and by using the following formula [24]:

$$E_g = h \cdot C / \lambda \quad \text{where}$$

$h$  is the Planck constant ( $6.626 \times 10^{-34}$  J·s)  
 $C$  is the light velocity ( $3.0 \times 10^8$  m·s<sup>-1</sup>)  
 $\lambda$  is the cut-off wavelength (m)  
1eV =  $1.6 \times 10^{-19}$  J

The energy band gap value for **OXT5a**, **OXT5b**, **OXT5c** and **OXT5d** were found to be 4.57, 3.64, 3.67 and 4.61 eV, respectively. It is also worth mentioning that in some cases sharp peaks were detected which might be associated to the vibronic structure of some electronic transition of the organic functionalities.

## V.7 Conclusion

Four functional trialkynylorganotins (**5a**, **5b**, **5c** and **5d**) were successfully synthesized through the selective alkylation of one equivalent of tetraphenylethynyltin by one equivalent of the corresponding Grignard reagent (functional bromide linked to at least one CH<sub>2</sub> were optimum) in the presence of anhydrous solvents of toluene and diethyl ether (2:1) at 40 °C for 18 hours. These optimized experimental conditions for synthesizing these organotin compounds do not only effectively shorten the conventional synthetic methods but also highlight the diversity of the organic functionalities within the alkynylorganotin structure which opens new avenues for the synthesis of dialkynyldiorganotin or alkynyltriorganotin derivatives for further organotin chemistry studies by the appropriately well-controlled proportion between tetraphenylalkynyltin and Grignard reagent. These alkynylorganotins were then successfully used as precursors of organic-inorganic tin-based hybrid materials obtained by the sol-gel process. The hydrolysis-condensation of the four functional alkynylorganotins yielded oxohydroorganotin hybrid powders and layers (**OXT5a**, **OXT5b**, **OXT5c** and **OXT5d**) which are thermally stable at least up to 200 °C under air. Bulk and surface chemical composition performed by FTIR, EDX and XPS studies revealed that the organic functionality was preserved during the hydrolysis-condensation processes and that tin-oxide network was formed with remaining dangling hydroxyl functions. In particular, a chemical formula could be proposed for **OXT5a**. On the other hand, the surface morphology and texture of the hybrid films strongly depend on the organic functionality nature. The hybrid materials including flexible alkyl units as **OXT5a** and **OXT5d** led to the denser and more homogeneous layers, whereas more porous textures were obtained for **OXT5b** and **OXT5c** which includes more rigid organic groups. The electronic properties of these hybrid materials were also determined. The energy band gap varied from 3.64 to 4.61 eV depending on the organic function, whereas the valence band energy position towards Fermi level

position was quite constant, i.e. 1.7-1.8 eV. Finally, as hybrid **OXT5a** led to the better defined films, it was selected for further gas sensing studies.

## References:

- [1] (a) L. Renard, H. Elhamzaoui, B. Jousseume, T. Toupance, G. Laurent, F. Ribot, H. Saadaoui, J. Broetz, H. Fuess, R. Riedel, A. Gurlo, *Chem. Commun.*, **2011**, 47, 1464-1466. (b) L. Renard, J. Broetz, H. Fuess, A. Gurlo, R. Riedel, T. Toupance, *ACS Appl. Mater. Interfaces*, **2014**, 6, 17093-17101.
- [2] C. J. Brinker, G. W. Scherer, in the book of “*Sol-gel science: the physics and chemistry of sol-gel processing*”, Academy Press Inc., **2013**.
- [3] (a) K. J. Shea, D. A. Loy, O. Webster, *J. Am. Chem. Soc.*, **1992**, 114, 6700-6710. (b) D. A. Loy, K. J. Shea, *Chem. Rev.*, **1995**, 95, 1431-1442. (c) G. Kickelbick, in “*Hybrid Materials: Synthesis, Characterization and Applications*“, Wiley-VCH, Weinheim, **2007**.
- [4] J. D. Kennedy, W. McFarlane, P.J. Smith, R.F.M. White, L. Smith, *J. Chem. Soc., Perkin 2*, **1973**, 1785-1788.
- [5] (a) R. West, C. S. Kraihanzel, *Inorg. Chem.*, **1962**, 1, 967-969. (b) M. L. Quan, P. Cadot, *C. R. Acad. Sci.*, **1962**, 254, 133.
- [6] A. G. Davies, in “*Organotin Chemistry*“, Wiley-VCH, Weinheim, **2007**, p 123-124.
- [7] W. P. Neumann, F. G. Kleiner, *Tetrahedron Lett.*, **1964**, 3779-3782.
- [8] D. Villemin, E. Schigeko, *J. Organometal. Chem.*, **1988**, 346, C24-C26.
- [9] (a) R.B. King, J. J. Eisch, in *Organometallic synthesis Vol. 4*, Amsterdam, **1988**. (b) L. Brandsma, H. D. Verkruisje, *Synthesis*, **1999**, 1727-1728.
- [10] P. Jaumier, B. Jousseume, M. Lahcini, F. Ribot, C. Sanchez, *Chem. Commun.*, **1998**, 369-370.
- [11] (a) B. Jousseume, H. Riague, T. Toupance, M. Lahcini, P. Mountford, B. R. Tyrell, *Organometallics*, **2002**, 21, 4590-4954. (b) H. El Hamzaoui, T. Toupance, B. Jousseume, H. Allouchi, *Organometallics*, **2007**, 26, 3908-3917.
- [12] (a) H. Elhamzaoui, B. Jousseume, H. Riague, T. Toupance, P. Dieudonné, C. Zakri, M. Maugey, H. Allouchi, *J. Am. Chem. Soc.* **2004**, 126, 8130-8131. (b) T. Toupance, M. de Borniol, H. Elhamzaoui, B. Jousseume, *Appl. Organometal. Chem.* **2007**, 21, 514-520.
- [13] P. Jaumier, M. Lahcini, B. Jousseume, F. Ribot, *Angew. Chem. Int. Ed.* **1999**, 42, 402-404.
- [14] P. Jaumier, *PhD Thesis*, University of Bordeaux 1, **1998**.
- [15] B. Wrackmeyer, *Annu. Rep. NMR Spectrosc.* **1985**, 16, 73-186.
- [16] T. Toupance, H. Elhamzaoui, B. Jousseume, H. Riague, I. Saadeddin, G. Campet, J. Brötz, *Chem. Mater.*, **2006**, 18, 6364-6372.
- [17] (a) H. Kriegsman, H. M. Hoffmann, H. Z. Geissler, *Anal. Allg. Chem.* **1965**, 24, 341. (b) J. S. Morrison, H. M. Haendler, *J. Inorg. Nucl. Chem.* **1967**, 29, 393. (c) T. D. Senguttuvan, L. K. Malhotra, *Thin Solid Films*, **1996**, 289, 22.
- [18] J. X. Wang, D. F. Liu, X. Q. Yan, H. J. Yuan, L. J. Ci, Z. P. Zhou, Y. Gao, L. Song, L. F. Liu, W. Y. Zhou, G. Wang, S. S. Xie, *Solid State Commun.* **2004**, 130, 89-94.
- [19] (a) A. Lachkar, A. Selmani, E. Sacher, M. Leclerc, R. Mokhliss, *Synth. Metal.* **1994**, 66, 209-2015. (b) F. Buckel, F. Effenberger, C. Yan, A. Götzhäuser, M. Grunze, *Adv. Mater.*

- 2002**, *12*, 902-905.
- [20] C. Körber, P. Á goston, A. Klein, A. *Sens. Actuators B* **2009**, *139*, 665-672.
- [21] A. Klein, TU Darmstadt, personal communication.
- [22] (a) M. Meillan, M. A. Ramin, T. Buffeteau, S. Marsaudon, M. Odorico, S.-W. W. Chen, J.-L. Pellequer, M. Degueil, K. Heuzé, L. Vellutini, B. Bennetau, *RSC Adv.* **2014**, *4*, 11927-11930. (b) M. Meillan, T. Buffeteau, G. Le Bourdon, L. Thomas, M. Degueil, K. Heuzé, B. Bennetau, L. Vellutini, *Chem. Select* **2016**, *2*, 11868-11874.
- [23] L. Renard, O. Babot, H. Saadaoui, H. Fuess, J. Brötz, A. Gurlo, E. Arveux, A. Klein, T. Toupance, *Nanoscale* **2012**, *4*, 6806-6813.
- [24] R. López, R. Gómez, *J. Sol-Gel Sci.Technol.* **2012**, *61*, 1-7.



# **Chapter VI Gas sensing properties of tin dioxide and hybrid oxohydroxoorganotin materials**

As reported in chapters IV and V, finely-tuned SnO<sub>2</sub> nanoparticles and hybrid oxohydroxoorganotin materials were successfully prepared. The next objective of this work was therefore the characterization of their response towards both reductive and oxidative gases. Before starting the sensing measurement, one of the important steps is the film preparation process on the sample substrate. The temperature calibration curve of the sample substrates should previously be determined in order to have an accurate estimation of the temperature while conducting the measurement. The difficulties are related to the need of depositing small amounts of material in order to avoid the material spreading over the substrate-edge (spreading would cause an electrical connection between the electrical circuits present over the upper and rear face of the substrates, thus making electrical measurements unreliable). At the same time, a relatively large amount of material is needed to obtain good electrical and gas sensing signal which has been learnt by trial and error. Electrical signal can be checked relatively fast with each sample, but it may happen that an acceptable electrical signal will then result in a non-reliable gas sensing signal. Therefore, the necessity of repeating the gas sensing measurements to have reliable data is inevitably required for academically scientific report.

## **VI.1 Gas sensing set-up and measurement principles**

The gas sensing setup was built in Brescia through the collaboration between the Department of Information and Engineering of the University of Brescia and the National Institute of Optics of the National Research Council (CNR). The gas sensing substrates with interdigital structures are designed and produced within the same collaboration. In order to heat the material, four gold wires have to be bounded to the sensing substrates to provide the ideal electrical power. There are four main steps before starting the gas sensing measurement (Figure VI-1): (a) the sample deposition on the gas sensing substrate; (b) the aging process; (c) the mounting step of substrates; (d) the setup of gas sensing parameters.

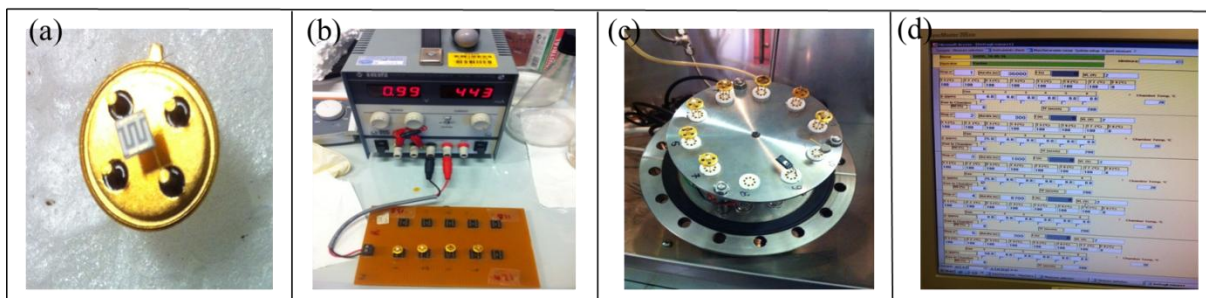


**Figure VI-1: The processes of gas sensing measurement: (a) sample deposition; (b) aging process; (c) mounting substrates; (d) the setup of gas sensing parameters.**

On the other hand, each step requires delicate skills and repeated attempts through trial and error to optimize the sensing result, for instance, for process (a) of gas sensing measurement, the appropriate sample deposition technique has to be chosen according to the quality of the sensing layer and the result in this thesis turns out that the drop casting is better than spin coating approach (Figure VI-2). Moreover, the number of drops has also a decisive impact on the result of gas sensing data; for process (b) of gas sensing measurement, the function of aging process not only helps stabilizing the sensing layer but also ameliorates the gas sensing data; for process (c) of gas sensing measurement, the bad connection from golden base to the power supplier and picoammeter may lead to wrong or broken gas sensing signals; for process (d) of gas sensing measurement, the selection of temperature, gases and gas concentrations are the major parameters which should be carefully considered before the measurement. The other parameters such as the stabilization temperature (usually the maximum of each measured temperature) and duration in the gas sensing chamber, duration of gas in, gas out and recovery time are seriously taken into account for gas sensing measurement.

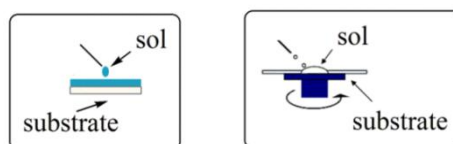


**Figure VI-2: Two common coating techniques: drop casting (left); spin coating (right).**

Gas sensing measurements were carried out in a thermostatic chamber (Figure VI-3) (stabilized at a temperature of 20 °C) working with both oxidizing (NO<sub>2</sub>) and reducing gases (CO, H<sub>2</sub>, ethanol, acetone) in a background of synthetic dry air generated from certified bottles. Gas concentration inside the test chamber was controlled by mixing the flows from the different bottles by means of mass flow controllers. The sensor signal was continuously monitored during measurements by applying a constant 1V bias (2V for oxohydroxoorganotins) to the electrodes and measuring the current flowing through the SnO<sub>2</sub> layers by means of a picoammeter. The sensor response will be expressed as  $(G_{\text{gas}} - G_{\text{air}}) / G_{\text{air}}$ ,

hereafter shortened as  $\Delta G/G$ , where  $G_{\text{gas}}$  and  $G_{\text{air}}$  are the steady-state conductance values measured during gas exposure and in air respectively.

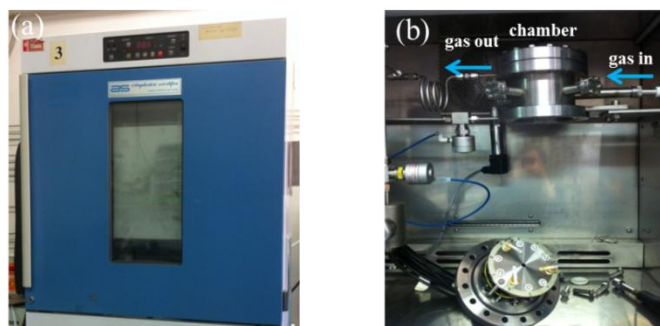


**Figure VI-3: Gas sensing equipment: (a) external structure; (b) internal structure.**

### VI.1.1 Structure of gas sensing substrates

Gas sensor devices used for  $\text{SnO}_2$  samples were prepared starting from  $2 \text{ mm} \times 2 \text{ mm} \times 0.25 \text{ mm}$  alumina substrates, provided on the top face by sputtered Pt contacts, having interdigitated shape, thickness of  $800 \text{ nm}$  and separation of about  $200 \mu\text{m}$ . On the rear side, a Pt meander acting as heating element to control the sensor temperature was deposited by magnetron direct current sputtering (Figure VI-4).

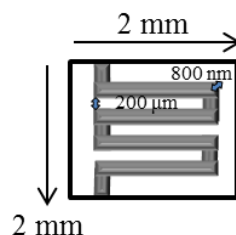


**Figure VI-4: The square gas sensing substrate for  $\text{SnO}_2$  materials.**

The substrate used for the deposition of oxohydroxoorganotin material is consisting of planar  $\text{Al}_2\text{O}_3$  substrate with Pt-electrodes on the front side for measuring the sensor resistance and a Pt-heater on the backside to heat the sensor at the temperature of interest (Figure VI-5). The electrodes have an interdigitated structure to allow measuring resistances on a small area.

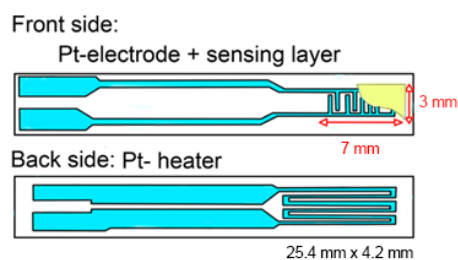


**Figure VI-5: The rectangular gas sensing substrate for oxohydroxoorganotin materials.**

### VI.1.2 Selection of gas sensing parameters

For SnO<sub>2</sub> and oxohydroxoorganotin materials, there are five gases (CO, H<sub>2</sub>, ethanol, acetone, NO<sub>2</sub>) selected as the testing gases in both batches (Table VI-1 and Table VI-2) and their measuring temperatures were chosen fixed at 200 °C, 300 °C, 400 °C for SnO<sub>2</sub> and 100 °C, 200 °C for oxohydroxoorganotin, respectively (Table VI-3). The concentrations selected are slightly different for CO (10, 25, 50, 100 ppm for the first measurement of SnO<sub>2</sub> prepared in acidic conditions whereas 100, 250, 500, 1000 ppm for the second measurement of SnO<sub>2</sub> prepared in acid and basic conditions; 25, 50, 100, 200 ppm for oxohydroxoorganotin) and NO<sub>2</sub> (0.5, 1, 2, 4 ppm for SnO<sub>2</sub> prepared in acidic conditions; 1, 2, 4, 8 ppm for oxohydroxoorganotin) whereas the rest of gases have the same testing concentrations (H<sub>2</sub>: 100, 200, 400, 800 ppm; ethanol: 10, 25, 50, 100 ppm; acetone: 25, 50, 100, 200 ppm). The operation time for each stage of gas sensing measurement was defined as below (s =second used as a time unit in this case):

1. Stabilization process (Aging) of sensing layers was set for 10 hours (10 x 60 x 60 = 36000 s).
2. Gas filling in the tubes was set for 5 minutes (5 x 60 = 300 s).
3. Opening the valve to let the gas fill in the chamber was set for 30 minutes (30 x 60 = 1800 s).
4. Evacuating gas and purging process was set for 2 hours and 25 minutes (60 x 2 + 25 = 145, 145 x 60 = 8700 s) for SnO<sub>2</sub> whereas 1 hour and 25 minutes (60 + 25 = 85, 85 x 60 = 5100 s) for oxohydroxoorganotin.
5. The total period of one cycle (2-4) is 3 hours for SnO<sub>2</sub> and 2 hours for oxohydroxoorganotin.

Gases	Number of experiment	Concentrations (ppm)
CO <sup>[i]</sup>	1 <sup>st</sup>	10, 25, 50, 100
	2 <sup>nd</sup>	100, 250, 500, 1000
H <sub>2</sub> <sup>[i]</sup>	1 <sup>st</sup> , 2 <sup>nd</sup>	100, 200, 400, 800
ethanol <sup>[i]</sup>	1 <sup>st</sup> , 2 <sup>nd</sup>	10, 25, 50, 100
acetone <sup>[i]</sup>	1 <sup>st</sup> , 2 <sup>nd</sup>	25, 50, 100, 200
NO <sub>2</sub> <sup>[ii]</sup>	1 <sup>st</sup>	0.5, 1, 2, 4
	2 <sup>nd</sup>	1, 2, 4, 8

**Table VI-1: SnO<sub>2</sub> nanoparticles were exposed to gases including different properties and concentration: (i) reducing gases (CO, H<sub>2</sub>, ethanol, acetone), (ii) oxidizing gas (NO<sub>2</sub>).**

Gases	Concentrations (ppm)
CO <sup>[i]</sup>	25, 50, 100, 200
H <sub>2</sub> <sup>[i]</sup>	100, 200, 400, 800
ethanol <sup>[i]</sup>	10, 25, 50, 100
acetone <sup>[i]</sup>	25, 50, 100, 200
NO <sub>2</sub> <sup>[ii]</sup>	1, 2, 4, 8

**Table VI-2: Oxohydroxoorganotin was exposed to gases including different properties and concentrations: (i) reducing gases (CO, H<sub>2</sub>, ethanol, acetone), (ii) oxidizing gas (NO<sub>2</sub>).**

	SnO <sub>2</sub>	oxohydroxoorganotin
Measuring temperatures (°C)	200, 300, 400	100, 200

**Table VI-3: The measuring sensing temperatures were chosen for SnO<sub>2</sub> and oxohydroxoorganotin.**

## VI.2 Electrical and gas sensing characterization of SnO<sub>2</sub> nanoparticles

### VI.2.1 Preliminary tests carried out with TOa<sup>90</sup> and TOa<sup>600</sup> nanoparticles

A first series of data was recorded for the nanoparticles synthesized in acidic conditions and the sensor responses at different temperatures are shown in Figure VI-6. First of all, regardless the temperature in the 200-400°C range and the gas nature, both samples gave rise to reversible responses with both fast response and recovery time (Figure VI-6, top right) (to be quantified). From the dynamic gas sensing performance of TOa samples (Figure VI-6), it can be clearly seen that the conductance of the layers increased when exposed to reducing gases (CO, H<sub>2</sub>, acetone and ethanol) and decreased in contact with oxidizing gas (NO<sub>2</sub>). This behavior is typical for a n-type metal oxide semiconductor as tin dioxide. Moreover, whatever the nanoparticles considered, the sensor response of the layers exposed to a reducing gas (CO, H<sub>2</sub>, acetone or ethanol) was enhanced when the heating temperature was increased from 200 °C to 400 °C. By contrast, in the presence of an oxidizing gas as NO<sub>2</sub>, the sensor response decreased as the temperature was increased.

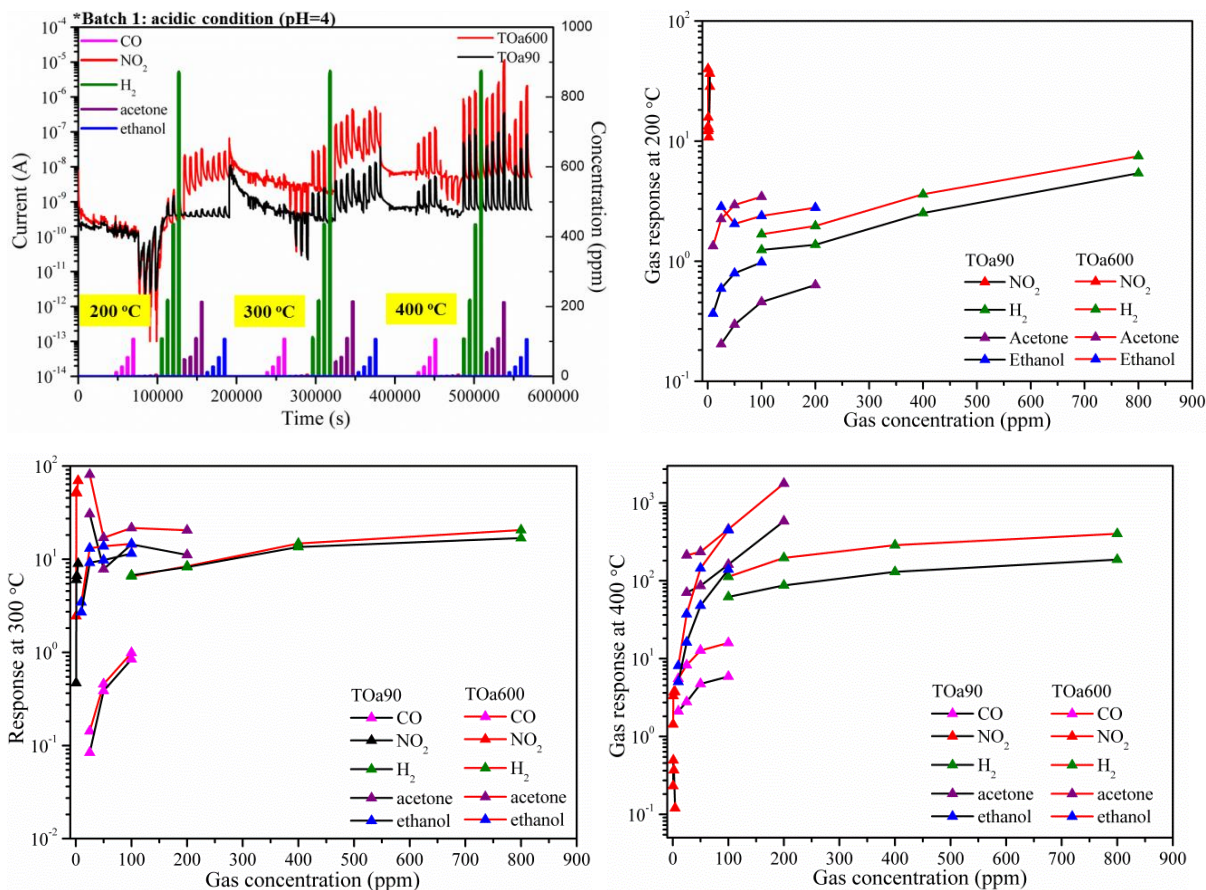


**Figure VI-6:** The dynamic gas sensing performance (upper-left) at 200 °C, 300 °C and 400 °C; the gas response at 200 °C (upper-right); the gas response at 300 °C (lower-left); the gas response at 400 °C (lower-right) of TOa<sup>90</sup> (black) and TOa<sup>600</sup> (red) towards CO (pink), NO<sub>2</sub> (red), H<sub>2</sub> (green), acetone (purple) and ethanol (blue).

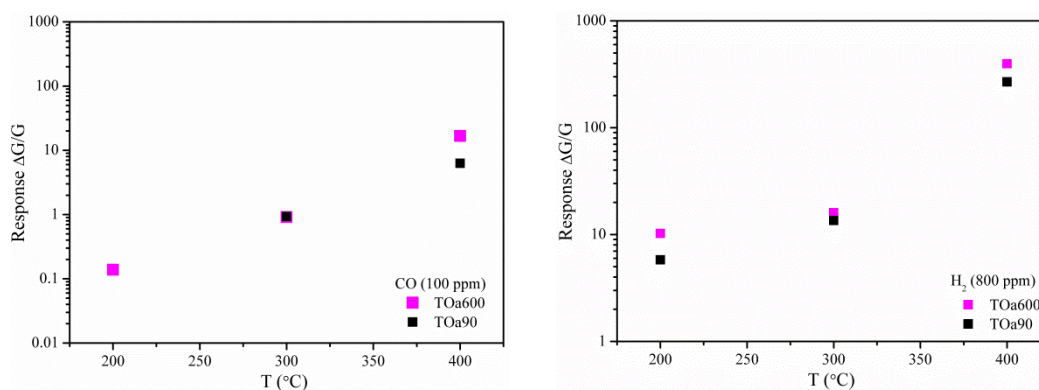
Testing gas	Concentration (ppm)	Working temperature (°C)	Gas response (S) at max. concentration of corresponding gas
CO	25-100	300, 400	0.91, 16.77
H <sub>2</sub>	100-800	200, 300, 400	10.24, 15.99, 397.27
acetone	25-200	200, 300, 400	5.87, 23.12, 1496.33
ethanol	10-100	200, 300, 400	4.29, 22.89, 450.63
NO <sub>2</sub>	0.5-4	200, 300, 400	73.76, 60.60, 2.84

**Table VI-4:** The optimal gas sensing condition for TOa<sup>600</sup> sample.

Testing gas	Concentration (ppm)	Working temperature (°C)	Gas response (S) at max. concentration of corresponding gas
CO	25-100	300, 400	0.93, 6.29
H <sub>2</sub>	100-800	200, 300, 400	5.8, 13.57, 268.63
acetone	25-200	200, 300, 400	1.05, 10.91, 554.53
ethanol	10-100	200, 300, 400	1.37, 12.80, 148.8
NO <sub>2</sub>	0.5-4	200, 300, 400	85.82, 13.98, 0.21

**Table VI-5: The optimal gas sensing condition for TOa<sup>90</sup> sample.**

From a more quantitative point of view, the highest responses were obtained for 200 ppm acetone with values of about 500 and 1500 for TOa<sup>90</sup> and TOa<sup>600</sup>, respectively. Ethanol and hydrogen gases also led to strong signals. For instance, TOa<sup>600</sup> nanoparticles yielded to sensor response of about 450 and 400 when exposed to 100 ppm ethanol and 800 ppm hydrogen, respectively. The gas sensing properties of TOa<sup>90</sup> and TOa<sup>600</sup> samples were then compared for 100 ppm of CO, 800 ppm of H<sub>2</sub>, 25 ppm of acetone, 10 ppm of ethanol and 4 ppm of NO<sub>2</sub> and the results are depicted in Figure IV-7. It can be seen that the SnO<sub>2</sub> nanoparticles treated at 600 °C showed better gas sensing performance than those treated at 90 °C. This may be attributed to the better crystallinity of the TOa<sup>600</sup> sample but this point will be discussed in more details below.





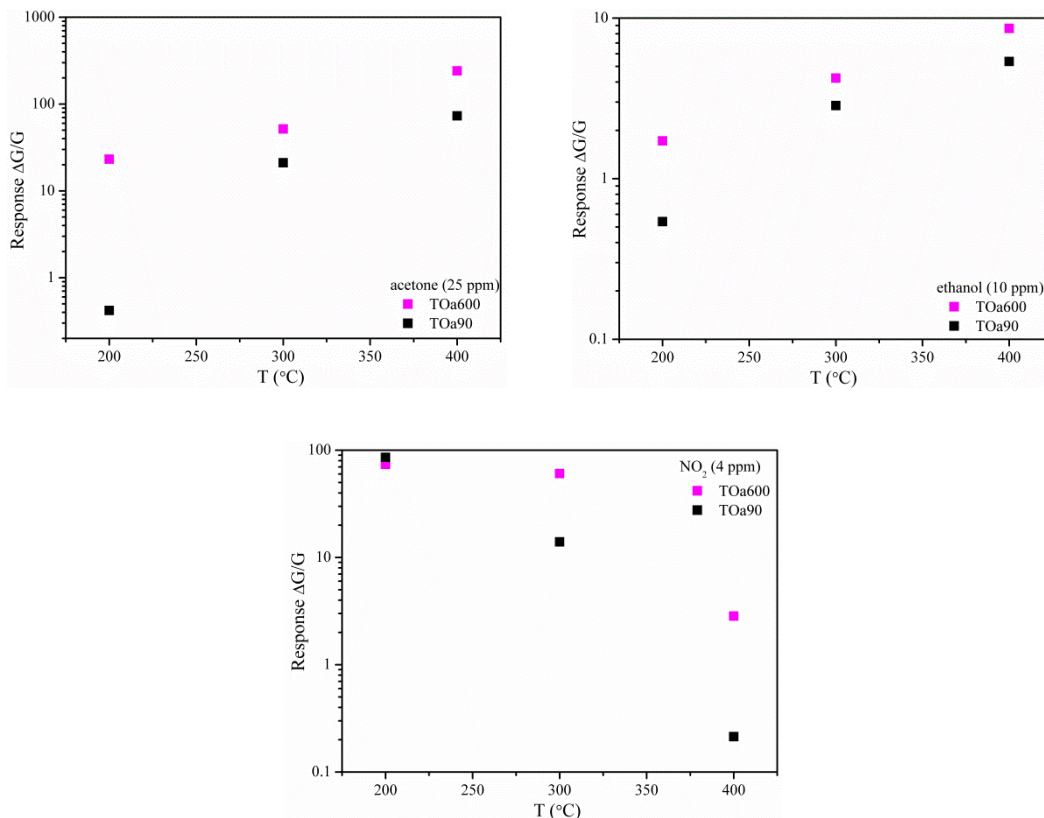


**Figure VI-7: Gas sensing performance of TOa samples at: 100 ppm of CO (upper-left); 800 ppm of H<sub>2</sub> (upper-right); 25 ppm of acetone (middle-left); 10ppm of ethanol (middle-right); 4 ppm of NO<sub>2</sub> (lowest).**

### VI.2.2 Characterization of the gas sensing properties of TOa and TOb samples

For the sake of reproducibility and to discuss data obtained in the same experimental conditions, the gas sensing tests were performed by using layers made of TOa or TOb nanoparticles. The corresponding dynamic gas sensing results are shown in Figure VI-8. For data recorded at 200 °C, 300 °C and 400 °C, it can be concluded that the TOa samples (TOa<sup>90</sup> and TOa<sup>600</sup>) which were prepared in acidic conditions yielded higher gas sensing signals than those (TOb<sup>90</sup> and TOb<sup>600</sup>) prepared in basic medium. On the other hand, TOb samples showed an irregular response to NO<sub>2</sub> (the conductance increases while exposure to NO<sub>2</sub>).

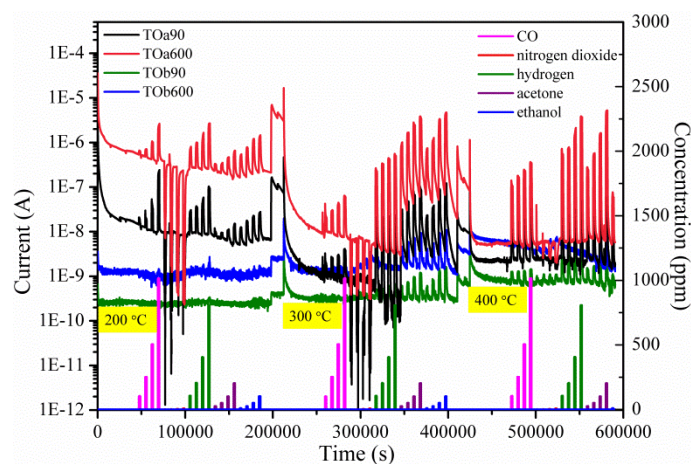


**Figure VI-8: The dynamic response of gas sensing performance of TOa and TOb samples.**



The temperature dependence of the device conductance has then been investigated in dry air in the temperature range between 200 and 400 °C, where the main features of oxygen chemisorption lies [1]. To measure steady state values, data reported in Figure VI-9 have been acquired waiting about 10 hours for the conductance reaching a stable value after the temperature is changed.

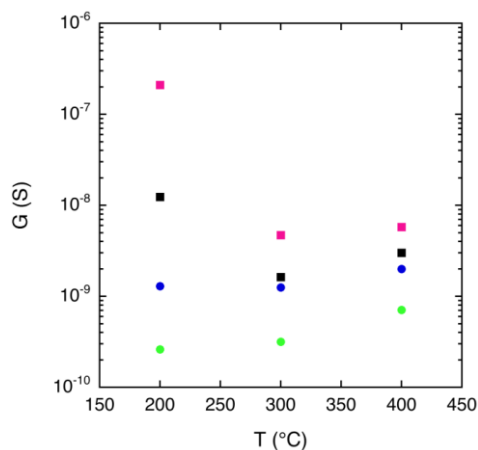


**Figure VI-9: Temperature dependence of the sensor conductance measured in dry air for the TOa<sup>90</sup> (black), TOa<sup>600</sup> (pink), TOB<sup>90</sup> (green) and TOB<sup>600</sup> (blue) samples.**

Materials prepared under acidic conditions show large conductance variation as a function of temperature (Figure VI-9). Thus, TOa samples present a conductance minimum at the temperature of 300 °C, which is commonly explained in literature as the fingerprint of oxygen chemisorptions [1]. This process is thermally activated, thus, increasing temperature causes the material to increase the population of chemisorbed oxygen. As a consequence, electrons are withdrawn from the conduction band and the material conductance drops. Further increasing the device temperature, desorption phenomena start to dominate over adsorption and the population of chemisorbed oxygen decreases. As a consequence, the electrons release back to the conduction band and the conductance increases again. On the contrary, TOB samples do not feature such characteristic minimum; instead, their conductance shows weak temperature dependence. Beside this difference, it is worth noting that TOa samples are systematically more conductive than TOB samples and, given the synthesis conditions (basic/acidic), the material treated at 600 °C is more conductive than the material treated at 90°C.

Gas sensing properties have been investigated in the same temperature range, revealing the important effects induced by the synthesis and thermal treatment conditions. As an example, Figure VI-10 (a) reports the time dependence of the sensor signal acquired with TOa devices during the exposure to NO<sub>2</sub> and H<sub>2</sub>. The sensor response shows the typical behavior of an n-type sensing mechanism: the material conductance increases upon exposure to reducing gases (CO) and decreases upon exposure to oxidizing gases (NO<sub>2</sub>). Differently, TOB samples

feature a conductance increase for both gases, suggesting the occurrence of more complex phenomena (Figure VI-10 (b)). The spectrum of tested chemicals has been expanded, including other reducing gases such as carbon monoxide, acetone and ethanol. The temperature dependence of the response to reducing gases is shown in Figure VI-10 (c) – (f).

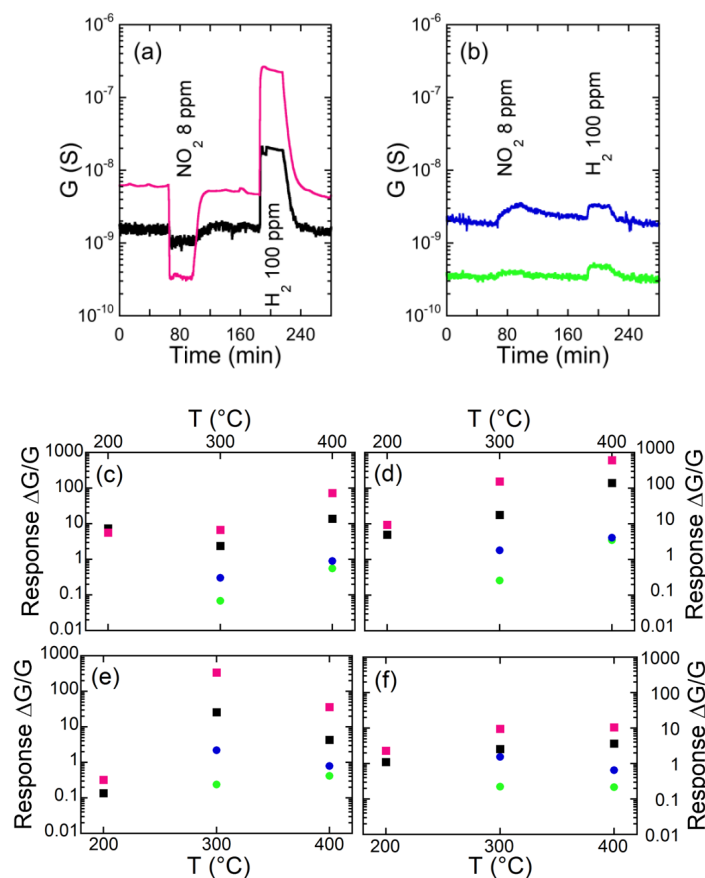


**Figure VI-10: Gas sensing characterization of TOa<sup>90</sup> (black), TOa<sup>600</sup> (pink), TOB<sup>90</sup> (green) and TOB<sup>600</sup> (blue) samples. Dynamic response to 8 ppm of NO<sub>2</sub> and to 100 ppm of H<sub>2</sub> exhibited by samples prepared in acidic conditions (a) and in basic conditions (b) at the working temperature of 300 °C. Temperature effects on the response amplitude measured for reducing gases: 1000 ppm of CO (c), 800 ppm of H<sub>2</sub> (d), 25 ppm of acetone (e), 10 ppm of ethanol (f).**

All sensors exhibited a regular n-type response to this set of compounds, with TOa samples showing responses higher (at least 1 order of magnitude) than those of TOB samples. Within TOa samples (as well as within TOB samples) performances are enhanced by the 600 °C thermal treatment. Thus, devices based on TOa<sup>600</sup> nanopowders showed the highest sensor responses at 400 °C to H<sub>2</sub> (100-450 for 100-800 ppm), CO (7-18 for 10-100 ppm), acetone (200-1500 for 25-200 ppm) and ethanol (7-450 for 10-100 ppm). A comparison with the literature indicates that this material competes well with state-of-the-art chemiresistors based on pure SnO<sub>2</sub>, in terms of both response amplitude and selectivity (Table VI-6) [2-8]. The response amplitude to ethanol is comparable to that measured for SnO<sub>2</sub> layers with sensing performance optimized by means of different strategies, including reduction of the grain size

down to 3.5 nm or by three dimensional hierarchical morphology [2,3].

Material structure	working T (°C)	resp.@ H <sub>2</sub> Conc.	resp.@ C <sub>3</sub> H <sub>6</sub> O Conc.	resp.@ C <sub>2</sub> H <sub>6</sub> O Conc.	resp.@ CO Conc.	ref.
TOa <sup>600</sup>	300	47 @ 100ppm	823 @ 100ppm	1591 @ 100ppm	0.95 @ 100ppm	this work
TOa <sup>600</sup>	300	87 @ 200ppm		1072 @ 50ppm	1.54 @ 250ppm	this work
Small diameter nanoparticles	350	120 @ 200ppm	--	1000 @ 50ppm	70 @ 200ppm	[2]
Hierarchical nanocones	325	--	175 @ 100ppm	100 @ 100ppm	--	[3]
Nanowire network	250	9 @ 100ppm	--	300 @ 100ppm	1 @ 100ppm	[4]
Nanowire network	450	2 @ 100ppm	--	62 @ 100ppm	2.4 @ 100ppm	[5]
Hollow nanospheres	250	--	--	30 @ 50ppm	--	[6]
biomorphic architecture	170	--	--	95 @ 100ppm	--	[7]
Nanowire network	400	3.1 @ 100ppm	9.6 @ 100ppm	10.5 @ 100ppm	3.3 @ 100ppm	[8]

**Table VI-6: Gas sensing performance of the TOa<sup>600</sup> materials and comparison with responses to hydrogen (H<sub>2</sub>), acetone (C<sub>3</sub>H<sub>6</sub>O), ethanol (C<sub>2</sub>H<sub>6</sub>O), and carbon monoxide (CO) reported in the literature for state-of-the-art chemiresistors based on pure SnO<sub>2</sub>. All of these results have been acquired in the same background (dry air).**

Concerning selectivity, this is usually assessed comparing the response intensity of possible interfering gases to the response intensity of the target compound at the same (or similar) concentrations. The overview provided in Table VI-4 confirms that the response to ethanol is much higher than the response to gases such as H<sub>2</sub> or CO (about 30 and 1500 times respectively), providing a selectivity at least comparable with literature data [2-4]. About acetone, the response intensity comparable to that for ethanol is typically observed in sensors based on pure SnO<sub>2</sub> nanostructures [3], and our results are in line with these observations.

In addition, TOa<sup>600</sup>-based devices exhibited high sensitivity to NO<sub>2</sub> in the 0.5-8 ppm range. However, in contrast to other analytes, sensor responses to NO<sub>2</sub> monotonically decreased with increasing the operating temperature between 200 and 400 °C. The highest sensor responses to NO<sub>2</sub> then reached 100-170 for 1-4 ppm at 200 °C, which competes well with the response of more sophisticated nanostructures [9,10].

### VI.2.3 Discussion

The behavior of oxide semiconductors is usually interpreted in the framework of the space charge layer, which allows rationalizing the interplay between the semiconducting and morphological properties exhibited by the material at the micro-/nanoscale and its macroscopic electrical transport and gas sensing properties [11,12].

Electrical conductance is dominated by the Schottky barrier developed at grain boundaries as a consequence of oxygen chemisorption. This induces the formation of surface acceptor states that capture electrons from the SnO<sub>2</sub> conduction band and rise up a space charge layer exhausted from bulk carriers. The thickness of such a layer ( $L_{SCL}$ ) is calculated from the Debye length and the Schottky barrier height ( $qV_s$ ) [12]:

$$L_{SCL} = L_D \sqrt{\frac{2qV_s}{kT}} \quad (1)$$

Depending on the ratio between the grain diameter ( $D$ ) and  $L_{SCL}$ , three different conduction regimes may be identified [11]: i) if  $2 \cdot L_{SCL} < D$ , the band structure recovers the bulk condition in the inner part of the crystallite (Figure VI-11 (a)); ii) if  $2 \cdot L_D < D < 2 \cdot L_{SCL}$ , the band bending has no more room to restore the bulk condition, but there is still an appreciable bending, i.e. the difference between the maximum and minimum of the band is larger than thermal energy (Figure VI-11 (b)); iii) if  $D < 2 \cdot L_D$ , the band bending is lower than the thermal energy of electrons and the material falls in the so-called flat band condition (Figure VI-11 (c)).

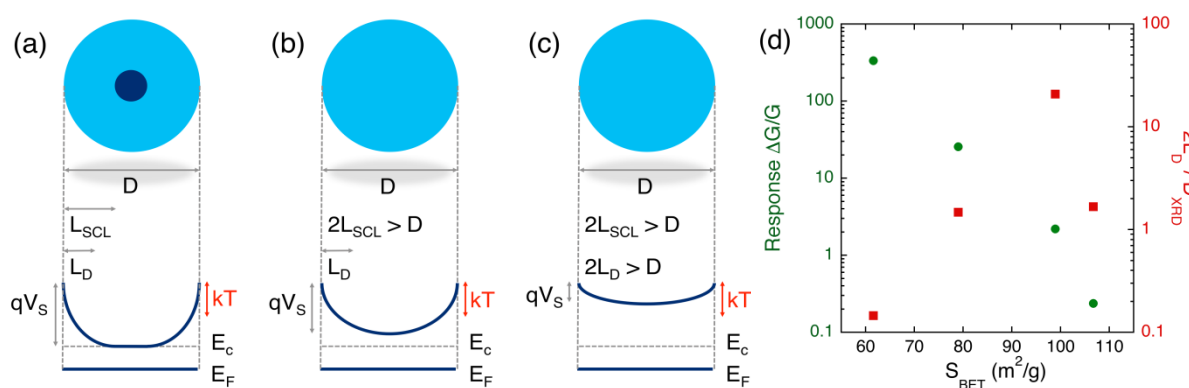


**Figure VI-11: Analysis of size and surface area effects. Schematic representation of the conduction band profile inside a grain as a function of the relationship among the Debye length ( $L_D$ ), the thickness of the space charge layer ( $L_{SCL}$ ) and the grain diameter ( $D$ ) for the three characteristic regimes:  $2 \cdot L_{SCL} < D$ ,**

leaving an inner (blue) area featuring unperturbed bulk properties and a surrounding (light blue) area fully depleted by electrons (a);  $2 \cdot L_D < D < 2 \cdot L_{SCL}$ , with the grain completely depleted by bulk electrons but a bend bending larger than the thermal energy (b);  $d < 2 \cdot L_D$ , with the grain completely depleted by bulk electrons and bend bending smaller than the thermal energy (c). Relationship among the response amplitude (toward 25 ppm of acetone, measured at the working temperature of 300 °C), the surface area ( $S_{BET}$ ) and the  $2 \cdot L_D / D_{XRD}$  ratio, (d).

On the other hand, all gas-sensing measurements are consistent with the opposite behavior: the response amplitude systematically decreases with the increase in the surface area. As an example, the response to 25 ppm of acetone at the temperature of 300 °C is shown in Figure VI-11 (d). Similarly, with respect to the  $2 \cdot L_D / D$  ratio, a counterintuitive behavior can be observed: the  $TOa^{600}$  sample is the only one featuring a bulk inner region ( $2 \cdot L_D / D < 1$ ) not affected by gas-sensing phenomena, but it is much more performing than all other samples working in the complete depletion regime.

Considering also the anomalous response exhibited by  $TOb$  samples to  $NO_2$ , all of these results suggest that additional mechanisms dominate the gas sensing mechanism. Electrical and gas sensing results indicate that samples are first classified according to the preparation conditions, in particular the acidic/basic preparation conditions, which leave potassium residuals in different amounts, larger for samples prepared without acid (Table IV-4, XPS measurements).

The presence of potassium does not have much effect on the Fermi-level energy (as reported in Table IV-3,  $E_{vf}$  is the same for  $TOa^{90}$  and  $TOb^{90}$  samples) but deeply influences the surface chemistry of materials. Its segregation at the grain surface is likely the reason of the anomalous response of  $TOb$  samples to  $NO_2$  and the suppressed response to reducing gases. Additionally, the treatment at 600 °C promotes the stabilization of grains according to a more crystalline degree, as suggested by the narrower Raman peaks, which has been proposed in literature as beneficial for gas sensing [13].

These results provide an important reference for the synthesis of nanomaterials. Indeed, effects arising from residual contamination in metal oxide nanostructures have been weakly investigated, especially concerning their impact on device and gas sensors performance. Some studies have been reported focusing mainly on chlorides, showing detrimental effects in terms of surface area [14] and modifications in the reaction mechanism of  $SnO_2$  with CO, the latter slightly reducing (by a factor of 2) the response amplitude to CO for samples prepared from tin tetrachloride with respect to that for samples prepared from tin hydroxide acetate [15]. Nevertheless, none of these previous studies show effects comparable to those observed in the present work, in which the whole set of morphological, structural, electrical and gas sensing measurements suggests the capability of potassium cation to decreasing the response to gases by orders of magnitude, despite a clear opposite trend in the material microstructure.

### VI.3 Electrical and gas sensing characterization of oxohydroxoorganotin materials (OXT5a)

Finally, one of the hybrid oxohydroxoorganotin materials prepared in chapter V was also investigated in gas sensor devices. Thus, films of oxohydroxoorganotin **OXT5a** were prepared using the procedure as described in V.2 (c) of Chapter V. They underwent a stabilization process at 100 °C for 10 hours in the gas sensing chamber and the dynamic gas sensing curves were recorded at 100 °C and 200 °C as depicted in Figure VI-12.

First of all, the data suggest the hybrid films behave as a n-type semiconducting material. Indeed, the conductance of these films increased when exposed to a reducing gas as hydrogen and decreased in the presence of an oxidizing gas as NO<sub>2</sub> (Figure VI-12, left). The results also reveal that gas selectivity has been successfully achieved at rather low temperature, i.e. 100 °C. Thus, **OXT5a** films showed at 100 °C quite nice selectivity towards 100, 200 and 400 ppm of H<sub>2</sub> (gas response of about 13, 30 and 49, respectively) and 1, 2, 4 ppm of NO<sub>2</sub> (gas response: 1.33, 8.13 and 18.98, respectively) among the other testing gases (CO, ethanol and acetone) (Figure VI-13A). It is worthwhile mentioning that this selectivity is rather unusual at such low temperature compared to literature data [16]. Furthermore, when the temperature rose up to 200 °C, the hydrogen sensing responses collapsed below 2 while the gas sensing signals for NO<sub>2</sub> surprisingly increased nearly 2.5 times compared to those recorded at 100 °C. Even though the gas sensing signals of the rest of the testing gases also slightly raised at 200 °C (Figure VI-13B), the gas response values still remained low comparing to those of NO<sub>2</sub>. As a consequence, **OXT5a** films showed an obvious selectivity towards NO<sub>2</sub> at 200 °C. In addition, regardless the temperature used, **OXT5a** exhibited prominent gas sensitivity to the low concentrations (1, 2, 4 and 8 ppm) of NO<sub>2</sub> which makes it a rather sensitive material for NO<sub>2</sub> detection. The possible explanation of this interesting gas sensing behavior of **OXT5a** could be attributed to the insertion of the thermally activated organic functionality – hexyl carbon chain for the formation of Sn-C bond, which modified the electronic structures of the oxohydroxoorganotin sites (Table VI-7), is activated at 200 °C rather than 100 °C (Figure VI-13) so the structural geometry of its pore size at 100 °C (physically), which allowed the first passage of H<sub>2</sub> and then the more complex chemical reaction happened at 200 °C (chemically) at the surface of the oxohydroxoorganotin layer of **OXT5a**. That would thus, favoring the NO<sub>2</sub> adsorption and increasing its response amplitude. The energy value of Sn3d<sub>3/2</sub> shifts from 495.4/495.5 to 495.2 could be the proof of the effect of linked carbonic functionality within the oxohydroxoorganotin framework (Table VI-7). Therefore, at 100 °C, physical effects (pore size) dominate while at higher temperature chemical effects dominate.

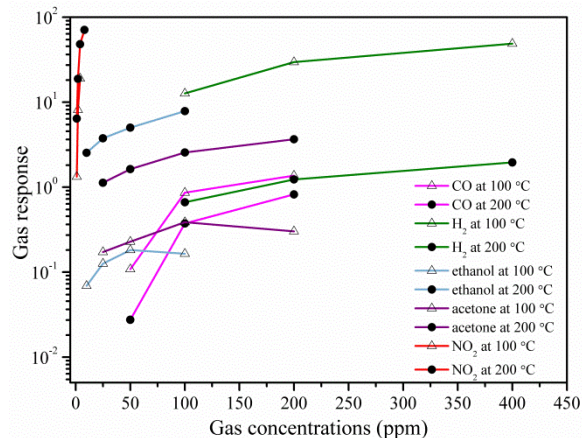
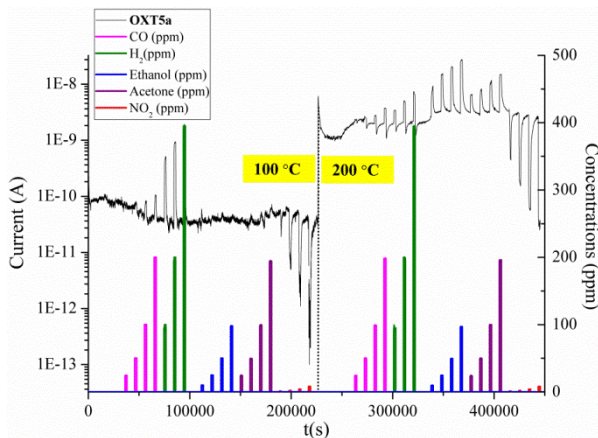


Figure VI-12: The dynamic gas sensing performance (left); the gas sensing response (right) of OXT5a towards CO (pink), H<sub>2</sub> (green), ethanol (blue), acetone (purple) and NO<sub>2</sub> (red) at 100 °C and 200 °C.

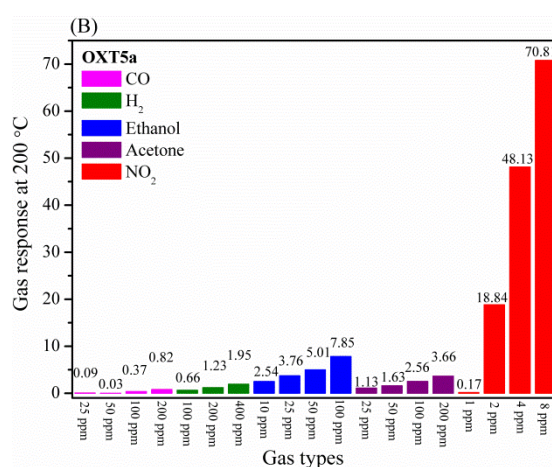
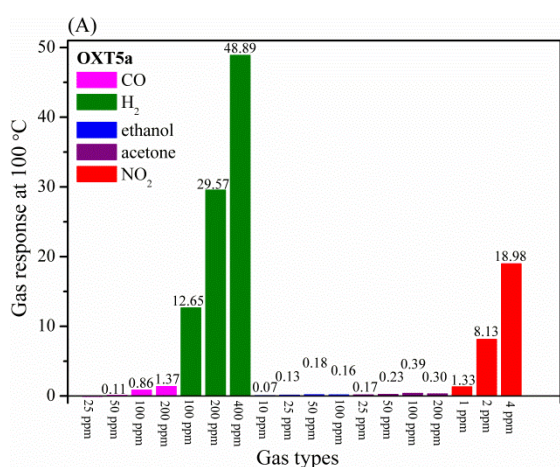


Figure VI-13: Gas response of OXT5a towards CO (pink), H<sub>2</sub> (green), ethanol (blue), acetone (purple) and NO<sub>2</sub> (red): (A) at 100 °C; (B) at 200 °C.

Tin oxide-based materials	Sn 3d <sub>3/2</sub> (eV) <sup>a</sup>	Sn 3d <sub>5/2</sub> (eV) <sup>a</sup>	O 1s (eV) <sup>a</sup>
OXT5a	495.2	486.8	530.8
TOa <sup>90</sup>	495.4	487.0	530.9
TOa <sup>600</sup>	495.5	487.1	531.0
TOb <sup>90</sup>	495.5	487.1	530.9
TOb <sup>600</sup>	495.4	486.9	530.8

Table VI-7: Comparison of energy values from XPS spectra between tin dioxide and hybrid oxohydroxoorganotin materials.



Typically the gas response of **OXT5a** is proportional to the gas concentration except for exposing to ethanol and acetone at 100 °C (Figure VI-14). The gas response values at 100 °C of ethanol and acetone are considerably low (0.07-0.39), indicating that there is almost no strong interaction between the surface of oxohydroxoorganotin layer and these testing gases. In addition, the gas responses to CO and H<sub>2</sub>, which are better at lower temperature (100 °C), show the distinct gas sensing behavior rather than those of ethanol, acetone and NO<sub>2</sub> gases. Normally, for metal-oxide materials, the possible theoretical explanation for the higher response intensity exhibited with increasing sensor temperature is based on the amount of oxygen atoms decreases; the more oxygen vacancies (concentrations) are formed and the more activating sites are provided for gas sensing [16]. This general rule is also often extended to materials other than metal-oxides, such as, for example, sulfide materials [17], but as for the special sensing behavior of **OXT5a**, there is no any specific knowledge about the sensing material. It is also noteworthy to mention that the response to the set of gases do not group based on their reducing/oxidizing nature. Differently, a similar behavior exhibited by the smallest molecules (H<sub>2</sub> and CO, which show optimal response at 100 °C) and larger molecules (C<sub>2</sub>H<sub>5</sub>OH, C<sub>3</sub>H<sub>6</sub>O and NO<sub>2</sub>, which show optimal response at 200 °C) as shown in Figure VI-14. Yet, this may suggest as above an involvement of physical effect (pore size) at low temperature (100 °C).

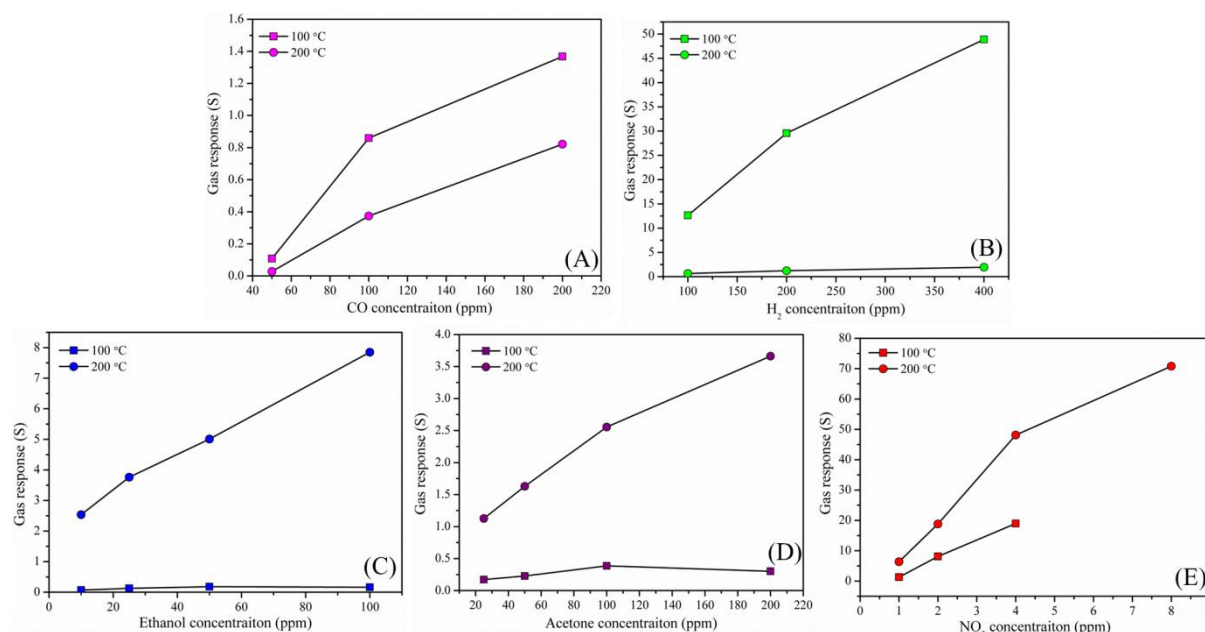


**Figure VI-14: Gas responses of OXT5a to: (A) CO; (B) H<sub>2</sub>; (C) ethanol; (D) acetone; (E) NO<sub>2</sub> at the testing temperatures of 100 °C and 200 °C. [The circles represent tests performed at 100 °C while the squares represent tests performed at 200 °C.]**

These data confirm that oxohydroxoorganotin hybrid materials are able to detect gases when used as active layer in chemoresistors. Indeed, **OXT5a** material is the second example of organotin-based hybrid material showing gas sensing properties after the first



demonstration of selective detection of H<sub>2</sub> using self-assembled oxohydroxoorganotin thin films [18, 19]. The new findings in this study rely on the ability of **OXT5a** material to detect both reductive and oxidative gases as H<sub>2</sub> and NO<sub>2</sub> at 100 °C and to be selective to NO<sub>2</sub> at 200 °C. As in the previous works of the group, all these findings are rather surprising because, as shown in chapter 5, the hybrid materials do not have crystalline SnO<sub>2</sub> structure and the temperature used for gas sensing tests are sufficiently low to prevent any decomposition of the sensing layer. In addition, these results indicated some differences between **OXT5a** material and SnO<sub>2</sub> particles synthesized in chapter IV. The first discrepancy is the efficiency of the hybrid material to detect H<sub>2</sub> and NO<sub>2</sub> at temperature below 100 °C. The second one concerns the high gas sensing selectivity of the hybrid layers. Finally, due to the amorphous character of the hybrid films, the sensing mechanism is probably different as proposed for self-assembled oxohydroxoorganotin thin films [18].

#### VI.4 Conclusion

In the presence of reducing (H<sub>2</sub>, CO, acetone or ethanol) and oxidizing (NO<sub>2</sub>) gases, the SnO<sub>2</sub> nanoparticles prepared in chapter IV led to highly sensitive, reversible and reproducible responses. The best sensing performances were obtained by employing SnO<sub>2</sub> nanoparticles prepared under acidic conditions and calcined in air because of a lower amount of potassium cations and higher crystallinity. This study suggests the detrimental influence of a small amount of alkali metal cations on the gas sensing response of tin dioxide nanoparticles although the material nanostructure fulfills all of the requirements for good sensor responses. The careful determination of the surface chemical composition of tin oxide nanoparticles appears to be a key parameter for gas sensing properties, which opens the way for a new approach for the rationalization of gas sensing responses.

On the other hand, the oxohydroxoorganotin layers bearing hexyl groups, **OXT5a**, showed unexpected gas selectivity for H<sub>2</sub> and NO<sub>2</sub> at rather low temperature, i.e. 100 °C. Thus, both the standout gas sensitivity and gas selectivity of **OXT5a** have been shown by the detection of reducing (H<sub>2</sub>, CO, acetone and ethanol) and oxidizing (NO<sub>2</sub>) gases, which the best gas responses to 100, 200 and 400 ppm of H<sub>2</sub> are 12.65, 29.57 and 48.89, individually at 100 °C and the best gas signals to 2, 4 and 8 ppm of NO<sub>2</sub> are 18.84, 48.13 and 70.87, separately at 200 °C whereas **OXT5a** displayed almost no gas sensing performance to the rest of gases tested. To the best of our knowledge, **OXT5a** hybrid material constitutes one of the rare examples of organic-inorganic hybrid layer able to detect gases, which validates the possibility to tune the selectivity by well design of organotin structure with an organic functionality. Finally, further understanding of these findings for oxohydroxoorganotin materials, both experimentally and theoretically, are required to highlight new features in gas sensing mechanisms and to design new active layers for gas sensors.

## References:

- [1] P. T. Moseley, Norris, J. O. W., D. E. Williams, in the book of “*Techniques and Mechanisms in Gas Sensing*”, Adam Hilger: Bristol, England, **1991**.
- [2] T. Kida, T. Doi, K. Shimanoe, *Chem. Mater.* **2010**, *22*, 2662– 2667.
- [3] Y.-X. Li, Z. Guo, Y. Su, X.-B. Jin, X.-H. Tang, J.-R. Huang, X.-J. Huang, M.-Q. Li, J.-H. Liu, *ACS Sens.* **2017**, *2*, 102– 110.
- [4] I.-S. Hwang, S.-J. Kim, J.-K. Choi, J.-J. Jung, D. J. Yoo, K.-Y. Dong, B.-K. Ju, J.-H. Lee, *Sens. Actuators, B* **2012**, *165*, 97– 103.
- [5] I.-S. Hwang, J.-K. Choi, H.-S. Woo, S.-J. Kim, S.-Y. Jung, T.-Y. Seong, I.-D. Kim, J.-H. Lee, *ACS Appl. Mater. Interfaces* **2011**, *3*, 3140– 3145.
- [6] R. Von Hagen, M. Sneha, S. Mathur, *J. Am. Ceram. Soc.* **2014**, *97*, 1035– 1040.
- [7] F. Song, H. Su, J. Han, J. Xu, D. Zhang, *Sens. Actuators, B* **2010**, *145*, 39– 45.
- [8] N. V. Hieu, H.-R. Kim, B.-K. Ju, J.-H. Lee, *Sens. Actuators, B* **2008**, *133*, 228– 234.
- [9] N. M. Shaalan, T. Yamazaki, T. Kikuta, *Sens. Actuators, B* **2011**, *156*, 784– 790.
- [10] H. W. Kim, H. G. Na, Y. G. Kwon, S. Y. Kang, M. S. Choi, J. H. Bang, P. Wu, S. S. Kim, *ACS Appl. Mater. Interfaces* **2017**, *9*, 31667– 31682.
- [11] J. W. Orton, M. J. Powell, *Rep. Prog. Phys.* **1980**, *43*, 1263– 1307.
- [12] N. Barsan, U. Weimar, *J. Electroceram.* **2001**, *7*, 143– 167.
- [13] M. D. Antonik, J. E. Schneider, E. L. Wittman, K. Snow, J. F. Vetelino, R. J. Lad, *Thin Solid Films* **1995**, *256*, 247– 252.
- [14] A. G. Shastri, A. Datye, J. Schwank, *Appl. Catal.* **1985**, *14*, 119–131.
- [15] R. G. Pavelko, J.-K. Choi, A. Urakawa, M. Yuasa, T. Kida, K. Shimanoe, *J. Phys. Chem. C* **2014**, *118*, 2554– 2563.
- [16] S. Cui, H. Pu, S. A. Wells, Z. Wang, S. Mao, J. Chang, M. C. Hersam, J. Chen, *Nat. Commun.* **2015**, *6*, 8632.
- [17] H.-Y. Li, J.-W. Yoon, C.-S. Lee, K. Lim, J.-W. Yoon, J.-H. Lee, *Sens. Actuators, B Chemical*, **2018**, *255*, 2963-2970.
- [18] L. Renard, H. Elhamzaoui, B. Jousseume, T. Toupance, G. Laurent, F. Ribot, H. Saadaoui, J. Brötz, H. Fuess, R. Riedel, A. Gurlo, *Chem. Commun.* **2011**, *47*, 1464-1466.
- [19] L. Renard, J. Brötz, H. Fuess, A Gurlo, R. Riedel, T. Toupance, *ACS Appl. Mater. & Interfaces* **2014**, *6*, 17093-17101.

## Chapter VII General conclusion and outlook

Environmental issues related to the wide use of fossil fuels and volatile organic compounds (VOC) along with the industrial applications of dangerous gasses as hydrogen require the development of efficient devices for the selective detection of these gases at very low level. In this context, solid-state gas sensors based on semiconducting metal oxide sensing layers play a major role, in particular chemiresistors. Thus, tetragonal tin dioxide appears to be the most commonly employed and the best-understood prototype material in commercial gas sensors. Nonetheless, despite the recent advances achieved in the field of gas detection, the design of efficient and selective new systems is still needed. The aim of this work was therefore to draw new prospects in the field of tin oxide based gas sensors by finely tuning the chemical nature, the texture and the morphology of the active layer. Two main approaches were thus investigated to prepare new materials. The first one involved a fine tuning of the hydrothermal conditions to grow well-defined tin dioxide particles from a widely available commercial colloid. The second approach, which was much more original, consisted in the synthesis of molecular organometallic single precursors leading to organotin hybrid materials after hydrolysis and condensation according to the sol-gel process.

First of all, tin dioxide ( $\text{SnO}_2$ ) nanoparticles were straightforwardly synthesized using an easily scaled-up liquid route that involves the hydrothermal treatment, either under acidic or basic conditions, of a commercial tin dioxide particle suspension including potassium counter-ions. After further thermal post-treatment, the as-obtained nanomaterials have been thoroughly characterized by FTIR and Raman spectroscopy, powder X-ray diffraction (XRD), transmission electron microscopy (TEM), X-ray photoelectron spectroscopy (XPS) and nitrogen sorption porosimetry. Whatever the conditions used, XRD and Raman spectroscopy confirmed the formation of tetragonal cassiterite  $\text{SnO}_2$  nanoparticles. However, varying pH conditions and temperature of the thermal treatment provided cassiterite  $\text{SnO}_2$  nanoparticles with crystallite sizes ranging from 7.3 to 9.7 nm and Brunauer-Emmett-Teller surface areas ranging from 61 to 106  $\text{m}^2\cdot\text{g}^{-1}$ , acidic conditions favouring potassium cation removal as evidenced by XPS studies. Exposed to reducing gas [hydrogen ( $\text{H}_2$ ), carbon monoxide (CO), ethanol ( $\text{C}_2\text{H}_5\text{OH}$ ), acetone ( $\text{C}_3\text{H}_6\text{O}$ )] or oxidizing [nitrogen dioxide ( $\text{NO}_2$ )] gases, layers of these  $\text{SnO}_2$  nanoparticles led to highly sensitive, reversible and reproducible responses. The sensing results were discussed in regard to crystallite size, specific area, valence band energy, Debye length and chemical composition. Results highlight the impact of the counter-ion residuals, which affect the gas-sensing performance to an extent much higher than size and surface area effects. Thus, it is noteworthy to focus on the fact that how the composition of commercial  $\text{SnO}_2$  colloidal suspension can affect the gas sensing behavior to an extent according to the amount of remaining counter-ions although the size effect are often found in the literature both from a theoretical [1] and an experimental [2] point of view to rule the

sensing efficiency, i.e. the lower the crystallite size, the higher the sensor response. Thus, tin dioxide nanoparticles prepared under acidic conditions and calcined in air at 600 °C showed the best sensing performances due to lower potassium cation amount and higher crystallinity. As far as selectivity is concerned, the response of these particles to ethanol is much higher than the response to gases such as H<sub>2</sub> or CO (about 30 and 1500 times respectively), leading to a selectivity at least comparable with literature data [3,4]. About acetone, responses are similar to those with ethanol which is in line with what it was reported with more complex nanostructures [5]. This study, which was recently published [6], provides an important reference for the synthesis of SnO<sub>2</sub> nanostructures to interpret the gas sensing performance from the residual contamination aspect resided in the commercial colloid precursor including polypyrrole and K<sup>+</sup> counter-ions.

In a second approach, four functional trialkynylorganotins bearing hexyl (**5a**), butylene (**5b**), benzyl (**5c**) and thiophenylbutyl (**5d**) were prepared with success through the selective alkylation of tetraphenylethynyltin by an equimolar amount of the suitable Grignard reagent in the presence of anhydrous solvents of toluene and diethyl ether (2:1) at 40 °C for 18 hours. These optimized experimental conditions for synthesizing these organotins do not only effectively shorten the conventional synthetic methods but also highlight the diversity of the organic functionalities within the alkynylorganotin structure which opens new avenues for the synthesis of dialkynyldiorganotin or alkynyltriorganotin derivatives for further organotin chemistry studies by the appropriately well-controlled proportion between tetraphenylalkynyltin and Grignard reagent. Organic-inorganic tin-based hybrid materials were then synthesized successfully from these alkynylorganotins using the sol-gel process. The hydrolysis-condensation of the four functional alkynylorganotins yielded oxohydroxoorganotin hybrid powders and layers (**OXT5a**, **OXT5b**, **OXT5c** and **OXT5d**) which were thermally stable up to 200 °C under air. Bulk and surface chemical composition performed by FTIR, EDX and XPS studies revealed that the organic functionality was preserved during the hydrolysis-condensation processes and that tin-oxide network was formed with remaining dangling hydroxyl functions. In particular, a chemical formula could be proposed for **OXT5a**. On the other hand, the surface morphology and texture of the hybrid films strongly depend on the organic functionality nature. The hybrid materials including flexible alkyl units as **OXT5a** and **OXT5d** led to the denser and more homogeneous layers, whereas more porous textures were obtained for **OXT5b** and **OXT5c** which includes more rigid organic groups. The electronic properties of these hybrid materials were also determined. The energy band gap varied from 3.64 to 4.61 eV depending on the organic function, whereas the valence band energy position towards Fermi level position was quite constant, i.e. 1.7-1.8 eV. Finally, as hybrid **OXT5a** led to the better defined films, class II organotin hybrids including hexyl groups in which both organic and inorganic networks are tightly associated through strong covalent bonds could be fast produced and easily fabricated on the gas sensing substrate. Exposed to reducing gas [hydrogen (H<sub>2</sub>), carbon monoxide (CO), ethanol

(C<sub>2</sub>H<sub>5</sub>OH), acetone (C<sub>3</sub>H<sub>6</sub>O)] or oxidizing [nitrogen dioxide (NO<sub>2</sub>)] gases, the hybrid **OXT5a** layers gave significant responses towards hydrogen (H<sub>2</sub>) and nitrogen dioxide (NO<sub>2</sub>) at two relatively low testing temperatures (100 °C and 200 °C). The sensing responses recorded are typical of a n-type material as already reported by our group for more complex self-assembled organotin hybrids [7]. Compared to the latter studies, the novelty with the **OXT5a** hybrid relies on its ability to detect selectively NO<sub>2</sub> at 200 °C. However, the gas sensing mechanism still remains unclear at this stage. The following explanation might be proposed to rationalize this unexpected selectivity: at 100 °C, the oxohydroxoorganotin layer (**OXT5a**) selects gas molecules primarily on the basis of a size-exclusion process; at 200 °C, the more complex chemical reaction generated on the surface of **OXT5a** layer, which dominates the selective gas sensing properties of oxohydroxoorganotin hybrid materials. Usually, the inorganic compounds show high chemical and thermal stability, and they can be synthesized by simple and low-cost processes and then deposited by various standard techniques, while organic compounds show novelty and versatility from the synthetic point of view that, together with actual functional reactivity, therefore allows the modification of the molecular structure to enhance interaction of the sensing material with specific analytes. In addition, the drop casting method was chosen in this work as it does serve a quick and accessible method to generate thin film on relatively small substrates for gas sensing application.

Regardless of the breakthrough in gas sensing area brought from the combination of oxohydrotin units and carbon chain, several challenges in realizing the oxohydroxoorganotin hybrid material (**OXT5a**) as a potential selective gas sensor have remained unsolved during the course of this research:

- 1) reproducibility issues for the synthesis of the trialkynylorganotin (**5b**);
- 2) the low thermal stability of oxohydroxoorganotin hybrids which could increase the chance of structural damages during the aging process or gas sensing measurement;
- 3) the difficulty to reproduce the gas sensing data for oxohydroxoorganotin material (**OXT5a**) which is probably due to the control of sol-gel fabrication but there are still many factors behind which will affect the gas sensing result;
- 4) the lack of optimal sol-gel conditions to fabricate the ideal thin films for the rest of oxohydroxoorganotin materials (**OXT5b**, **OXT5c**, and **OXT5d**.) to obtain the viable gas sensing data;
- 5) the unrevealed gas sensing mechanism of this type of hybrid oxohydroxoorganotin materials which requires more complex gas sensing instruments to explore the possible explanation.

To extend this work in the future, more different types of organic functionalities should be employed in the oxohydroxoorganotin hybrid materials synthesis and the sol-gel condition should be well-controlled for further studies to offer a complete view of the role of organic moieties in gas sensing studies. Meanwhile, the more complex experimental facility for *in situ* and *operando* spectroscopic characterisation of gas-sensing, electrical and catalytic properties

should be introduced as it is the key component for gas sensing studies. The system which couples electrical (dc conductance and ac impedance spectroscopy) and spectroscopic techniques (Raman spectroscopy and XAS/EXAFS) with on-line gas analysis (micro GC, FTIR gas analyzers, O<sub>2</sub>-sensor) will establish the correlation between the sensor activity and the spectroscopic data obtained under the same conditions and on the same sample. The further analysis could be therefore investigated: (i) gas phase changes and reaction products (if any) from the on-line gas analysis, (ii) adsorbed surface species, (iii) changes in the oxide surface and bulk (if any) and correlate all this with simultaneously monitoring the gas composition and sensor activity. This deep insight into gas sensor operation obtained on functionality-controlled oxohydroxoorganotin hybrids could help in better understanding of surface and bulk reactions responsible for gas sensing effects and will finally lead to the development of better sensors with increased selectivity and sensitivity in the chemical determination of gases.

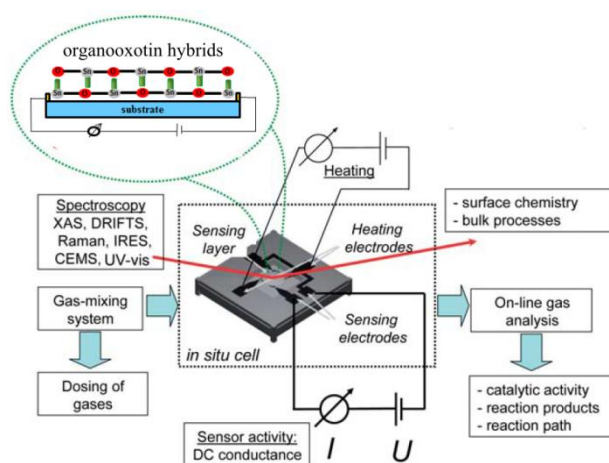


**Figure VII-1:** The ideal set-up for operando and in-situ characterization of gas-sensing properties proposed for the future study. The system couples electrical (dc conductance and ac impedance spectroscopy) and spectroscopic techniques (Raman spectroscopy and XAS/EXAFS) with on-line gas analysis (micro GC, FTIR gas analyzers, O<sub>2</sub>-sensor). Using this system, it can help to establish the correlation between the sensor activity and the spectroscopic data obtained under the same conditions and on the same sample.

In summary, two main novelties were highlighted in this PhD thesis: 1) the impact of the counter-ion residuals from the commercial colloidal suspension on the SnO<sub>2</sub> gas sensing performance despite of the crystalline size and surface area effects, which brings a new vision to explain the SnO<sub>2</sub> gas sensing behavior; 2) the straightforward preparation of functional organotins bearing diverse organic functionalities able to yield class-II tin-based hybrid materials in three steps from commercial products possess good selective gas sensing properties for H<sub>2</sub> and NO<sub>2</sub> that make them the possibility to compete with respect to the systems currently in use. In other words, the advent of this type of organotin hybrid materials could revolutionized not only the formation of the carbon-tin bond in organotin chemistry but

also the possible applications in gas sensing field or even the other areas.



## References:

- [1] a) N. Yamazoe, K. Shimano, *J. Electrochem. Soc.*, **2008**, *155*, J85–J92. b) N. Yamazoe, K. Shimano, *J. Electrochem. Soc.*, **2008**, *155*, J93–J98.
- [2] a) N. Yamazoe, *Sens. Actuators, B*, **1991**, *5*, 7–19. b) B. Panchapakesan, D. L. DeVoe, M. R. Widmaier, R. Cavicchi, S. Semancik, *Nanotechnology*, **2001**, *12*, 336–349.
- [3] T. Kida, T. Doi, K. Shimano, *Chem. Mater.* **2010**, *22*, 2662– 2667.
- [4] I.-S. Hwang, S.-J. Kim, J.-K. Choi, J.-J. Jung, D. J. Yoo, K.-Y. Dong, B.-K. Ju, J.-H. Lee, *Sens. Actuators, B* **2012**, *165*, 97– 103.
- [5] Y.-X. Li, Z. Guo, Y. Su, X.-B. Jin, X.-H. Tang, J.-R. Huang, X.-J. Huang, M.-Q. Li, J.-H. Liu, *ACS Sens.* **2017**, *2*, 102– 110.
- [6] S.-H. Lee, S.-H. Lee, V. Galstyan, A. Ponzoni, I. Gonzalo-Juan, R. Riedel, M.-A. Dourges, Y. Nicolas, T. Toupance, *ACS Appl. Mater. Interfaces* **2018**, *10*, 10173–10184.
- [7] (a) L. Renard, H. Elhamzaoui, B. Jousseume, T. Toupance, G. Laurent, F. Ribot, H. Saadaoui, J. Brötz, H. Fuess, R. Riedel, A. Gurlo, *Chem. Commun.* **2011**, *47*, 1464-1466. (b) L. Renard, J. Brötz, H. Fuess, A Gurlo, R. Riedel, T. Toupance, *ACS Appl. Mater. & Interfaces* **2014**, *6*, 17093-17101.

## Appendix

### JCPDS File No. 41-1445

Before analyzing the TEM results, it is complementary to get the complete powder diffraction reported data from JCPDS\* (Table 1). Each interplanar spacing (d-spacing) data relates to the corresponding orientation surface (Miller indices). Hence, by the calculations of the distance ( $d_{hkl}$ ) between two adjacent parallel planes of atoms with the same Miller indices from TEM images, the corresponding surface could be identified which presents the favorable crystallographic orientations of each SnO<sub>2</sub> sample before and after the calcination step.

SnO <sub>2</sub>				Miller indices		
$d_{hkl}$ (Å)	Angle (°)	2*Angle(°)	Intensity	h	k	l
3.347	13.3057023	26.6114046	100	1	1	0
2.6427	16.94672812	33.89345623	75	1	0	1
2.369	18.97518152	37.95036304	21	2	0	0
2.3094	19.48439502	38.96879003	4	1	1	1
2.1189	21.317635	42.63527	1	2	1	0
1.7641	25.89056141	51.78112283	57	2	1	1
1.675	27.37942604	54.75885208	14	2	2	0
1.5934	28.90979418	57.81958835	6	0	0	2
1.4984	30.93611954	61.87223908	11	3	1	0
1.4829	31.29573567	62.59147134	< 1	2	2	1
1.4392	32.35939598	64.71879196	12	1	1	2
1.4155	32.96931069	65.93862137	14	3	0	1
1.356	34.61562967	69.23125933	< 1	3	1	1
1.322	35.63913343	71.27826685	6	2	0	2
1.3141	35.88647211	71.77294423	< 1	3	2	0
1.2733	37.22624546	74.45249093	< 1	2	1	2
1.2147	39.35688096	78.71376192	9	3	2	1
1.1844	40.56965121	81.13930243	3	4	0	0
1.1544	41.85697954	83.71395907	6	2	2	2
1.1492	42.08967019	84.17934037	< 1	4	1	0
1.1167	43.61434015	87.22868031	3	3	3	0
1.0916	44.88304143	89.76608286	7	3	1	2
1.081	45.44533626	90.89067253	8	4	1	1

**Table 1: SnO<sub>2</sub>\_JCPDS\*-41-1445.**

\*JCPDS stands for Joint Committee on Powder Diffraction Standards.

## Debye Length

The density of charge carriers, which is usually considered equal to the density of donors (oxygen vacancies or Sn interstitials in SnO<sub>2</sub>), is calculated as:

$$n = N_C \frac{2}{\sqrt{\pi}} F_{\frac{1}{2}}(\eta_F)$$

Where  $N_C$  is the density of states in the conduction band  $N_C = 2M_C \left( \frac{2\pi m k T}{h^2} \right)^{3/2}$ .

Here  $M_C$  is the number of equivalent minima in the conduction band,  $m$  is the effective electron mass in SnO<sub>2</sub>,  $k$  the Boltzmann constant,  $T$  the temperature in K,  $h$  the Planck constant.

$F_{1/2}$  is the Fermi integral, which is solved numerically:

$$F_{\frac{1}{2}}(\eta_F) = \int_0^{\infty} \frac{\eta^{1/2}}{1 + \exp(\eta - \eta_F)} d\eta$$

Where  $\eta = (E - E_C)/kT$  and  $\eta_F = (E_F - E_C)/kT$

$\eta$  and  $\eta_F$  are calculated starting from VBE values extrapolated from XPS data:

Being  $VBE = E_F - E_V$ ,  $\eta_F$  is conveniently expressed as a function of VBE (and the energy gap  $E_g$ ) as follows:

$$\eta_F = (E_F - E_C)/kT = (E_F - E_C + E_V - E_V)/kT = (VBE - E_g)/kT$$

## Amplitude and Height Parameters for Atomic Force Microscopy

The amplitude parameters are the principal parameters in characterizing the surface topography for AFM study. Table 2 lists the most common parameters together with the definitions. The average roughness ( $R_a$ ) and the root mean square roughness ( $R_q$ ) are the most used amplitude parameters. Particularly, the last one is used to study temporal changes in the creation of a new surface as well as spatial differences when studying the surface feature using different scales. The reason for this is that this parameter is more sensitive to large deviations with respect to the mean line.

Parameter	Definition
Average roughness ( $R_a$ )	Gives the deviation in height. Different profiles can give the same $R_a$ .
	$R_a(N, M) = \frac{1}{N} \sum_{x=1}^N (z(x, y) - \bar{z}(N, M)) \quad (2D)$
	$R_a(N, M) = \frac{1}{NM} \sum_{x=1}^N \sum_{y=1}^M (z(x, y) - \bar{z}(N, M)) \quad (3D)$

---

Root Mean Square (RMS) Represents the standard deviation of surface heights.  
roughness ( $R_q$ )

$$R_q(N, M) = \sqrt{\frac{1}{N} \sum_{x=1}^N (z(x, y) - \bar{z}(N, M))^2} \quad (2D)$$

$$R_q(N, M) = \sqrt{\frac{1}{NM} \sum_{x=1}^N \sum_{y=1}^M (z(x, y) - \bar{z}(N, M))^2} \quad (3D)$$

---

**Table 2: Principle amplitude or height parameters.**

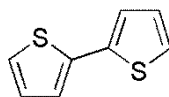
## Experimental part

### I. Organic and organometallic synthesis

#### I.1 Experimental procedure of bithiophene

##### 2,2'-bithiophene (1)

$C_8H_6S_2$  ( $M_W = 166.26$  g/mol)



In a 500 mL three-necked round bottom flask equipped with a reflux condenser and a dropping funnel, a solution of 2-bromothiophene (15.86 g, 97.28 mmol) in 50 mL of anhydrous diethyl ether was added drop by drop to preactivated (addition of dibromoethane (0.6 mL)) magnesium (2.96 g, 121.76 mmol) in 20 mL of anhydrous diethyl ether. The reaction mixture was refluxed at 50 °C for 1 hour and then it was cooled down to room temperature. The black supernatant was transferred under nitrogen via cannula to another dropping funnel and added drop by drop into another 500 mL three necked round bottom flask containing a mixture of 2-bromothiophene (15.86 g, 97.28 mmol), 0.42 g Ni catalyst ( $NidppCl_2$ ), and 40 mL anhydrous diethyl ether. The resulting mixture was refluxed for 15 hours and then cooled down to room temperature. The mixture was carefully quenched by adding 30-40 mL of 1 M HCl and the resulting layers were separated. The organic layer was washed with 100 mL water twice until the pH value equaled to 7, and then dried over anhydrous  $MgSO_4$  and evaporated to give a black oily product. It was purified by column chromatography over silica gel using pentane as eluent ( $R_f = 0.435$ ), followed by evaporating pentane solvent under reduced pressure. The expected product was obtained as colorless oil that converted to a solid after staying at room temperature (yield: 16.03 g, 99 %).

$^1H$ -NMR (300 MHz,  $CDCl_3$ ,  $\delta$  ppm): 7.22 (dd,  $^3J = 5.1$  Hz,  $^4J = 1.2$  Hz, 2H,  $H^1$ ); 7.19 (dd,  $^3J = 3.6$ ,  $^4J = 1.2$  Hz, 2H,  $H^3$ ); 7.03 (dd,  $^3J = 5.1$  Hz,  $^3J = 3.6$  Hz, 2H,  $H^2$ )

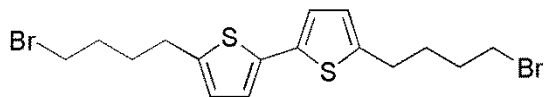
$^{13}C$ -NMR (75.4 MHz,  $CDCl_3$ ,  $\delta$  ppm): 137.5 ( $C^4$ ); 127.9 ( $C^2$ ); 124.4( $C^1$ ); 123.9( $C^3$ )

EI mass: found: 165.99123; calcd: 165.99109 ( $\delta = 0.83$  ppm)

#### I.2 Experimental procedure of bromo-thiophene-based materials

##### 5,5'-dibromobutyl-2,2'-bithiophene (2a)

$C_{16}H_{20}Br_2S_2$  ( $M_W = 436.27$  g/mol)



Using the same equipment as the one described above, *n*-BuLi in hexanes (2.15 M, 30.8 mL, 66.22 mmol) was added dropwise at -20 °C (bath of ethanol cooled by liquid N<sub>2</sub>) to a solution of bithiophene (5 g, 30.07 mmol) at -20 °C (ethanol and liquid nitrogen) in 75 mL of anhydrous THF. The mixture was stirred for 45 min and then 1,4-dibromobutane (14.3 mL, 119.74 mmol) was added. The reaction mixture was stirred overnight at room temperature. The solution was hydrolyzed with 75 mL of an aqueous saturated NH<sub>4</sub>Cl solution and extracted into 100 mL of CH<sub>2</sub>Cl<sub>2</sub>. The resulting organic phase was washed with deionized water until pH went to 7 and then dried over MgSO<sub>4</sub>, and concentrated under reduced pressure. The dark oily mixture was purified by two successive column chromatography over silica gel using pentane and dichloromethane as eluents ( $R_f = 0.162\{\text{CH}_2\text{Cl}_2/\text{pentane} = 1:9 \text{ v}\}$ ) to yield **2a** as a yellow solid (yield: 5.52 g, 42.07 %).

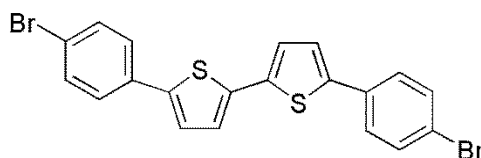
<sup>1</sup>H-NMR (300 MHz, CDCl<sub>3</sub>, δ ppm): 6.90 (d, <sup>3</sup>J = 3.5 Hz, 2H, H<sup>b</sup>); 6.67 (d, <sup>3</sup>J = 3.5 Hz, 2H, H<sup>a</sup>); 3.43 (t, 4H, H<sup>4</sup>); 2.82 (t, 4H, H<sup>1</sup>); 1.99 – 1.78 (m, 8H, H<sup>3,2</sup>)

<sup>13</sup>C-NMR (75.4 MHz, CDCl<sub>3</sub>, δ ppm): 143.6(C<sup>d</sup>); 135.7(C<sup>c</sup>); 125.2(C<sup>b</sup>); 123.0(C<sup>a</sup>); 33.5(C<sup>1</sup>); 32.1(C<sup>4</sup>); 30.1(C<sup>3</sup>); 29.4(C<sup>2</sup>)

FD mass: found: 434.0; calcd: 433.9

### 5,5'-dibromophenyl-2,2'-bithiophene (2b)

C<sub>20</sub>H<sub>12</sub>Br<sub>2</sub>S<sub>2</sub> (M<sub>w</sub> = 476.25 g/mol)



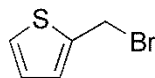
Same procedure as for **2a** from *n*-BuLi in hexanes (2.28 M, 17.5 mL, 39.9 mmol), bithiophene (3.0 g, 18.04 mmol) and 1,4-dibromobenzene (12.81 g, 54.30 mmol). The amounts of anhydrous THF used for bithiophene and 1,4-dibromobenzene solutions are 50 mL and 20mL respectively. The solution was recrystallized from 100 mL of boiling toluene overnight, and then followed by filtrating, washing with toluene and pentane to get a yellow solid compound (yield: 3.18 g, 37 %).

<sup>1</sup>H-NMR (400 MHz, C<sub>2</sub>D<sub>2</sub>Cl<sub>4</sub>, δ ppm): 7.59-7.50 (dd, <sup>3</sup>J = 8.42 Hz, <sup>3</sup>J = 8.6 Hz, 8H, H<sup>d,e,f</sup>); 7.28-7.22 (m, t, 4H, H<sup>a,b</sup>)

FD mass: found: 473.87543; calcd: 473.87472 (δ = 1.51 ppm)

## 2-(bromomethyl)thiophene (2c)

C<sub>5</sub>H<sub>5</sub>BrS (M<sub>w</sub> = 177.06 g/mol)



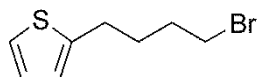
In a 500 mL three-necked round bottom flask equipped with a cooler and a dropping funnel, 2-(hydroxymethyl)thiophene (6.4557 g, 56.54 mmol) was added to a solution containing 182 mL of anhydrous dichloromethane, triphenylphosphine (17.74g, 67.65 mmol) and carbon tetrabromide (29.91 g, 90.2 mmol) at 0 °C under a nitrogen flow. The temperature was raised to room temperature and stirred for 22 hours. After the reaction completed, the clear yellow mixture was added to a saturated aqueous sodium hydrogen carbonate solution (200 mL) and the resulting mixture was then extracted into chloroform (200 mL). The resulting organic phase was then washed with distilled water (200 mL) to remove the remaining salts and residues. The yellow solution was dried over anhydrous magnesium sulfate, filtrated, and concentrated under reduced pressure to give a brownish clear crude oil. The latter was distilled under vacuum ( $E_b^{2 \text{ mbar}} = 52 \text{ °C}$ ) to give the title compound as transparent oil containing traces of CHBr<sub>3</sub> (yield: 13.46 g, 100 %).

<sup>1</sup>H-NMR (300 MHz, CDCl<sub>3</sub>, δ ppm): 7.32 (dd, <sup>3</sup>J = 5.1 Hz, <sup>4</sup>J = 1.2 Hz, 1H, H<sup>c</sup>); 7.12 (d, <sup>3</sup>J = 4.1 Hz, 1H, H<sup>a</sup>); 6.94 (dd, <sup>3</sup>J = 5.1 Hz, <sup>3</sup>J = 3.5 Hz, 1 H, H<sup>b</sup>); 4.76 (s, 2H, H<sup>1</sup>)

<sup>13</sup>C-NMR (75.4 MHz, CDCl<sub>3</sub>, δ ppm): 140.6(C<sup>d</sup>); 128.2(C<sup>b</sup>); 127.3(C<sup>a,c</sup>); 26.9(C<sup>1</sup>);

## 2-(bromobutyl)thiophene (2d)

C<sub>8</sub>H<sub>11</sub>BrS (M<sub>w</sub> = 219.14 g/mol)



In a 250 mL three-necked round bottom flask equipped with a cooler and a dropping funnel, 70 mL of anhydrous THF and thiophene (4.60 g, 54.65 mmol) were introduced and mixed under nitrogen flow. After 30 minutes under vigorous stirring, *n*-BuLi in hexane (2.5 M, 24 mL, 60 mmol) was added dropwise at -78 °C to the mixture and stirred for a further 1 hour. 1,4-dibromobutane (14.76g, 68.31 mmol) was then added and the obtained mixture was stirred at room temperature overnight. The reaction medium was then hydrolyzed with an aqueous saturated NH<sub>4</sub>Cl solution and extracted into CH<sub>2</sub>Cl<sub>2</sub> twice. The organic phase was dried over MgSO<sub>4</sub> and concentrated under reduced pressure. The crude mixture was distilled under vacuum ( $E_b^{0.001 \text{ mbar}} = 84 \text{ °C}$ ) to give a colorless liquid (yield: 6.23 g, 52%).

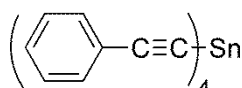
$^1\text{H-NMR}$  (300 MHz,  $\text{CDCl}_3$ ,  $\delta$  ppm): 7.16 (dd,  $^3J=5.1$  Hz,  $^3J=1.2$  Hz, 1H,  $\text{H}^c$ ); 6.96 (dd,  $^3J=5.1$ ,  $^3J=3.4$ Hz, 1H,  $\text{H}^b$ ); 6.84 (dd, 1H,  $\text{H}^a$ ); 3.44 (t, 2H,  $\text{H}^4$ ); 2.89 (t, 2H,  $\text{H}^1$ ); 2.02-1.78 (m, 4H,  $\text{H}^{2,3}$ )

$^{13}\text{C-NMR}$  (75.4 MHz,  $\text{CDCl}_3$ ,  $\delta$  ppm): 144.5( $\text{C}^d$ ); 126.8( $\text{C}^b$ ); 124.3( $\text{C}^a$ ); 123.1( $\text{C}^c$ ); 33.5( $\text{C}^1$ ); 32.0( $\text{C}^4$ ); 30.2( $\text{C}^3$ ); 29.0( $\text{C}^2$ )

### I.3 Experimental procedure of tetrakis(phenylethynyl)tin

#### **Tetrakis(phenylethynyl)tin (3)**

$\text{C}_{32}\text{H}_{20}\text{Sn}$  ( $M_w = 523.21$  g/mol)



In a 500 mL three-necked round bottom flask equipped with a cooler and a dropping funnel, 70 mL of anhydrous toluene and phenylacetylene (6.6 mL, 60 mmole) were introduced under nitrogen. The as-obtained solution was cooled down to  $0^\circ\text{C}$  and *n*-BuLi in hexanes (2.5 M, 24 mL, 60 mmole) was added drop by drop and then 15 mL of toluene was used to rinse the *n*-BuLi remaining in the funnel. After returning to the room temperature, the mixture was stirred for 3-4 hours. Then  $\text{SnCl}_4$  (1.6 mL, 13.63 mmol) was added drop by drop at  $-78^\circ\text{C}$ . After warming up to the room temperature, the mixture was heated at  $60^\circ\text{C}$  for 18 hours. The resulting mixture was chromatographed over  $\text{MgSO}_4$  using toluene as eluent under a nitrogen flow by the means of a Schlenck line. The obtained solution was then evaporated under reduced pressure to yield a pale yellow powder which was stored under argon (yield: 5.7 g, 80.88 %).

$^1\text{H-NMR}$  (300 MHz,  $\text{CDCl}_3$ ,  $\delta$  ppm): 7.67-7.59(m,  $^3J = 7.6$  Hz,  $^4J = 2.0$ Hz, 8H,  $\text{H}^d$ ); 7.43-7.34(m, 12H,  $\text{H}^{e,f}$ )

$^{13}\text{C-NMR}$  (75.4 MHz,  $\text{CDCl}_3$ ,  $\delta$  ppm): 132.4( $\text{C}^d$ ); 129.4( $\text{C}^f$ ); 128.4( $\text{C}^e$ ); 122.1( $\text{C}^c$ ); 109.7( $\text{C}^b$ ); 85.3( $\text{C}^a$ )

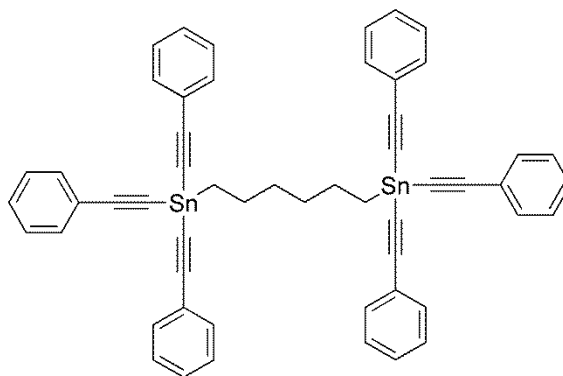
$^{119}\text{Sn-NMR}$  (111.9 MHz,  $\text{CDCl}_3$ ,  $\delta$  ppm): -334.96

### I.4 Experimental procedure of bridged ditins

#### **1-(2-(bis(2-phenylethynyl)(6-(tris(2-phenylethynyl)stannyl)hexyl)stannyl)ethynyl)benzene (4)**

$\text{C}_{54}\text{H}_{42}\text{Sn}_2$  ( $M_w = 928.33$ )





In a 500 mL three-necked round bottom flask equipped with a cooler, a dropping funnel and a stirring magnet, magnesium (9.96 g, 0.41 mol) was introduced and covered by 70 mL of anhydrous THF under a nitrogen flow. The magnesium was activated by few milliliters of 1,6-dibromohexane and the solution suddenly formed a white cloudy solution after about 10 minutes. After the formation of a cloudy mixture, 1,6-dibromohexane (10.03 g, 0.04 mol) in 135 mL of anhydrous THF was added dropwise to the above solution. The reaction mixture was refluxed overnight and then cooled down to the room temperature for titration.

**Titration procedure:** 10 mL of anhydrous ether, few milligrams of 1,10-phenanthroline and 4 mL of Grignard solution were stirred in a 25 mL of pre-dried two-necked round bottom flask for 20 minutes under a flow of nitrogen. Then 1.11 mL of benzyl alcohol (1M in anhydrous toluene) was necessary to titrate 4 mL of the Grignard solution which gave a Grignard concentration ( $[RMgX] = V/4$  (M) with  $V = 1.11$  mL) of about 0.275 M (yield: 67.7 %). Then, tetrakis(phenylethynyl)tin (0.51 g, 0.97 mmol) in anhydrous toluene (20 mL) and anhydrous diethyl ether (10 mL) was treated with one equivalent of the Grignard reagent (3.5 mL, 0.97 mmol) and the resulting mixture was heated at 40 °C for 21 hours. Then, the resulting mixture was naturally cooled to room temperature and the resulting products were chromatographed over  $MgSO_4$  using anhydrous toluene as eluent under a nitrogen flow employing a Schlenk line and concentrated under reduced pressure. Finally, the target compound was dried under vacuum overnight and stored under argon (yield: 5.7 mg, 0.63 %).

$^1H$ -NMR (300 MHz,  $CDCl_3$ ,  $\delta$  ppm): 7.62-7.01 (m, 30H); 1.85-1.22 (m, 12H)

$^{13}C$ -NMR (75.4 MHz,  $CDCl_3$ ,  $\delta$  ppm): 14.22(C); 16.05(C); 22.67(C); 25.65(C); 31.41(C); 32.59(C); 87.57(C); 110.19(C); 122.77(C); 128.36(C); 128.95(C); 132.32(C)

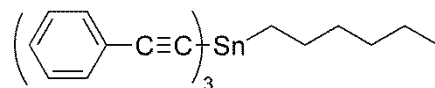
$^{119}Sn$ -NMR (111.9 MHz,  $CDCl_3$ ,  $\delta$  ppm): -241.72

MS-Maldi (dctb+Na): found: 951.1 calcd: 951.1

## I.5 Experimental procedure of trialkynylorganotin

### hexyltris(2-phenylethynyl)stannane (**5a**)

$C_{30}H_{28}Sn$  ( $M_w = 507.25$ )



In a 100 mL three-necked round bottom flask equipped with a cooler, a dropping funnel and a stirring magnet, magnesium (2.028 g, 83.42 mmol) was introduced and covered by 10 mL of anhydrous ether under a nitrogen flow. The magnesium was activated by few milliliters of 1-bromohexane and the solution suddenly formed a white cloudy solution after about 10 minutes. After the formation of a cloudy mixture, 1-bromohexane (12.89 g, 78.08 mmol) in 40 mL of anhydrous ether was added dropwise to the above solution. The reaction mixture was then stirred for 2 hours at 55 °C and then cooled down to room temperature for titration.

**Titration procedure:** 10 mL of anhydrous ether, few milligrams of 1,10-phenanthroline and 4 mL of Grignard solution were stirred in a 25 mL of pre-dried two-necked round bottom flask for 20 minutes under a flow of nitrogen. After addition of 3.2 mL of benzyl alcohol (1M in anhydrous toluene), used as titrant, the color of the solution turned from pink to colorless which led to a Grignard concentration ( $[RMgX] = V/4$  (M) with  $V = 3.2$  mL) of about 0.8 M (yield: 51.2 %).

Subsequently, 3.875 mL of the Grignard solution was taken under nitrogen using a 5 mL of syringe and added to a solution of tetrakis(phenylethynyl)tin (1.62 g, 3.10 mmol) in anhydrous toluene (30 mL) and anhydrous diethyl ether (10 mL) placed in a three-necked round bottom flask pre-cooled at -78 °C (bath of ethanol cooled by liquid N<sub>2</sub>) for 30 minutes. The resulting solution was heated at 40 °C for 17 hours and then naturally cooled to room temperature. The resulting products were chromatographed over MgSO<sub>4</sub> using anhydrous toluene as eluent under a nitrogen flow employing a Schlenk line and concentrated under reduced pressure. Finally, the obtained product was dried under vacuum overnight and stored under argon (yield: 1.2775 g, 81.24 %).

<sup>1</sup>H-NMR (300 MHz, CDCl<sub>3</sub>, δ ppm): 7.62-7.49 (m, 6H, H<sup>d</sup>); 7.41-7.26 (m, 9H, H<sup>e,f</sup>); 1.91-1.81 (m, 2H, H<sup>3</sup>); 1.59-1.46 (m, 4H, H<sup>1,2</sup>); 1.43-1.29 (m, 4H, H<sup>5,4</sup>); 0.91 (t, 3H, H<sup>6</sup>)

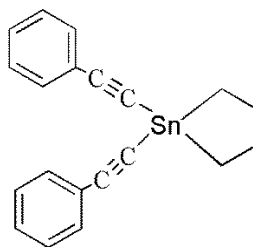
<sup>13</sup>C-NMR (75.4 MHz, CDCl<sub>3</sub>, δ ppm): 132.3(C<sup>d</sup>); 128.9(C<sup>f</sup>); 128.3(C<sup>e</sup>); 122.8(C<sup>c</sup>); 110.0(C<sup>b</sup>); 87.6(C<sup>a</sup>); 32.7(C<sup>2</sup>); 31.3(C<sup>4</sup>); 25.6(C<sup>3</sup>); 22.6(C<sup>5</sup>); 16.1(C<sup>1</sup>); 14.1(C<sup>6</sup>)

<sup>119</sup>Sn-NMR (111.9 MHz, CDCl<sub>3</sub>, δ ppm): -241.55

ESI mass: found 531.1124; calcd 531.1105 (δ = 3.5374 ppm)

### 1,1-bis(2-phenylethynyl)stannolane (5b)

C<sub>20</sub>H<sub>18</sub>Sn (M<sub>w</sub> = 377.07 g/mol)



In a 100 mL three-necked round bottom flask equipped with a cooler, a dropping funnel and a stirring magnet, magnesium (0.445 g, 18.3 mmol) was covered by 20 mL of anhydrous diethyl ether under a nitrogen flow. The magnesium was activated by few milliliters of 1,4-dibromobutane and after about 10 minutes, the solution suddenly formed a white cloudy solution. After the appearance of a cloudy aspect, 0.92 mL (7.7 mmol) of 1,4-dibromobutane in 15 mL anhydrous ether was added drop by drop at room temperature to the above solution. The mixture was then refluxed for 1.5 hour and then cooled down to the room temperature for titration.

**Titration procedure:** 10 mL of anhydrous ether, few milligrams of 1,10-phenanthroline and 5 mL of Grignard solution were stirred in a 25 mL of two-necked round bottom flask for 20 minutes under a flow of nitrogen. After addition of 0.74 mL of benzyl alcohol (1M in anhydrous toluene), used as titrant, the color of the solution turned from pink to colorless which led to a di-Grignard concentration ( $[2RMgX] = V/10$  (M) with  $V = 0.74$  mL) of about 0.074 M (yield: 33.6%).

Subsequently, 29 mL of the Grignard solution was taken under nitrogen using a 30 mL of syringe and added to a solution of tetrakis(phenylethynyl)tin (2.23 g, 4.26 mmol) in anhydrous toluene (40 mL) and anhydrous diethyl ether (20 mL) placed in a three-necked round bottom flask pre-cooled down at  $-78$  °C (bath of ethanol cooled by liquid  $N_2$ ) for 30 minutes. The resulting solution was heated at  $50$  °C overnight. Then, the solution was naturally cooled to room temperature and the resulting products were chromatographed over  $MgSO_4$  using anhydrous toluene as eluent under a nitrogen flow employing a Schlenck line. Finally, the obtained product was dried under vacuum overnight and stored under argon (yield: 1.015 g, 63.15 %).

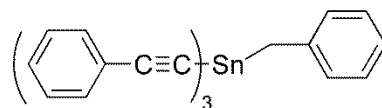
$^1H$ -NMR (300 MHz,  $CDCl_3$ ,  $\delta$  ppm): 7.62-7.43 (m, 4H,  $H^d$ ); 7.43-7.27 (m, 6H,  $H^{e,f}$ ); 1.81 (t, 2 H,  $H^1$ ); 1.27 (m, 4H,  $H^{2,3}$ ); 0.89 (m, 2H,  $^3J = 7.4$  Hz,  $H^4$ )

$^{119}Sn$ -NMR (111.9 MHz,  $CDCl_3$ ,  $\delta$  ppm): -103.78

**FD Mass:** found 370.04597; calcd 370.04567 ( $\delta = 0.8$  ppm)

### benzyltris(2-phenylethynyl)stannane (5c)

$C_{31}H_{22}Sn$  ( $M_w = 513.22$ )



Same synthetic procedure as for **5a** from 50 mL of anhydrous diethyl ether, magnesium (3.0031 g, 123.53 mmol) and benzyl bromide (13.3642 g, 78.11 mmol). The mixture was refluxed for 1 hour and 15 minutes and then cooled down to the room temperature for titration. Using the titration procedure described above, 4.7 mL of benzyl alcohol were necessary to titrate 4 mL of the Grignard solution which gave a Grignard concentration ( $[RMgX] = V/4$  (M) with  $V = 4.7$  mL) of 1.175 M (yield: 73.7 %). Then, tetrakis(phenylethynyl)tin (1.98 g, 3.78 mmol) in anhydrous toluene (25 mL) and anhydrous diethyl ether (10 mL) was treated with same equivalent of the Grignard reagent (3.21 mL, 3.78 mmol) and the resulting mixture was heated at 40 °C for 17 hours. After purification over  $MgSO_4$  as described above, an orange oily compound was isolated (yield: 0.578 g, 29.79 %).

$^1H$ -NMR (600 MHz,  $CDCl_3$ ,  $\delta$  ppm): 7.75–7.69 (m, 6H,  $H^h$ ); 7.57–7.43 (m, 11H,  $H^{c,i,j}$ ); 7.43–7.31 (m, 3H,  $H^{b,d}$ ); 3.14 (s, 2H,  $H^l$ )

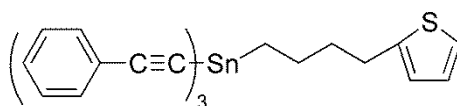
$^{13}C$ -NMR (150.8 MHz,  $CDCl_3$ ,  $\delta$  ppm): 137.1( $C^a$ ); 132.1( $C^h$ ); 129.0( $C^b$ ); 128.6( $C^j$ ); 128.2( $C^i$ ); 128.1( $C^c$ ); 125.3( $C^d$ ); 122.3( $C^g$ ); 110.6( $C^f$ ); 86.7( $C^e$ ); 23.5( $C^l$ )

$^{119}Sn$ -NMR (223.8 MHz,  $CDCl_3$ ,  $\delta$  ppm): -251.95

FD Mass: found  $[M^+] = 506.07489$ ; calculated  $[M^+] = 506.07697$  ( $\delta = 4.12$  ppm)

#### tris(2-phenylethynyl)(4-(thiophen-2-yl)butyl)stannane (**5d**)

$C_{32}H_{26}SSn$  ( $M_w = 561.32$ )



Same synthetic procedure as for **5a** from 30 mL of anhydrous diethyl ether, magnesium (1.5 g, 61.7 mmol) and 2-(bromobutyl)thiophene (6.23 g, 28.43 mmol). The mixture was refluxed for 2 hours and then cooled down to the room temperature for titration. Using the titration procedure described above, 2.21 mL of benzyl alcohol were necessary to titrate 3 mL of the Grignard solution which gave a Grignard concentration ( $[RMgX] = V/3$  (M) with  $V = 2.21$  mL) of 0.737 M (yield: 77.8 %). Then, tetrakis(phenylethynyl)tin (3.062 g, 5.85 mmol) in anhydrous toluene (43.5 mL) and anhydrous diethyl ether (19 mL) was treated with same equivalent of the Grignard reagent (7.94 mL, 5.85 mmol) and the resulting mixture was heated at 40 °C for 18 hours. After purification over  $MgSO_4$  as described above and evaporation of the solvent, the obtained solids were washed with anhydrous pentane (30 mL) three times under nitrogen to yield a white solid compound (yield: 2.0162 g, 61.37 %).

$^1\text{H}$ -NMR (600 MHz,  $\text{CDCl}_3$ ,  $\delta$  ppm): 7.55 (dd,  $J = 8.0\text{Hz}$ ,  $J = 1.6\text{Hz}$ , 6H,  $\text{H}^{\text{h}}$ ); 7.38–7.32 (m, 9H,  $\text{H}^{\text{i,j}}$ ); 7.10 (dd,  $^3J = 5.1\text{Hz}$ ,  $^4J = 1.2\text{Hz}$ , 1H,  $\text{H}^{\text{c}}$ ), 6.90 (dd,  $^3J = 5.1\text{Hz}$ ,  $^3J = 3.4\text{Hz}$ , 1H,  $\text{H}^{\text{b}}$ ), 6.82 (1H, dd,  $^3J = 3.4\text{Hz}$ ,  $^4J = 1.0\text{Hz}$ ,  $\text{H}^{\text{a}}$ ), 2.94 (t, 2H,  $\text{H}^{\text{d}}$ ), 2.01–1.87 (m, 4H,  $\text{H}^{\text{2,3}}$ ), 1.59 (t, 2H,  $\text{H}^{\text{1}}$ ).

$^{13}\text{C}$ -NMR (150.8 MHz,  $\text{CDCl}_3$ ,  $\delta$  ppm): 145.1( $\text{C}^{\text{d}}$ ); 132.4( $\text{C}^{\text{h}}$ ); 129.0( $\text{C}^{\text{j}}$ ); 128.4( $\text{C}^{\text{i}}$ ); 126.8( $\text{C}^{\text{b}}$ ); 124.3( $\text{C}^{\text{a}}$ ); 123.0( $\text{C}^{\text{g}}$ ); 122.8( $\text{C}^{\text{c}}$ ); 110.3( $\text{C}^{\text{f}}$ ); 87.4( $\text{C}^{\text{e}}$ ); 35.0( $\text{C}^{\text{2}}$ ); 29.5( $\text{C}^{\text{4}}$ ); 25.2( $\text{C}^{\text{3}}$ ); 15.7( $\text{C}^{\text{1}}$ )

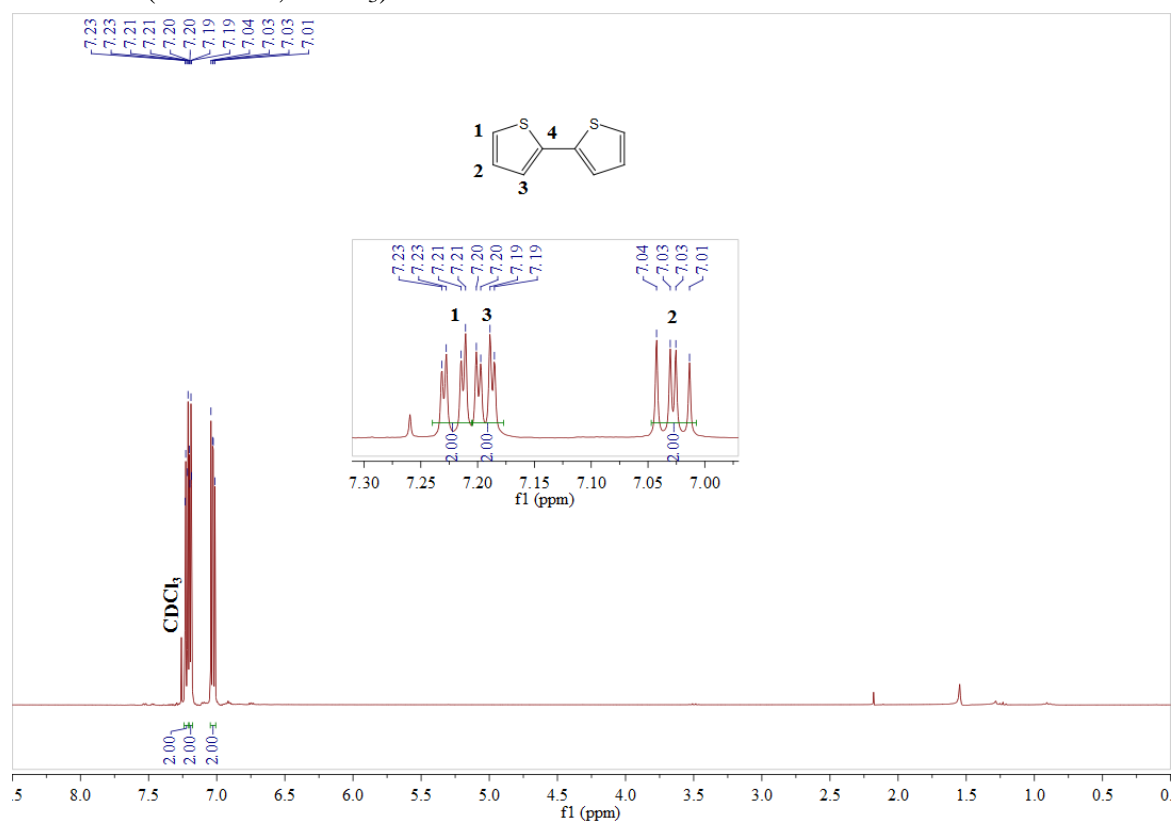
$^{119}\text{Sn}$ -NMR (223.8 MHz,  $\text{CDCl}_3$ ,  $\delta$  ppm): -241.38

FD Mass: found  $[\text{M}^+] = 554.08142$ ; calculated  $[\text{M}^+] = 554.08034$  ( $\delta = 1.94$  ppm)

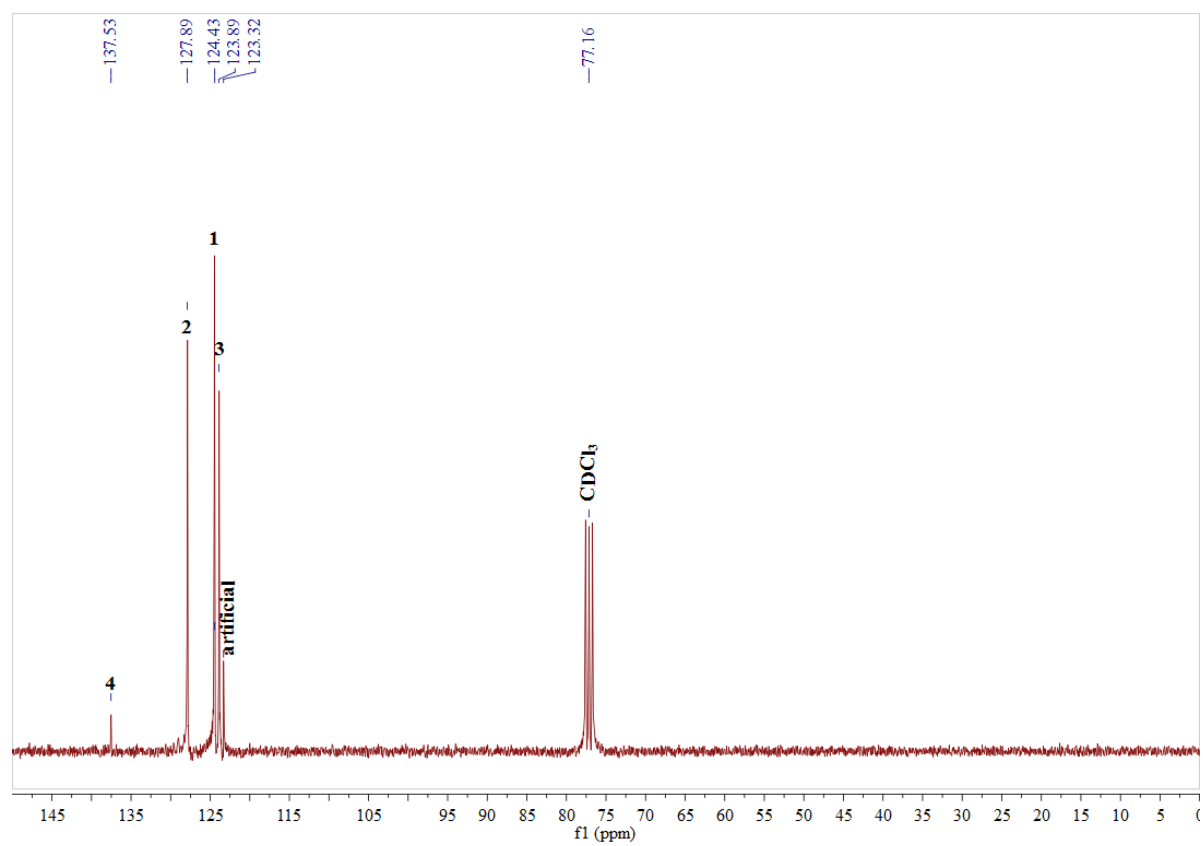
## II. NMR data of organic and organometallic materials

### 2,2'-bithiophene (1)

$^1\text{H}$ -NMR (300 MHz,  $\text{CDCl}_3$ ):

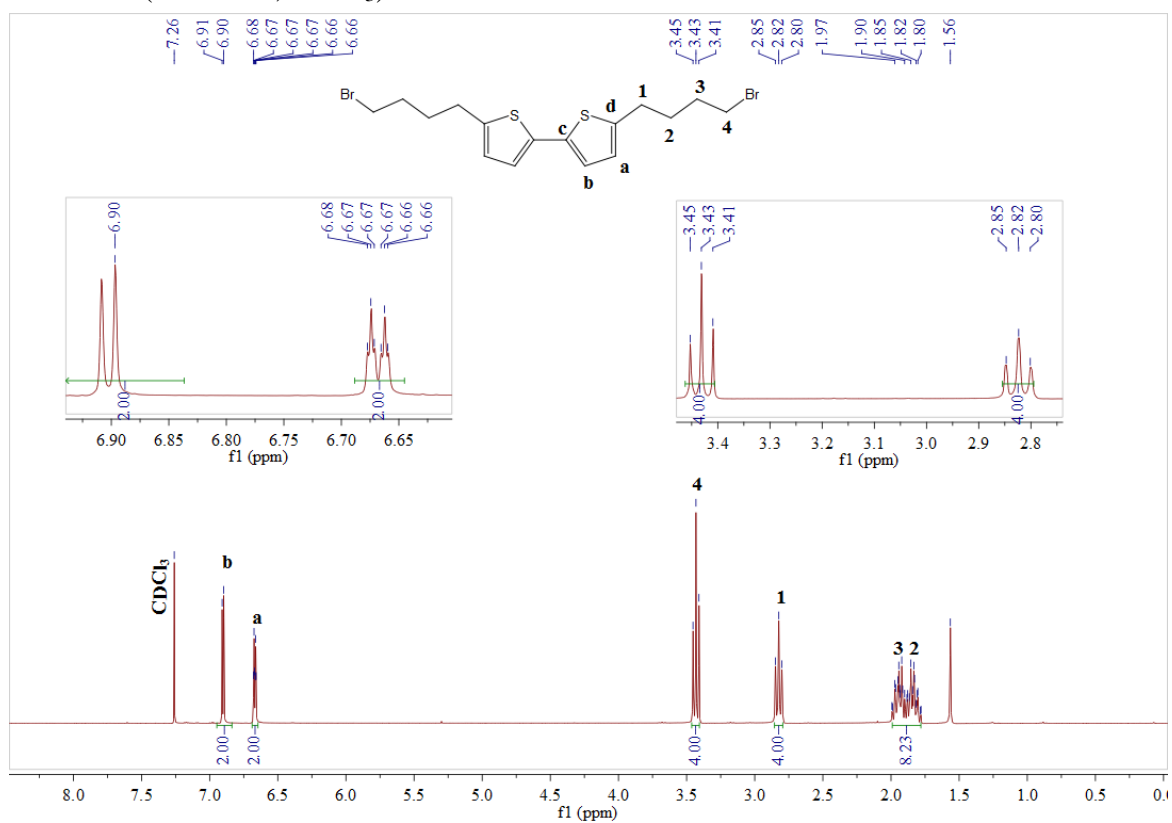


$^{13}\text{C}$ -NMR (75.4 MHz,  $\text{CDCl}_3$ ):

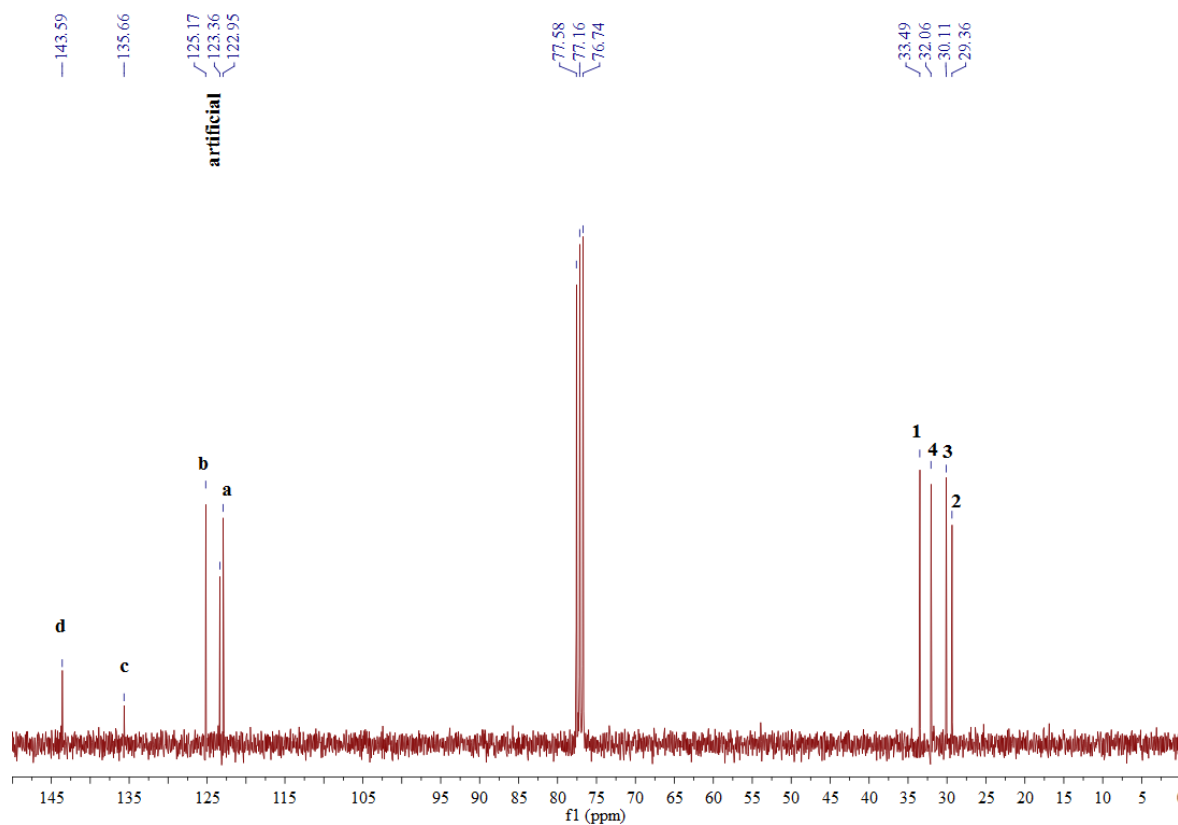


## 5,5'-dibromobutyl-2,2'-bithiophene (2a)

$^1\text{H-NMR}$  (300 MHz,  $\text{CDCl}_3$ ):

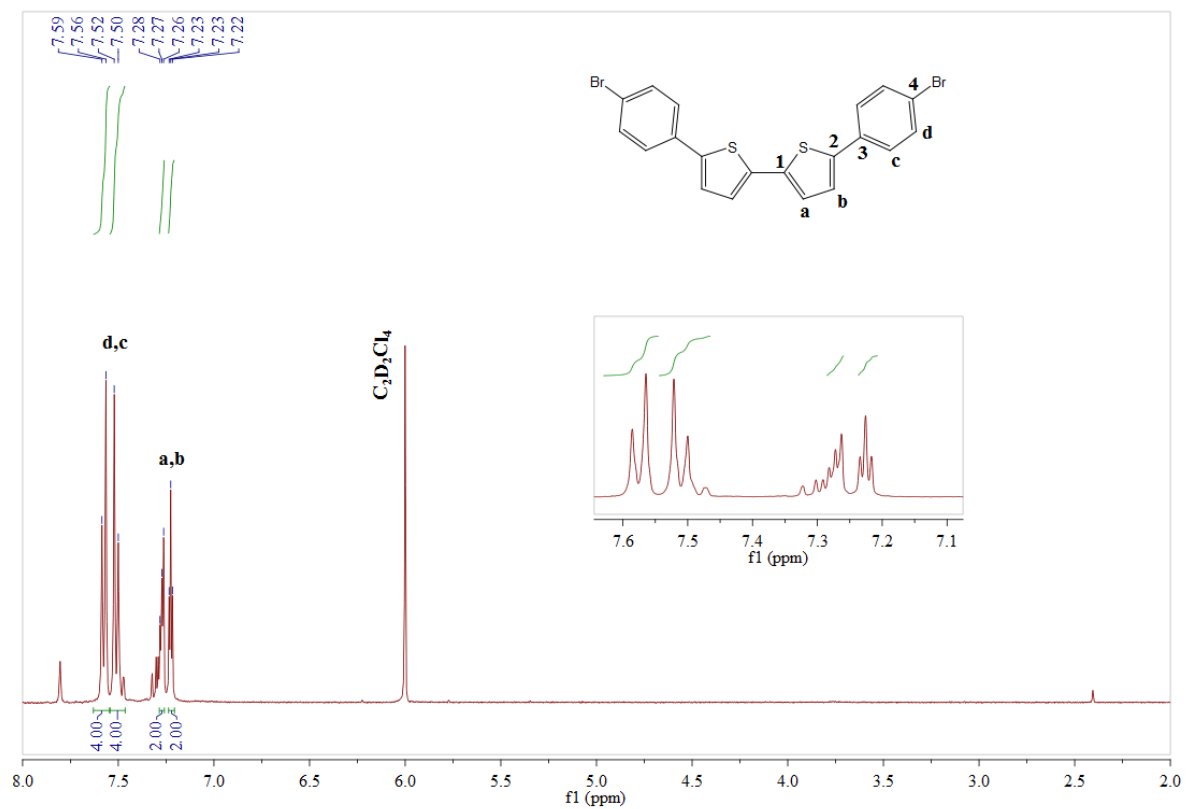


$^{13}\text{C-NMR}$  (75.4 MHz,  $\text{CDCl}_3$ ):

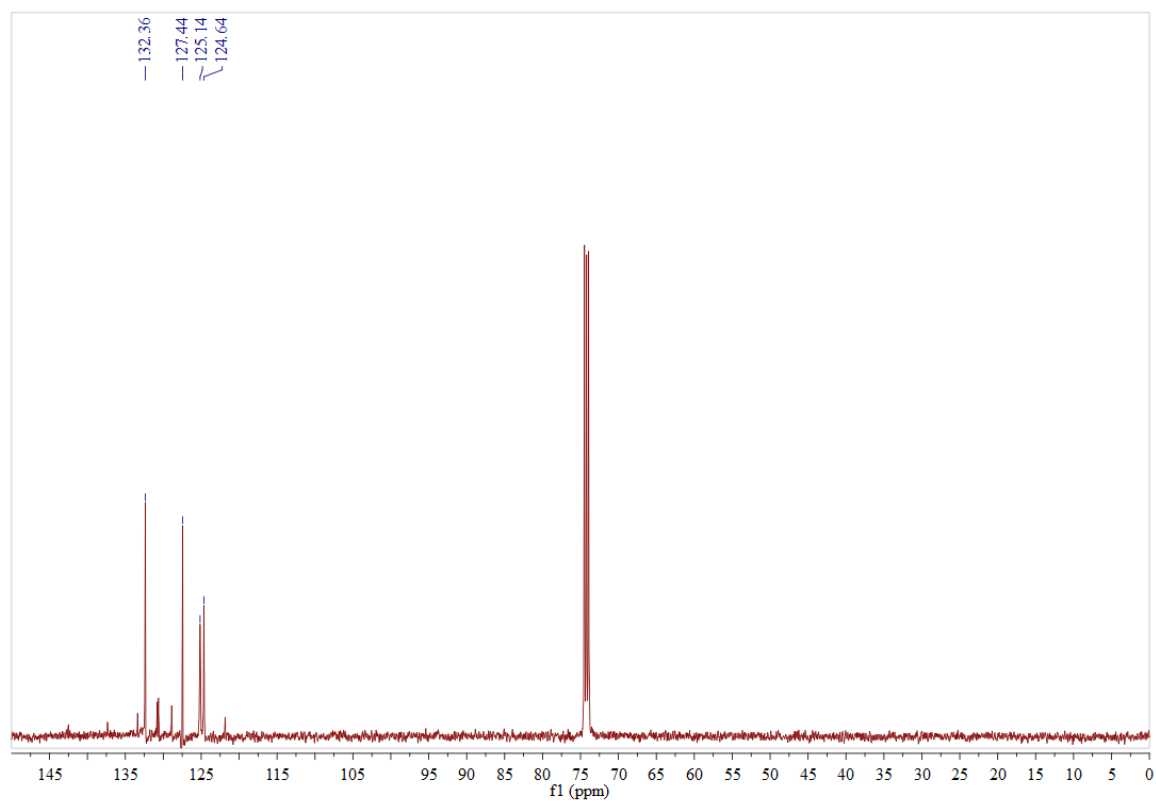


## 5,5'-dibromophenyl-2,2'-bithiophene (2b)

$^1\text{H-NMR}$  (400 MHz,  $\text{C}_2\text{D}_2\text{Cl}_4$ ):



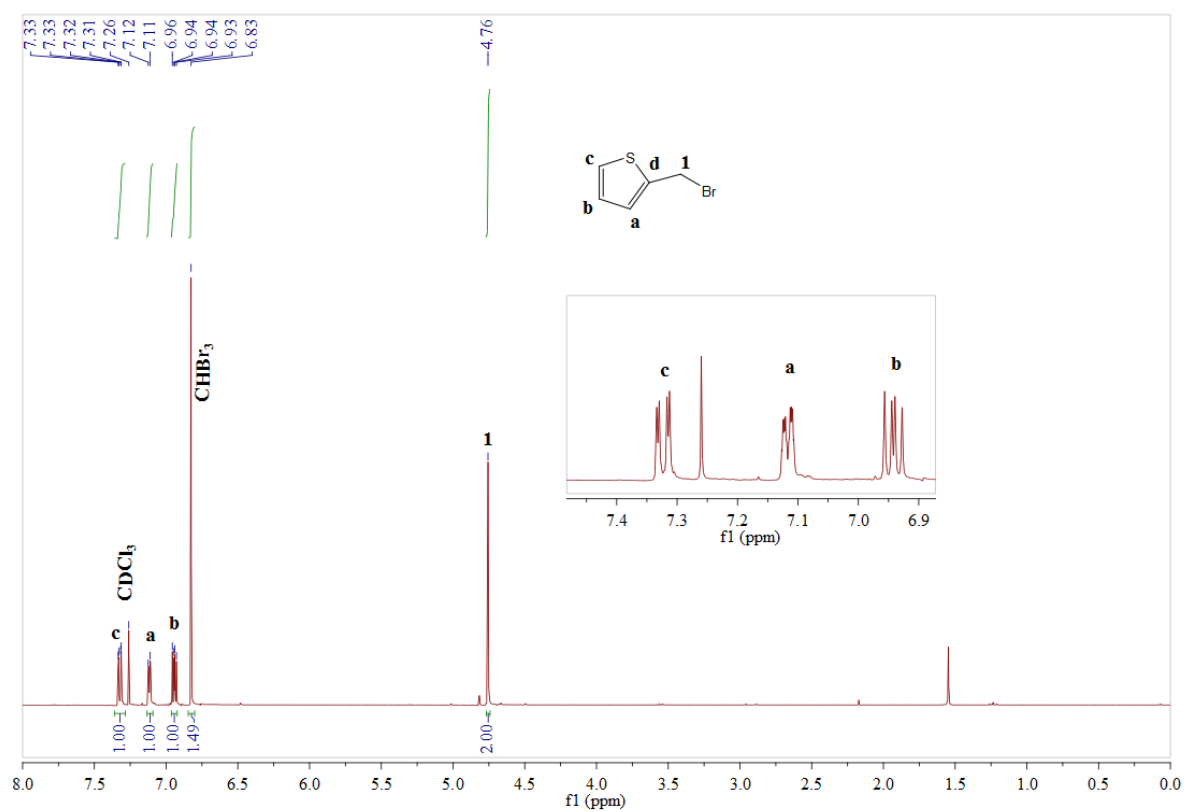
$^{13}\text{C-NMR}$  (100.5 MHz,  $\text{CDCl}_3$ ):



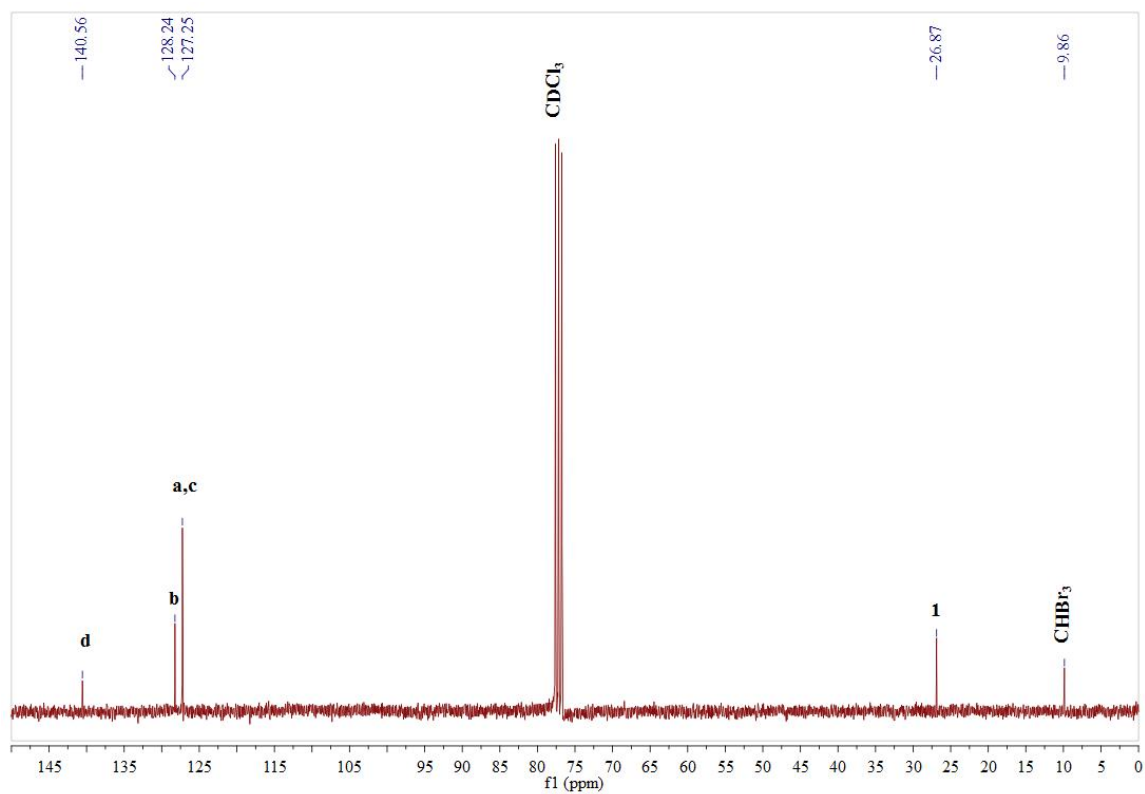


## 2-(bromomethyl)thiophene (2c)

$^1\text{H-NMR}$  (300 MHz,  $\text{CDCl}_3$ ):

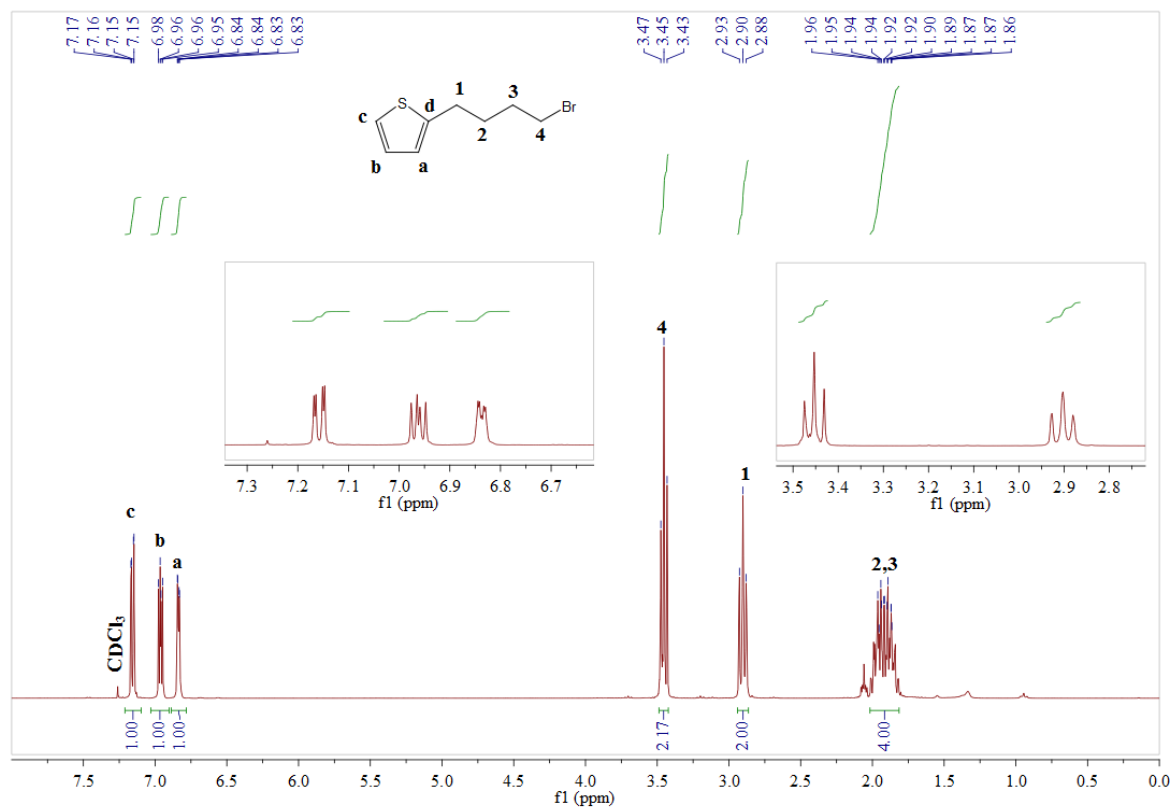


$^{13}\text{C-NMR}$  (75.4 MHz,  $\text{CDCl}_3$ ):

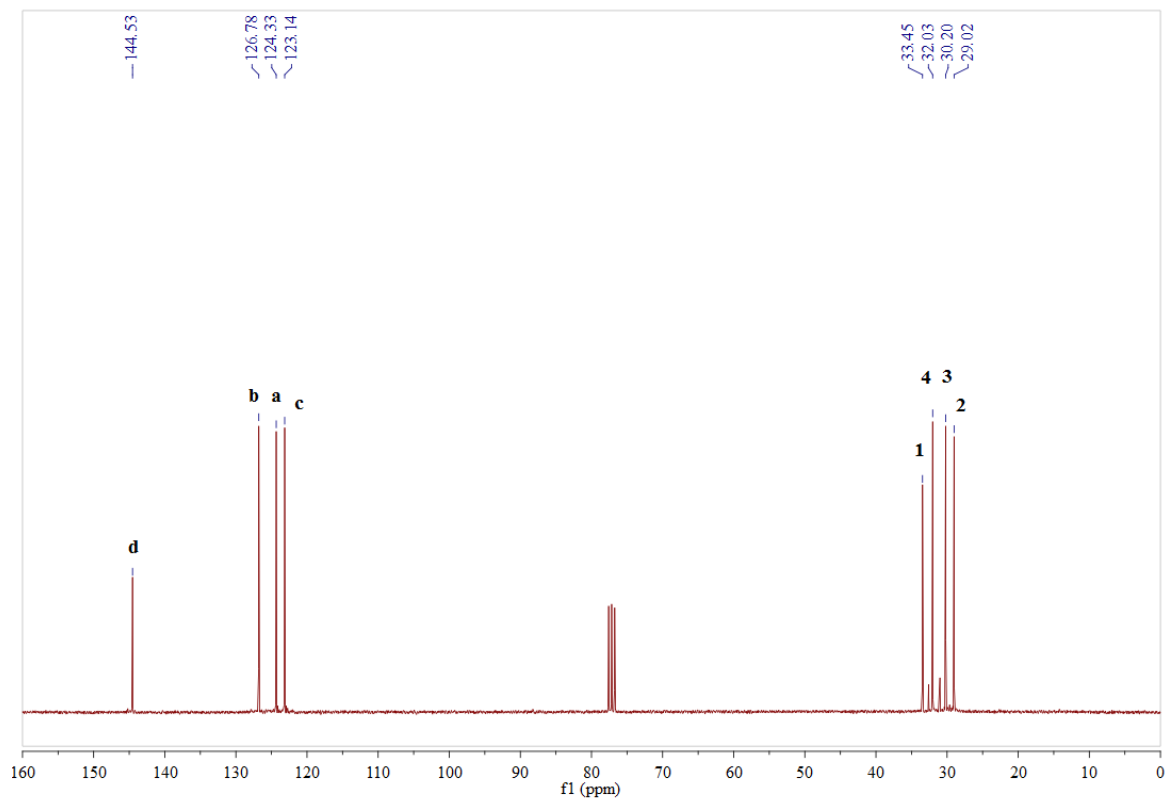


## 2-(bromobutyl)thiophene (2d)

$^1\text{H-NMR}$  (300 MHz,  $\text{CDCl}_3$ ):

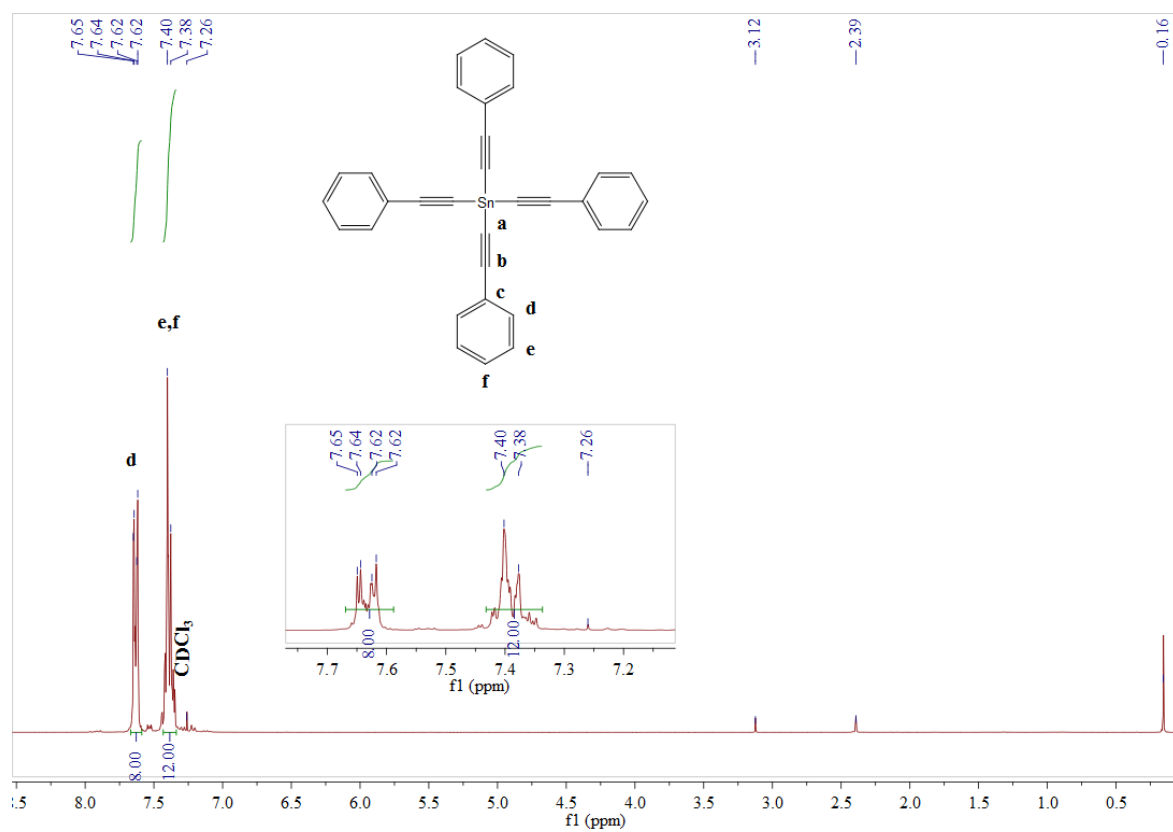


$^{13}\text{C-NMR}$  (75.4 MHz,  $\text{CDCl}_3$ ):

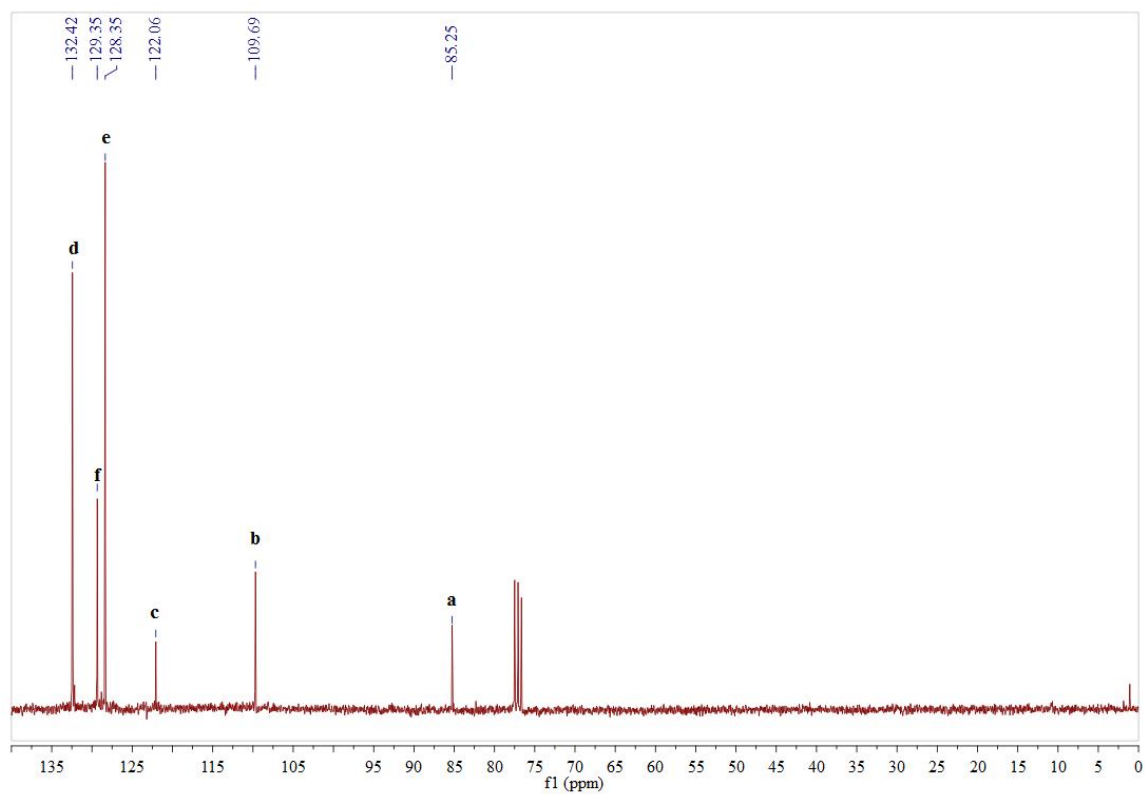


### Tetrakis(phenylethynyl)tin (3)

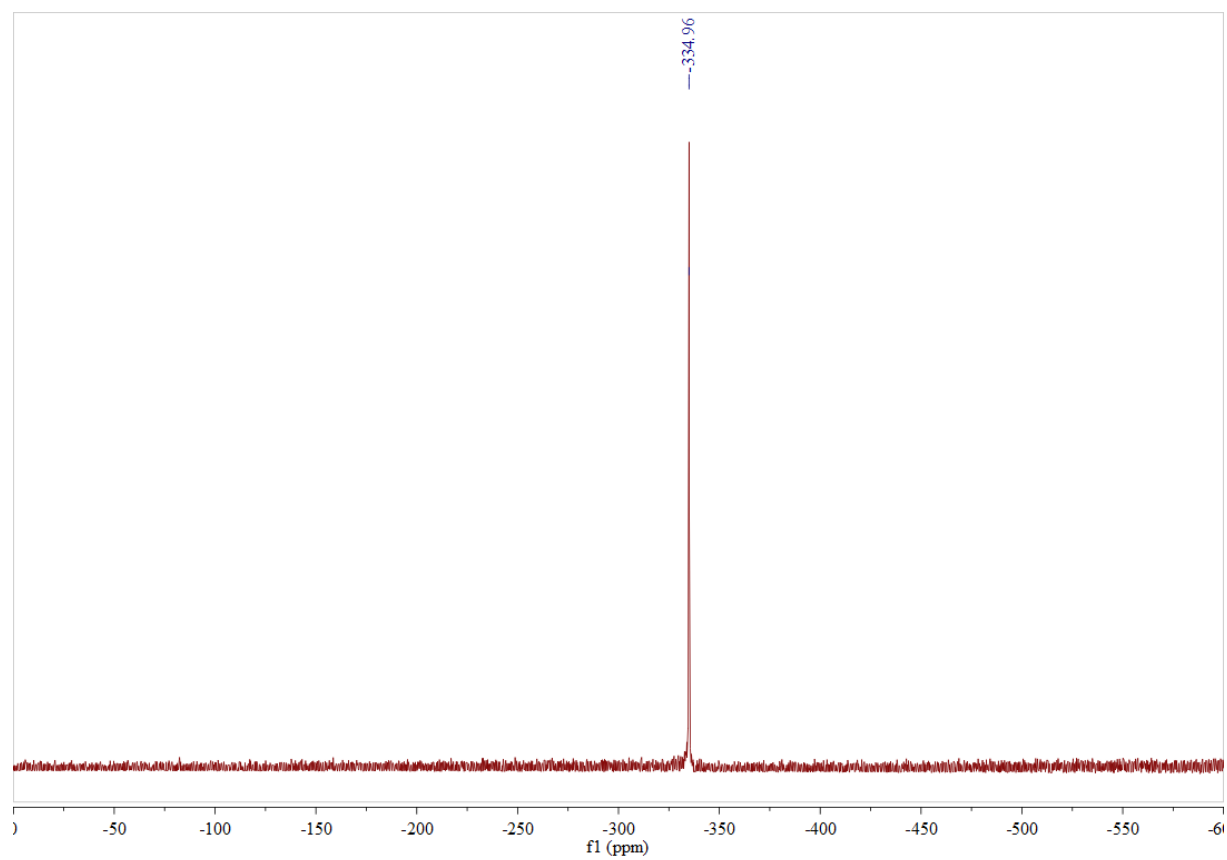
$^1\text{H-NMR}$  (300 MHz,  $\text{CDCl}_3$ ):



$^{13}\text{C-NMR}$  (75.4 MHz,  $\text{CDCl}_3$ ):

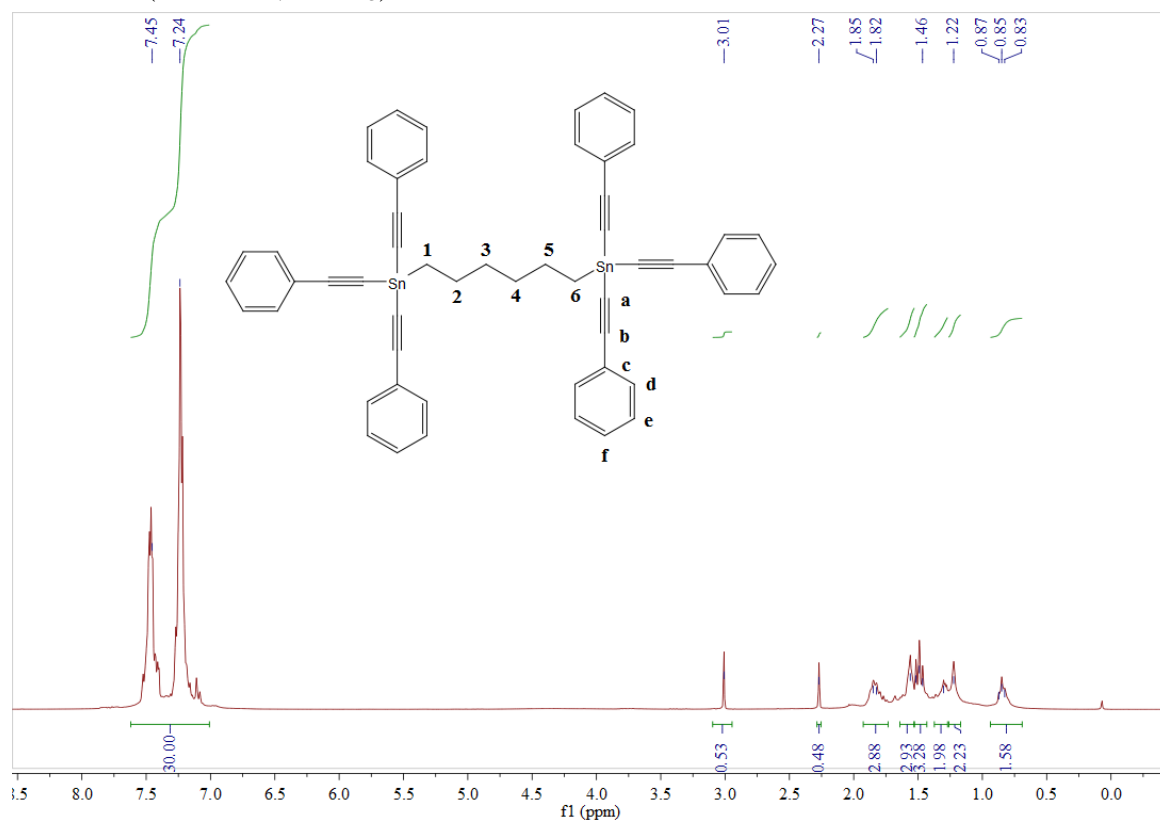


$^{119}\text{Sn}$ -NMR (111.9 MHz,  $\text{CDCl}_3$ ):

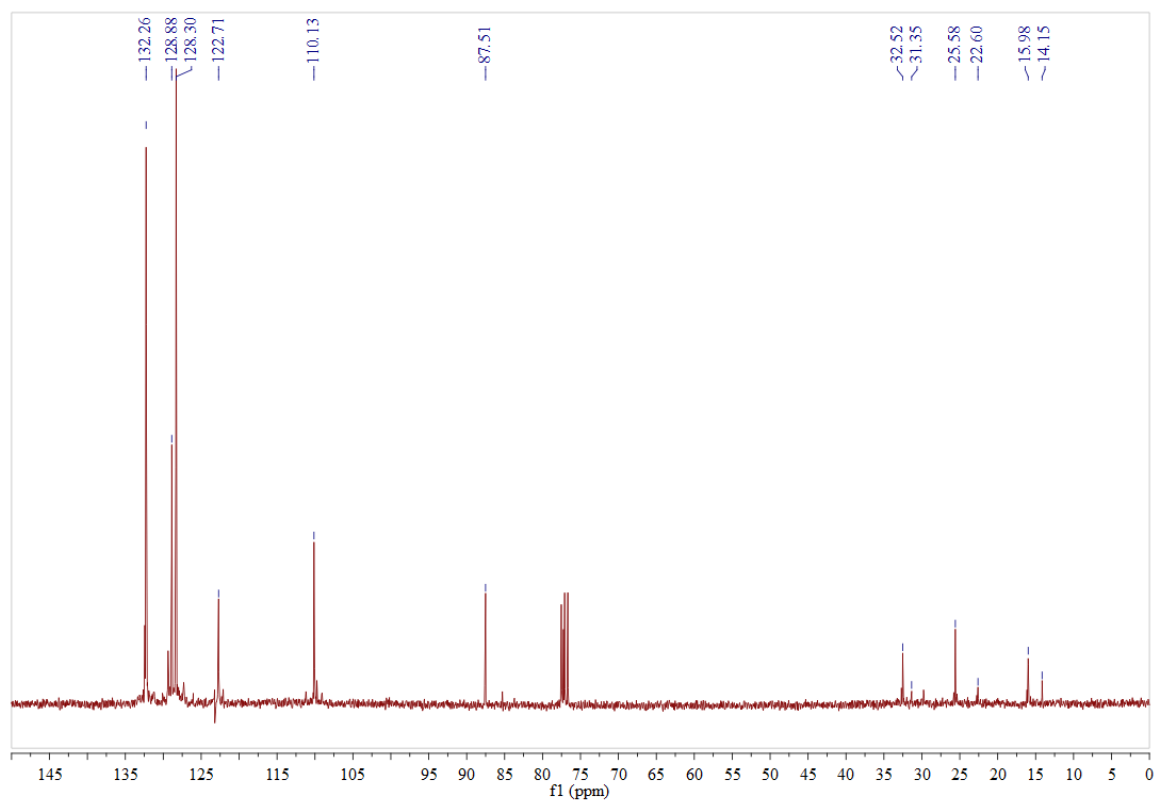


**1-(2-(bis(2-phenylethynyl)(6-(tris(2-phenylethynyl)stannyl)hexyl)stannyl)ethynyl)benzene (4)**

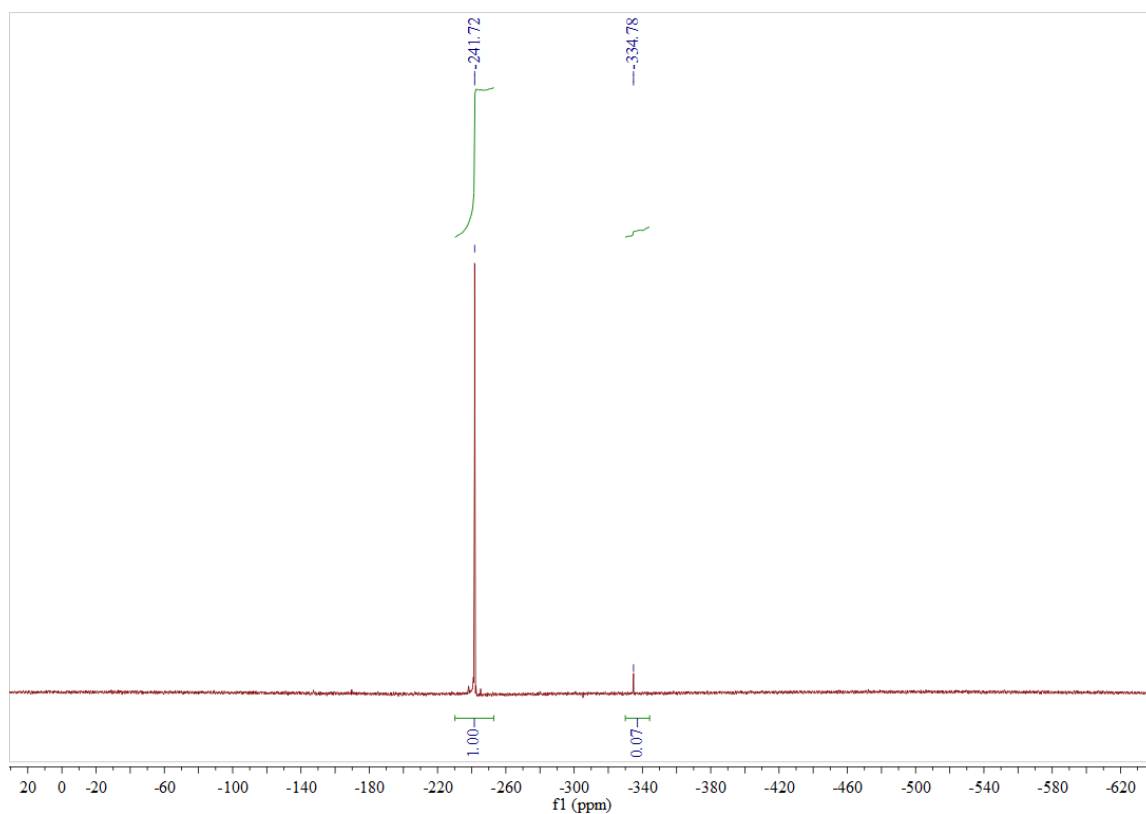
$^1\text{H-NMR}$  (300 MHz,  $\text{CDCl}_3$ ):



$^{13}\text{C-NMR}$  (75.4 MHz,  $\text{CDCl}_3$ ):

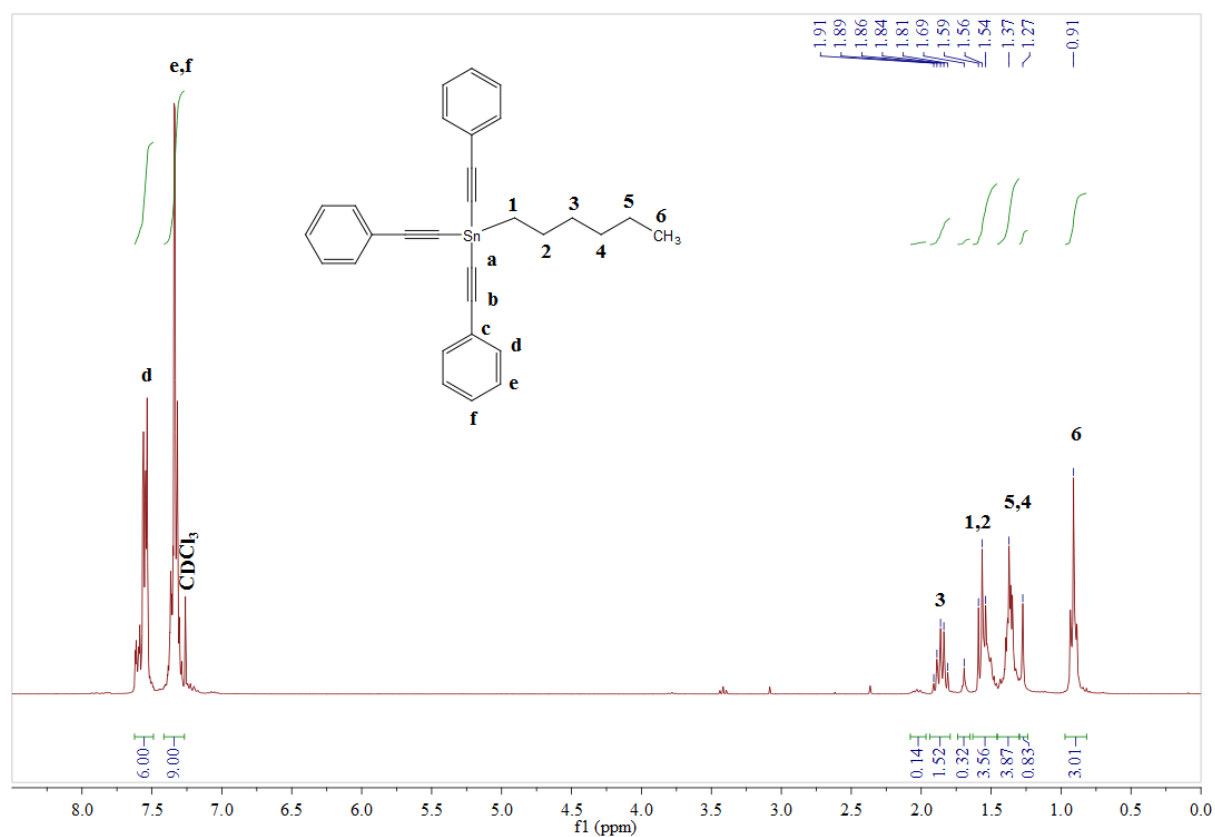


$^{119}\text{Sn}$ -NMR (111.9 MHz,  $\text{CDCl}_3$ ):

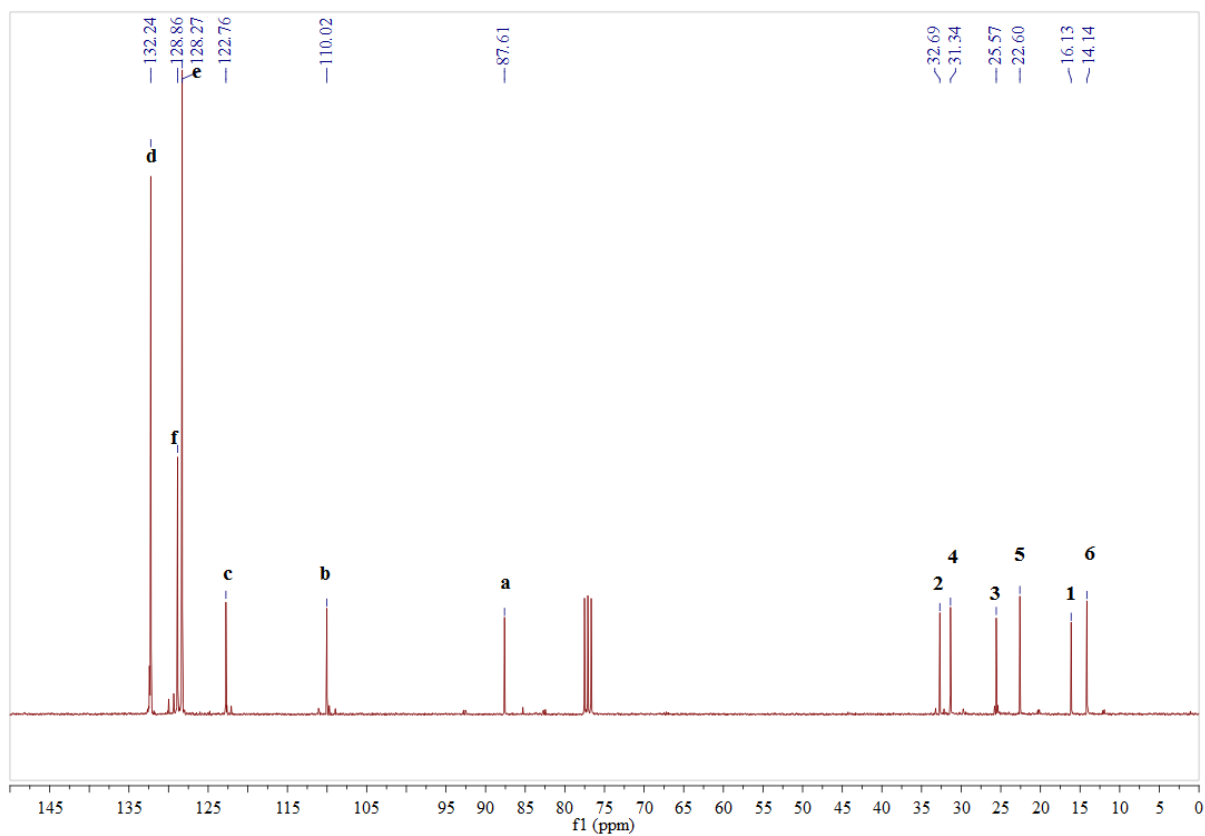


hexyltris(2-phenylethynyl)stannane (**5a**)

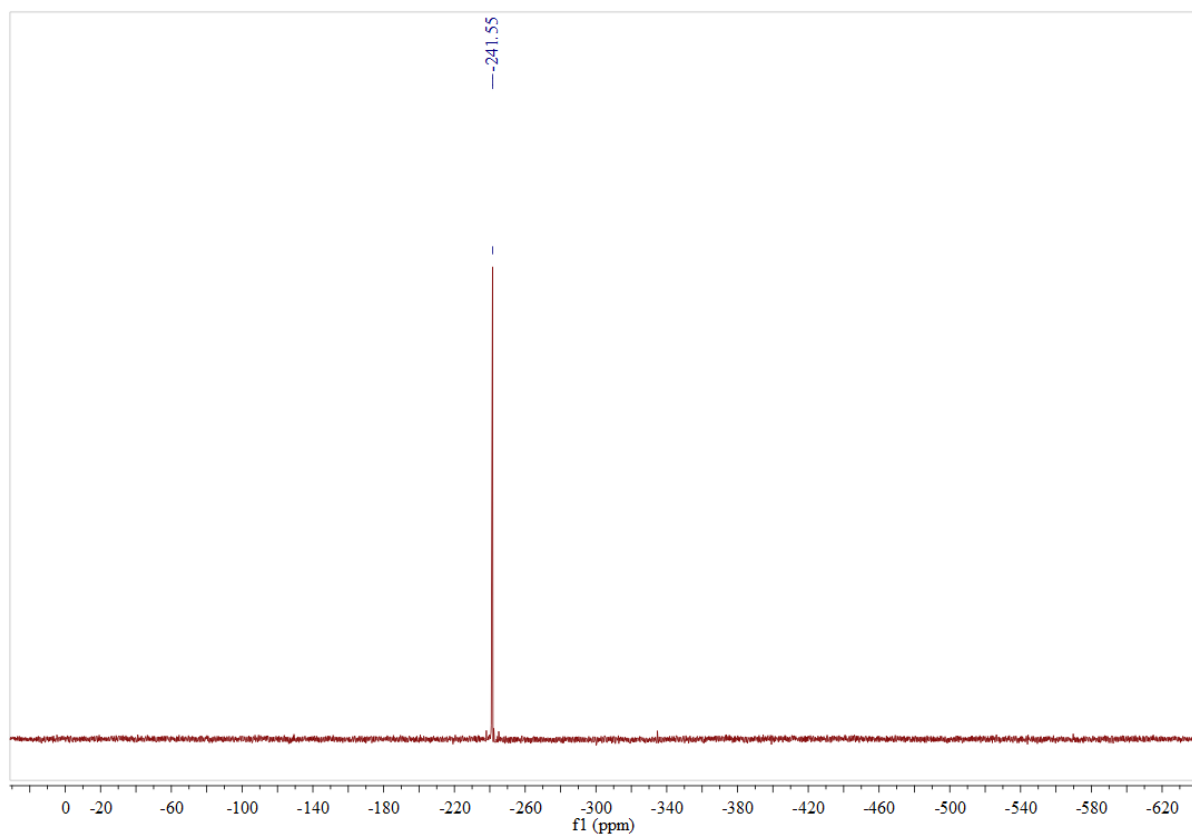
$^1\text{H}$ -NMR (300 MHz,  $\text{CDCl}_3$ ):



$^{13}\text{C}$ -NMR (75.4 MHz,  $\text{CDCl}_3$ ):

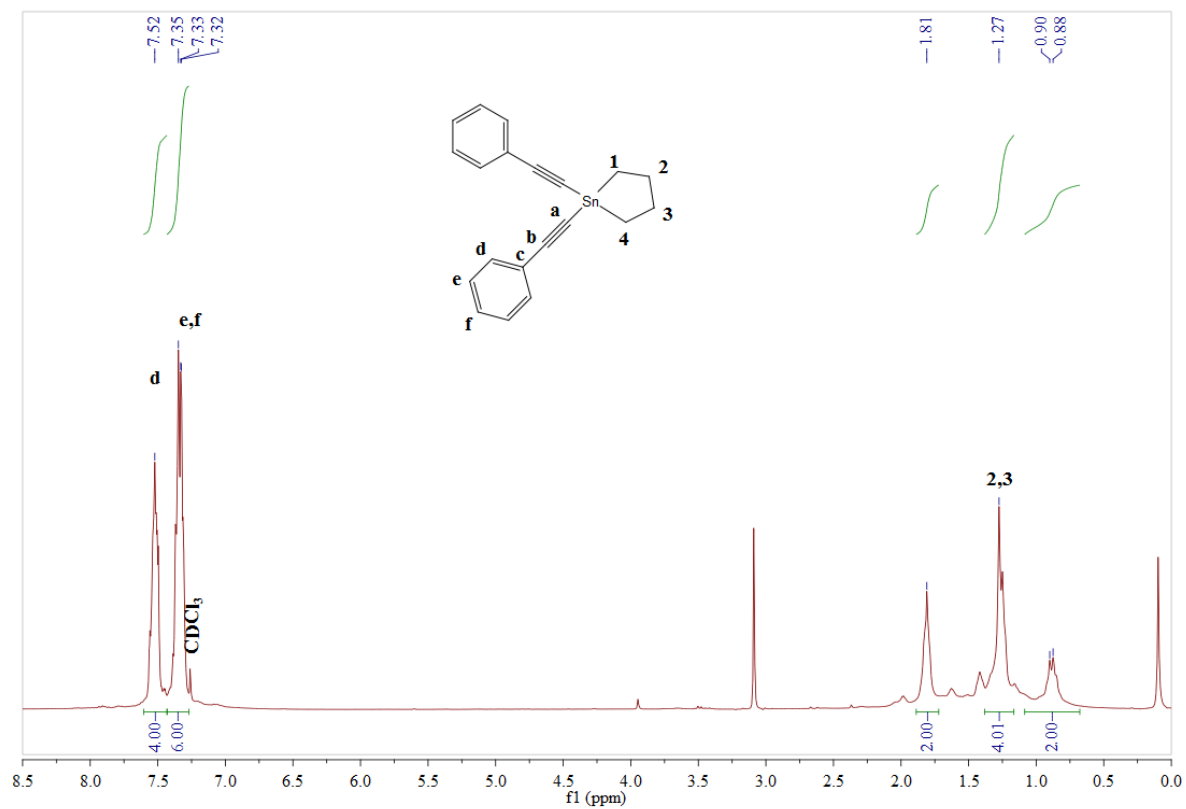


$^{119}\text{Sn}$ -NMR (111.9 MHz,  $\text{CDCl}_3$ ):

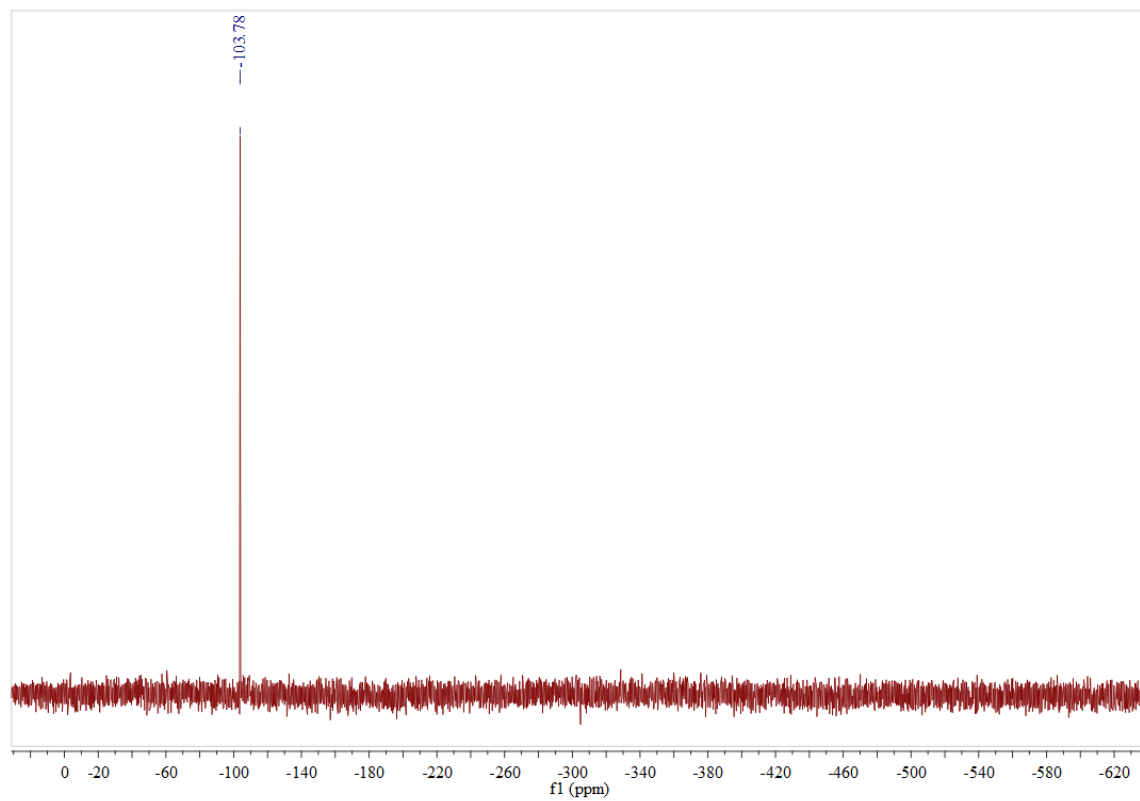


## 1,1-bis(2-phenylethynyl)stannolane (5b)

$^1\text{H-NMR}$  (300 MHz,  $\text{CDCl}_3$ ):



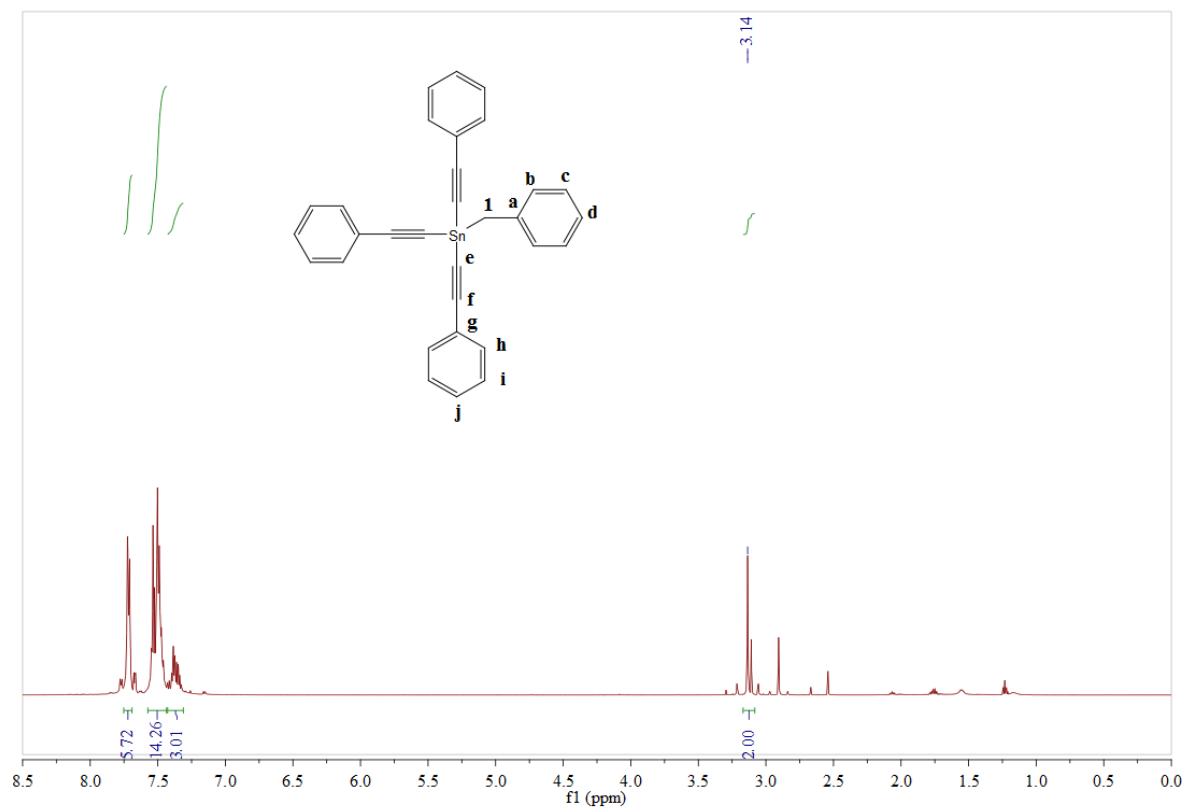
$^{119}\text{Sn-NMR}$  (111.9 MHz,  $\text{CDCl}_3$ ):



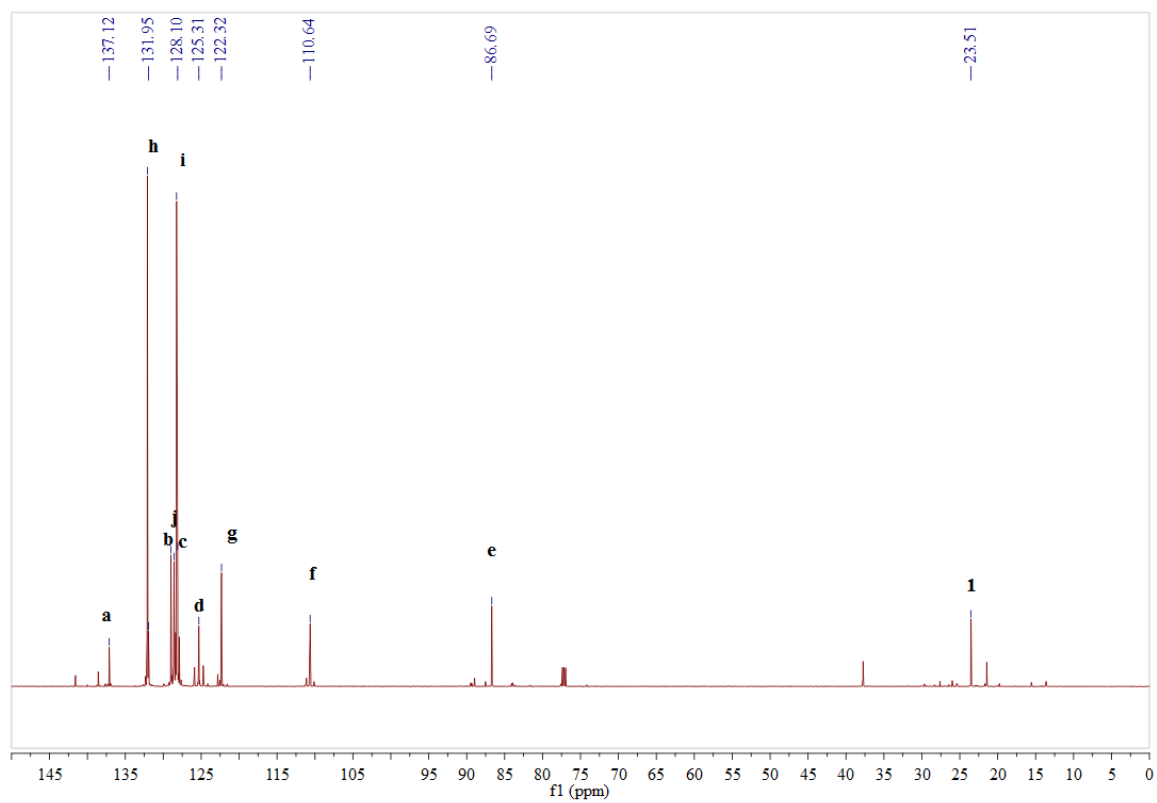


# benzyltris(2-phenylethynyl)stannane (5c)

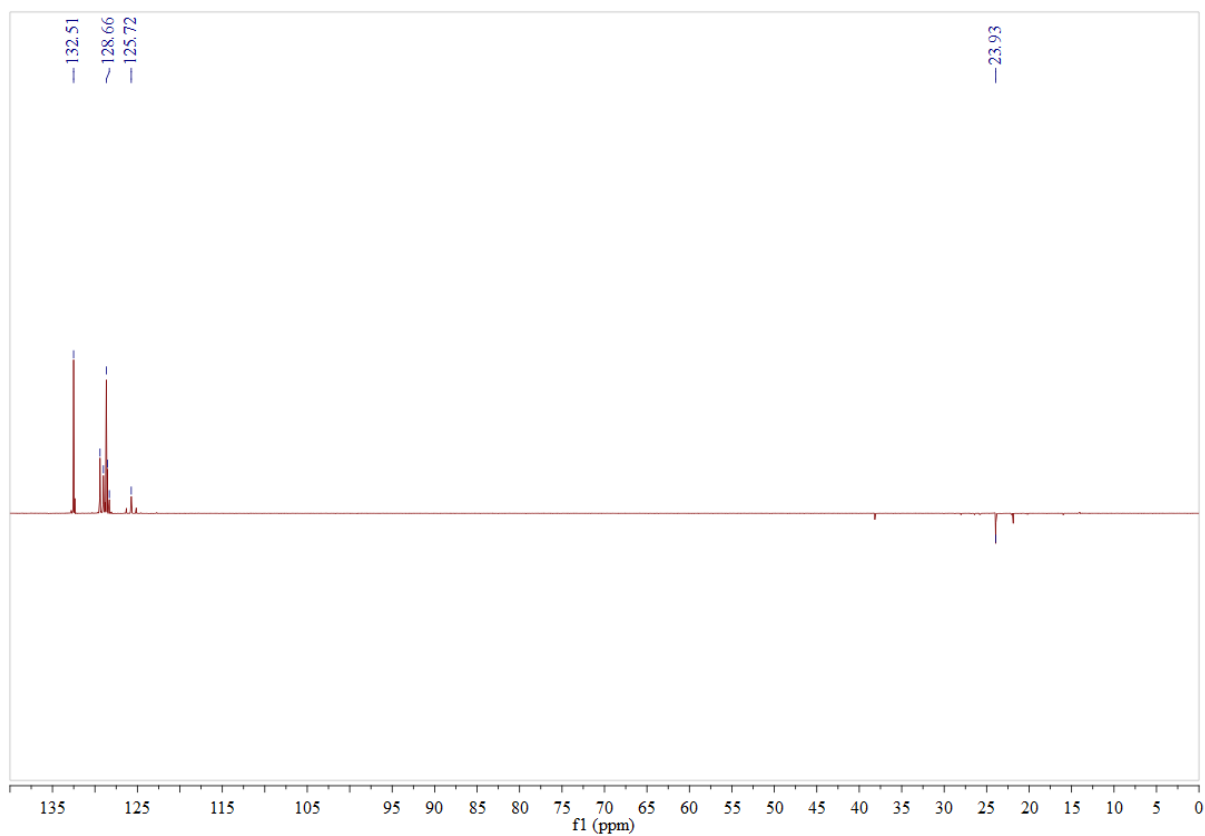
$^1\text{H-NMR}$  (600 MHz,  $\text{CDCl}_3$ ):



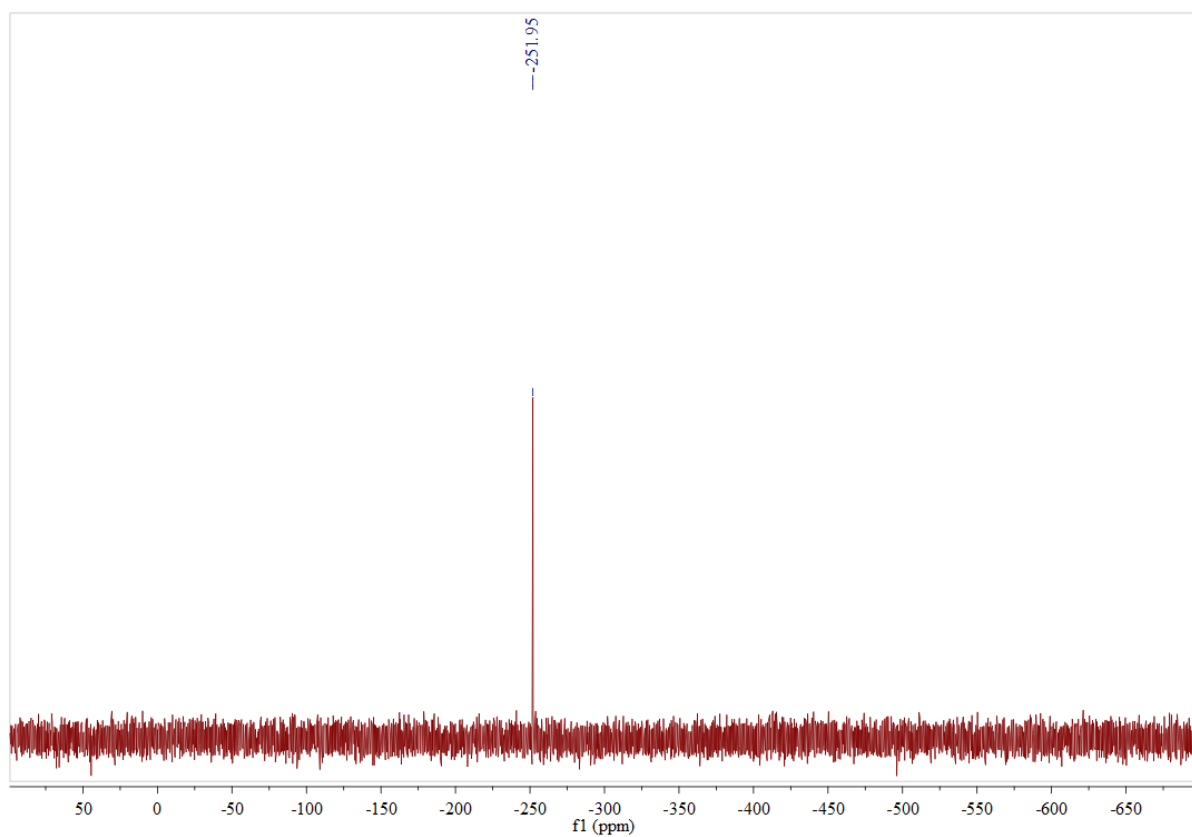
$^{13}\text{C-NMR}$  (223.8 MHz,  $\text{CDCl}_3$ ):



DEPT  $^{13}\text{C}$ -NMR:

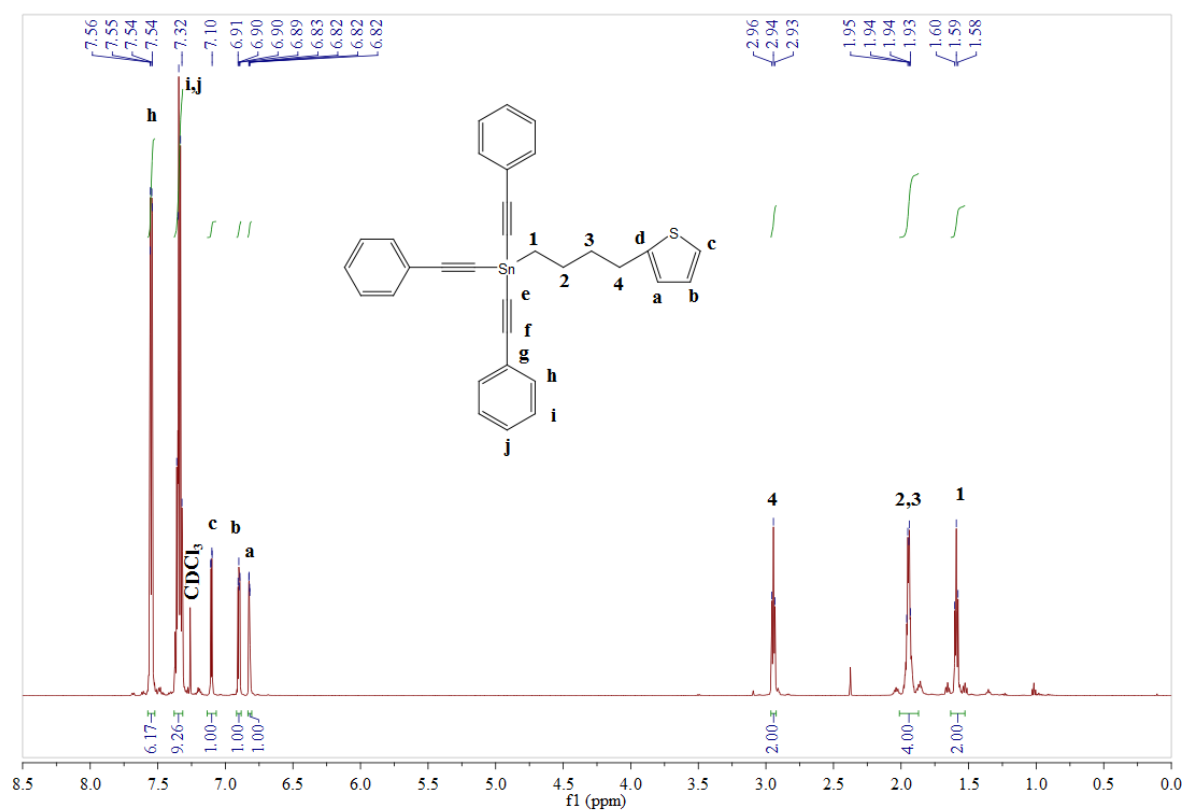


$^{119}\text{Sn}$ -NMR (223.8 MHz,  $\text{CDCl}_3$ ):

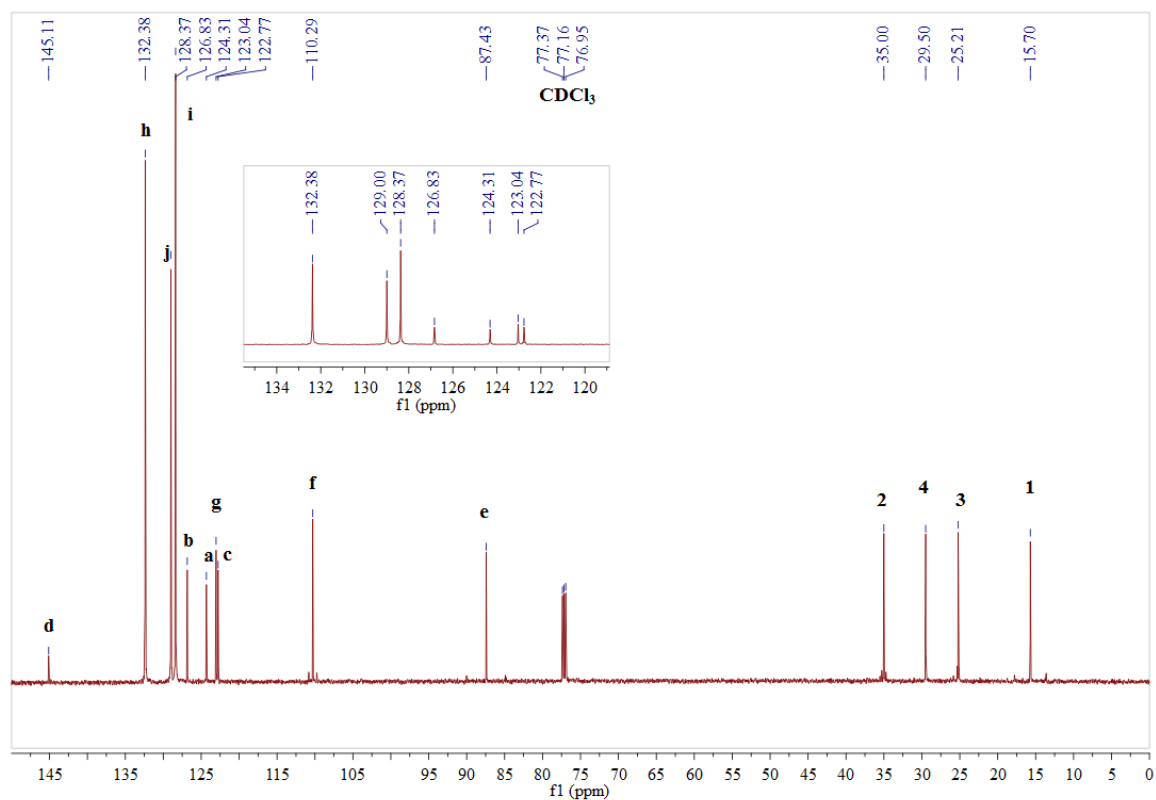


# tris(2-phenylethynyl)(4-(thiophen-2-yl)butyl)stannane (5d)

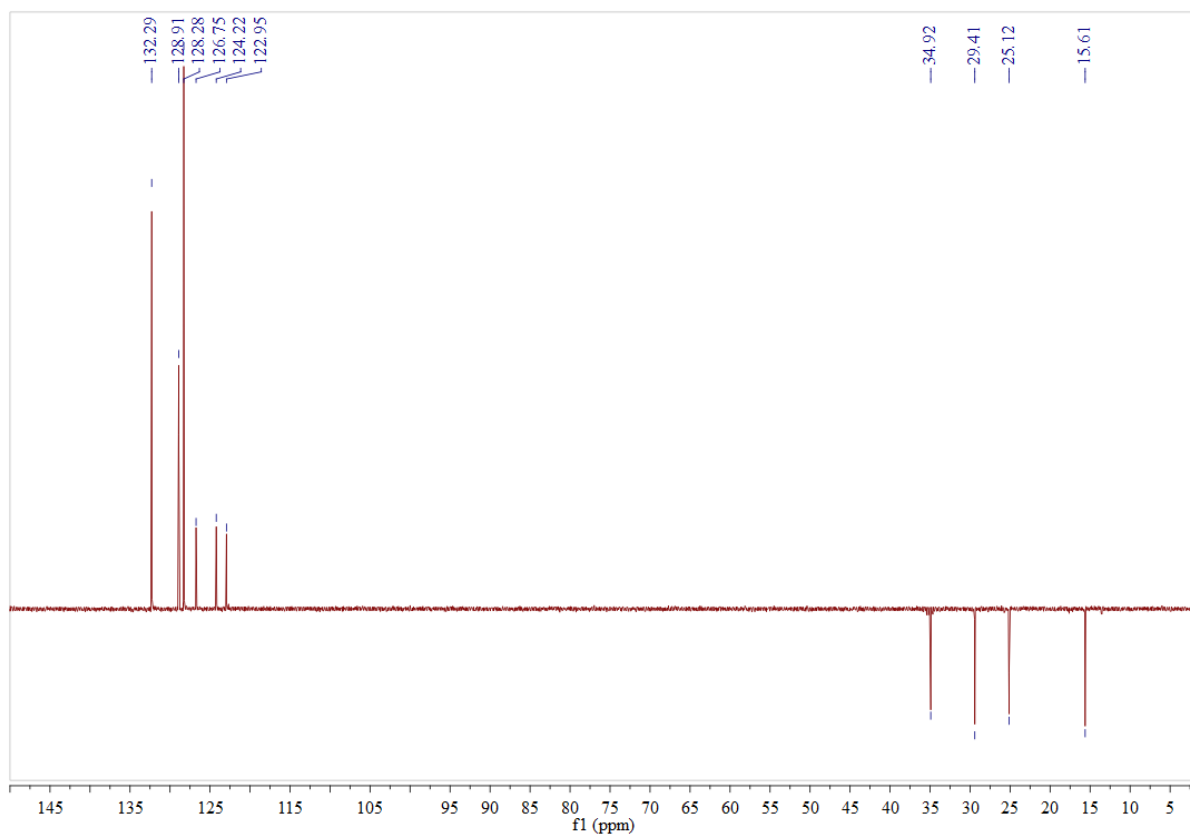
$^1\text{H-NMR}$  (600 MHz,  $\text{CDCl}_3$ ):



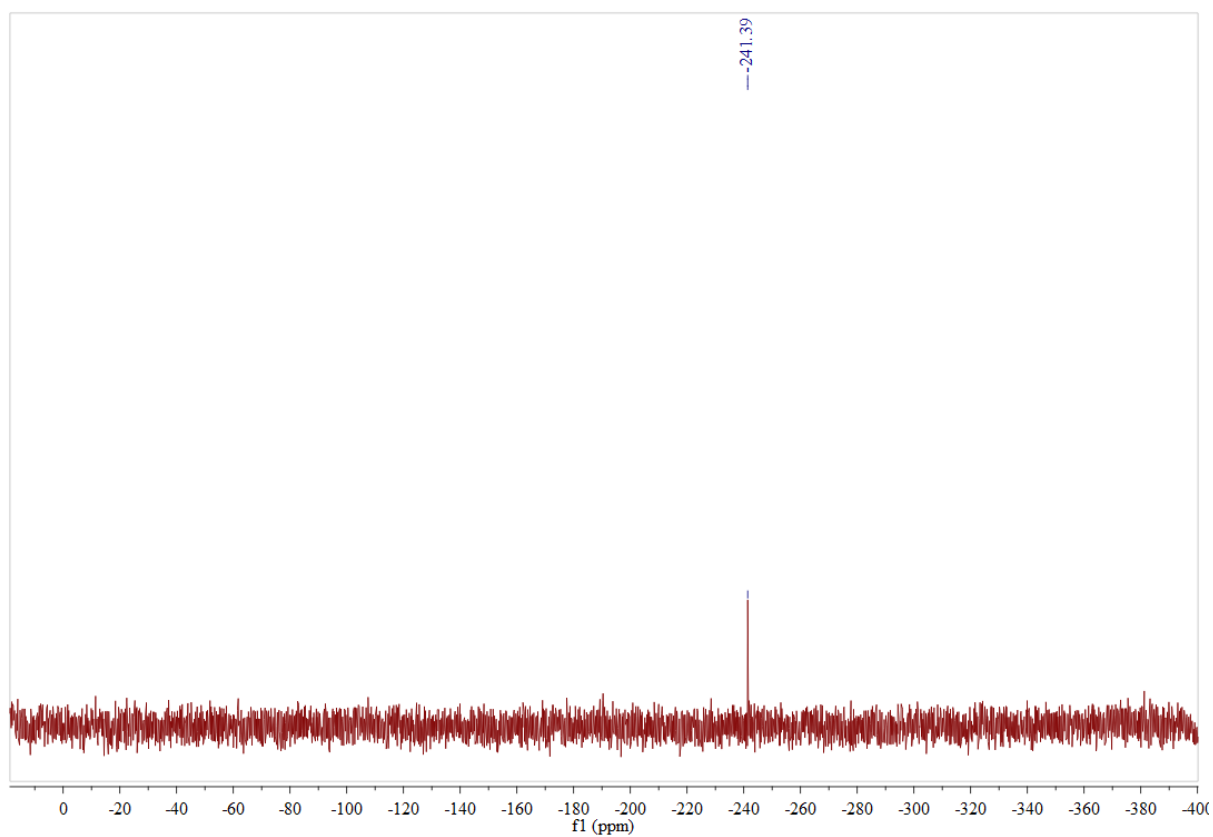
$^{13}\text{C-NMR}$  (223.8 MHz,  $\text{CDCl}_3$ ):



DEPT  $^{13}\text{C}$ -NMR:



$^{119}\text{Sn}$ -NMR (223.8 MHz,  $\text{CDCl}_3$ ):



# Finely Tuned SnO<sub>2</sub> Nanoparticles for Efficient Detection of Reducing and Oxidizing Gases: The Influence of Alkali Metal Cation on Gas-Sensing Properties

Szu-Hsuan Lee,<sup>†,‡</sup> Vardan Galstyan,<sup>§,||</sup> Andrea Ponzoni,<sup>§,||</sup> Isabel Gonzalo-Juan,<sup>‡</sup> Ralf Riedel,<sup>‡</sup> Marie-Anne Dourges,<sup>†</sup> Yohann Nicolas,<sup>†</sup> and Thierry Toupance<sup>\*,†,||</sup>

<sup>†</sup>Institut des Sciences Moléculaires, Université de Bordeaux, UMR 5255 CNRS, Talence 33405, France

<sup>‡</sup>Fachbereich Material- und Geowissenschaften, Technische Universität Darmstadt, Darmstadt D-64287, Germany

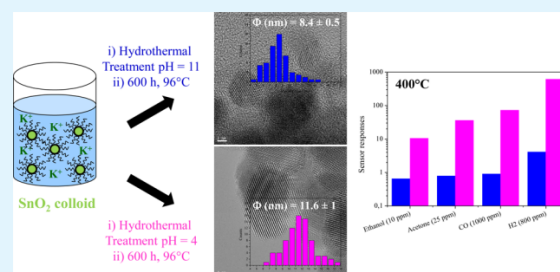
<sup>§</sup>Department of information Engineering, University of Brescia, SENSOR Laboratory, Brescia 25133, Italy

<sup>||</sup>National Research Council (CNR), National Institute of Optics (INO) – Unit of Brescia, Brescia 25123, Italy

## Supporting Information

**ABSTRACT:** Tin dioxide (SnO<sub>2</sub>) nanoparticles were straightforwardly synthesized using an easily scaled-up liquid route that involves the hydrothermal treatment, either under acidic or basic conditions, of a commercial tin dioxide particle suspension including potassium counterions. After further thermal post-treatment, the nanomaterials have been thoroughly characterized by Fourier transform infrared and Raman spectroscopy, powder X-ray diffraction, transmission electron microscopy, X-ray photoelectron spectroscopy, and nitrogen sorption porosimetry. Varying pH conditions and temperature of the thermal treatment provided cassiterite SnO<sub>2</sub> nanoparticles with crystallite sizes ranging from 7.3 to 9.7 nm and Brunauer–Emmett–Teller surface areas ranging from 61 to 106 m<sup>2</sup>·g<sup>-1</sup>, acidic conditions favoring potassium cation removal. Upon exposure to a reducing gas (H<sub>2</sub>, CO, and volatile organic compounds such as ethanol and acetone) or oxidizing gas (NO<sub>2</sub>), layers of these SnO<sub>2</sub> nanoparticles led to highly sensitive, reversible, and reproducible responses. The sensing results were discussed in regard to the crystallite size, specific area, valence band energy, Debye length, and chemical composition. Results highlight the impact of the counterion residuals, which affect the gas-sensing performance to an extent much higher than that of size and surface area effects. Tin dioxide nanoparticles prepared under acidic conditions and calcined in air showed the best sensing performances because of lower amount of potassium cations and higher crystallinity, despite the lower surface area.

**KEYWORDS:** SnO<sub>2</sub> nanoparticles, nanostructures, gas sensing, reducing gases (H<sub>2</sub>, CO), oxidizing gases (NO<sub>2</sub>), volatile organic compounds



## 1. INTRODUCTION

Technologies related to air quality assessment, combustible or explosive gas detection, environmental pollution monitoring, people safety, and medical diagnostics appear among the main concerns of industrial and modern societies.<sup>1–3</sup> To address these issues, chemical sensors including active layers based on semiconducting metal oxides have been widely investigated owing to their straightforward processing routes and high sensitivity to oxidizing and reducing gases.<sup>4–6</sup> Among the n-type wide-band-gap semiconductors available, tin dioxide (SnO<sub>2</sub>) is one of the more attractive semiconductors because it exhibits the highest chemical and thermal stabilities along with remarkable properties including environmental friendliness, transparency, and photochemical durability related to a large direct band gap (3.6–3.7 eV), high electron mobility both as single crystals (up to 240 cm<sup>2</sup>·V<sup>-1</sup>·s<sup>-1</sup>)<sup>7</sup> and as nanomaterials (up to 128 cm<sup>2</sup>·V<sup>-1</sup>·s<sup>-1</sup>),<sup>8</sup> and unique resistivity change under a

gas atmosphere.<sup>9</sup> As a consequence, SnO<sub>2</sub>-based materials found widespread applications in many fields such as photocatalysis,<sup>10,11</sup> optoelectronics,<sup>12</sup> electrochemical storage of energy,<sup>13</sup> photovoltaic conversion,<sup>14,15</sup> and gas sensors.<sup>16–18</sup>

Thus, SnO<sub>2</sub> is the best-understood prototype active material widely investigated in the processing of commercial gas sensors. Although the detailed sensing mechanisms is still to be completely unraveled,<sup>19,20</sup> a first working principle of SnO<sub>2</sub>-based sensors relies on the diffusion of target gas molecules into the sensing layer through its pores and their reaction with chemisorbed oxygen species (O<sub>2</sub><sup>-</sup>, O<sup>-</sup>, O<sub>2</sub><sup>-•</sup>).<sup>21,22</sup> Modification of the amount of adsorbed oxygen molecules upon interaction with gases drastically affects electron depletion on the SnO<sub>2</sub>

Received: November 29, 2017

Accepted: March 5, 2018

Published: March 5, 2018

surface, i.e., the concentration of charge carriers, which induces electric conductance changes. Such variations in the electrical conductivity are then exploited as the sensor response. Furthermore, the alternate formation and filling of oxygen vacancies, such as  $V_{\text{O}}^{\bullet}$ , during the gas pulse was also proposed to rationalize the gas-sensing properties of  $\text{SnO}_2$  nanomaterials.<sup>23–25</sup> Although the actual knowledge on the gas-sensing mechanism is still demanding for deeper understanding, wide agreement is found in the literature concerning size effects both from a theoretical<sup>26,27</sup> and an experimental<sup>28,29</sup> point of view: the lower the crystallite size, the higher the sensor response. This is in agreement with surface area arguments, often invoked as the most intuitive motivation underlying the behavior of metal oxide gas sensors, because the surface area usually increases with the decreasing grain radius. Such size/surface area effects are so strong in gas sensing that they often dominate over other effects. For example, addition of dopants is a method widely adopted to enhance and tune the sensor performances, but it is extremely difficult to completely disentangle the control over crystallite size and material composition during the synthesis process. As a consequence, papers pursuing gas-sensing improvement through a controlled doping process often find out a strict relationship between grain size (surface area) and sensing response, making it hard to understand whether performance optimization is effectively related to the dopant concentration or to size/surface area effects.<sup>30–32</sup>

In this context, owing to the importance of structure and morphology (crystallite size and shapes) of the particles as well as texture (porosity, surface-to-volume ratio) in the sensing properties of  $\text{SnO}_2$  layers, nanostructured tin dioxide with various morphologies and structures, including nanospheres,<sup>33</sup> nanotubes,<sup>34</sup> nanorods,<sup>35</sup> nanowires,<sup>36</sup> nanoplates,<sup>37</sup> and hollow spheres,<sup>38</sup> has been designed within this work to improve the gas-sensing performances. On the other hand, gas selectivity of  $\text{SnO}_2$ -based sensors is one of the most critical issues for application purposes. Several strategies have been proposed to control gas selectivity such as doping the active layer with rare metal oxides or noble metals,<sup>39–41</sup> fine-tuning of the operating temperature,<sup>42</sup> and tailoring the nanostructure of  $\text{SnO}_2$ -based films using purely inorganic<sup>43,44</sup> or hybrid organic–inorganic nanocomposites.<sup>45–47</sup> Nonetheless, these methods usually involve long synthetic strategies or processing and do not allow the preparation of large quantities of materials. To circumvent this limitation, hydrothermal treatments of an available commercial  $\text{SnO}_2$  suspension under acidic conditions have been developed to obtain large amounts of 18 nm  $\text{SnO}_2$  colloids employed for fabricating porous photoanodes for dye-sensitized solar cells.<sup>48,49</sup>

In the present work, we investigated a similar approach using hydrothermal treatment of a commercial colloid by tuning the pH conditions and the thermal post-treatment used. This approach, which can be easily scaled up, gave rise to well-defined tin dioxide nanoparticles. The obtained nanoparticles were characterized by Fourier transform infrared (FTIR), Raman, X-ray diffraction (XRD), transmission electron microscopy (TEM), X-ray photoelectron spectroscopy (XPS), and  $\text{N}_2$  sorption analyses, and their ability to detecting a series of reductive or oxidative gases was highlighted. These gas-sensing properties were then rationalized in terms of chemical composition and structural, textural, and electronic properties of the nanopowders obtained.

## 2. EXPERIMENTAL SECTION

**2.1. Materials Synthesis.** Tin dioxide particle growth was achieved by hydrothermal treatment of a commercial  $\text{SnO}_2$  particle suspension (Alfa Aesar,  $\text{SnO}_2$ , 15% w/v in water, pH = 11–12, counterion  $\text{K}^+$ )<sup>50</sup> under either acidic or basic conditions.

In a first procedure, 37 g of the colloidal  $\text{SnO}_2$  particle suspension and 1 g of glacial acetic acid (Fisher Scientific) were mixed in a closed vessel and stirred for 48 h at room temperature (RT). The resulting acidic slurry (pH = 4.0) in a homemade glass vessel was placed into a stainless steel autoclave (300 mL) and kept at 240 °C (28 bars) for 90 h. After naturally returning to RT, the obtained solids were isolated by centrifugation and then cleaned by several cycles of redispersion, sonication, and centrifugation using water and ethanol as solvents. Drying in air at 90 °C overnight yielded a light greenish powder, hereafter named TOa<sup>90</sup>. This was finally annealed in air at 600 °C for 96 h to give 4 g of white particles, hereafter denoted TOa<sup>600</sup>.

As far as the synthesis under basic conditions is concerned, the same procedure was employed with solely 37 g of the commercial  $\text{SnO}_2$  particle suspension (pH = 11, ammonia solution). After the hydrothermal treatment, washings, centrifugation, and drying at 90 °C overnight, a light yellowish powder, hereafter named TOb<sup>90</sup>, was obtained. Annealing in air at 600 °C for 96 h led to 4 g of white particles, hereafter denoted TOb<sup>600</sup>.

**2.2. Materials Characterization.** Infrared and Raman analyses were carried out with a FTIR Perkin-Elmer spectrophotometer and a Jobin-Yvon Horiba XploRA confocal spectrometer, respectively. Raman spectra were recorded in the spectral range 200–1900  $\text{cm}^{-1}$  using incident wavelengths of  $\lambda = 532$  nm at 45 mW and a resolution of 4.3  $\text{cm}^{-1}$ . The signal-to-noise ratio was enhanced by the accumulation of two successive spectra using an acquisition time of 60 s for each spectrum. The crystalline structure was checked by X-ray diffraction (D2 PHASER, Bruker AXS) using monochromatic Cu K $\alpha$  radiation ( $\lambda = 1.54056$  Å) and a current/voltage of 10 mA/30 kV. Scanning was carried out for  $2\theta$  ranging from 10 to 90° with a step of 0.02°. For transmission electron microscopy analyses, a suspension of the powders in ethanol was deposited on a holey carbon (Cu) grid and images were then recorded on JEOL JEM-2100 (low-resolution TEM) and JEOL JEM-2200FS (high-resolution TEM) microscopes. Surface analyses by X-ray photoelectron spectroscopy (XPS) were performed with a K-Alpha spectrometer (ThermoFisher Scientific) for powders pressed onto indium foil. The monochromatized Al K $\alpha$  source ( $h\nu = 1486.6$  eV) was activated with a spot size 200  $\mu\text{m}$  in diameter. The full spectra (0–1100 eV) were obtained with a constant pass energy of 200 eV and high-resolution spectra with a constant pass energy of 40 eV (dwell time 200 ms). Fitting and quantitative analyses of XPS spectra were performed using AVANTAGE software (ThermoFisher Scientific). Specific surface areas (Brunauer–Emmett–Teller (BET)) were determined from  $\text{N}_2$  sorption data collected with a Micromeritics ASAP2010 equipment. The  $\text{N}_2$  adsorption–desorption isotherms were recorded at 77 K in the 0–0.99 relative pressure ( $P/P_0$ ) range. Pore size distributions were deduced from the adsorption branch of the isotherms using the Barrett, Joyner, Halenda (BJH) theory.

**2.3. Gas-Sensing Tests.** Gas sensor devices were prepared starting from 2 mm  $\times$  2 mm  $\times$  0.25 mm alumina substrates, provided on the top face by sputtered Pt contacts, having interdigitated shape, thickness of 800 nm, and separation of about 200  $\mu\text{m}$ . On the rear side, a Pt meander acting as a heating element to control the sensor temperature was deposited by magnetron direct current sputtering. TOa or TOb nanopowders were dispersed in a mixture of water (1.5 mL) and acetone (1 mL) in the presence of Triton X-100 (1 drop) and acetic acid (1 drop), and they were casted (3 droplets, each 0.3  $\mu\text{L}$ ) over the functional substrates. The resulting layers were heated at 200 °C for 3 days in air. Gas-sensing measurements were carried out in a thermostatic chamber (stabilized at a temperature of 20 °C) working with both oxidizing ( $\text{NO}_2$ ) and reducing gases ( $\text{CO}$ ,  $\text{H}_2$ , ethanol, acetone) in a background of synthetic dry air generated from certified bottles. Gas concentration inside the test chamber was controlled by mixing the flows from the different bottles by means of mass flow controllers. The sensor signal was continuously monitored during



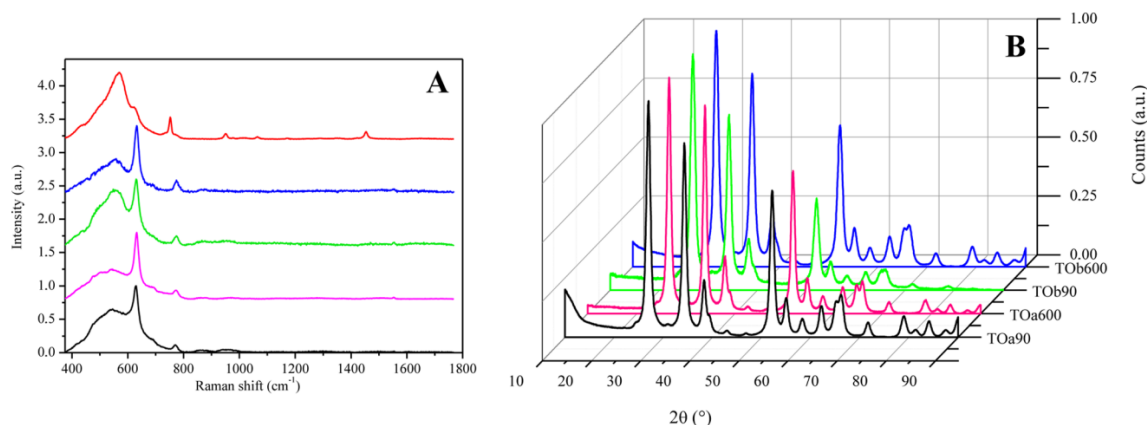


**Figure 1.** (A) Raman spectra and (B) powder XRD patterns of SnO<sub>2</sub> particles: TOa<sup>90</sup> (black), TOa<sup>600</sup> (pink), TOb<sup>90</sup> (green), and TOb<sup>600</sup> (blue). The Raman spectrum of the dried commercial colloid is given as a reference (red).

**Table 1.** Average Crystallite Sizes, Average Particle Sizes, and Nitrogen Sorption Porosimetry Data for SnO<sub>2</sub> Nanopowders

sample	average crystallite size from XRD (nm) <sup>a</sup>	average particle size from TEM (nm) <sup>b</sup>	S <sub>BET</sub> (m <sup>2</sup> ·g <sup>-1</sup> ) <sup>c</sup>	total pore volume (cm <sup>3</sup> ·g <sup>-1</sup> ) <sup>d</sup>	average pore size (nm) <sup>e</sup>
TOa <sup>90</sup>	8.6 ± 0.5	10.7 ± 1.0	79.0 ± 2.5	0.31 ± 0.04	15.6 ± 2.0
TOa <sup>600</sup>	9.7 ± 0.5	11.6 ± 1.0	61.0 ± 2.0	0.29 ± 0.04	19.7 ± 2.6
TOb <sup>90</sup>	7.6 ± 0.4	8.5 ± 0.5	106.0 ± 3.0	0.53 ± 0.07	20.7 ± 2.7
TOb <sup>600</sup>	7.3 ± 0.4	8.4 ± 0.5	98.0 ± 3.0	0.50 ± 0.07	20.6 ± 2.7

<sup>a</sup>Estimated from full width at half-maximum of the diffraction peak using the Scherrer equation. <sup>b</sup>Deduced from TEM images. <sup>c</sup>Surface areas determined by BET. <sup>d</sup>Pore volumes estimated by single-point analysis. <sup>e</sup>Average pore sizes calculated by the BJH model (applied to the adsorption branch).

measurements by applying a constant 1 V bias to the electrodes and measuring the current flowing through the SnO<sub>2</sub> layers by means of a picoammeter. The sensor response will be expressed as  $(G_{\text{gas}} - G_{\text{air}})/G_{\text{air}}$ , hereafter shortened as  $\Delta G/G$ , where  $G_{\text{gas}}$  and  $G_{\text{air}}$  are the steady-state conductance values measured during gas exposure and in air, respectively.

### 3. RESULTS AND DISCUSSION

**3.1. Particle Characterization.** First of all, it is worth mentioning that the commercial colloid used as a precursor includes polypyrrole and K<sup>+</sup> counterions.<sup>50</sup> Evolution of composition depending on the preparation conditions was first studied by FTIR and Raman spectroscopy. Regardless of the preparation conditions, no band characteristics of organics were observed in the FTIR spectra, indicating that most of the organic polymer has been removed during the purification steps (Figure S1). In the case of TOa samples, typical features of adsorbed water or surface hydroxyl groups (broad bands centered at 3430 ( $\nu_{\text{O-H}}$ ) and 1630 ( $\delta_{\text{O-H}}$ ) cm<sup>-1</sup>) and tin oxide moieties (675–650 and 575 (sh) ( $\nu_{\text{Sn-O-Sn}}$  and  $\nu_{\text{Sn-O}}$ ) cm<sup>-1</sup>)<sup>51,52</sup> were observed. Furthermore, a significant shift, i.e., from 651 cm<sup>-1</sup> for TOa<sup>90</sup> to 675 cm<sup>-1</sup> for TOa<sup>600</sup>, of the  $\nu_{\text{Sn-O-Sn}}$  vibration mode was observed, which accounts for the change in crystallite size upon calcination.<sup>53</sup> Similar features were detected for TOb samples with some additional bands in the 1200–900 cm<sup>-1</sup> region that could be assigned to hydroxyl-metal bonds.<sup>54</sup> On the other hand, the rutile-type phase of SnO<sub>2</sub> can be sensitively evidenced by Raman spectroscopy. According to group theory analysis, rutile SnO<sub>2</sub> has four Raman-active modes ( $A_{1g} + B_{1g} + B_{2g} + E_g$ )<sup>55</sup> and rutile-type SnO<sub>2</sub> single crystal shows vibrational bands at 123 cm<sup>-1</sup> ( $B_{1g}$ ), 473 cm<sup>-1</sup> ( $E_g$ ), 633 cm<sup>-1</sup> ( $A_{1g}$ ), and 773 cm<sup>-1</sup> ( $B_{2g}$ ).<sup>56</sup> The

Raman spectrum of the dried commercial colloid exhibits no clear evidence of crystalline SnO<sub>2</sub> species (Figure 1A). By contrast, after hydrothermal treatment in acidic or basic medium, with or without further calcination, Figure 1A shows the Raman bands of SnO<sub>2</sub> nanoparticles at 632 cm<sup>-1</sup> ( $A_{1g}$ ) and 773 cm<sup>-1</sup> ( $B_{2g}$ ) along with a very broad band centered at around 550 cm<sup>-1</sup>, which can be attributed to modes related to the local lattice disorder and vacant site<sup>55</sup> or to oxo-hydroxotin species.<sup>57</sup> It is generally admitted that expansion and contraction of vibrational modes of Sn–O bonds are at the origin of  $A_{1g}$  and  $B_{2g}$  modes and that the tetragonal rutile structure of SnO<sub>2</sub> is assessed by the presence of these Raman features.<sup>58</sup> Moreover, the relative intensity of the sharp peak at 632 cm<sup>-1</sup> with respect to that at 550 cm<sup>-1</sup> increases after calcination, suggesting an improved crystallization of the nanoparticles. In addition, no feature was detected in the 900–1800 cm<sup>-1</sup> wavenumber range, confirming that the remaining organics and polymers have been removed both in dried and calcined samples.

Powder X-ray diffraction confirmed the crystalline structure of the particles formed (Figure 1B). Whatever preparation condition used, the tetragonal, i.e., rutile-like, tin dioxide phase was obtained, as revealed by the X-ray diffraction pattern of each sample studied with main features at  $d$  (Å) values of {110} (3.35), {101} (2.64), {200} (2.37), {211} (1.76), {220} (1.68), {002} (1.59), {310} (1.50), {112} (1.44), and {301} (1.42) in close agreement with the reported data (Joint Committee on Powder Diffraction Standards, JCPDS, card no. 41-1445). This is consistent with the formation of pure cassiterite SnO<sub>2</sub> crystallite without any doping. Furthermore, the average crystal sizes of SnO<sub>2</sub>, estimated from the average of line broadening of

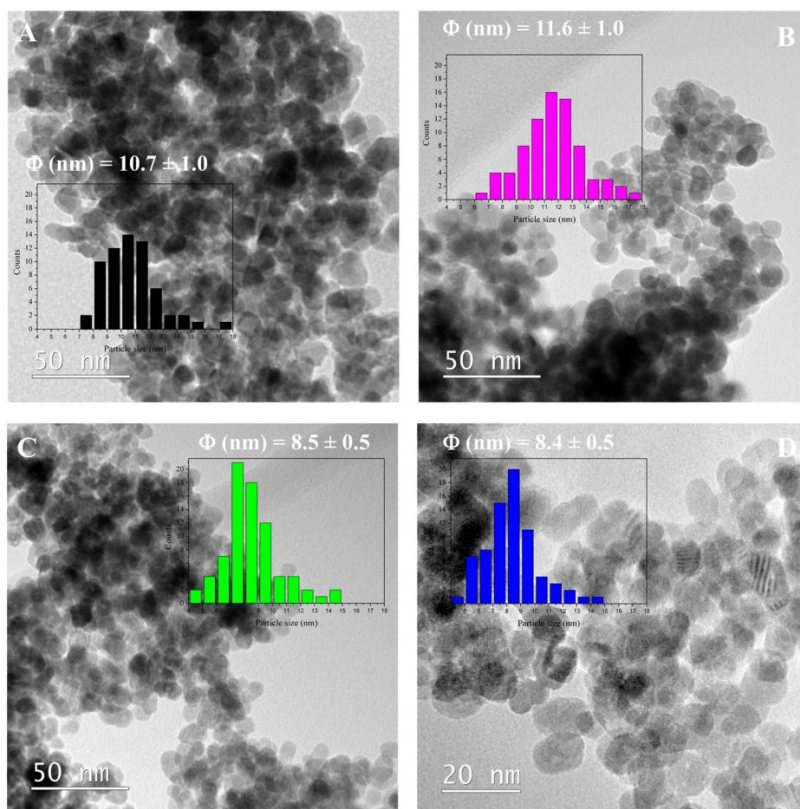


Figure 2. TEM micrographs and particle size distribution of (A) TOa<sup>90</sup>, (B) TOa<sup>600</sup>, (C) TOb<sup>90</sup>, and (D) TOb<sup>600</sup>.

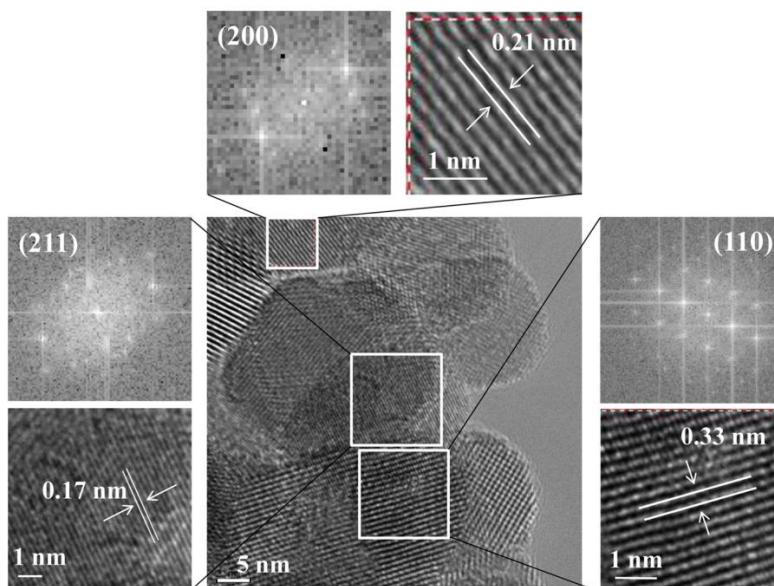
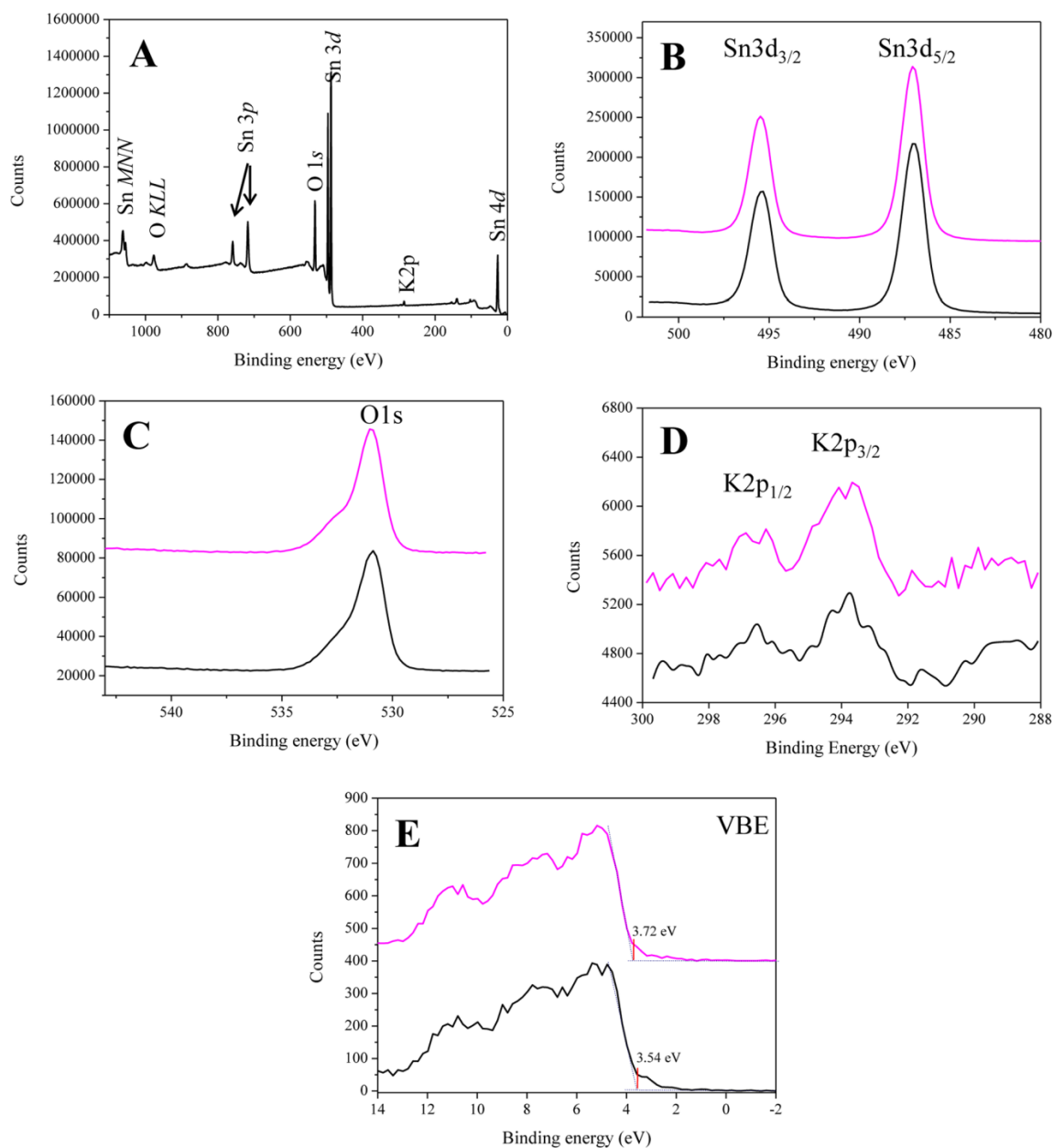


Figure 3. HR-TEM images and selected-area electron diffraction (SAED) pattern of TOa<sup>90</sup>.

the  $\{110\}$  and  $\{101\}$  diffraction peaks according to the Scherrer equation,<sup>59</sup> were estimated to be  $7.6 \pm 0.4$ ,  $7.3 \pm 0.4$ ,  $8.5 \pm 0.5$ ,

and  $9.7 \pm 0.5$  nm for TOb<sup>90</sup>, TOb<sup>600</sup>, TOa<sup>90</sup>, and TOa<sup>600</sup>, respectively (Table 1). As a consequence, the calcination step





**Figure 4.** XPS patterns of the TOa<sup>90</sup> (black) and TOa<sup>600</sup> (magenta) particles: (A) XPS survey spectrum, (B) Sn 3d region, (C) O 1s region, (D) K 2p region (full), and (E) valence-band XPS spectra.

induced a slight increase in the mean crystallite size for samples prepared in acidic conditions but has no influence for those synthesized in basic medium.

TEM micrographs show that TOa and TOb samples are composed of a network of aggregated pseudospherical nanocrystallites with a rather narrow particle size distribution and confirm the crystallite sizes estimated from the XRD pattern, whereas their average size is slightly larger (Figure 2).

Thus, the calcination step does not influence the average particle size for particles prepared under basic conditions,

whereas it induces a slight increase in the mean particle size in the case of particles synthesized in acidic medium. On the other hand, HR-TEM micrographs and selected-area electron diffraction (SAED) pattern of each sample showed the formation of well-crystallized SnO<sub>2</sub> particles exposing well-defined facets typical of the formation of rutile-like tin dioxide (Figures 3 and S2–S4). For instance, TOa<sup>90</sup> showed particles exposing lattice fringes with *d*-spacings of 0.33, 0.21, and 0.17 nm corresponding to the (110), (200), and (211) planes of cassiterite, i.e., rutile-like, SnO<sub>2</sub> (Figure 3).

The same exposed facets were also observed in the HR-TEM micrographs of the other samples. As a consequence, the nanopowders obtained just after the hydrothermal treatment already expose low-surface-energy facets as (110) ( $1.554 \text{ J} \cdot \text{m}^{-2}$ ),<sup>60</sup> explaining the absence of change in the nature of the exposed facets after calcination.

Surface chemical elements and chemical states of tin dioxide particles were then investigated by X-ray photoelectron spectroscopy. Apart from weak C 1s and Si 2p peaks located at around 285 and 102 eV, respectively, which could be ascribed to environmental carbon and silicon contaminations, emission typical of only tin, oxygen, and potassium elements were observed in the survey of the TOa and TOB samples (Figures 4 and S5). Energies of the main features detected are reported in Table 2. Whatever the preparation conditions, the

**Table 2. Binding Energies of the Different Elements Detected by X-ray Photoelectron Spectroscopy, Valence Band Energy ( $E_{\text{vf}}$ ), and Related Estimation of Debye Lengths ( $L_{\text{D}}$ )**

sample	Sn 3d <sub>5/2</sub> (eV) <sup>a</sup>	Sn 3d <sub>3/2</sub> (eV) <sup>a</sup>	O 1s (eV) <sup>a</sup>	K 2p <sub>3/2</sub> (eV) <sup>a</sup>	$E_{\text{vf}}$ (eV) <sup>b</sup>	$L_{\text{D}}$ (nm) <sup>c</sup>
TOa <sup>90</sup>	495.4	487.0	530.9	293.9	3.54	$6.4 \pm 3.8$
TOa <sup>600</sup>	495.5	487.1	531.0	293.8	3.72	$0.7 \pm 0.1$
TOB <sup>90</sup>	495.5	487.1	530.9	293.6	3.54	$6.4 \pm 3.8$
TOB <sup>600</sup>	495.4	486.9	530.8	293.7	3.41	$76 \pm 48$

<sup>a</sup>Calibration has been done by fixing C 1s at 285.0 eV (uncertainty:  $\pm 0.1$  eV). <sup>b</sup>Determined by linear extrapolation of the valence band emission edge to the spectrum background<sup>63</sup> (uncertainty:  $\pm 0.03$  eV). <sup>c</sup> $L_{\text{D}}$  has been calculated at room temperature from eq 1 along with its uncertainty arising from the uncertainty of  $E_{\text{vf}}$ .

Sn 3d region showed two lines at  $487.0 \pm 0.1$  and  $495.4 \pm 0.1$  eV arising from spin–orbit coupling of the 3d state. The splitting between the Sn 3d doublet was found to be  $8.4 \pm 0.1$  eV, which is consistent with that reported for SnO<sub>2</sub> and the presence of Sn(IV) states.<sup>61</sup>

On the other hand, the O 1s spectrum of TOa showed a main component at  $530.9 \pm 0.1$  eV, which can be attributed to the lattice oxygen O<sup>2-</sup> (Figure 4, O 1s). Additional shoulders located at  $531.9$  and  $533.0 \pm 0.1$  eV next to the main peak indicate that several other chemical states are present according to the measured binding energy. They are caused by air contamination (water, OH, O–C), which is typical for ex situ samples, the calcination step diminishing the amount of these chemical states (Table S1, Figure S6). Finally, surface K/Sn atomic ratios were found to be 0.01–0.02 and 0.08–0.09 for TOa and TOB samples, respectively, which are significantly lower than those of the dried commercial colloid (Table S1). As a consequence, the acidic treatment favors the elimination of potassium counterions present in the starting colloid.

Figure 4 also shows the valence-band XPS spectra of the TOa samples with and without calcination. The upper valence band is predominantly composed of O 2p states with some contributions of Sn–O states.<sup>62</sup> The binding energy of the valence-band maximum with respect to the Fermi level ( $E_{\text{vf}}$ ) was determined as reported in the literature (Table 2).<sup>63</sup> Whatever the thermal post-treatment used, the values are comprised between 3.4 and 3.7 eV, which match well with the band gap energy of SnO<sub>2</sub> (3.6 eV at 300 K) and are in good accordance with those described for undoped SnO<sub>2</sub> films fabricated by in situ sputter deposition.<sup>63,64</sup> These features

suggest a Fermi-level position near the bottom of the conduction band and the presence of few oxygen vacancies in the tin dioxide particles prepared.<sup>62</sup> In addition, the spectra of the annealed samples exhibit no further band gap emission above the valence-band maximum, evidencing the stoichiometric termination of the SnO<sub>2</sub> nanoparticle surface, where each tin surface atom exists as Sn<sup>4+</sup> centers.<sup>61,65</sup> Such a surface termination is conventionally observed for tin oxide materials thermally treated in an oxidizing atmosphere.<sup>66</sup>

On the other hand, the observed differences in the  $E_{\text{vf}}$  values (Table 2) have deep implications from an electrical point of view. On the basis of  $E_{\text{vf}}$  values, the density of charge carriers ( $n$ ) has been calculated through the Fermi integral using an energy gap value  $E_{\text{g}} = 3.6$  eV.<sup>67</sup> On the basis of  $n$ , the Debye length ( $L_{\text{D}}$ ) has been further calculated as an essential parameter controlling the gas-sensing performance of metal oxide chemiresistors

$$L_{\text{D}} = \sqrt{\frac{\epsilon k T}{q^2 n}} \quad (1)$$

where  $\epsilon$  is the dielectric constant of the semiconductor ( $\epsilon \approx 10^{-10} \text{ F} \cdot \text{m}^{-1}$  for SnO<sub>2</sub>),<sup>65</sup>  $k$  is the Boltzmann constant,  $T$  is the temperature (in K), and  $q$  is the elementary charge.  $L_{\text{D}}$  values calculated for  $T = 300$  K are reported in Table 2. Although the vacuum condition of the XPS measurement could induce oxygen desorption from SnO<sub>2</sub>, XPS data being acquired at room temperature, oxygen removal is expected to occur only to a small extent, thus suggesting that  $n$  and  $L_{\text{D}}$  values reported in Table 2 could be reasonably adopted to compare the electrical properties of the prepared materials.

Textural properties of the different SnO<sub>2</sub> nanopowders were determined by N<sub>2</sub> adsorption–desorption analysis (Figure 5).

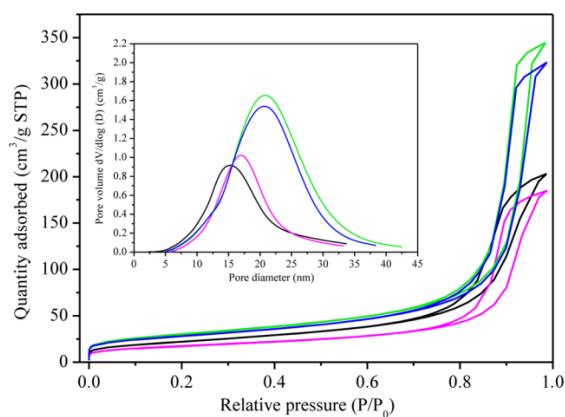


**Figure 5. Nitrogen adsorption–desorption isotherms and pore size distributions (inset) of TOa<sup>90</sup> (black), TOa<sup>600</sup> (pink), TOB<sup>90</sup> (green), and TOB<sup>600</sup> (blue).**

Each sample led to a type IV sorption isotherm, showing a hysteresis loop of type H<sub>2</sub>, which is a characteristic of mesoporous solids according to the IUPAC classification.<sup>68</sup> Furthermore, all powders exhibit a well-defined and rather narrow pore size distribution with average pore sizes of about 16 and 21 nm for TOa and TOB, respectively. As a consequence, the mesoporosity detected can be attributed to the interparticle space that can be seen in the porous network

of aggregated cassiterite SnO<sub>2</sub> nanoparticles evidenced by TEM studies.<sup>68</sup>

Nonetheless, a strong influence of the use of acetic acid was observed on the BET surface areas and total pore volumes. Thus,  $S_{\text{BET}}$  values collapse from  $106.0 \pm 3.0$  and  $98.0 \pm 3.0 \text{ m}^2 \cdot \text{g}^{-1}$  for TOB samples to  $79.0 \pm 2.5$  and  $61.0 \pm 2.0 \text{ m}^2 \cdot \text{g}^{-1}$  for TOA samples. Similarly, total pore volumes obtained for the powder synthesized under acidic conditions are 1.7 lower than those of the samples prepared in basic medium. Moreover, the calcination step affects more the textural properties of the powders prepared in acidic conditions as it was already mentioned for the mean crystallite and particle sizes deduced from XRD and TEM analyses. This trend might be rationalized as follows. Under basic conditions, the presence of potassium counterions adsorbed on the tin oxide surface hinders particle growth during both the solvothermal and the calcination treatment, which led to smaller crystals and higher specific surface areas. By contrast, in acidic medium, potassium counterions adsorbed on the tin oxide surface were exchanged with the protons provided by acetic acid, which favored the condensation reaction and, as a consequence, allowed the crystallites to grow bigger.

**3.2. Electrical and Gas-Sensing Characterization.** The temperature dependence of the device conductance has been investigated in dry air in the temperature range between 200 and 400 °C, where the main features of oxygen chemisorption lie.<sup>70</sup> To measure steady-state values, data reported in Figure 6 have been acquired waiting about 10 h for the conductance reaching a stable value after the temperature is changed.

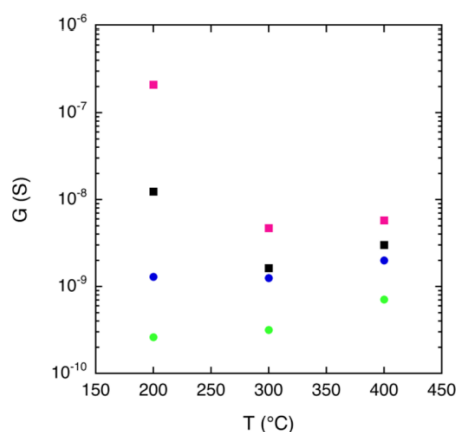


**Figure 6.** Temperature dependence of the sensor conductance measured in dry air for the TOa<sup>90</sup> (black), TOa<sup>600</sup> (pink), TOB<sup>90</sup> (green) and TOB<sup>600</sup> (blue) samples.

Materials prepared under acidic conditions show large conductance variation as a function of temperature (Figure 6). Thus, TOa samples present a conductance minimum at the temperature of 300 °C, which is commonly explained in the literature as the fingerprint of oxygen chemisorption.<sup>70</sup> This process is thermally activated; thus, increasing temperature causes the material to increase the population of chemisorbed oxygen. As a consequence, electrons are withdrawn from the conduction band and the material conductance drops. On further increasing the device temperature, desorption phenomena start to dominate over adsorption and the population of

chemisorbed oxygen decreases. As a consequence, the electrons release back to the conduction band and the conductance increases again. On the contrary, TOB samples do not feature such a characteristic minimum; instead, their conductance shows weak temperature dependence. Besides this difference, it is worth noting that TOa samples are systematically more conductive than TOB samples and, given the synthesis conditions (basic/acidic), the material treated at 600 °C is more conductive than the material treated at 90 °C.

Gas-sensing properties have been investigated in the same temperature range, revealing the important effects induced by the synthesis and thermal treatment conditions. As an example, Figure 7a reports the time dependence of the sensor signal acquired with TOa devices during the exposure to NO<sub>2</sub> and H<sub>2</sub>. The sensor response shows the typical behavior of an n-type sensing mechanism: the material conductance increases upon exposure to reducing gases (CO) and decreases upon exposure to oxidizing gases (NO<sub>2</sub>). Differently, TOB samples feature a conductance increase for both gases, suggesting the occurrence of more complex phenomena (Figure 7b). The spectrum of tested chemicals has been expanded, including other reducing gases such as carbon monoxide, acetone, and ethanol. The temperature dependence of the response to reducing gases is shown in Figure 7c–f.

All sensors exhibited a regular n-type response to this set of compounds, with TOa samples showing responses higher (at least 1 order of magnitude) than those of TOB samples. Within TOa samples (as well as within TOB samples) performances are enhanced by the 600 °C thermal treatment. Thus, devices based on TOa<sup>600</sup> nanopowders showed the highest sensor responses at 400 °C to H<sub>2</sub> (100–450 for 100–800 ppm), CO (7–18 for 10–100 ppm), acetone (200–1500 for 25–200 ppm), and ethanol (7–450 for 10–100 ppm). A comparison with the literature indicates that this material competes well with state-of-the-art chemiresistors based on pure SnO<sub>2</sub>, in terms of both response amplitude and selectivity (Table 3).<sup>33,71–76</sup> The response amplitude to ethanol is comparable to that measured for SnO<sub>2</sub> layers with sensing performance optimized by means of different strategies, including reduction of the grain size down to 3.5 nm or by three-dimensional hierarchical morphology.<sup>33,71</sup>

Concerning selectivity, this is usually assessed comparing the response intensity of possible interfering gases to the response intensity of the target compound at the same (or similar) concentrations. The overview provided in Table 3 confirms that the response to ethanol is much higher than the response to gases such as H<sub>2</sub> or CO (about 30 and 1500 times, respectively), providing a selectivity at least comparable with literature data.<sup>33,72</sup> About acetone, the response intensity comparable to that for ethanol is typically observed in sensors based on pure SnO<sub>2</sub> nanostructures,<sup>71</sup> and our results are in line with these observations.

In addition, TOa<sup>600</sup>-based devices exhibited high sensitivity to NO<sub>2</sub> in the 0.5–8 ppm range. However, in contrast to other analytes, sensor responses to NO<sub>2</sub> monotonically decreased with increasing the operating temperature between 200 and 400 °C. The highest sensor responses to NO<sub>2</sub> then reached 100–170 for 1–4 ppm at 200 °C, which competes well with the response of more sophisticated nanostructures.<sup>77,78</sup>

**3.3. Discussion.** The behavior of oxide semiconductors is usually interpreted in the framework of the space charge layer, which allows rationalizing the interplay between the semi-conducting and morphological properties exhibited by the

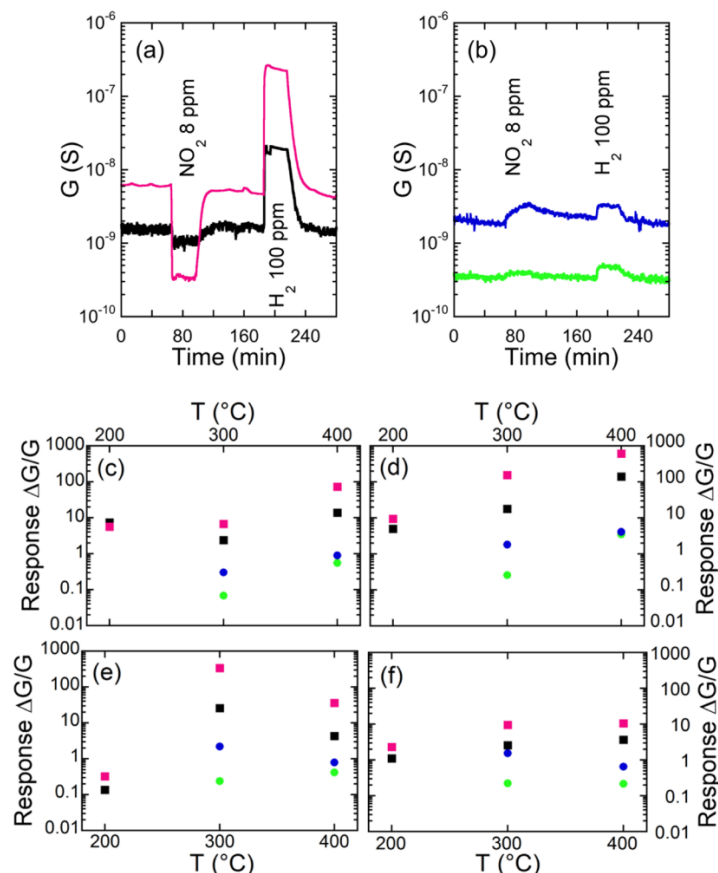


**Figure 7.** Gas-sensing characterization of TOa<sup>90</sup> (black), TOa<sup>600</sup> (pink), TOb<sup>90</sup> (green), and TOb<sup>600</sup> (blue) samples. Dynamic response to 8 ppm of NO<sub>2</sub> and to 100 ppm of H<sub>2</sub> exhibited by samples prepared in acidic conditions (a) and in basic conditions (b) at the working temperature of 300 °C. Temperature effects on the response amplitude measured for reducing gases: 1000 ppm of CO (c), 800 ppm of H<sub>2</sub> (d), 25 ppm of acetone (e), and 10 ppm of ethanol (f).

**Table 3. Gas-Sensing Performance of the TOa<sup>600</sup> Material and Comparison with Responses to Hydrogen (H<sub>2</sub>), Acetone (C<sub>3</sub>H<sub>6</sub>O), Ethanol (C<sub>2</sub>H<sub>6</sub>O), and Carbon Monoxide (CO) Reported in the Literature for State-of-the-Art Chemiresistors Based on Pure SnO<sub>2</sub><sup>44</sup>**

material structure	working T (°C)	resp. @ H <sub>2</sub> conc.	resp. @ C <sub>3</sub> H <sub>6</sub> O conc.	resp. @ C <sub>2</sub> H <sub>6</sub> O conc.	resp. @ CO conc.	ref
TOa <sup>600</sup>	300	47 @ 100 ppm	823 @ 100 ppm	1591 @ 100 ppm	0.95 @ 100 ppm	this work
TOa <sup>600</sup>	300	87 @ 200 ppm		1072 @ 50 ppm	1.54 @ 250 ppm	this work
small diameter nanoparticles	350	120 @ 200 ppm		1000 @ 50 ppm	70 @ 200 ppm	33
hierarchical nanocones	325		175 @ 100 ppm	100 @ 100 ppm		71
nanowire network	250	9 @ 100 ppm		300 @ 100 ppm	1 @ 100 ppm	72
nanowire network	450	2 @ 100 ppm		62 @ 100 ppm	2.4 @ 100 ppm	73
hollow nanospheres	250			30 @ 50 ppm		74
biomorphic architecture	170			95 @ 100 ppm		75
nanowire network	400	3.1 @ 100 ppm	9.6 @ 100 ppm	10.5 @ 100 ppm	3.3 @ 100 ppm	76

<sup>44</sup>All of these results have been acquired in the same background (dry air).

material at the micro-/nanoscale and its macroscopic electrical transport and gas-sensing properties.<sup>79,80</sup>

Electrical conductance is dominated by the Schottky barrier developed at grain boundaries as a consequence of oxygen chemisorption. This induces the formation of surface acceptor states that capture electrons from the SnO<sub>2</sub> conduction band and rise up a space charge layer exhausted from bulk carriers.

The thickness of such a layer ( $L_{SCL}$ ) is calculated from the Debye length and the Schottky barrier height ( $qV_S$ )<sup>80</sup>

$$L_{SCL} = L_D \sqrt{\frac{2qV_S}{kT}} \quad (2)$$

Depending on the ratio of the grain diameter ( $D$ ) and  $L_{SCL}$ , three different conduction regimes may be identified:<sup>79</sup> (i) if



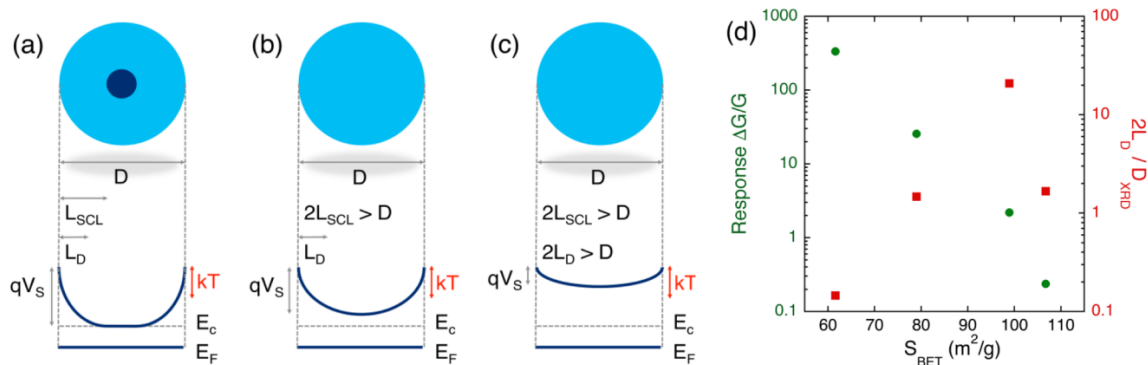


**Figure 8.** Analysis of size and surface area effects. Schematic representation of the conduction band profile inside a grain as a function of the relationship among the Debye length ( $L_D$ ), the thickness of the space charge layer ( $L_{SCL}$ ), and the grain diameter ( $D$ ) for the three characteristic regimes:  $2L_{SCL} < D$ , leaving an inner (blue) area featuring unperturbed bulk properties and a surrounding (light blue) area fully depleted by electrons (a);  $2L_D < D < 2L_{SCL}$ , with the grain completely depleted by bulk electrons but a band bending larger than the thermal energy (b); and  $D < 2L_D$ , with the grain completely depleted by bulk electrons and band bending smaller than the thermal energy (c). Relationship among the response amplitude (toward 25 ppm of acetone, measured at the working temperature of 300 °C), the surface area ( $S_{BET}$ ), and the  $2L_D/D_{XRD}$  ratio (d).

$2L_{SCL} < D$ , the band structure recovers the bulk condition in the inner part of the crystallite (Figure 8a); (ii) if  $2L_D < D < 2L_{SCL}$ , the band bending has no more room to restore the bulk condition, but there is still an appreciable bending, i.e., the difference between the maximum and minimum of the band is larger than thermal energy (Figure 8b); (iii) if  $D < 2L_D$ , the band bending is lower than the thermal energy of electrons and the material falls in the so-called flat band condition (Figure 8c).

Concerning the present samples, all of the measured/calculated morphological (XRD, TEM), electronic ( $E_{vf}$  and  $L_D$  from XPS data), and textural (specific surface area ( $S_{BET}$ )) properties clearly suggest basic medium as the most effective synthesis condition to achieve a microstructure suitable for gas sensing. In particular, the material treated at low temperature (TOB<sup>90</sup>) features the optimal structure.

On the other hand, all gas-sensing measurements are consistent with the opposite behavior: the response amplitude systematically decreases with the increase in the surface area. As an example, the response to 25 ppm of acetone at the temperature of 300 °C is shown in Figure 8d. Similarly, with respect to the  $2L_D/D$  ratio, a counterintuitive behavior can be observed: the TOA<sup>600</sup> sample is the only one featuring a bulk inner region ( $2L_D/D < 1$ ) not affected by gas-sensing phenomena, but it is much more performing than all other samples working in the complete depletion regime.

Considering also the anomalous response exhibited by TOB samples to NO<sub>2</sub>, all of these results suggest that additional mechanisms dominate the gas-sensing mechanism. Electrical and gas-sensing results indicate that samples are first classified according to the preparation conditions, in particular the acidic/basic preparation conditions, which leave potassium residuals in different amounts, larger for samples prepared without acid (Table 2, XPS measurements).

The presence of potassium does not have much effect on the Fermi-level energy (as reported in Table 2,  $E_{vf}$  is the same for TOA<sup>90</sup> and TOB<sup>90</sup> samples) but deeply influences the surface chemistry of materials. Its segregation at the grain surface is likely the reason of the anomalous response of TOB samples to NO<sub>2</sub> and the suppressed response to reducing gases. Additionally, the treatment at 600 °C promotes the stabilization of

grains according to a more crystalline degree, as suggested by the narrower Raman peaks, which has been proposed in the literature as beneficial for gas sensing.<sup>81</sup>

These results provide an important reference for the synthesis of nanomaterials. Indeed, effects arising from residual contamination in metal oxide nanostructures have been weakly investigated, especially concerning their impact on device and gas sensor performance. Some studies have been reported focusing mainly on chlorides, showing detrimental effects in terms of surface area<sup>82</sup> and modifications in the reaction mechanism of SnO<sub>2</sub> with CO, the latter slightly reducing (by a factor of 2) the response amplitude to CO for samples prepared from tin tetrachloride with respect to that for samples prepared from tin hydroxide acetate.<sup>83</sup> Nevertheless, none of these previous studies show effects comparable to those observed in the present work, in which the whole set of morphological, structural, electrical, and gas-sensing measurements suggests the capability of K to decreasing the response to gases by orders of magnitude, despite a clear opposite trend in the material microstructure.

#### 4. CONCLUSIONS

Tin dioxide nanopowders were prepared through the hydrothermal treatment of a commercial colloidal tin dioxide suspension including potassium counterions. Fine-tuning of pH conditions and nature of the thermal post-treatment yielded tetragonal SnO<sub>2</sub> nanoparticles with crystallite sizes ranging from 7.3 to 9.7 nm and BET specific areas comprised between 61 and 106 m<sup>2</sup>·g<sup>-1</sup>. The nanopowders obtained consist of a porous network of aggregated nanoparticles, and the mesoporosity observed is corresponding to the interparticle space. In the presence of reducing (H<sub>2</sub>, CO, acetone or ethanol) and oxidizing (NO<sub>2</sub>) gases, these SnO<sub>2</sub> nanoparticles led to highly sensitive, reversible, and reproducible responses. The best sensing performances were obtained by employing SnO<sub>2</sub> nanoparticles prepared under acidic conditions and calcined in air because of a lower amount of potassium cations and higher crystallinity. This study suggests the detrimental influence of a small amount of alkali metal cations on the gas-sensing response of tin dioxide nanoparticles although the material nanostructure fulfills all of the requirements for good

sensor responses. The careful determination of the surface chemical composition of tin oxide nanoparticles appears to be a key parameter for gas-sensing properties, which opens the way for a new approach for the rationalization of gas-sensing responses.

## ■ ASSOCIATED CONTENT

### Supporting Information

The Supporting Information is available free of charge on the ACS Publications website at DOI: 10.1021/acsami.7b18140.

FTIR spectra and complementary HR-TEM and XPS data (PDF)

## ■ AUTHOR INFORMATION

### Corresponding Author

\*E-mail: thierry.toupance@u-bordeaux.fr.

### ORCID

Andrea Ponzoni: 0000-0001-9955-5118

Thierry Toupance: 0000-0001-8234-7064

### Funding

This work was partly supported by the Erasmus Mundus Joint Doctoral program International Doctoral School in Functional Materials for Energy, Information Technology and Health (Szu-Hsuan Lee fellowship) and the French-German University (UFA Doctoral College in Functional Materials for Energy and Information Technology) and was carried out within the framework of European Multifunctional Material Institute.

### Notes

The authors declare no competing financial interest.

## ■ ACKNOWLEDGMENTS

Dr. Thierry Tassaing (ISM), Dr. Christine Labrugère (PLACAMAT), and Marion Gaillot (PLACAMAT) are acknowledged for their precious assistance for recording the Raman and XPS spectra and HR-TEM images, respectively.

## ■ REFERENCES

- (1) Tsujita, W.; Yoshino, A.; Ishida, H.; Morizumi, T. Gas Sensor Network for Air-Pollution Monitoring. *Sens. Actuators, B* **2005**, *110*, 304–311.
- (2) Choi, N. J.; Lee, H. K.; Moon, S. E.; Yang, W. S. Fast Response Formaldehyde Gas Sensor for USN Application. *Sens. Actuators, B* **2012**, *175*, 132–136.
- (3) Ryabtsev, S. V.; Shaposhnick, A. V.; Lukin, A. N.; Domashevskaya, E. P. Application of Semiconductor Gas Sensors for Medical Diagnostics. *Sens. Actuators, B* **1999**, *59*, 26–29.
- (4) Barsan, N.; Koziej, D.; Weimar, U. Metal Oxide-based gas sensor research: How to? *Sens. Actuators, B* **2007**, *121*, 18–35.
- (5) Fan, K.; Guo, J.; Cha, L.; Chen, Q.; Ma, J. Atomic Layer Deposition of ZnO onto Fe<sub>2</sub>O<sub>3</sub> Nanoplates for Enhanced H<sub>2</sub>S Sensing. *J. Alloys Compd.* **2017**, *698*, 336–340.
- (6) Deng, X.; Zhang, L.; Guo, J.; Chen, Q.; Ma, J. ZnO Enhanced NiO-based gas sensors towards ethanol. *Mater. Res. Bull.* **2017**, *90*, 170–174.
- (7) Nagasawa, M.; Shionoya, S.; Makishima, S. Vapor Reaction Growth of SnO<sub>2</sub> Single Crystals and their Properties. *Jpn. J. Appl. Phys.* **1965**, *4*, 195–202.
- (8) Liu, H.; Wan, Q. Low-voltage SnO<sub>2</sub> Nanowire Transistors Gated by Solution-processed Chitosan-based Proton Conductors. *Nanoscale* **2012**, *4*, 4481–4484.
- (9) Barsan, N.; Schweizer-Berberich, M.; Göpel, W. Fundamental and Practical Aspects in the Design of Nanoscaled SnO<sub>2</sub> Gas Sensors: A Status Report. *Fresenius' J. Anal. Chem.* **1999**, *365*, 287–304.
- (10) Wu, S.; Cao, H.; Yin, S.; Liu, X.; Zhang, X. Amino Acid-Assisted Hydrothermal Synthesis and Photocatalysis of SnO<sub>2</sub> Nanocrystals. *J. Phys. Chem. C* **2009**, *113*, 17893–17898.
- (11) Cheng, G.; Chen, J.; Ke, H.; Shang, J.; Chu, R. Synthesis, Characterization and Photocatalysis of SnO<sub>2</sub> Nanorods with Large Aspect Ratio. *Mater. Lett.* **2011**, *65*, 3327–3329.
- (12) Luo, L.-B.; Liang, F.-X.; Jie, J.-S. Sn-catalyzed Synthesis of SnO<sub>2</sub> Nanowires and their Optoelectronic Characteristics. *Nanotechnology* **2011**, *22*, No. 485701.
- (13) Hu, R.; Ouyang, Y.; Liang, T.; Wang, H.; Liu, J.; Chen, J.; Yang, C.; Yang, L.; Zhu, M. Stabilizing the Nanostructure of SnO<sub>2</sub> Anodes by Transition metals: A Route to Achieve High Initial Coulombic Efficiency and Stable Capacities for Lithium Storage. *Adv. Mater.* **2017**, *29*, No. 1605006.
- (14) Wang, Y.; Tian, J.; Fei, C.; Lv, L.; Liu, X.; Zhao, Z.; Cao, G. Microwave-Assisted Synthesis of SnO<sub>2</sub> Nanosheets Photoanodes for Dye-Sensitized Solar Cells. *J. Phys. Chem. C* **2014**, *118*, 25931–25938.
- (15) Abd-Ellah, M.; Bazargan, S.; Thomas, J.; Rahman, M. A.; Srivastava, S.; Wang, X.; Heinig, N. F.; Leung, K. T. Hierarchical Tin Oxide Nanostructures for Dye-Sensitized Solar Cell Application. *Adv. Electron. Mater.* **2015**, *1*, No. 1500032.
- (16) Yang, P.; Zhao, D.; Margolese, D. I.; Chmelka, B. F.; Stucky, G. D. Generalized Syntheses of Large-pore Mesoporous Metal Oxides with Semicrystalline Frameworks. *Nature* **1998**, *396*, 152–155.
- (17) Ba, J.; Polleux, J.; Antonietti, M.; Niederberger, M. Non-aqueous Synthesis of Tin Oxide Nanocrystals and Their Assembly into Ordered Porous Mesoporous Structures. *Adv. Mater.* **2005**, *17*, 2509–2512.
- (18) Li, L. L.; Zhang, W.-M.; Yuan, Q.; Li, Z.-X.; Fang, C.-J.; Sun, L.-D.; Wan, L.-J.; Yan, C.-H. Room Temperature Ionic Liquids Assisted Green Synthesis of Nanocrystalline Porous SnO<sub>2</sub> and Their Gas Sensor Behaviors. *Cryst. Growth Des.* **2008**, *8*, 4165–4171.
- (19) Gurlo, A. Interplay between O<sub>2</sub> and SnO<sub>2</sub>: Oxygen Ionosorption and Spectroscopic Evidence for Adsorbed Oxygen. *ChemPhysChem* **2006**, *7*, 2041–2052.
- (20) Gurlo, A.; Riedel, R. In Situ and Operando Spectroscopy for Assessing Mechanism of Gas Sensing. *Angew. Chem., Int. Ed.* **2007**, *46*, 3826–3848.
- (21) Xu, C.; Tamaki, J.; Miura, N.; Yamazoe, N. Grain Size Effects on Gas Sensitivity of Porous SnO<sub>2</sub>-based Element. *Sens. Actuators, B* **1991**, *3*, 147–155.
- (22) Huang, J. N.; Matsunaga, K.; Shimanoe, N.; Yamazoe, N.; Kunitake, T. Nanotubular SnO<sub>2</sub> Templated by Cellulose Fibers: Synthesis and Gas Sensing. *Chem. Mater.* **2005**, *17*, 3513–3518.
- (23) Armelao, L.; Barreca, D.; Bontempi, E.; Canevali, C.; Depero, L. E.; Mari, C. M.; Ruffo, R.; Scotti, R.; Tondello, E.; Morazzoni, F. Can Electron Paramagnetic Resonance Measurements Predict the Electrical Sensitivity of SnO<sub>2</sub>-Based Film? *Appl. Magn. Reson.* **2002**, *22*, 89–100.
- (24) Canevali, C.; Mari, C. M.; Mattoni, M.; Morazzoni, F.; Nodari, L.; Ruffo, U.; Ruffo, R.; Scotti, R. Interaction of NO with Nanosized Ru-, Pd-, and Pt-Doped SnO<sub>2</sub>: Electron Paramagnetic Resonance, Mössbauer, and Electrical Investigation. *J. Phys. Chem. B* **2005**, *109*, 7195–7202.
- (25) D'Arienzo, M.; Cristofori, D.; Scotti, R.; Morazzoni, F. New Insight into the SnO<sub>2</sub> Sensing Mechanism Based on the Properties of Shape Controlled Tin Oxide Nanoparticles. *Chem. Mater.* **2013**, *25*, 3675–3686.
- (26) Yamazoe, N.; Shimanoe, K. Role of Shape and Size of Component Crystals in Semiconductor Gas Sensors. I. Response to Oxygen. *J. Electrochem. Soc.* **2008**, *155*, J85–J92.
- (27) Yamazoe, N.; Shimanoe, K. Role of Shape and Size of Component Crystals in Semiconductor Gas Sensors. II. Response to NO<sub>2</sub> and H<sub>2</sub>. *J. Electrochem. Soc.* **2008**, *155*, J93–J98.
- (28) Yamazoe, N. New Approaches for Improving Semiconductor Gas Sensors. *Sens. Actuators, B* **1991**, *5*, 7–19.
- (29) Panchapakesan, B.; DeVoe, D. L.; Widmaier, M. K.; Cavicchi, R.; Semancik, S. Nanoparticle Engineering and Control of Tin Oxide Microstructures for Chemical Microsensor Applications. *Nanotechnology* **2001**, *12*, 336–349.



- (30) Rumyantseva, M.; Kovalenko, V.; Gaskov, A.; Makshina, E.; Yuschenko, V.; Ivanova, I.; Ponzoni, A.; Faglia, G.; Comini, E. Nanocomposites SnO<sub>2</sub>/Fe<sub>2</sub>O<sub>3</sub>: Sensor and Catalytic Properties. *Sens. Actuators, B* **2006**, *118*, 208–214.
- (31) Lian, X.; Li, Y.; Tong, X.; Zou, Y.; Liu, X.; An, D.; Wang, Q. Synthesis of Ce-doped SnO<sub>2</sub> Nanoparticles and Their Acetone Gas Sensing Properties. *Appl. Surf. Sci.* **2017**, *407*, 447–455.
- (32) Singh, G.; Kohli, N.; Singh, R. C. Sensitive and Selective Ethanol Sensor Based on Zn-doped SnO<sub>2</sub> Nanostructures. *J. Mater. Sci. Mater. Electron.* **2017**, *28*, 13013–13023.
- (33) Kida, T.; Doi, T.; Shimanoe, K. Synthesis of Monodispersed SnO<sub>2</sub> Nanocrystals and Their Remarkably High Sensitivity to Volatile Organic Compounds. *Chem. Mater.* **2010**, *22*, 2662–2667.
- (34) Cho, I.; Kang, K.; Yang, D.; Yun, J.; Park, I. Localized Liquid-Phase Synthesis of Porous SnO<sub>2</sub> Nanotubes on MEMS Platform for Low-Power, High Performance Gas Sensors. *ACS Appl. Mater. Interfaces* **2017**, *9*, 27111–27119.
- (35) Li, T.; Zeng, W. New Insight into the Gas Sensing Performance of SnO<sub>2</sub> Nanorod-assembled Urchins Based on their Assembly Density. *Ceram. Int.* **2017**, *43*, 728–735.
- (36) Kolmakov, A.; Zhang, Y.; Cheng, G.; Moskovits, M. Detection of CO and O<sub>2</sub> Using Tin Oxide Nanowire Sensors. *Adv. Mater.* **2003**, *15*, 997–1000.
- (37) Li, F.; Chen, Y.; Ma, J. Porous SnO<sub>2</sub> nanoplates for Highly Sensitive NO Detection. *J. Mater. Chem. A* **2014**, *2*, 7175–7178.
- (38) Von Hagen, R.; Sneha, M.; Mathur, S. Ink-jet Printing of Hollow SnO<sub>2</sub> Nanospheres for Gas Sensing Applications. *J. Am. Ceram. Soc.* **2014**, *97*, 1035–1040.
- (39) Zhang, J.; Liu, X.; Wu, S.; Xu, M.; Guo, X.; Wang, S. Au Nanoparticle-decorated Porous SnO<sub>2</sub> Hollow Spheres: A New Model for a Chemical Sensor. *J. Mater. Chem.* **2010**, *20*, 6453–6459.
- (40) Hübner, M.; Koziej, D.; Bauer, M.; Barsan, N.; Kvashnina, K.; Rossell, M. D.; Weimar, U.; Grunwaldt, J.-D. The Structure and Behavior of Platinum in SnO<sub>2</sub>-Based Sensors under Working Conditions. *Angew. Chem., Int. Ed.* **2011**, *50*, 2841–2844.
- (41) Suematsu, K.; Kodama, K.; Ma, N.; Yuasa, M.; Kida, T.; Shimanoe, K. Role of Vanadium Oxide and Palladium Multiple Loading on the Sensitivity and Recovery Kinetics of Tin Dioxide Based Gas Sensors. *RSC Adv.* **2016**, *6*, 5169–5176.
- (42) Zakrzewski, J.; Domanski, W.; Chaitas, P.; Laopoulos, T. Improving Sensitivity and Selectivity of SnO<sub>2</sub> Gas Sensors by Temperature Variation. *IEEE Trans. Instrum. Meas.* **2006**, *55*, 14–20.
- (43) Li, Y.; Deng, D.; Xing, X.; Chen, N.; Liu, X.; Xiao, X.; Wang, Y. A High Performance Methanol Gas Sensor Based on Palladium-platinum-In<sub>2</sub>O<sub>3</sub> Compositing Nanocrystalline SnO<sub>2</sub>. *Sens. Actuators, B* **2016**, *237*, 133–141.
- (44) Hu, D.; Han, B.; Deng, S.; Feng, Z.; Wang, Y.; Popovic, J.; Nuskol, M.; Wang, Y.; Djerdj, I. Novel Mixed Phase SnO<sub>2</sub> Nanorods Assembled with SnO<sub>2</sub> Nanocrystals for Enhancing Gas-Sensing Performance toward Isopropanol Gas. *J. Phys. Chem. C* **2014**, *118*, 9832–9840.
- (45) Renard, L.; Elhamzaoui, H.; Jousseume, B.; Toupance, T.; Laurent, G.; Ribot, F.; Saadaoui, H.; Brötz, J.; Fuess, H.; Riedel, R.; Gurlo, A. Low-temperature H<sub>2</sub> Sensing in Self-assembled Organotin Thin Films. *Chem. Commun.* **2011**, *47*, 1464–1466.
- (46) Renard, L.; Brötz, J.; Fuess, H.; Gurlo, A.; Riedel, R.; Toupance, T. Hybrid Organotin and Tin Oxide-based Thin Films Processed from Alkynylorganotinols: Synthesis, Characterization, and Gas Sensing Properties. *ACS Appl. Mater. Interfaces* **2014**, *6*, 17093–17101.
- (47) Russo, P. A.; Donato, N.; Leonardi, S. G.; Baek, S.; Conte, D. E.; Neri, G.; Pinna, N. Room-Temperature Hydrogen Sensing with Heteronanostructures Based on Reduced Graphene Oxide and Tin Oxide. *Angew. Chem., Int. Ed.* **2012**, *51*, 11053–11057.
- (48) Green, A. N. M.; Palomares, E.; Haque, S.; Kroon, J. M.; Durrant, J. R. Charge Transport versus Recombination in Dye-sensitized Solar Cells Employing Nanocrystalline TiO<sub>2</sub> and SnO<sub>2</sub> Films. *J. Phys. Chem. B* **2005**, *109*, 12525–12533.
- (49) Cojocaru, L.; Olivier, C.; Toupance, T.; Sellier, E.; Hirsch, L. Size and Shape Fine-Tuning of SnO<sub>2</sub> Nanoparticles for Highly Efficient and Stable Dye-Sensitized Solar Cells. *J. Mater. Chem. A* **2013**, *1*, 13789–13799.
- (50) Maeda, S.; Armes, S. P. Preparation and Characterization of Polypyrrole-Tin(IV) Oxide Nanocomposite Colloids. *Chem. Mater.* **1995**, *7*, 171–178.
- (51) Harrison, P. G.; Guest, A. Tin Oxide Surfaces. Part 17.—An Infrared and Thermogravimetric Analysis of the Thermal Dehydration of Tin(IV) Oxide gel. *J. Chem. Soc. Faraday Trans 1* **1987**, *83*, 3383–3397.
- (52) Harrison, P. G.; Lloyd, N. C.; Daniell, W.; Bailey, C.; Azelee, W. Evolution of Microstructure during the Thermal Activation of Chromium-Promoted Tin(IV) Oxide Catalysts: An FT-IR, FT-Raman, XRD, TEM, and XANES/EXAFS Study. *Chem. Mater.* **1999**, *11*, 896–909.
- (53) Ocaña, M.; Serna, C. J.; Matijevic, E. Formation of “monodispersed” SnO<sub>2</sub> powders of various morphologies. *Colloid Polym. Sci.* **1995**, *273*, 681–686.
- (54) Hiratsuka, R. S.; Pulcinelli, S. H.; Santilli, C. V. Formation of SnO<sub>2</sub> Gels from Dispersed Sols in Aqueous Colloidal Solutions. *J. Non-Cryst. Solids* **1990**, *121*, 76–83.
- (55) Sangeetha, P.; Sasirekha, V.; Ramakrishnan, V. Micro-Raman Investigation of Tin Dioxide Nanostructured Material Based on Annealing Effect. *J. Raman Spectrosc.* **2011**, *42*, 1634–1639.
- (56) Ansari, S. G.; Dar, M. A.; Dhage, M. S.; Kim, Y. S.; Ansari, Z. A.; Al-Hajry, A.; Shin, H. S. A Novel Method for Preparing Stoichiometric SnO(2) Thin Films at Low Temperature. *Rev. Sci. Instrum.* **2009**, *80*, No. 045112.
- (57) Vock, S. M.; Sharygin, L. M.; Bobovich, Y. S.; Gonchar, V. F.; Loguntsev, E. N. Size Effects in Raman Light-Scattering Spectra of Hydrate Tin Dioxide. *J. Appl. Spectrosc.* **1986**, *44*, 636–639.
- (58) Wang, J. X.; Liu, D. F.; Yan, X. Q.; Yuan, H. J.; Ci, L. J.; Zhou, Z. P.; Gao, Y.; Song, L.; Liu, L. F.; Zhou, W. Y.; Wang, G.; Xie, S. S. Growth of SnO<sub>2</sub> Nanowires with Uniform Branched Structures. *Solid State Commun.* **2004**, *130*, 89–94.
- (59) The average crystallite size is calculated from the Scherrer relation  $t = (0.9\lambda)/(\beta \cos \theta)$ , where  $\lambda$  is the wavelength,  $\beta$  is the angular half-width of the  $hkl$  peak for the studied sample and  $\theta$  is the Bragg angle for the chosen  $hkl$  reflection. Jenkins, R.; Synder, R. L. *Introduction to X-ray Powder Diffractometry*; Winefordner, J. D., Ed.; John Wiley and Sons Inc.: New York, 1996; Chapter 3, pp 89–91.
- (60) Wang, X.; Han, X.; Xie, S.; Kuang, Q.; Jiang, Y.; Zhang, S.; Mu, X.; Chen, G.; Xie, Z.; Zheng, L. Controlled Synthesis and Enhanced Catalytic and Gas-Sensing Properties of Tin Dioxide Nanoparticles with Exposed High-Energy Facets. *Chem. Eur. J.* **2012**, *18*, 2283–2289.
- (61) Moulder, J. F.; Stickle, W. F.; Sobol, P. E.; Bomben, K. D. *Handbook of X-ray Photoelectron Spectroscopy*; Physical Electronics, Inc.: Eden Prairie, 1995.
- (62) Renard, L.; Babet, O.; Saadaoui, H.; Fuess, H.; Brötz, J.; Gurlo, A.; Arveux, E.; Klein, A.; Toupance, T. Nanoscaled Tin Dioxide Films Processed from Organotin-based Hybrid Materials: An Organometallic Route Towards Metal Oxide Gas Sensors. *Nanoscale* **2012**, *4*, 6806–6813.
- (63) Körber, C.; Ágoston, P.; Klein, A. Surface and Bulk Properties of Sputter Deposited Undoped and Sb-doped SnO<sub>2</sub> Thin Films. *Sens. Actuators, B* **2009**, *139*, 665–672.
- (64) Körber, C.; Harvey, S. P.; Mason, T. O.; Klein, A. Barrier Heights at the SnO<sub>2</sub>/Pt Interface: *In situ* Photoemission and Electrical Properties. *Surf. Sci.* **2008**, *602*, 3246–3252.
- (65) Batzill, M.; Diebold, U. The Surface and Materials Science of Tin Oxide. *Prog. Surf. Sci.* **2005**, *79*, 47–154.
- (66) Körber, C.; Wachau, A.; Ágoston, P.; Albe, K.; Klein, A. Self-Limited Oxygen Exchange Kinetics at SnO<sub>2</sub> Surfaces. *Phys. Chem. Chem. Phys.* **2011**, *13*, 3223–3226.
- (67) Sze, S. M.; Kwok, K. N. G. *Physics of Semiconductor Devices*, 3rd ed.; Wiley: Hoboken, NJ, 2007; Chapter 1.
- (68) Sing, K. S. W. Reporting Physisorption Data for Gas/Solid Systems with Special Reference to the Determination of Surface Area and Porosity. *Pure Appl. Chem.* **1985**, *57*, 603–619.

- (69) Toupance, T.; Elhamzaoui, H.; Jousseau, B.; Riague, H.; Sadeddin, I.; Campet, G.; Broetz, J. Bridged Polystannoxane: A New Route toward Nanoporous Tin Dioxide. *Chem. Mater.* **2006**, *18*, 6364–6372.
- (70) Moseley, P. T.; Williams, D. E. In *Techniques and Mechanisms in Gas Sensing*; Moseley, P. T., Norris, J. O. W., Williams, D. E., Eds.; Adam Hilger: Bristol, England, 1991.
- (71) Li, Y.-X.; Guo, Z.; Su, Y.; Jin, X.-B.; Tang, X.-H.; Huang, J.-R.; Huang, X.-J.; Li, M.-Q.; Liu, J.-H. Hierarchical Morphology-Dependent Gas-Sensing Performances of Three-Dimensional SnO<sub>2</sub> Nanostructures. *ACS Sens.* **2017**, *2*, 102–110.
- (72) Hwang, I.-S.; Kim, S.-J.; Choi, J.-K.; Jung, J.-J.; Yoo, D. J.; Dong, K.-Y.; Ju, B.-K.; Lee, J.-H. Large-scale Fabrication of Highly Sensitive SnO<sub>2</sub> Nanowire Network Gas Sensors by Single Step Vapor Phase Growth. *Sens. Actuators, B* **2012**, *165*, 97–103.
- (73) Hwang, I.-S.; Choi, J.-K.; Woo, H.-S.; Kim, S.-J.; Jung, S.-Y.; Seong, T.-Y.; Kim, I.-D.; Lee, J.-H. Facile Control of C<sub>2</sub>H<sub>5</sub>OH Sensing Characteristics by Decorating Discrete Ag Nanoclusters on SnO<sub>2</sub> Nanowire Networks. *ACS Appl. Mater. Interfaces* **2011**, *3*, 3140–3145.
- (74) Von Hagen, R.; Sneha, M.; Mathur, S. Ink-jet Printing of Hollow SnO<sub>2</sub> Nanospheres for Gas Sensing Applications. *J. Am. Ceram. Soc.* **2014**, *97*, 1035–1040.
- (75) Song, F.; Su, H.; Han, J.; Xu, J.; Zhang, D. Controllable Synthesis and Gas Response of Biomimetic SnO<sub>2</sub> with Architecture Hierarchy of Butterfly Wings. *Sens. Actuators, B* **2010**, *145*, 39–45.
- (76) Hieu, N. V.; Kim, H.-R.; Ju, B.-K.; Lee, J.-H. Enhanced Performance of SnO<sub>2</sub> Nanowires Ethanol Sensor by Functionalizing with La<sub>2</sub>O<sub>3</sub>. *Sens. Actuators, B* **2008**, *133*, 228–234.
- (77) Shaalan, N. M.; Yamazaki, T.; Kikuta, T. Effect of Micro-electrode geometry on NO<sub>2</sub> Gas-sensing Characteristics of One-dimensional Tin Dioxide Nanostructure Microsensors. *Sens. Actuators, B* **2011**, *156*, 784–790.
- (78) Kim, H. W.; Na, H. G.; Kwon, Y. G.; Kang, S. Y.; Choi, M. S.; Bang, J. H.; Wu, P.; Kim, S. S. Microwave-Assisted Synthesis of Graphene–SnO<sub>2</sub> Nanocomposites and Their Applications in Gas Sensors. *ACS Appl. Mater. Interfaces* **2017**, *9*, 31667–31682.
- (79) Orton, J. W.; Powell, M. J. The Hall Effect in Polycrystalline and Powdered Semiconductors. *Rep. Prog. Phys.* **1980**, *43*, 1263–1307.
- (80) Barsan, N.; Weimar, U. Conduction Model of Metal Oxide Gas Sensors. *J. Electroceram.* **2001**, *7*, 143–167.
- (81) Antonik, M. D.; Schneider, J. E.; Wittman, E. L.; Snow, K.; Vetelino, J. F.; Lad, R. J. Microstructural Effects in WO<sub>3</sub> Gas-Sensing Films. *Thin Solid Films* **1995**, *256*, 247–252.
- (82) Shastri, A. G.; Datye, A.; Schwank, J. Influence of Chlorine on the Surface Area and Morphology of TiO<sub>2</sub>. *Appl. Catal.* **1985**, *14*, 119–131.
- (83) Pavelko, R. G.; Choi, J.-K.; Urakawa, A.; Yuasa, M.; Kida, T.; Shimanoe, K. H<sub>2</sub>O/D<sub>2</sub>O Exchange on SnO<sub>2</sub> Materials in the Presence of CO: Operando Spectroscopic and Electric Resistance Measurements. *J. Phys. Chem. C* **2014**, *118*, 2554–2563.



# Curriculum Vitae

## PERSONAL DATA:

### Szu-Hsuan Lee

Date and place of birth: 16/08/1987, Keelung (Taiwan)

Nationality: Taiwanese

Email address: aoutseize@gmail.com

## EDUCATION:

10/2014-10/2017 **University of Bordeaux (UB), France ; Technische Universität Darmstadt (TUD), Germany**

Erasmus Mundus IDS-FunMat PhD student

09/2010-01/2013 **Fu Jen Catholic University (FJU), New Taipei City, Taiwan**

Master of Science in Chemistry

09/2005-06/2009 **Fu Jen Catholic University (FJU), New Taipei City, Taiwan**

Bachelor of Science in Chemistry

09/2002-06/2005 **Taipei Municipal Nei Hu Senior High School (NHSH), Taipei, Taiwan**

## PUBLICATIONS:

03/2018 Finely Tuned SnO<sub>2</sub> Nanoparticles for Efficient Detection of Reducing and Oxidizing Gases: The Influence of Alkali Metal Cation on Gas-Sensing Properties

**Lee, S.-H.**; Galstyan, V.; Ponzoni, A.; Gonzalo-Juan, I.; Riedel, R.; Dourges, M.-A.; Nicolas, Y.; Toupance, T.

*ACS Appl. Mater. Interfaces*, **2018**, *10* (12), 10173–10184.

2013

1. **Dehydration induced 2D-to-3D Crystal-to-Crystal Network Re-Assembly and Ferromagnetism Tuning within Two Chiral Copper(II)-Tartrate Coordination Polymers**

Liu, Y.-H.; **Lee, S.-H.**; Chiang, J.-C.; Chen, P.-C.; Chien, P.-H.; Yang, C.-I.

*Dalton Trans.*, **2013**, *42*, 16857-16867.

2. **In-Situ Resolved Ligand Chirality in Preparing a Chiral 3D Zinc-Cyclopentane-Tetracarboxylate based Coordination Polymer**

Liu, Y.-H.; Peng, C.-C.; Lee, S.-H.; Chien, P.-H.; Wu, P.-C.

*CrystEngComm.*, **2013**, *15*, 10333-10339.

12/2012 **Design and Syntheses of Metal-Polycarboxylate Coordination Polymers and the Analyses of Magnetic and Luminescent Properties (Master Thesis)**

**CONFERENCES PRESENTATIONS:**

10/07/2017-13/07/2017

**Oral and poster presentation:** Selective gas sensors based on organooxotin-based and tin oxide-based materials, 13th International Conference on Materials Chemistry (MC13), Liverpool, UK

2015/2016/2017 **Oral and poster presentation:** Selective gas sensors based on organooxotin-based and tin oxide-based materials, IDS-FunMat training school annual meeting, Vallendar (Germany) /Bordeaux (France) /Aveiro (Portugal)

07/2012 **Poster presentation:** A Series of 4,4'-sulfonyldibenzolate based Coordination Polymers with Novel Net Topologies), American Crystallographic Association 62<sup>nd</sup> Annual Meeting, The Westin Boston Waterfront Hotel, Boston, USA

11/2011 **Poster presentation:** Luminescent Properties of a Cadmium based 3D Supramolecular Network), The 10th International Symposium on Organic Reactions (ISOR10), Keio University, Yokohama, Japan

**Titre:** Capteurs de gaz sélectifs à base de matériaux hybrides organooxoétain et d'oxyde d'étain

## **Résumé:**

L'objectif de cette recherche est d'explorer de nouvelles voies dans le domaine de la détection de gaz, en ajustant finement la nature chimique, la texture et la morphologie de la couche active pour concevoir de nouveaux capteurs de gaz sélectifs. Ainsi, l'obtention de matériau présentant une haute sélectivité vis-à-vis des gaz, constitue un enjeu majeur dans le domaine des capteurs de gaz. Notre approche est basée sur la conception de précurseurs moléculaires uniques - les alcynylorganoétains - qui contiennent toutes les fonctionnalités requises pour obtenir des matériaux hybrides stables par le procédé sol-gel, ces matériaux permettant une détection sélective des gaz nocifs/toxiques. Ensuite, les propriétés de détection de gaz de ces matériaux ont été comparées à celles des nanoparticules de dioxyde d'étain ( $\text{SnO}_2$ ), synthétisées à pression autogène.

Une série de matériaux fonctionnels à base d'organooxoétains a été déposée sous forme de films minces par le procédé d'enduction centrifuge, puis ces films ont été caractérisés par des mesures de XRD, FT-IR, RAMAN, AFM, SEM, TEM, sorption d'azote et TGA-DTA. Les études de détection de gaz montrent que l'un des oxydes d'organoétain hybride présente une réponse sélective de détection de gaz tels que le CO,  $\text{H}_2$ , l'éthanol, l'acétone et le  $\text{NO}_2$ , tandis que les nanoparticules  $\text{SnO}_2$  conduisent à une détection non sélective des mêmes gaz dans les mêmes conditions. Ainsi, la meilleure sélectivité vis-à-vis du CO (à 100 et 200 ppm), de  $\text{H}_2$  (à 100, 200 et 400 ppm) et de  $\text{NO}_2$  (à 1, 2, 4 et 8 ppm) a été obtenue à 100 °C pour le matériau hybride organostannique tandis que ce matériau ne conduisait à aucune réponse avec l'éthanol et l'acétone. Par ailleurs, les films de  $\text{SnO}_2$  nanoparticulaires sont sensibles à tous les gaz testés à de faibles concentrations (CO: 10 ~ 100 ppm,  $\text{NO}_2$ : 0.5 à 4 ppm,  $\text{H}_2$ : 100 à 800 ppm, acétone: 25 à 200 ppm, éthanol : 10 ~ 100 ppm) sur une plage de température comprise entre 200 et 400 °C. En outre, la sélectivité des matériaux  $\text{SnO}_2$  vis-à-vis de  $\text{NO}_2$  (entre 0.5 à 4 ppm) peut être optimisée en contrôlant bien la température de détection.

Enfin, les matériaux à base d'organoétains et de dioxyde d'étain présentent une capacité de détection de gaz très élevée, à de faibles concentrations en gaz. Ces résultats ont permis de développer une classe de matériaux entièrement nouvelle pour la détection sélective de gaz et offrent la possibilité d'intégrer une fonctionnalité organique dans les oxydes métalliques capables de détecter les gaz.

**Mots clés:** sélectivité, capteurs de gaz, oxyde d'étain, matériaux hybrides

**Title:** Selective gas sensors based on tin dioxide and hybrid oxohydroxoorganotin materials

**Abstract:**

The ultimate objective of this research is to draw new prospects in the gas sensing field by finely tuning the chemical nature, the texture and the morphology of the active layer to develop new type selective gas sensors. As an efficient gas sensor, selectivity is a remarkable parameter. Our approach is based on the design of molecular single precursors – alkynylorganotins which contain suitable functionalities required to obtain stable hybrid materials by the sol-gel method exhibiting selective gas detection towards harmful/toxic gases. Their gas sensing properties have been compared with those of tin dioxide (SnO<sub>2</sub>) nanoparticles synthesized by the hydrothermal route.

A series of functional oxohydroxoorganotin-based materials (**OXT5a**, **OXT5b**, **OXT5c**, and **OXT5d**) as well as the SnO<sub>2</sub> nanoparticles have been processed as films by the spin or drop coating method and characterized by XRD, FT-IR, RAMAN, AFM, SEM, TEM, N<sub>2</sub> sorption and TGA-DTA measurements. Gas sensing studies show that one of the hybrid oxohydroxoorganotins exhibits an outstanding selective gas sensing response towards various gases, such as CO, H<sub>2</sub>, ethanol, acetone and NO<sub>2</sub> whereas SnO<sub>2</sub> nanoparticles present no obvious selective gas sensing ability under the same experimental condition. Thus, the best gas selectivity toward 100, 200, and 400 ppm of H<sub>2</sub> (gas response: 12.65, 29.57 and 48.89) and 2, 4, and 8 ppm of NO<sub>2</sub> (gas response: 18.84, 48.13 and 70.87 ppm) was achieved respectively at 100 °C and 200 °C for hybrid oxohydroxoorganotin-based film (**OXT5a**). On the other hand, SnO<sub>2</sub> nanoparticles which prepared via a hydrothermal route under acidic and basic conditions, of a commercial tin dioxide particle suspension including potassium counterions, show how the impact of the counterion residuals on gas sensing behavior to an extent rather than size and surface area effects.

Finally, both oxohydroxoorganotin-based and tin dioxide materials display superior gas sensing ability at low gas concentrations and even at low operating temperature which opens a fully new class of gas sensing materials as well as a new possibility to integrate organic functionality in gas sensing metal oxides.

**Keywords:** gas sensors, selectivity, tin dioxide, tin-based hybrid materials